120
82

AN ABSOLUTE MEASUREMENT OF THE PHOTODISINTEGRATION OF HELIUM-4

by

Richard Thurston Jones

Dissertation submitted to the Faculty of the
Virginia Polytechnic Institute and State University
in partial fulfillment of the requirements for the degree of

DOCTOR OF PHILOSOPHY
in
Physics

APPROVED:

D. A. Jenkins, Chairman

A. L. Ritter

T. Mizutani

J. Ficenec

P. T. Debevec

D. Schutt

December, 1988

Blacksburg, Virginia

AN ABSOLUTE MEASUREMENT OF THE PHOTODISINTEGRATION OF HELIUM-4

by

Richard Thurston Jones

Committee Chairman: David A. Jenkins
Physics

(ABSTRACT)

A measurement of the differential cross section has been performed for the photodisintegration of ^{4}He into a proton plus a triton. This reaction is highly sensitive to the electromagnetic currents in the nucleus which arise from the exchange of mesons between nucleons. The study of light nuclei such as ^{4}He , whose nucleonic structure is the simplest, holds the promise of perfecting a microscopic theory of nuclear dynamics, in which nuclear structure and reactions are understood in terms of fundamental particle interactions. The measurement was performed with a tagged-photon beam, using a large solid-angle charged particle detector developed for this and other similar experiments. The measurement was performed within the photon energy range between 63 and 71 MeV, and divided into four energy bins of 2 MeV each. The measurement of the differential cross section was confined to the angular range 36° -141° in the center-of-mass reference frame. The total cross section was determined to within a total uncertainty of 5%. The angular distribution was fitted to an expansion of Legendre polynomials in $\cos\theta$ including terms of order 0-3. This measurement is in agreement with a previous measurement, and improves on the precision of the total cross section from the previous measurement by a factor of 6. A comparison is made with several theoretical calculations, and a qualitative

agreement is found. These data suggest refinements to these calculations, in order to account for the quantitative differences.

Acknowledgements

I would like to express my gratitude to my advisor, Prof. David Jenkins for his guidance and support through my years as his student. His helpful criticism in the preparation of this thesis is also acknowledged. I would like to also thank Prof. Paul Debevec of the University of Illinois, who led the experimental program in which I participated, for what I have learned from him, and also the interest he has taken in my success. I acknowledge Dr Jonathan Knott, the originator of the LASA detector, with whom it has been a pleasure to work. The assistance of Dr Peter Harty throughout the duration of this project, and particularly in the analysis of the data presented in this thesis, is gratefully acknowledged. I would like to extend a general thankyou to the faculty of the VPI Physics Department, and particularly the members of my committee, for their part in my education. My final thanks are to my wife , for her selfless patience and support throughout my time as a student.

Contents

List of Tables

List of Figures

Chapter 1

Introduction

1.1 Motivation

The existence of the atomic nucleus was discovered by Rutherford in an electromagnetic scattering experiment, in which alpha particles were scattered off a gold target. Much of what is known today about nuclear sizes and shapes is derived from electromagnetic scattering experiments involving electrons [1]. The advantage of electromagnetic studies of the nucleus is that the "probe" is well understood. In the framework of the fundamental quantum theory of electromagnetism (QED), the scattering between an incident charged particle and the nucleus takes place by the exchange of virtual photons. Since the electromagnetic coupling to the nucleus is via the photon, this suggests that one can alternatively study photon-nucleus scattering directly by scattering real photons.

The atomic nucleus is a cluster of neutrons and protons (nucleons) bound together by the strong force. In the fundamental theory of the strong force, known as quantum chromodynamics (QCD), protons and neutrons are not elementary particles, but are themselves bound states of quarks. The interaction between quarks, mediated by strongly interacting bosons called gluons, gives rise to a spectrum of tightly bound states of three quarks (baryons) and quark-antiquark pairs (mesons). The QCD condensation of quarks into baryons and mesons takes place at an energy much greater than the mass of the proton, which is about 1 GeV, whereas most of what is currently known about nuclei pertains to the "intermediate energy" region

below 1 GeV. In the intermediate energy regime, baryons (neutrons and protons) appear as fairly rigid objects, and their interaction is described in conventional nuclear theory, by the exchange of mesons, of which the pion is the most important.

The disparity between descriptions of the strong interaction in the QCD regime and the intermediate energy regime demonstrates the need for further investigation. If the two pictures are to be harmonized, the fundamental interaction of QCD must be shown to give rise to the potential which binds nucleons in the nucleus, and to generate observed nuclear structure and dynamics. On the part of intermediate energy physics, this objective requires an accurate knowledge of the nuclear interaction; hence precise measurements of intermediate energy nuclear processes are needed.

The difficulty of calculating the dynamics of a system of many interacting particles has necessitated the introduction of nuclear models, which incorporate approximations into the calculation of the particle motions in order to make the problem tractable. While nuclear models are useful for understanding the role of dominant processes in a reaction, it is difficult to distinguish disagreements with experimental data which arise out of poor approximations from those which arise from failure of the underlying nuclear interaction. For this reason, studies of the fundamental nuclear interaction have focused on the simplest nuclei, isotopes of hydrogen and helium. The static properties of the four lightest nuclei are given in Table 1.1.

The simplest interacting nuclear system is the deuterium (^{2}H) nucleus. The deuteron is a unique laboratory for investigation of the nuclear force in that the exact calculation of observable quantities, given a form for the two-body interaction, is straightforward. The precise values for the deuteron binding energy, charge radius, and magnetic moment, together with the nucleon-nucleon (N-N) scattering data, have served as powerful constraints on the form of the two-nucleon interaction. These data principally relate to the long-range part of the interaction, the force which acts between nucleons separated by distances beyond about 3 fm [2]. At

such distances, the force arises primarily from the exchange of single pions between weakly bound (on-shell) nucleons.

The general features of the deuterium and N-N scattering data are satisfied if the one-pion exchange potential is used, along with a repulsive core at small separation distances. Apart from fixing the average depth of the potential well, the data do not distinguish between the many ways of smoothly connecting the core to the tail, and hence are not useful in determining the details of the force at small distances. In the typical atomic nucleus, the mean separation between nucleons is approximately 1 fm, a regime where multiple-pion exchange processes are important, and where the nucleons are expected to be significantly modified by the nuclear medium (off-shell effects).

In contrast to the strong nuclear force, the electromagnetic interaction couples weakly to nucleons. Weak coupling means that the motions of the nucleons are only slightly disturbed by the photon, and that transition rates can be calculated by use of perturbation theory. In the process of nuclear photodisintegration, a photon is absorbed by a nucleus, which decays by emitting nucleons or nuclear fragments. In the case of the deuteron, photodisintegration results in a final state with a neutron and proton moving in opposite directions in the center-of-mass (c.m.) reference frame. Since the photon couples to electromagnetic charges and currents, it not only senses the nucleons, but also the mesons which are continuously exchanged between them. The photodisintegration cross section shows a significant sensitivity to mesonic currents in the deuteron, as well as off-shell effects [3]. Hadjimichael and Saylor [4] suggest that deuteron photodisintegration data may contain the signature of the quark substructure of nucleons, which is important when the nucleons are very close together.

As can be seen from Table 1.1, the deuteron is a relatively diffuse nuclear system. The ^{3}H and ^{3}He nuclei, the bound states of the $A = 3$ system, are significantly more dense. They form an isospin doublet, which means that the exchange of

the role of neutrons and protons transforms ^{3}H into ^{3}He , and vice versa. The isospin symmetry of the strong force implies that the binding energy and structure of the two nuclides are identical. The observed differences are primarily due to the electromagnetic asymmetry between neutron and proton. In spite of its increased complexity, the problem of three bodies interacting via pair-wise interactions can be solved "exactly". By an exact solution, it is meant that the equations of motion can be solved exactly, given a fundamental interaction, in a similar way that the two-body problem has rigorous solutions. The photodisintegration of the $A = 3$ nuclei has been calculated within this framework [5,6]. Experimental data on the photodisintegration of ^{3}H and ^{3}He [7] are in qualitative agreement with the theory [6]. There is some evidence that these data contain the signature of a three-body component in the nuclear force [8].

The ^{4}He nucleus is the most tightly bound of light nuclei. Also known as the alpha particle, this nuclide is emitted by heavy nuclei in alpha radioactive decay. The alpha particle is a self-conjugate nucleus, which means that it is invariant upon conjugation of protons and neutrons. The total spin is zero, and hence it has no static magnetic moment. In the context of the shell model, ^{4}He is a closed-shell nucleus, with four nucleons in the S-shell. The actual ground state of ^{4}He is not pure S-wave, but contains a small D-wave component as well [9].

Because of their intrinsic symmetry, closed-shell nuclei provide a unique proving ground for theoretical calculations of photonuclear processes [10,11]. Photodisintegration is the dominant photonuclear process below the pion threshold. The five possible channels for alpha photodisintegration are shown in Table 1.2. The single-nucleon knockout channels are the dominant ones. With a threshold around 20 MeV, the cross section for these processes peaks around 27 MeV, with a long monotonically-decreasing tail. These channels are the ones which have received the bulk of theoretical attention.

Above 26 MeV, the channel for breakup into a p-n pair plus a deuteron is

Table 1.1: Static properties of few-body nuclei [2], showing number of neutrons (N), number of protons (Z), isospin (I) and spin (J), nuclear binding energy (B.E. in MeV), rms charge radius (r_{rms} in 10^{-13} cm), and magnetic moment (μ in nuclear magnetons)

Nuclide	N	Z	I	J	B.E.	r_{rms}	μ
^{2}H	1	1	0	1	2.225	2.16	0.857
^{3}H	2	1	1/2	1/2	7.718	1.68	2.979
^{3}He	1	2	1/2	1/2	8.482	1.88	−2.128
^{4}He	2	2	0	0	28.296	1.63	0.000

Table 1.2: Properties of the five photodisintegration channels of ^{4}He , center-of-mass photon energy threshold in MeV, and two energy moments of the total channel cross section integrated from threshold up to 75 MeV. Data for channels 1-4 are taken from Ref. [13]. The $^4\mathrm{He}(\gamma, ^2\mathrm{H})^2\mathrm{H}$ channel data are taken from Ref. [14]

Scattering channel	Photodisintegration threshold (MeV)	$\int \sigma(k)dk$ (mb · MeV)	$\int \frac{\sigma(k)}{k}dk$ (mb)
$^4\mathrm{He}(\gamma, \mathrm{p})^3\mathrm{H}$	19.81	36.6 ± 0.8	1.09 ± 0.02
$^4\mathrm{He}(\gamma, \mathrm{n})^3\mathrm{He}$	20.58	36.9 ± 0.9	1.09 ± 0.02
$^4\mathrm{He}(\gamma, \mathrm{np})^2\mathrm{H}$	26.07	6.9 ± 1.0	0.19 ± 0.02
$^4\mathrm{He}(\gamma, \mathrm{nnpp})$	28.30	2.9 ± 1.0	0.06 ± 0.01
$^4\mathrm{He}(\gamma, ^2\mathrm{H})^2\mathrm{H}$	23.85	$(7.9 \pm 1.2) \times 10^{-2}$	$(17.8 \pm 2.6) \times 10^{-4}$

open, and complete breakup is possible above 28 MeV. The approximate energy-weighted total cross sections are listed to show the relative probability for each channel. The fifth channel is symmetric breakup into a pair of deuterons. The symmetry of the final state forbids $\alpha \rightarrow d, d$ breakup to proceed by the absorption of E1 radiation (see Sec. 1.2) and suppresses M1 transitions, with the result that the reaction proceeds primarily by E2 absorption [12]. The small magnitude of the cross section for this channel demonstrates the fast convergence, at intermediate energies, of the multipole expansion of the electromagnetic field, to be presented in the following section.

1.2 Theory

Since the coupling between the nucleus and the photon is weak, the photodisintegration transition amplitude can be calculated in the framework of perturbation theory [15] as $\langle \mathrm{f}|H_{e.m.}|\mathrm{i}\rangle$, where the initial state $|\mathrm{i}\rangle$ represents the incoming alpha particle in its ground state, $H_{e.m.}$ contains the incoming photon, and the final state $|\mathrm{f}\rangle$ is a nuclear scattering state in one of the five photodisintegration channels. The electromagnetic perturbation potential $H_{e.m.}$ is, assuming the Coulomb gauge $\nabla \cdot \mathbf{A} = 0$ ($\hbar = c = 1$),

$$H_{e.m.} = -\int d\mathbf{r}\, \mathbf{J}(\mathbf{r}) \cdot \mathbf{A}(\mathbf{r}) \quad , \tag{1.1}$$

where $\mathbf{J}(\mathbf{r})$ is the nuclear current operator and $\mathbf{A}(\mathbf{r})$ is the vector potential of the incident photon. The differential cross section for a *two-body breakup* channel, in the c.m. reference frame, is written as

$$\frac{d\sigma}{d\Omega} = 2\pi \left|\langle \mathrm{f}|H_{e.m.}|\mathrm{i}\rangle\right|^2 \left(\frac{\rho_f}{\Phi}\right) \quad , \tag{1.2}$$

where ρ_f is the final-state density of states, and Φ is the incident photon flux. If the photon is normalized within a box of volume V, the transition amplitude is

$$\langle \mathrm{f}|H_{e.m.}|\mathrm{i}\rangle = \left(\frac{2\pi}{\omega V}\right)^{\frac{1}{2}} M_{fi}(\mathbf{k}, \lambda) \quad , \tag{1.3}$$

where

$$M_{fi}(\mathbf{k},\lambda) = \int d\mathbf{r}\, \exp(i\mathbf{k}\cdot\mathbf{r})\, \epsilon_{\mathbf{k}\lambda} \cdot \langle \mathrm{f}|\mathbf{J}(\mathbf{r})|\mathrm{i}\rangle \quad . \tag{1.4}$$

The state of the incident photon is labeled by its momentum $\mathbf{k}$ and its polarization vector $\epsilon_{\mathbf{k}\lambda} = \frac{1}{\sqrt{2}}(\hat{\mathbf{e}}_1 + i\lambda\hat{\mathbf{e}}_2)$ with $\lambda = \pm 1$, $(\hat{\mathbf{e}}_1, \hat{\mathbf{e}}_2, \hat{\mathbf{k}})$ forming a right-handed coordinate system. The final-state density of states is

$$\rho_f = \int dp\, p^2 \delta(E_f - E_i) = m^* p_f \quad , \tag{1.5}$$

where m^* is the reduced mass of the final-state particles, and p_f is the c.m. momentum of the photodisintegration fragments. The incident photon flux is given by

$$\Phi = \frac{1}{V}\left(1 + \frac{\omega}{\mathrm{M}_\alpha}\right) \simeq \frac{1}{V} \quad . \tag{1.6}$$

The transition matrix element consists of a part which depends upon internal motion of the system, and a part which expresses the overall motion. The integral over the c.m. coordinate in the initial and final states imposes the requirement of momentum conservation. Thus,

$$M_{fi} = \left(\frac{1}{2\pi}\right)^{\frac{3}{2}} \delta(\mathbf{k} + \mathbf{P}_\alpha - \mathbf{q} - \mathbf{P}_R)\, \mathcal{M}_{\beta\alpha} \quad , \tag{1.7}$$

where

$$\mathcal{M}_{\beta\alpha} = \int d\mathbf{r}\, \exp(i\mathbf{k}\cdot\mathbf{r}) \left\langle \beta^{(-)} \middle| \mathbf{J}(\mathbf{r}) \middle| \alpha^{(0)} \right\rangle \cdot \epsilon_{\mathbf{k}\lambda} \tag{1.8}$$

depends only on internal coordinates. Here the initial state $\left|\alpha^{(0)}\right\rangle$ is simply the ground state of the alpha particle, and the final state $\left|\beta^{(-)}\right\rangle$ is a two-body outgoing scattering state with $\mathbf{q}$ as the momentum of the ejected nucleon, and $\mathbf{P}_R$ as the recoil momentum of the residual nucleus. The unpolarized cross section in the c.m. frame is expressed in terms of the $\mathcal{M}_{\beta\alpha}$ matrix elements as

$$\frac{d\sigma}{d\Omega} = \frac{1}{2\pi}\frac{pm^*}{\omega}\frac{1}{2}\sum_{\lambda, M_R, m_s} |\mathcal{M}_{\beta\alpha}|^2 \quad , \tag{1.9}$$

where the sum averages over incident photon polarization λ and sums over the spin substate of the outgoing nucleon, s, and the recoil nucleus, M_R.

To take advantage of angular momentum conservation, the plane wave radiation field can be expressed as a sum of terms with definite angular momentum. If the incident photon direction is fixed along the z axis,

$$e^{ikz}\epsilon_{\mathbf{k}\lambda} = \sum_{L=1}^{\infty} i^L \sqrt{2\pi(2L+1)} \left[j_L(kr)\mathbf{X}_{L\lambda}(\hat{\mathbf{r}}) + \lambda \frac{1}{k} \nabla \times [j_L(kr)\mathbf{X}_{L\lambda}(\hat{\mathbf{r}})] \right] \quad , \tag{1.10}$$

where $\mathbf{X}_{LM}$ are the vector harmonics defined by

$$\mathbf{X}_{LM}(\hat{\mathbf{r}}) = \frac{1}{\sqrt{L(L+1)}} \mathbf{L} Y_{LM}(\hat{\mathbf{r}}) \quad , \quad \mathbf{L} = \frac{1}{i} \mathbf{r} \times \nabla \quad , \tag{1.11}$$

and Y_{LM} are the ordinary spherical harmonics. Introducing the magnetic and electric multipoles of the free radiation field, Eq. 1.8 reduces to

$$\mathcal{M}_{\beta\alpha} = \sqrt{2\pi} \sum_{L=1}^{\infty} \hat{L} \left[T^{(M)}_{L\lambda}(\beta,\alpha) + \lambda T^{(E)}_{L\lambda}(\beta,\alpha) \right] \quad , \quad \hat{L} = \sqrt{2L+1} \quad . \tag{1.12}$$

The $T(\beta,\alpha)$ terms are matrix elements of the magnetic and electric transition operators, defined by

$$T^{(M)}_{L\lambda} = i^L \int d\mathbf{r} \, \{ j_L(kr)\mathbf{X}_{L\lambda}(\hat{\mathbf{r}}) \} \cdot \mathbf{J}(\mathbf{r}) \quad , \tag{1.13}$$

$$T^{(E)}_{L\lambda} = \frac{i^L}{k} \int d\mathbf{r} \, \{ \nabla \times [j_L(kr)\mathbf{X}_{L\lambda}(\hat{\mathbf{r}})] \} \cdot \mathbf{J}(\mathbf{r}) \quad . \tag{1.14}$$

The implicit dependence of the T operators on photon momentum k is omitted for simplicity. If the states $|\alpha\rangle$,$|\beta\rangle$ have definite total angular momentum, the matrix elements can be reduced by use of the Wigner-Eckart theorem [2] so that Eq. 1.12 becomes

$$\begin{aligned} \mathcal{M}_{\beta\alpha} \;=\; & \sqrt{2\pi} \sum_{L=1}^{\infty} \hat{L} (-)^{J_\beta - M_\beta} \begin{pmatrix} J_\beta & L & J_\alpha \\ -M_\beta & \lambda & M_\alpha \end{pmatrix} \\ & \left[\langle \beta \parallel T^{(M)}_{L\lambda} \parallel \alpha \rangle + \lambda \langle \beta \parallel T^{(E)}_{L\lambda} \parallel \alpha \rangle \right] \quad . \end{aligned} \tag{1.15}$$

The array of angular momentum quantum numbers enclosed in parentheses is a Clebsh-Gordon coefficient represented by Wigner's 3-j symbols [2].

The calculation of the reduced matrix elements involves evaluating the integrals of Eqs. 1.13,1.14, where $\mathbf{J}(\mathbf{r})$ is sandwiched between initial and final nuclear states. In a first approximation, the nuclear current can be written simply as a sum of the convection current of the protons and the current associated with the magnetic moment of the nucleons. This is called a one-body current because it is a sum of terms which depend only on the coordinates and momenta of a single nucleon. In addition to this is the two-body current associated with the exchange of mesons between pairs of nucleons. The evaluation of this current requires a model of meson exchange, since the dynamics of exchange currents is not completely understood. However in the long-wavelength limit, the Siegert theorem [16] provides an expression for $T^{(E)}$ in terms of nucleon coordinates alone, which incorporates both one-body and two-body currents. The Siegert theory expresses the electric multipole operator of Eq. 1.14 as the sum of two terms:

$$T^{(E)}_{L\lambda} = T^{(E)a}_{L\lambda} + T^{(E)b}_{L\lambda} \quad , \tag{1.16}$$

where

$$T^{(E)a}_{L\lambda} = \frac{i^{L+1}}{k}\frac{1}{\sqrt{L(L+1)}}\int d\mathbf{r}\,(\nabla\Phi_{L\lambda})\cdot\mathbf{J}(\mathbf{r}) \quad , \tag{1.17}$$

$$T^{(E)b}_{L\lambda} = i^{L+1}\frac{k}{\sqrt{L(L+1)}}\int d\mathbf{r}\,[\mathbf{r}j_L(kr)Y_{L\lambda}(\hat{\mathbf{r}})]\cdot\mathbf{J}(\mathbf{r}) \quad , \tag{1.18}$$

having defined

$$\Phi_{L\lambda} = \left(1 + r\frac{d}{dr}\right) j_L(kr)Y_{L\lambda}(\hat{\mathbf{r}}) \quad . \tag{1.19}$$

The integral in Eq. 1.17 can be integrated by parts to obtain

$$T^{(E)a}_{L\lambda} = -\frac{i^{L+1}}{k}\frac{1}{\sqrt{L(L+1)}}\int d\mathbf{r}\,\Phi_{L\lambda}\nabla\cdot\mathbf{J}(\mathbf{r}) \quad , \tag{1.20}$$

where $\nabla\cdot\mathbf{J}(\mathbf{r})$ can be replaced by the commutator of the charge density with the nuclear Hamiltonian by use of the current conservation equation, $\nabla\cdot\mathbf{J}+i\,[H,\rho]=0$:

$$T^{(E)a}_{L\lambda} = -\frac{1}{k}\,[H, D_{L\lambda}] \quad , \tag{1.21}$$

where

$$D_{L\lambda} = \frac{i^L}{\sqrt{L(L+1)}} \int d\mathbf{r}\, \rho(\mathbf{r}) \left(1 + r\frac{d}{dr}\right) j_L(kr) Y_{L\lambda}(\mathbf{r}) \quad . \tag{1.22}$$

Since Eq. 1.18 has an additional factor of kr in the integrand, in the long-wavelength limit $T^{(E)a}_{L\lambda}$ dominates over $T^{(E)b}_{L\lambda}$. For a similar reason, $T^{(E)}_{L\lambda}$ dominates over $T^{(M)}_{L\lambda}$ for the same multipolarity L. Hence, Siegert's theorem can be stated as,

$$T^{(E)}_{L\lambda} \underset{k=0}{=} -\frac{1}{k}\left[H, D_{L\lambda}\right] \quad . \tag{1.23}$$

To see that the expression for $T^{(E)a}_{L\lambda}$ includes exchange current effects, consider the charge density and current operators, and the nuclear Hamiltonian, decomposed into one-body and two-body parts.

$$\rho = \rho_{[1]} + \rho_{[2]} \cdots$$

$$\mathbf{J} = \mathbf{J}_{[1]} + \mathbf{J}_{[2]} \cdots$$

$$H = T_{[1]} + V_{[2]} \cdots$$

Here $T_{[1]}$ contains both the kinetic energy and the one-body potential operator, and $V_{[2]}$ contains two-body corrections. The one-body pieces satisfy current conservation,

$$\nabla \cdot \mathbf{J}_{[1]} + i\left[T_{[1]}, \rho_{[1]}\right] = 0 \quad . \tag{1.24}$$

Overall current conservation implies a similar term for the two-body pieces,

$$\nabla \cdot \mathbf{J}_{[2]} + i\left[V_{[2]}, \rho_{[1]}\right] + i\left[H, \rho_{[2]}\right] = 0 \quad . \tag{1.25}$$

Assuming Siegert's hypothesis $\rho_{[2]} \simeq 0$,

$$\nabla \cdot \mathbf{J} + i\left[H, \rho_{[1]}\right] = 0 \quad . \tag{1.26}$$

This shows that, considering only the one-body density $\rho_{[1]}$ in Eq. 1.22, both $\mathbf{J}_{[1]}$ and $\mathbf{J}_{[2]}$ are included.

The remaining ingredients required for evaluating the matrix elements $\mathcal{M}_{\beta\alpha}$ are the initial and final nuclear states. It is in the choice of these states that existing

theoretical calculations differ. Early calculations used shell-model wave functions for both initial and final states [17,18,19,20]. Gari and Hebach begin with shell-model wave functions and attempt to add in effects of nucleon correlations [10,11]. Several exact methods for calculating the ground state of ^{4}He , beginning with different effective two-body interactions, have been advanced [8,21,22,23]. Although these results are only as good as the two-body input, they do provide a rigorous method for calculating nucleon correlations. The Carlson and Pandharipande [8] introduce a three-body potential to the interaction in an attempt to improve the agreement between their exact calculations and the known binding energy and charge distribution of light nuclei.

The final state is an outgoing scattering state containing a nucleon and a recoiling $A = 3$ nucleus. Neglecting coupling to the three-body and four-body breakup channels, the two-body outgoing state ϕ_β can be expanded as a product of the $A = 3$ ground state ϕ, and the wavefunction φ^- which contains the relative motion of the nucleon and $A = 3$ system:

$$\psi_\beta(s, M_R) = 4\pi\phi(J_R M_R)\sum_{\ell m} i^\ell Y^*_{\ell m}(\hat{\mathbf{q}})\varphi^-_{\ell m s} \quad , \tag{1.27}$$

where the final-state is specified by momentum $\mathbf{q}$, nucleon spin substate s, and recoiling nucleus spin J_R, M_R. The states $\varphi^-_{\ell m s}$ are solutions to the effective two-body Schrodinger equation, treating the nucleon as a spin-$\frac{1}{2}$ particle of mass m^* in the potential of $A = 3$ nucleus, with an outgoing wave of definite ℓ, m, s. They may be explicitly written as

$$\varphi^-_{\ell m s}(\mathbf{x}) = \sum_{j j_z m' s'} (2j+1) \begin{pmatrix} \ell & \frac{1}{2} & j \\ m & s & j_z \end{pmatrix} \begin{pmatrix} \ell & \frac{1}{2} & j \\ m' & s' & j_z \end{pmatrix} \frac{u_{j\ell}(q,x)}{x} Y_{\ell m'}(\hat{\mathbf{x}})\chi_{s'} \quad , \tag{1.28}$$

where $\mathbf{x}$ is the relative coordinate between the two particles in the final state. The radial functions $u_{j\ell}$ are the solutions to the radial wave equation, once the angular dependence of the wave has been fixed by the choice of definite angular momentum.

They may be thought of as analogous to the Laguerre polynomials in the solution to the bound states of the hydrogen atom.

For a fixed value of orbital angular momentum ℓ, $u_{j\ell}$ only depends upon j through spin-orbit coupling in the final state. In order to take advantage of Eq. 1.16, the state ψ_β may be decomposed into a sum of states with definite total angular momentum. The order of coupling angular momenta is given in Fig. 1.1. The initial state of $J_i = 0, M_i = 0$ is coupled via the photon of type p (electric or magnetic), angular momentum L, and polarization λ to the total angular momentum I, I_z. In the final state this total angular momentum couples via the orbital part ℓ, m to channel spin S, S_z, which is the sum of the nucleon spin $\frac{1}{2}, s$ and the spin of the recoil nucleus $J_R = \frac{1}{2}, M_R$. The states of definite total angular momenta can be expanded in terms of the direct product basis states, $\phi(J_R M_R)\varphi^-_{\ell m s}$, as

$$\varphi^-_{\ell S I I_z}(\mathbf{x}) = \sum_{M_R s m S_z} \hat{S}\hat{I}(-)^{J_R-\frac{1}{2}+S_z+S-\ell+I_z} \begin{pmatrix} J_R & \frac{1}{2} & S \\ M_R & s & -S_z \end{pmatrix} \begin{pmatrix} S & \ell & I \\ S_z & m & -I_z \end{pmatrix} \phi(J_R M_R)\varphi^-_{\ell m s}(\mathbf{x}) \quad , \tag{1.29}$$

with the inverse expansion,

$$\phi(J_R M_R)\varphi^-_{\ell m s}(\mathbf{x}) = \sum_{M_R s m S_z} \hat{S}\hat{I}(-)^{J_R-\frac{1}{2}+S_z+S-\ell+I_z} \begin{pmatrix} J_R & \frac{1}{2} & S \\ M_R & s & -S_z \end{pmatrix} \begin{pmatrix} S & \ell & I \\ S_z & m & -I_z \end{pmatrix} \varphi^-_{\ell S I I_z}(\mathbf{x}) \quad . \tag{1.30}$$

These relations follow directly from the definition of the Clebsh-Gordon coefficients, and represent the transformation between the direct-product basis and the basis of definite total angular momentum.

With these expansions for the final state, the matrix element $\mathcal{M}_{\beta\alpha}$ can be written as

$$\mathcal{M}_{\beta\alpha} = 2(2\pi)^{\frac{3}{2}} \sum_{\ell m p L S S_z I I_z} (-)^{\frac{1}{2}-J_R-S+\ell-S_z-2I_z+p(1-\lambda/2)+I} \hat{S}\hat{L}\hat{I}^2$$

$$\begin{pmatrix} J_R & \frac{1}{2} & S \\ M_R & s & -S_z \end{pmatrix} \begin{pmatrix} S & \ell & I \\ S_z & m & -I_z \end{pmatrix} \begin{pmatrix} I & L & J_i \\ -I_z & \lambda & M_i \end{pmatrix}$$
$$Y_{\ell m}(\hat{\mathbf{q}}) T_L^{(p)}(S\ell I) \quad , \tag{1.31}$$

where the multipole matrix element can be written, ignoring spin-orbit effects in the final state, as

$$T_L^{(p)}(S\ell I) = \frac{1}{\hat{I}} \langle \varphi^-_{\ell SI} \parallel T_L^{(p)} \parallel \alpha(J_i) \rangle \quad . \tag{1.32}$$

This result may be substituted into Eq. 1.9 to yield, after summing over incident photon polarizations,

$$\begin{aligned} \frac{d\sigma}{d\Omega} \;=\; & 4\pi \frac{m^* p}{\omega} \frac{1}{2J_i+1} \sum_{p_1 L_1 I_1 \ell_1 p_2 L_2 I_2 \ell_2 S n} \frac{1}{2}[1+(-)^{p_1+L_1+\ell_1+p_2+L_2+\ell_2}] \\ & i^{\ell_1-\ell_2-n}(-)^{J_i-2J_R-S} Z(\ell_1 I_1 \ell_2 I_2; Sn) Z_\gamma(L_1 I_1 L_2 I_2; J_i n) \\ & P_n(\cos\theta) \Re e\{T_{L_2}^{(p)}(S\ell_2 I_2)^* T_{L_1}^{(p)}(S\ell_1 I_1)\} \quad . \end{aligned} \tag{1.33}$$

The Z functions, sums of 3-j and 6-j symbols, are defined in Ref. [15], and the P_n functions are Legendre polynomials in $\cos\theta$. This equation provides a convenient decomposition of the differential cross section into a sum of Legendre functions. This series converges rapidly in the case that the photon wavelength is much larger than the dimensions of the nucleus. At a gamma energy of 50 MeV, $kR = 0.40$, where R is the charge radius of ^{4}He from Table 1.1, and since the small-distance behavior of $j_L(kR)$ is $(kR/2)^L/L!$, an error under 2% is made by truncating the series after $L = 2$.

The Z coefficients in Eq. 1.33 contain the basic angular momentum conservation rules represented in Fig. 1.1. In addition to these constraints, the reduced matrix elements also respect parity conservation

$$\Pi_R = \Pi_i (-)^{p+L+\ell} \tag{1.34}$$

where $p = 0$ labels electric, and $p = 1$ labels magnetic transitions. Time reversal invariance implies that all transition matrix elements are real and

$$\langle J_f \parallel T_L^{(p)} \parallel J_i \rangle = (-)^{J_i - J_f + L + 1} \langle J_i \parallel T_L^{(p)} \parallel J_f \rangle \quad . \tag{1.35}$$

Table 1.3 shows which multipole matrix elements contribute to which term in the Legendre expansion of the cross section in Eq. 1.33. Only E1, M1, and E2 matrix elements are included. The columns are arranged from left to right in order of descending magnitude, each column differing from its neighbor by an additional factor of kR. Notice that the total cross section, contained in the $n = 0$ term, depends only upon sums of squares of multipole matrix elements. The interferences enter in the angular distribution.

Inasmuch as the Siegert electric operator accounts for the meson exchange currents in the nucleus, the photodisintegration reaction is a direct probe of the nuclear wave functions. In the case where reliable methods have been used to generate these wave functions, disagreement between theoretical calculations and experiment is evidence for the inadequacy of the underlying interaction used as input to the calculations. An example of this is the large asymmetry between the total photoneutron and photoproton cross sections apparent in some of the best ^{4}He photodisintegration data below 30 MeV. Early calculations within the framework of the continuum shell model [17,18,20,24] indicated that such a large ratio could not be accounted for without introduction of a charge symmetry non-conserving component in the nuclear force. More recent calculations within the framework of the resonating group model [25,26] are in agreement with this conclusion. Because of disagreements between existing experimental data sets, the reality of this effect is not yet established, and better experimental data are required.

In the energy region between the giant dipole resonance (GDR) and the delta resonance region (between 50 MeV and 150 MeV), several calculations have been done [10,27,28,29]. Gari and Hebach indicate that two-body currents are the dominant contribution to the total ^{4}He photodisintegration cross section [10]. Christillin defends a three-nucleon mechanism for photoabsorption which may be important above 100 MeV [30]. This is in distinction to the case of quasi-free electron scattering, where the dominant disintegration mechanism in this region of missing energy

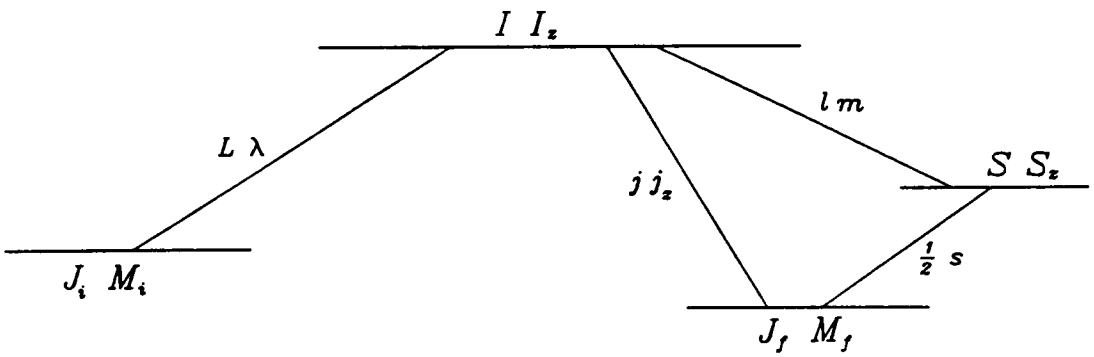

Figure 1.1: Schematic representation of the coupling of angular momenta in the initial and final states for a two-body photodisintegration channel

Table 1.3: Contributions from each multipole transition to the differential cross section, arranged according to magnitude and Legendre polynomial. The matrix elements which contribute to each term $P_n(\cos\theta)$ in Eq. 1.33 are arranged by rows according to n. The magnitude of each matrix element, in the long-wavelength limit, is indicated by its column. Proceeding from left to right, matrix elements decrease in magnitude by a factor kR for each column, where k is the photon momentum and R is the dimension of the nucleus.

n	contributing matrix elements		
0	$\|E1\|^2$		$\|E2\|^2 + \|M1\|^2$
1		$(E1, E2)$	
		$(E1, M1)$	
2	$\|E1\|^2$		$\|E2\|^2 + \|M1\|^2$
	$(E1, E1')$		$(M1, E2)$
			$(E2, E2')$
			$(M1, M1')$
3		$(E1, E2)$	
4			$\|E2\|^2$
			$(E2, E2')$

is single-nucleon knockout [31]. Calculations of photodisintegration cross sections in this energy region, using exact wave functions, will provide a sensitive test of how meson exchange currents couple to nucleons in the nucleus. While most of the effort in calculating exact few-body wave functions in the continuum have focused on the $A = 3$ systems [6,23,32], some progress has recently been made for $A = 4$ [33,34].

In the case of the three-body and total photodisintegration channels, less theoretical work has been done. Considerable success has been achieved in explaining the two-nucleon knockout photoreaction by treating the ejected pair as a "quasi-deuteron" imbedded in the nuclear medium [36]. Noguchi and Prats calculate the cross section for the $^4\mathrm{He}(\gamma, \mathrm{pn})^2\mathrm{H}$ reaction within the framework of the quasi-deuteron model [35], between the photon energies of 60 MeV and 170 MeV. They attempt to explain both the $^4\mathrm{He}(\gamma, \mathrm{pn})^2\mathrm{H}$ cross section, and that of the $^4\mathrm{He}(\gamma, \mathrm{p})^3\mathrm{H}$ and the $^4\mathrm{He}(\gamma, \mathrm{n})^3\mathrm{He}$ channels within the framework of the quasi-deuteron model.

An exact framework exists in AGS (Alt-Grassberger-Sandhas) theory [37] for the solution to the four-body problem, but it has not yet been worked out for these channels. The availability of precise experimental data for the three-body and four-body breakup channels is required to stimulate theoretical investigation.

1.3 Previous Experiments

The photodisintegration reaction is closely related to the inverse reaction, radiative capture, in which the target nucleus captures a particle from the beam (nucleon or light nucleus) and emits a gamma ray, decaying to the ground state of the composite nucleus. An example of this is the $^3\mathrm{H}(p, \gamma)^4\mathrm{He}$ capture reaction which is the inverse of $^4\mathrm{He}(\gamma, \mathrm{p})^3\mathrm{H}$. The cross sections for the two reactions are the same, by virtue of the principle of detailed balance, to within a kinematic factor. Experimentally, the radiative capture reaction is only useful in the investigation of the two-body channels.

Another reaction which is closely related to photodisintegration is electrodisintegration, in which the initial-state photon is replaced with an electron, and the final state contains the scattered electron in addition to the disintegration fragments. The additional kinematic freedom of electron scattering (the angle and energy of the scattered electron) permits the independent selection of the energy and momentum of the exchanged virtual photon. In quasi-free scattering kinematics, the momentum exchange four-vector is space-like. In this regime, the photon interacts primarily with one nucleon, facilitating the measurement of one-body observables like charge density, and the nucleon momentum distribution. These measurements [38,39,40] have yielded precise constraints for exact calculations of the ground-state wave function of the alpha particle. If the momentum exchange q^2 is chosen to be small, electron scattering is analogous to real-photon absorption, and the two cross sections are related by a transformation [42,41].

The first $^4\mathrm{He}(\gamma,\mathrm{p})^3\mathrm{H}$ measurements [43,44] were performed using the inverse reaction $^3\mathrm{H}(p,\gamma)^4\mathrm{He}$ in a proton beam of energy $3 < E_p < 20$ MeV. This translates to a gamma energy range of $23 < E_\gamma < 40$ MeV, the region of the giant dipole resonance. The photodisintegration reaction for this channel has the disadvantage, in the GDR region, that the photoproton is very slow, and it is easily absorbed before it reaches the detector. For this reason, radiative capture results are the best data for the $^4\mathrm{He}(\gamma,\mathrm{p})^3\mathrm{H}$ channel in the GDR region. The early capture measurements have been repeated more recently [45,46] with greater accuracy, and are in agreement with the early results.

Since slow neutrons have a long range in matter, measurements of the reaction $^4\mathrm{He}(\gamma,\mathrm{n})^3\mathrm{He}$ in the GDR region do not suffer the same difficulties as the proton channel. Nevertheless, detection of low-energy neutrons has its own problems. The measurement of Berman *et al.* [47] yielded a photoneutron total cross section well below the photoproton result. Since E1 absorption leads to the near-equality of the photoproton and photoneutron cross sections in the GDR region, this result

presented an anomaly. A subsequent measurement with electrons [42] reported a cross-section ratio, for the two channels, close to 1.

Measurements followed using a photon beam [48,49,50], with results that were consistent with a ratio of 1. The group who first reported the anomaly repeated the experiment [51] and again reported a photoneutron cross section well below the existing photoproton result. The reaction was then studied using the inverse reaction ^{3}He$(n,\gamma)^4$He [52,53]. The results again showed a ratio significantly different from 1. Preliminary results from a recent electron scattering experiment [54], in which both the recoil ^{3}H and ^{3}He nuclei were detected, indicate a ratio close to 1. The situation remains essentially as it was reviewed by Calarco *et al.* [55]. At this point the experimental results are inconclusive.

A few measurements of these two channels extend into the intermediate energy region above the GDR [56]. Measurements have also been reported for these channels in the delta resonance region above 150 MeV [57,58,59,60]. The single most comprehensive data set [61,13] spans the energy region from threshold to 260 MeV. Data are reported for all five alpha photodisintegration channels, but the precision of the measurement in all but the ^{4}He$(\gamma,\mathrm{p})^3$H and ^{4}He$(\gamma,\mathrm{n})^3$He channels is poor. The total cross section reported for the ^{4}He$(\gamma,\mathrm{p})^3$H reaction is shown in Fig. 1.2, and for ^{4}He$(\gamma,\mathrm{n})^3$He in Fig. 1.3. The experiments were performed with a bremsstrahlung photon beam and a cloud chamber. The energy of the photon was determined by kinematics from the tracks of the charged particles. At energies below 30 MeV, the cloud chamber tracks were very short, which calls into question these results in the GDR region, particularly for the ^{4}He$(\gamma,\mathrm{n})^3$He channel [55]. Other results using the same technique have also been reported [62,63].

The total cross section for these reactions was determined by measuring the differential cross section at several angles, and fitting to a Legendre polynomial expansion. Many chose the alternative expansion,

$$\frac{d\sigma}{d\Omega} = A(\sin^2\theta + \beta\sin^2\theta\cos\theta + \gamma\sin^2\theta\cos^2\theta + \delta + \varepsilon\cos\theta) \quad . \tag{1.36}$$

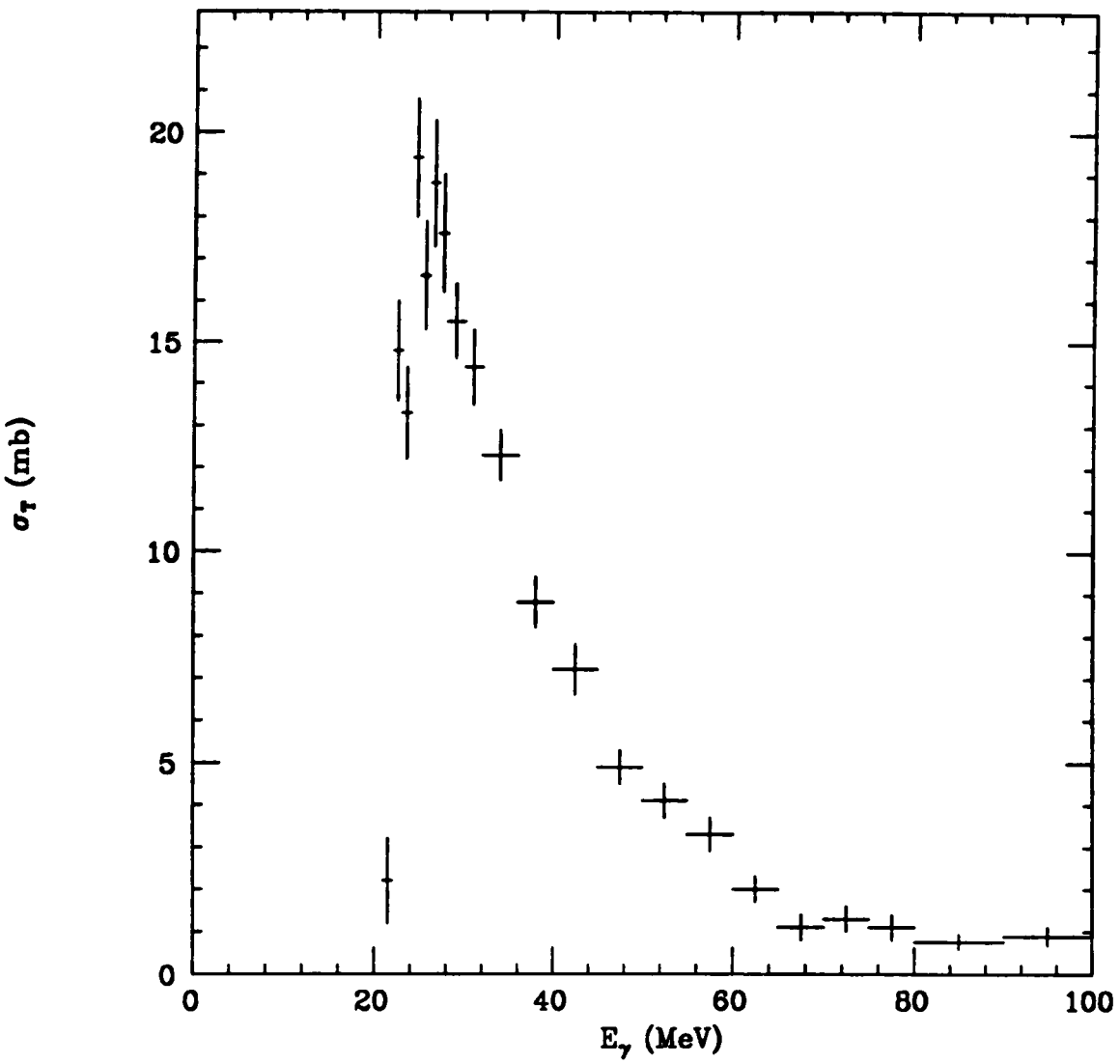

Figure 1.2: Total cross section for the reaction $^4He(\gamma, p)^3H$ between threshold and 100 MeV, from Ref. [13].

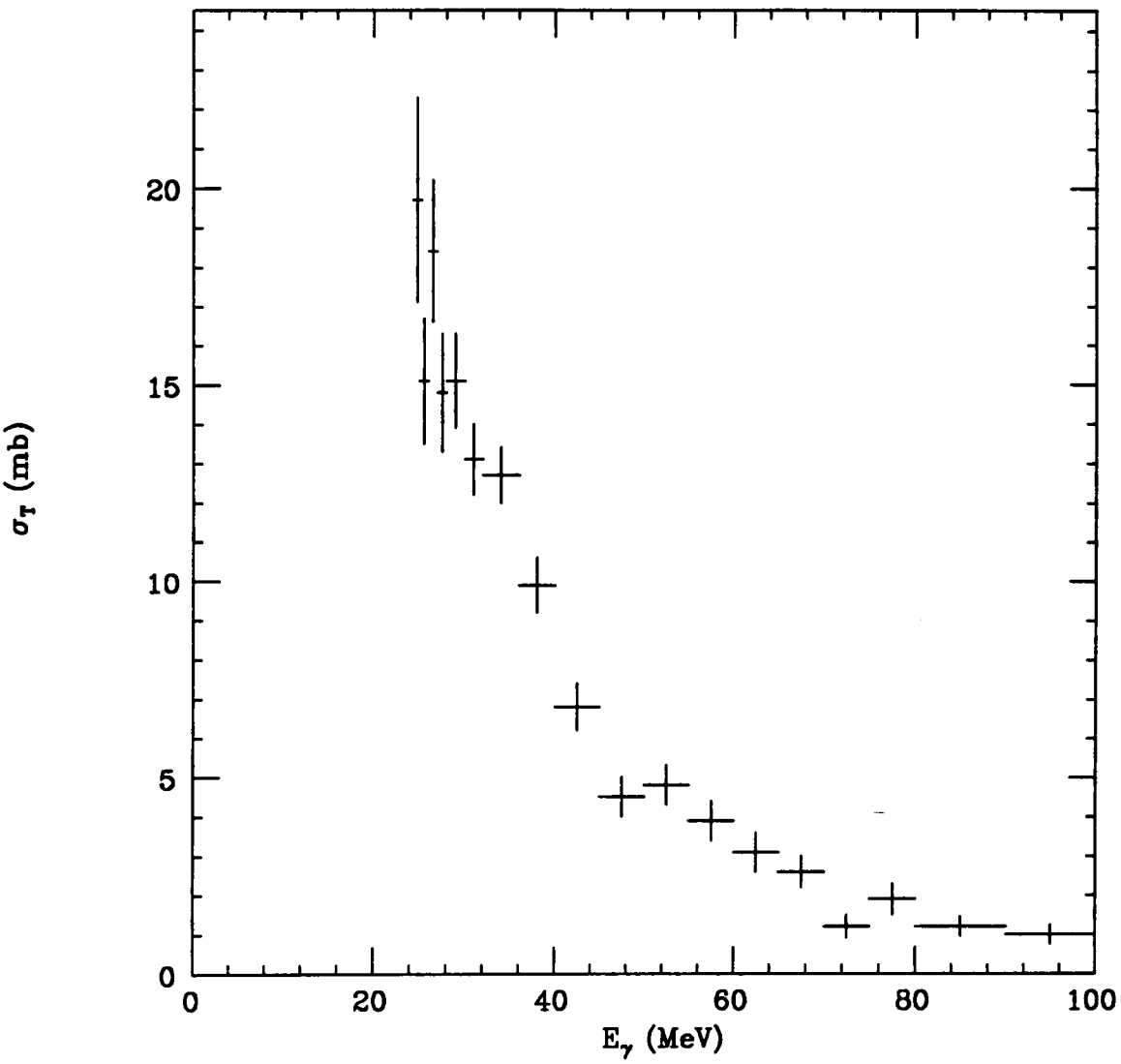

Figure 1.3: Total cross section for the reaction $^4He(\gamma, n)^3He$ between threshold and 100 MeV, from Ref. [13].

These are related to the a_n coefficients of the Legendre expansion,

$$\frac{d\sigma}{d\Omega} = A_0 \left(1 + \sum_{n=1}^{\infty} a_n P_n(\cos\theta)\right) \tag{1.37}$$

through the following transformation, neglecting terms in the Legendre expansion beyond a_4.

$$\begin{aligned}
A &= -\tfrac{3}{2}A_0\left(a_2 + \tfrac{5}{12}a_4\right) & A_0 &= \tfrac{2}{3}A\left(1 + \tfrac{1}{5}\gamma + \tfrac{3}{2}\delta\right) \\
A\beta &= -\tfrac{5}{2}A_0 a_3 & A_0 a_1 &= A(\varepsilon + \beta) \\
A\gamma &= -\tfrac{35}{8}A_0 a_4 & A_0 a_2 &= \tfrac{2}{3}A\left(1 - \tfrac{1}{7}\gamma\right) \\
A\delta &= A_0(1 + a_2 + a_4) & A_0 a_3 &= -\tfrac{2}{5}A\beta \\
A\varepsilon &= A_0(a_1 + a_3) & A_0 a_4 &= -\tfrac{8}{35}A\gamma
\end{aligned} \tag{1.38}$$

The precision of the angular distribution data of Ref. [13] was not sufficient to constrain γ, δ, or ε. The best fit in A and β for the ^{4}He$(\gamma,\mathrm{p})^3$H differential cross section data of Ref. [13] is shown by the curve in Fig. 1.4. The error on this curve is approximately 20%. This data was summed over the energy region from 65 MeV to 170 MeV. A more recent bremsstrahlung measurement, which used silicon detectors to detect the recoil nucleus, has been published in a brief note [64]. Their angular distribution at 100 MeV is shown by the data points in Fig. 1.4. The absolute normalization of this measurement was not reported. However, the difference in shape between the two data sets in Fig. 1.4 indicates that the two measurements do not agree.

A major difficulty with photodisintegration experiments using a bremsstrahlung photon beam is the fact that the beam contains a continuous distribution of photon energies from zero up to a maximum energy, called the endpoint. In order to extract a cross section at a particular photon energy, it is necessary to find a way to (a) assign counts to the proper gamma energy bin, and (b) determine the total flux of photons in each energy bin. Several methods have been developed for generating monochromatic photons to bypass this problem. The photoneutron experiments which first suggested the large difference between the photoproton

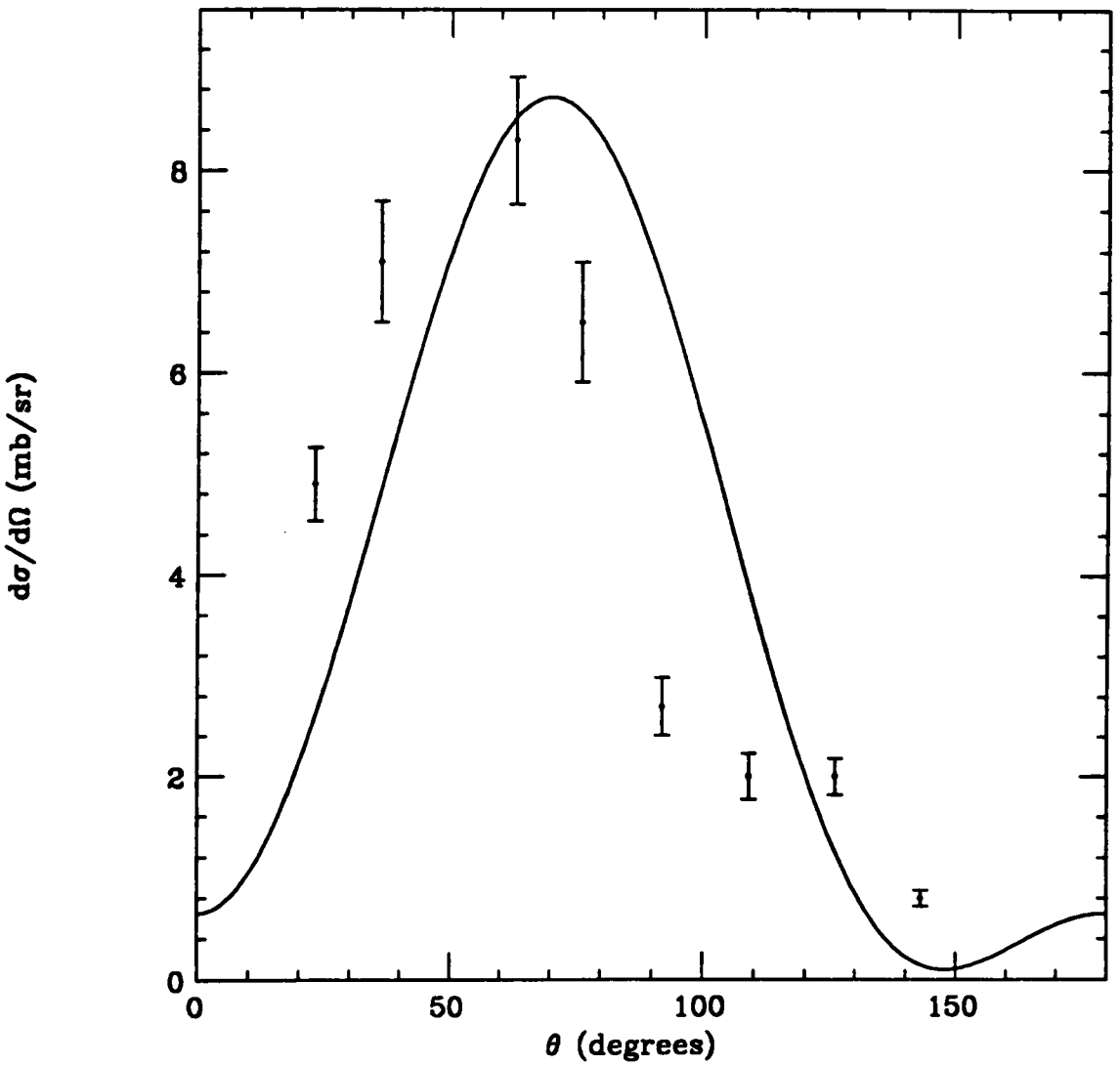

Figure 1.4: Differential cross section for the reaction ^{4}He$(\gamma, \mathrm{p})^3$H. The curve is a fit to the data of Ref. [13], using a bremsstrahlung-weighted average over the energy region 65-170 MeV. The data points are the (unnormalized) data from Ref. [64]. The normalization of the data points was adjusted for best comparison.

and photoneutron cross sections were done using the positron annihilation-in-flight technique [65]. Berman and Fultz also point out in Ref. [65] the promise of the bremsstrahlung-tagging technique, which had been recently introduced. It is noteworthy that, whereas several measurements of the ^{4}He$(\gamma, \mathrm{n})^3$He reaction have been done with monochromatic photons, the ^{4}He$(\gamma, \mathrm{p})^3$H experiments have all been done with bremsstrahlung [46].

There is limited data available for the three remaining alpha photodisintegration channels. The best data for the ^{4}He$(\gamma, ^2\mathrm{H})^2$H channel in the GDR region come from radiative capture experiments [66,67]. Measurements at higher energies have been reported using electron scattering [12], and with bremsstrahlung [14]. These results have been reviewed by Meyerhof and Fiarman [68]. The only known data for the three-body and four-body breakup channels is that reported in Ref. [13]. The statistical precision of this data is at the level of 30-50%.

Chapter 2

Experimental Design

In Chap. 1 the body of data which presently exists for the photodisintegration of ^{4}He has been reviewed. While there is general agreement between the data sets concerning the total photodisintegration cross section between threshold and 50 MeV, important problems remain, calling for further experimental investigation. The first problem is the lack of good differential cross sections. Angular distributions in addition to the total cross section offer further critical tests of theory and the approximations made in the calculational procedure. Second, the statistical precision of the current total cross section data is poor (10% or worse), and disagreements between data sets suggest systematic uncertainties at about the same level. The newly arrived calculations based upon exact few-body theory may be expected to reproduce experimental results to better than 10%, hence data of improved precision are required for their guidance. Third, the data in the region above 50 MeV are quite sparse. Yet this is the region where effects from final state interactions are expected to be minimal, and theoretical predictions are most reliable [33,34].

Comparison of existing results with theory is further hampered by the difficulty that much of the data is reported for the inclusive reactions (γ, p) and (γ, n) instead of for the individual channels. At present, theoretical calculations are only available for the two-body breakup channels. Comparison with inclusive data requires an estimate of the contribution from the three-body and four-body channels, which are not well known experimentally or theoretically. The design of this experiment

is presented below in the light of these deficiencies.

2.1 Goals

The general experimental goal is the systematic measurement of the photodisintegration of ^{4}He from threshold up to 100 MeV. This range should be considered in two segments: the region from photodisintegration threshold up to about 35 MeV, known as the giant dipole resonance (GDR) region, and the region from 35 to 100 MeV. For reasons presented above, the region above the dipole resonance is given first priority. These measurements must lead to differential cross sections with reliable absolute normalization. Determination of the total cross section to within 5% is a reasonable goal. The experimental design must admit the separation of each of the five disintegration channels of ^{4}He .

The first requirement is a monochromatic gamma beam with a sufficient flux and duty factor. In order to separate the different breakup channels of ^{4}He it is necessary to be able to identify the multiple decay particles from a single event by their timing coincidence. This requires that the beam must have a duty factor on the order of unity. The conventional way of producing intense photon beams is electron bremsstrahlung. A bremsstrahlung photon beam contains gammas with a continuous energy distribution from zero up to the energy of the electron beam, called the endpoint energy. All of the experiments reviewed in Chap. 1 that used photon beams were done with bremsstrahlung.

Measurements with bremsstrahlung beams have two major difficulties. First, the beam contains a continuum of energies. The extraction of a cross section at any particular energy must rely on kinematic reconstruction using the energy of the detected fragments (this is not possible in general for inclusive experiments) or the unfolding of yields from a sequence of electron beam energies. Second, the normalization of the useful flux of a bremsstrahlung beam is difficult to ascertain. While the total energy in the gamma beam can be measured directly, the fraction

of that which is in the useful energy band requires a precise knowledge of the bremsstrahlung spectrum. Flux normalization is an important source of uncertainty in these experiments. Both of these difficulties can be circumvented by use of a technique called bremsstrahlung tagging. The tagged photon facility at the University of Illinois [69] is described below in Sec. 2.2.

The products of photodisintegration are light nuclear fragments: protons, neutrons, deuterons, tritons and ^{3}He nuclei. At gamma energies below 100 MeV these particles move slowly compared to the speed of light. This means that the charged particles lose their energy rapidly via ionization as they travel through matter, with the disadvantage that they are easily absorbed. The neutron, being neutral, does not lose energy by ionization and so has a relatively long range in matter. The advantage of the charged particle is that it leaves a trail of ionization which is readily sensed by a detector. Neutron detection, which must rely upon nuclear processes, is plagued by a variety of systematic uncertainties. These are aggravated by the presence of high levels of neutron background in the experimental hall when a photon beam is present. Since each of the disintegration channels involves at least one charged particle, it is sufficient to only detect the charged particles. There is one exception: in the ^{4}He(γ, ppnn) reaction, one kinematical variable (e.g. the azimuth of the plane containing the two neutron tracks) is left unconstrained by detecting only the protons.

The ^{4}He target is required to be very thin in order to permit the charged reaction products to escape. At a gamma energy of 30 MeV, the range of the proton in the reaction ^{4}He$(\gamma, \mathrm{p})^3$H is only 70 cm in air [70]. At 50 MeV the range of the triton in the same reaction is under 40 cm in air. The detectors must therefore be arranged compactly around the target, and the amount of passive material between them must be minimal. The detector must be able to distinguish different types of particles. The timing signals must have a resolution of 1 ns or better in order to be used with the tagger. In order to operate in the photon tagging hall, the detectors

used must be relatively insensitive to the presence of electromagnetic and neutron background.

A large solid angle (LASA) detector has been built at the University of Illinois for the purpose of these and other similar experiments [71]. The target was chosen to be a gas at room temperature and pressure. This permits the use of a very thin target vessel. However the limits on beam flux imposed by the tagging technique, and the small target density conspire together with the smallness of the photodisintegration cross section to yield an extremely low experimental counting rate. To compensate for this fact, the target was extended in the shape of a long tube along the beam axis. The use of an extended target requires that the disintegration-fragment detectors must have particle tracking ability, if angular distributions are to be measured. A multiwire proportional chamber surrounding the target serves as a low-density tracking device and provides a level of particle discrimination as well. The LASA detector is described in greater detail in Sec. 2.3 below.

Being a highly segmented device, the LASA detector has required an elaborate design for data acquisition. A great deal of the work involved in the construction and testing of the detector fell in this area, for which the author of this thesis was primarily responsible. A separate chapter in this thesis is devoted to the data acquisition aspects of the program for this reason.

While the general experimental goal is a systematic coverage of all energies from above threshold to 100 MeV, including all of the breakup channels, the experiments have only begun. The data reported in this thesis only span the gamma energy region between 60 and 70 MeV. Furthermore only the $^4\mathrm{He}(\gamma,\mathrm{p})^3\mathrm{H}$ results are presented. Since theoretical calculations currently exist for only the two-body channels, and since it is in the region above 50 MeV where the new few-body calculations are expected to be the most reliable, it appears that this was the right place to begin. The results of this experiment demonstrate the fruitfulness of this new program.

2.2 Monochromator

The University of Illinois tagged photon facility is located at the Nuclear Physics Laboratory in Champaign, Illinois. The NPL houses a 100 MeV microtron which produces a continuous electron beam with excellent energy definition (30 keV) and an emittance of 5π mm mrad. This beam can be directed to one of several experimental end-stations, one of which is the tagged photon area. The layout of this area is shown in Fig. 2.1. The electron beam from the MUSL II accelerator enters at the bottom of the figure. Prior to entering the field of the magnet, it passes through a thin metal foil, called the converter, and produces bremsstrahlung radiation in the forward direction. The electron beam is then deflected by the magnetic field into a beam dump, while the photons exit the vacuum through a thin window and are incident on a target. The electron beam dump is heavily shielded to minimize room background, and is equipped with a Faraday cup for monitoring beam current.

Not shown in Fig. 2.1 is the photon beam dump. The distance from the bremsstrahlung converter foil to the dump at the back of the monochromator hall is approximately 9 m. The diameter of the photon beam is a function of the beam energy and increases linearly with distance from the converter. If the electron beam spot on the converter is considered a point source, the photons are emitted in a small cone about the incident electron direction. The transverse profile of the beam can be approximated by a Gaussian with a sigma of roughly m/E measured in radians, where m is the mass of the electron and E is its energy. At an electron beam energy of 90 MeV the diameter of the photon beam spot is about 10 cm at the photon beam dump.

The bremsstrahlung converter is a piece of 5 mil aluminum foil, which is only 0.0014 radiation lengths of material. Most of the electrons in the beam pass through the converter without radiating, and pass directly into the dump. Those that emit bremsstrahlung do so at the expense of their kinetic energy, and are bent in tighter

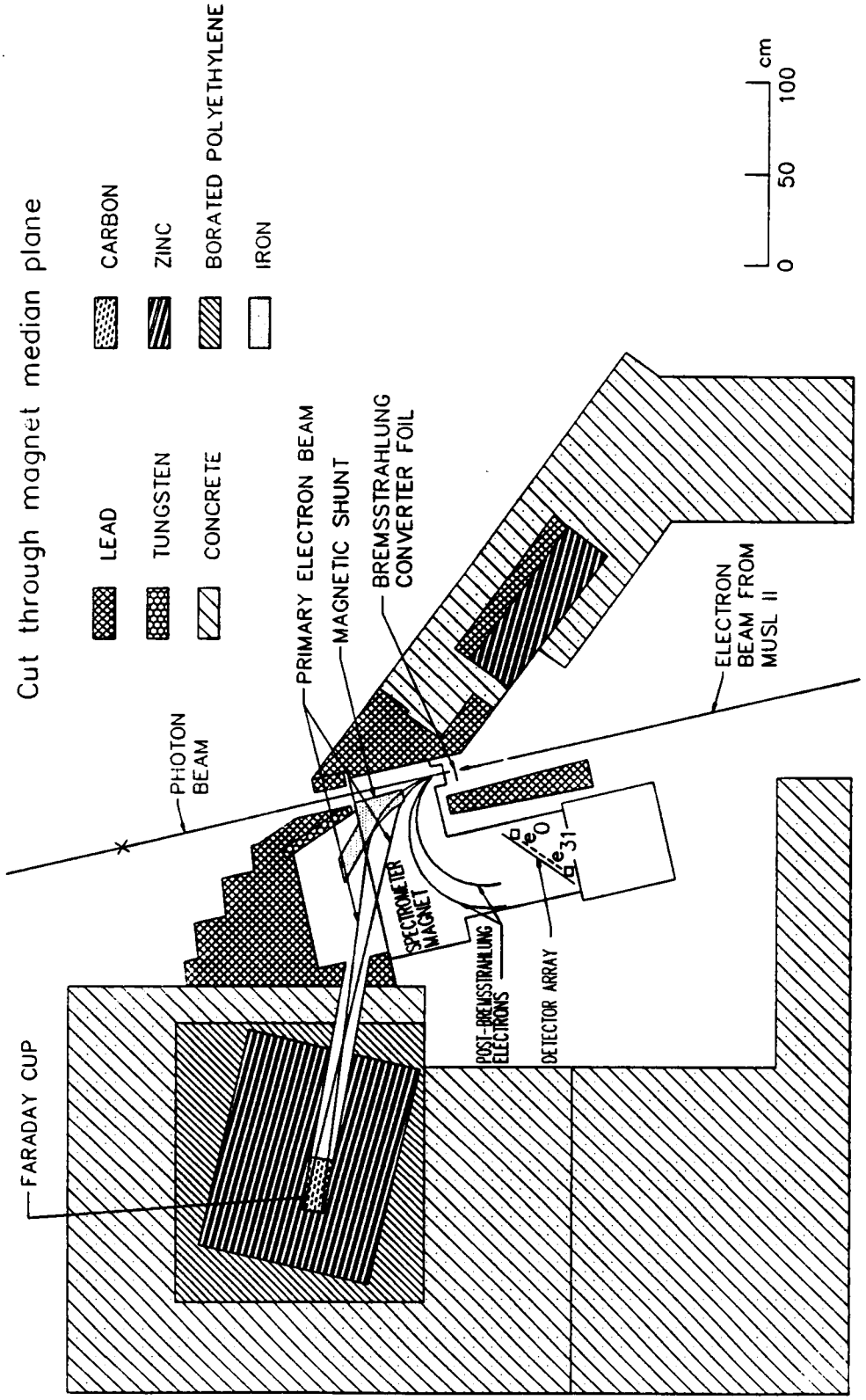

Figure 2.1: Layout of the monochromator experimental area, showing a cutaway view of the tagger magnet, electron beam dump, and shielding

orbits by the magnetic field. Hence the same magnet that diverts the primary beam into the dump also serves to analyze the energy of the post-bremsstrahlung electrons. Those electrons which radiated gammas of sufficient energy are bent full circle in the spectrometer and strike a hodoscope of 32 plastic scintillators located on the focal plane of the magnet. The time coincidence between a gamma in the photon beam and one of the focal plane counters "tags" the gamma ray energy. Thus in spite of the fact that the full bremsstrahlung spectrum of gamma energies is present in the beam, the use of tagging permits the selection of a monochromatic sample of photons; hence the name monochromator.

A detector of a type appropriate to the reaction being studied generates a trigger whenever it receives a hit from a scattering event in the target. This trigger is used to start a bank of TDCs (time-to-digital converters), one for each of the focal plane counters. Each TDC stops on a timing signal from its focal plane counter. If none of the focal plane counters receives a hit within a preset time coincidence window, the TDCs and other electronics are reset with a fast-clear pulse to prepare for the next trigger. If there was a coincidence in one or more tagging counters, the electronics proceed to latch the data for that event, and a computer interrupt is generated.

The cross section for a reaction is derived from the ratio of the count of coincident events to the total number of gammas that passed through the target during the live time of the experiment[1]. The denominator of this ratio, also called the flux normalization, is obtained by scaling the number of times each of the tagging counters fire. The dead-time correction to these counts is performed automatically by gating the focal plane scalers with the experimental on/off signal, which disables the scalers while the experiment is dead.

Actually the focal plane scalers overestimate the number of tagged photons in the beam. The reason for the excess of electrons striking the focal plane which are

[1]The experiment is said to be "live" any time it is not "dead". The experiment is dead when the detector electronics are in a latched state and are being read out by the computer.

not associated with a photon in the beam is not entirely understood. Nevertheless this excess is proportional to the beam flux, and can be eliminated by the use of a multiplicative constant, called the tagging efficiency. Tagging efficiency is a function of beam energy and magnetic field setting, and is measured individually for each tagging counter in a series of calibration runs interspersed throughout the experiment. This procedure is described in Chap. 4.

The range of energies that can be tagged at once is determined by the properties of the tagging magnet. The NPL monochromator can tag a range of about 8 MeV with an average of 0.25 MeV subtended by each tagging counter. This limit is enforced by the momentum bite of the tagging spectrometer, given by $\Delta p/p = 37\%$. This means that, if the magnetic field is set such that a recoil electron of 22 MeV strikes the middle of the focal plane, electrons at 18 MeV are detected at one end of the focal plane, and those at 26 MeV are detected at the other. If the magnetic field is increased, the range of tagged gamma energies is broadened and moved further down from the endpoint energy. However the field in the present tagging magnet is nearly saturated at the setting which bends a 22 MeV electron into the middle of the focal plane. With this constraint, the choice is between lower energy photons with a maximum tagging range, and a smaller range of gamma energies closer to the endpoint. The maximum energy for an incident electron beam which can be cleanly dumped in the monochromator hall is 90 MeV. The choice for this experiment was for a beam energy of 88 MeV, tagging gammas in the energy range 63-71 MeV.

One important limitation of an experiment with tagged photons is the maximum beam flux that can be obtained. The absolute upper limit is set by the rate capacity of the tagging counters and the associated electronic hardware. This limit is approximately 10^7 s^{-1} for the NPL tagger. However since the rate of random coincidences increases as the square of the beam flux, while the reaction rate rises only linearly, the optimum counting rate is somewhat below the hardware limit.

When the ratio of trues to randoms within the coincidence window of the experiment falls below one, the statistical precision that may be obtained in a given number of beam shifts saturates. For reasons of minimizing experimental dead time, this ratio is usually kept greater than one, which typically leads to a rate of 10^6 s^{-1} per tagging counter.

In the case of experiments with the LASA detector, it was the trigger rate of the detector that determined the maximum beam current which could be used. The high rate of event triggers, which was discovered during early test runs to exceed calculated estimates by more than one order of magnitude, was found to arise from electromagnetic background processes. The result was that the photodisintegration measurements were done using a beam flux of only 10^5 s^{-1} per tagging counter. Summing all 32 tagging counters, the total tagged flux in the beam used in this experiment was approximately 3×10^6 s^{-1}.

2.3 LASA Detector

The photodisintegration of ^{4}He was the first production experiment done with the University of Illinois LArge Solid Angle (LASA) detector. This detector was designed for photodisintegration measurements of $A = 2$, 3 and 4 nuclei at gamma energies up to 100 MeV. The general structure of the LASA detector is similar to a typical high energy physics detector such as the Collider Detector Facility (CDF) at Fermilab [72], scaled down several orders of magnitude in size. The basic detector elements, wire chambers and plastic scintillators, are well understood devices in common use in nuclear physics. Nevertheless the application of such a 4π structure to the design of a detector for nuclear physics experiments at intermediate energies is an innovation of this experiment.

A schematic picture of the LASA detector is shown in Fig. 2.2. The long tube extending beyond both ends of the detector is the target vessel. Surrounding the middle portion of the target is a cylindrical wire chamber consisting of three

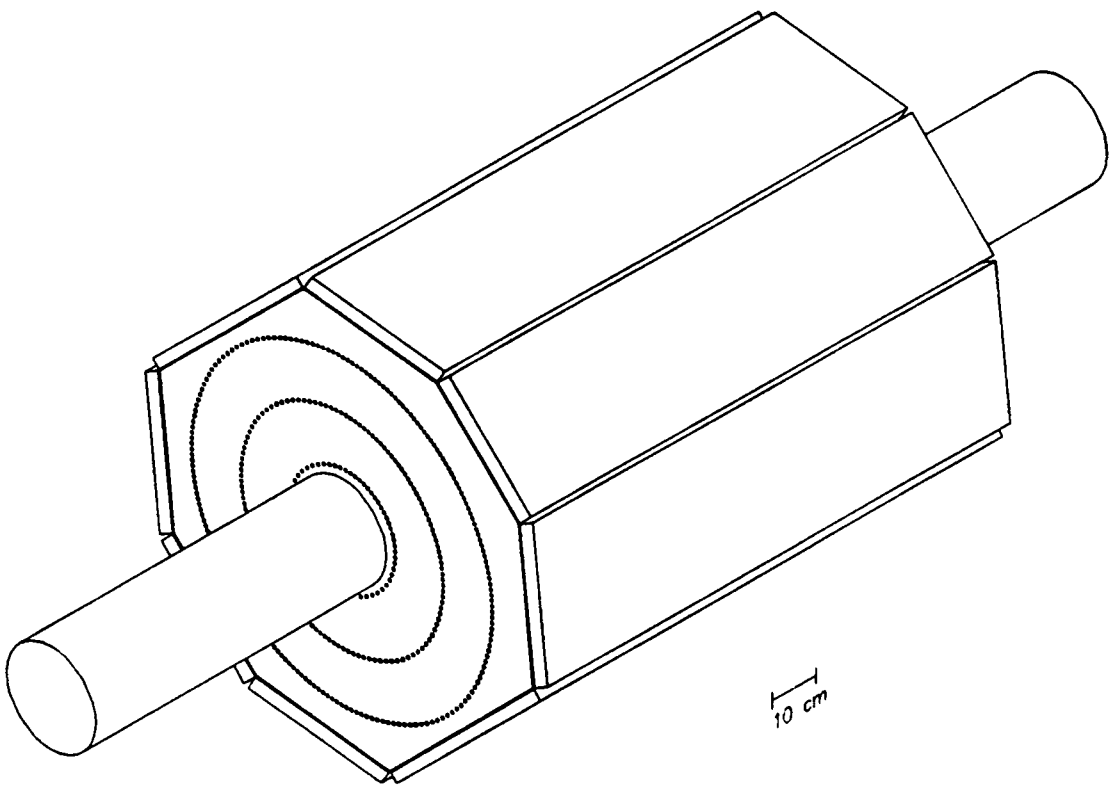

Figure 2.2: Schematic picture of the LASA detector

concentric levels of wires. These wires run parallel to the detector axis and are fastened at each end to the detector end plates. Surrounding the wire chamber is a double layer of plastic scintillator. This layer is broken up into 8 planar sections, forming an octagonal cross section. The inner layer is 0.318 cm thick, used for ΔE measurement. The outer layer thickness is 2.54 cm, which is sufficiently thick to stop all charged particles, and is used for the total E measurement. Such a combination of ΔE, E scintillators is useful for obtaining information both about the particle energy and particle type.

The photon beam is directed down the central axis of the detector. Photodisintegrations in the target gas generate charged particles, many of which pass through the target vessel walls and into the detector volume. As the particle passes through each successive wire level, it creates a pulse which registers a "hit" in the nearby wires. Each hit contains both coordinate and energy information. Finally the particle enters the thin scintillator and is detected. If the particle has sufficient energy, it passes through the thin and into the thick scintillator and registers a hit there before it stops.

In Fig. 2.3 is shown a typical ^{4}He$(\gamma, \mathrm{p})^3$H event. The proton makes a hit in the three wire levels, in the ΔE and the E scintillator before it stops. The more massive triton, having less energy, leaves hits in the three wire levels and stops in the ΔE scintillator. Note that the opening angle between the two tracks is only slightly less than 180°. This is due to the fact that the momentum carried by the photon is small compared to the mass of the ^{4}He nucleus. The velocity in the lab of the center of mass (c.m.) reference system, in which the proton and triton are exactly back-to-back, is $.019\,c$ for a gamma energy of 70 MeV. Because of the near identity of the c.m. theta and lab theta, it is possible to cover most of the angular range without having to position detectors at extreme forward angles, as would be necessary at higher energies or with a heavy probe. Requiring that a track pass through all three wire layers and intersect the thin plastic scintillator restricts theta

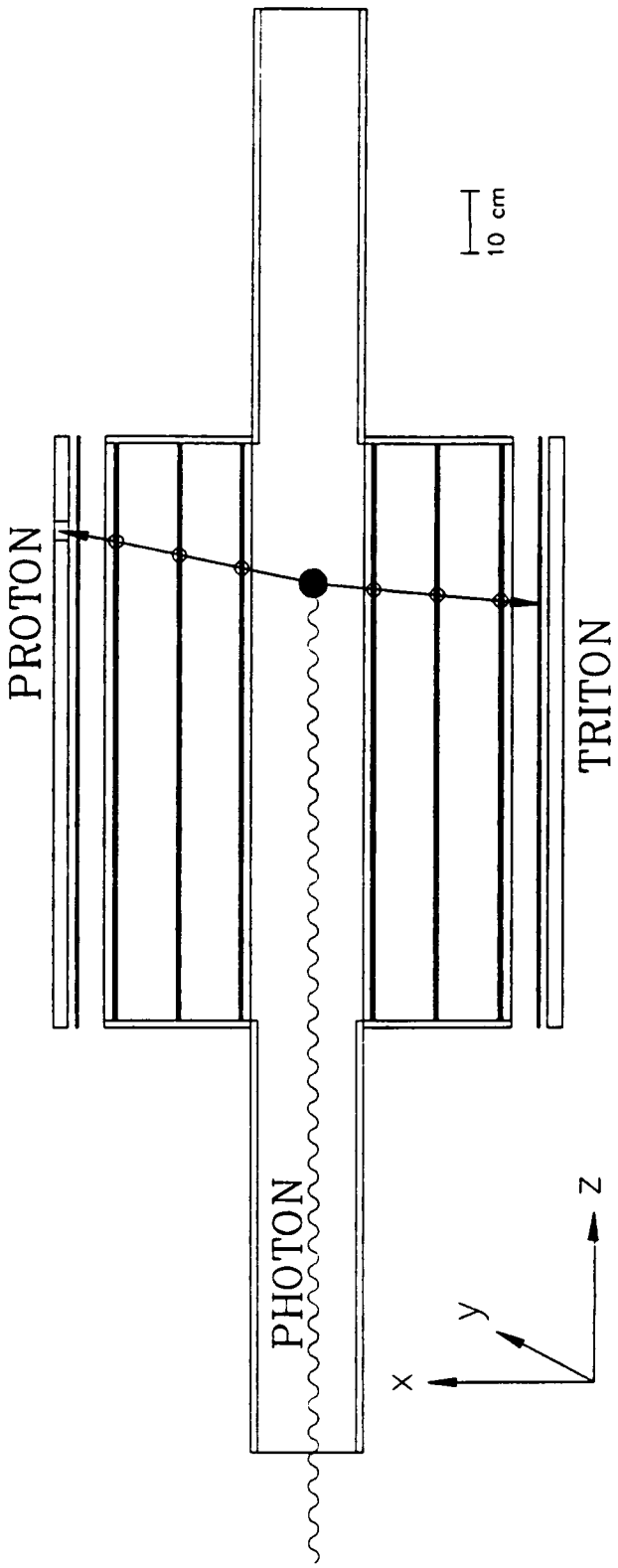

Figure 2.3: Cross-sectional view of the LASA detector, showing a typical two-body photodisintegration event.

to the range 16° to 164°, over 95% of 4π sr.

The extension of the target beyond the length of the detector has two purposes. First it permits the detection of events which generate tracks at the maximum forward and backward angles. Tracks with a theta angle of 21° or less must originate somewhat upstream of the detector boundary in order to hit all three wire layers and the plastic scintillator. Similarly tracks at a theta of 159° or greater must originate in the downstream end of the target in order to be counted.

The second reason for the long target is to exclude as much material as possible from the path of the beam upstream of the detector. This is because electromagnetic processes, which are the primary background for these experiments, are sharply forward-peaked in their angular distribution. Material in the beam upstream of the detector generates a shower of electrons which contributes to the background rate in the wires and scintillators. Since the target gas has only 1/7 the density of air, it obviates the need for shielding. The target extension was chosen to be long enough that interactions in the target windows could not directly illuminate the plastic scintillators.

2.3.1 target vessel

The target gas is contained within a long tubular balloon 10 cm in radius. The balloon material is nylon, only 28 microns thick with a 0.2 micron layer of aluminum deposited on one side. The aluminum coating is necessary to contain the light gas, which leaks through organic membranes at a high rate. Being produced commercially to make helium balloons, this material sustains a very low helium leak rate, and has the convenient property that it can be sealed with a heat press. In the two end sections of the target, the balloon is contained within an aluminum tube which lends mechanical support and provides a seal between the balloon and the end windows. Within the volume of the detector, the balloon is bare and completely self-supporting, providing a minimum barrier to charged particles going

from the target into the chamber. For a particle passing through the balloon at normal incidence, the energy loss is equivalent to that in 3 cm of air.

2.3.2 wire chamber

The multiwire proportional chamber (MWPC) consists of a barrel 37 cm in radius, 105 cm long surrounding the target. Within the chamber are three concentric cylindrical wire levels, each of which consists of three layers of wires. The substructure of a wire level is shown in Fig. 2.4. The solid dots are the sense wires and the open circles are the field wires. The field wires are held at a high negative voltage relative to the sense wire at the center (which is at ground potential) to generate the necessary cylindrical electric field around the sense wire. When a charged particle passes through the volume of a cell, it leaves behind a track of ionized electrons which drift under the influence of the electric field to the nearest sense wire, where they produce an electric pulse. These individual cells are stacked compactly together, as shown at the right of Fig. 2.4, to form a continuous circle with a 1 cm spacing between the sense wires. In the inner level there are 64 sense wires, 128 in the middle, and 192 in the outer level.

The volume of the wire chamber is sealed and filled with a special gas. A gas mixture must be chosen which has the right properties for good efficiency, high gain, and suppression of breakdown in the desired mode of operation. The LASA wire chamber is designed to operate in proportional mode [73], in which the signal size induced on the sense wire is proportional to the ionization energy loss of the charged particle in the cell volume. For efficient operation in this mode, the dominant component of the mixture must be a gas with low electronegativity, so that ionization electrons have a high probability for drifting to the sense wire without being captured. A rare gas such as argon is the typical choice. For the helium photodisintegration experiment, a chamber gas with a lower density is desirable, so that the low-energy charged particles have as much range as possible. Thus the

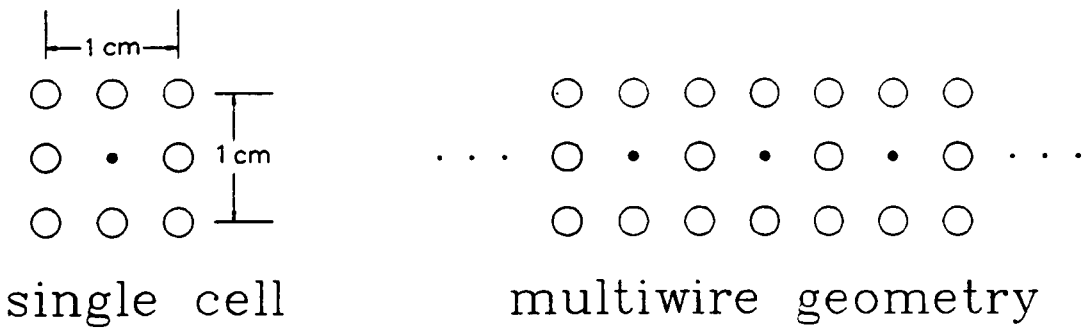

Figure 2.4: Substructure of a wire level in the MWPC

choice was made for helium as chamber gas. In order to obtain stable operation at appreciable gain, it was necessary to mix some organic gas with the helium in the chamber [73]. The proportions chosen were were 90% helium, 10% methane (CH_4) by volume.

In the lower left corner of Fig. 2.3 is shown the orientation of the LASA detector coordinate system. The origin of the coordinate system is at the geometric center of the detector. The beam is in the $+\hat{z}$ direction. The x and y coordinates of a hit in the wire chamber are derived from the index of the wire that fired. The z coordinate of the hit is determined by a method called charge division. The passage of an ionizing particle through a wire cell generates a pulse of current on the sense wire. In proportional mode, this current source is confined to a small segment of the wire, delimited by the projection onto the wire of the points where the track entered and exited the cell. The sense wire, being made of a conductor with appreciable resistance to electric current, acts as a current divider, delivering an amount of the total charge to each end of the wire in inverse proportion to the total resistance along that path. By measuring the charge received at each end of the wire, the z coordinate of the hit along the wire can be determined.

The sense wires are 76.2 μm diameter Stableohm 800, a steel alloy with an exceptionally constant value of resistance per unit length. The field wires are 254 μm diameter copper-coated stainless steel. While these wire diameters are larger than commonly used in wire chambers, the difficulty of replacing broken wires in this device makes good mechanical durability a necessity. The wires pass through the end plates through a brass tube set in an insulating plastic feedthrough and are fastened on the outside by solder. The sense wires were strung at a tension of 1 N, the field wires at 5 N. Following construction the wire tensions were measured using an electrostatic oscillator [74]. The scan revealed several wires that required replacement at that time. In the intervening 24 months of use, not a single wire has needed to be replaced due to breakage or loss of tension.

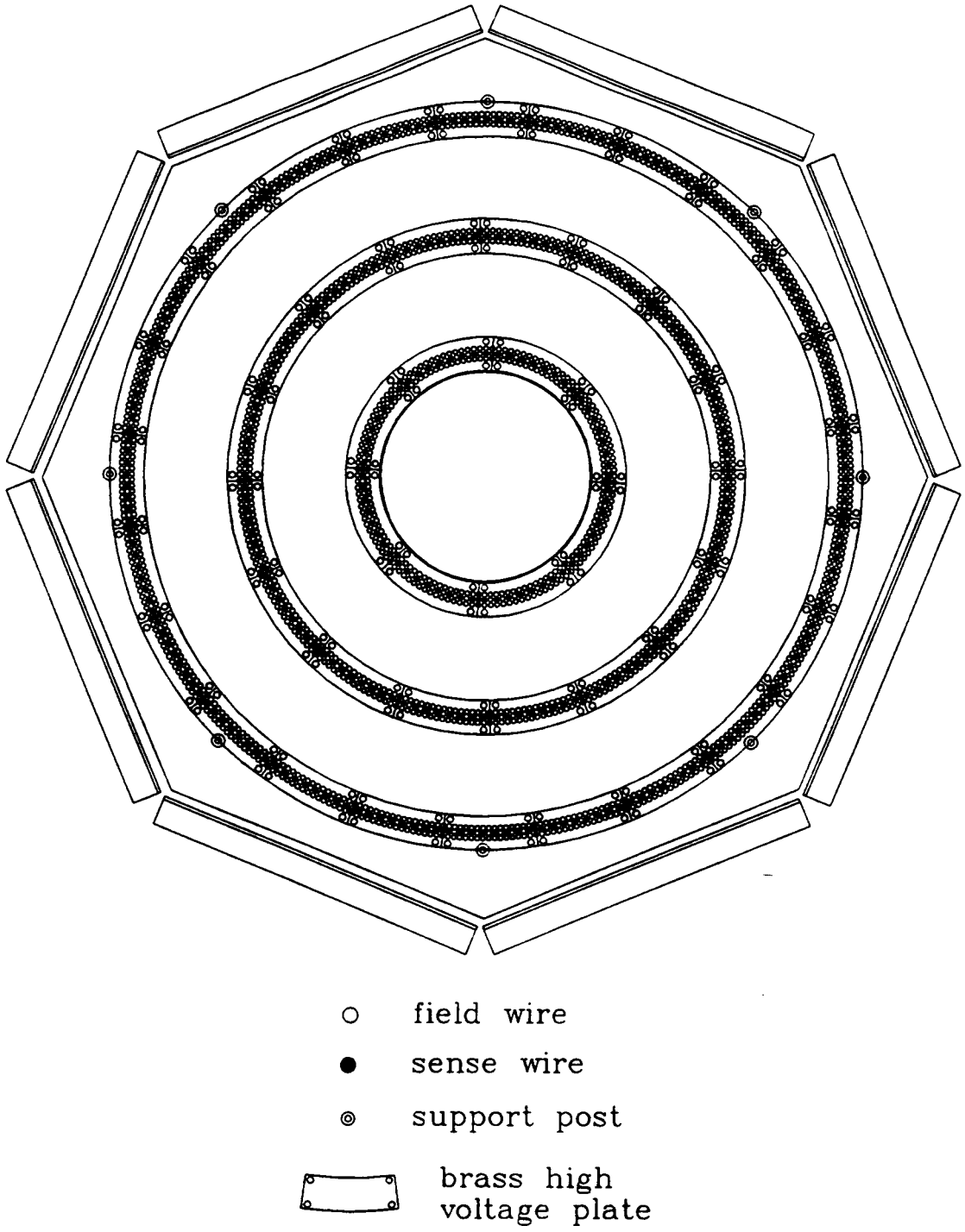

Figure 2.5: Wire chamber end plate of LASA detector

A view of the wire chamber end plates is shown in Fig. 2.5. They are made of 1/2 in. aluminum plate. The outside edges form an octagon to mate with the array of scintillator paddles which surround the wire chamber. The plates are held apart by eight 1/2 in. stainless steel rods spaced evenly around the circumference, just outside the outer wire level. They are aligned with the joints between scintillators so as not to cast a shadow on them. These rods provide the counter-support for the wires whose tensions sum to a force greater than 10^4 N.

The wire levels are divided into segments, each containing eight sense wires. All of the field wires in each group are ganged together. The end of the field wire feedthroughs that stick out of the end plate are fitted with conducting rubber feet. When the brass high voltage plate shown in Fig. 2.5 is tightened down, it makes electrical contact with all of the high voltage wires in the group. A profile of the connections on the end plate is shown in Fig. 2.6. The high voltage is supplied by a LeCroy 4032A mainframe power supply. One -7 kV supply pod is devoted to each of the three wire levels. The HV is distributed to the brass plates through inline resistors of 100 kΩ which serve to suppress radio-frequency (rf) noise from the power supply, and limit current in the case of a short. While there are brass plates on both ends of the chamber, the high voltage connection is only made on one end.

The sense wire feedthroughs are longer than those of the field wires, and they protrude through holes in the brass plates. These feedthroughs are also fitted with conducting rubber feet. A circuit board cut in the same shape as the brass plates is pressed down onto the sense wire contact feet. Circular pads etched from the solder mask on the bottom of the boards line up with the feet and provide electrical contact between the end of the sense wire and the preamplifier electronics on the board. A ground post mounted on each amplifier card to make contact with the end plate is shown at the right in Fig. 2.6. This references the signals from the sense wires to a common low impedance earth, in order to minimize ground loop

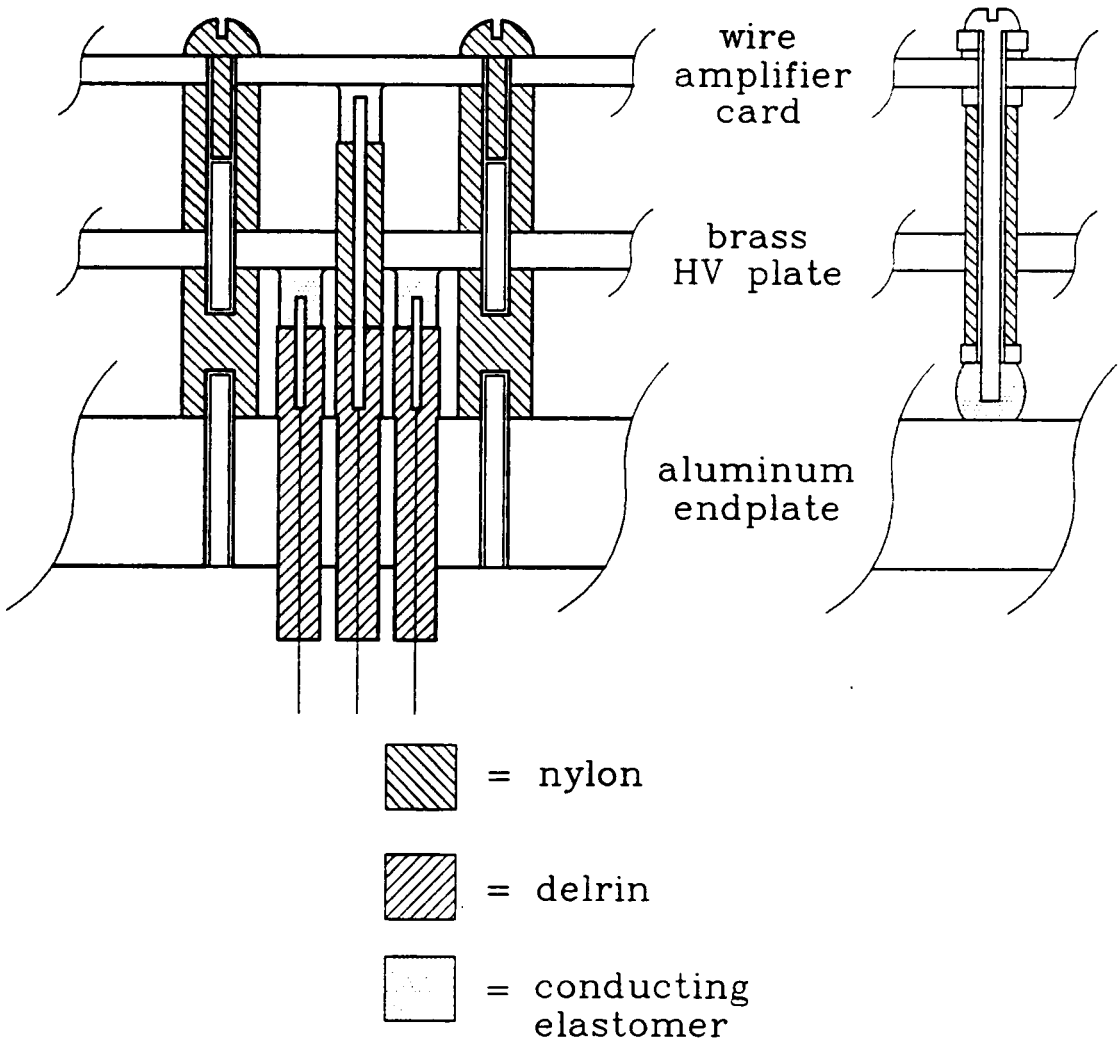

Figure 2.6: Profile of the electrical connections on the end plates

interference. In Fig. 2.7 is shown the schematic of the preamplifier electronics. Most of the circuit is contained on a hybrid circuit which was designed by V. Radeka [75] and mass produced for the CDF experiment.

2.3.3 plastic scintillators

The plastic scintillator annulus consists of eight ΔE, E sandwiches. The paddles are 30.5 cm wide by 102 cm long and 0.318 cm and 2.54 cm thick, respectively. The scintillator material is BC-400 from Bicron Corporation. The light pulses are detected by phototubes at either end of each paddle. Long twisted strips of lucite of the same thickness as the scintillator serve as light guides on the ends of the paddles to collect the scintillation light and direct it onto the phototube. Between the phototube and the face of the light guides is a short lucite cylinder which serves to disperse the light uniformly over the face of the photocathode. A picture of the assembled scintillators is shown in Fig. 2.8. For the thin paddles, 2 in. diameter Hamamatsu R329 phototubes were used. The thick paddles have 5 in. diameter Amperex XP2041 tubes.

The light guides were bent so that the scintillators could lie flat against one another. The ends of the paddles from the light guides back to the tube were wrapped individually with aluminum foil and black tape. The scintillator sheets themselves were left bare until they were mounted into the sandwich cradles. A sheet of 1 mil aluminized mylar was then placed between the two plastic layers and then they were wrapped together with 0.7 mil aluminum foil. This thickness of foil is equivalent in terms of ionization energy loss to 4 cm of air. Thinner foils were tried but without success, due to light leaks.

The measured rise time of signals from the LASA scintillators is 2.8 ns, with a fall time around 10 ns. Very accurate timing, with an uncertainty less than 1/2 ns, can be derived from the leading edge of these pulses. With this resolution, it is possible to observe the propagation delay of the light pulse inside the plastic. By

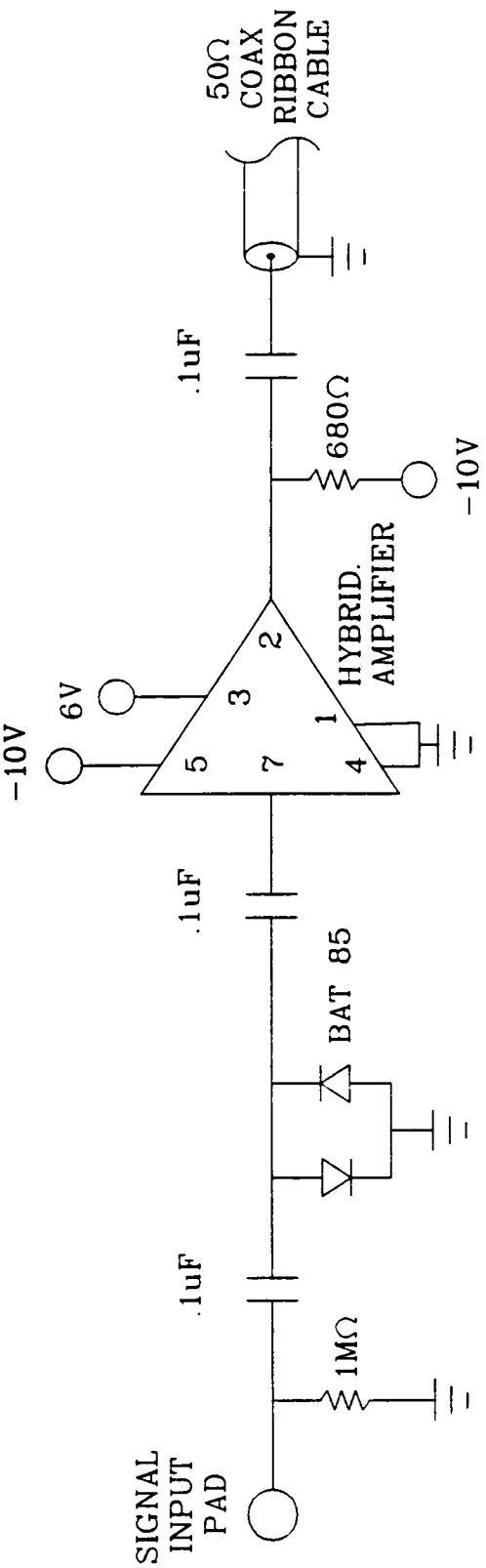

Figure 2.7: Schematic of the wire preamplifier card

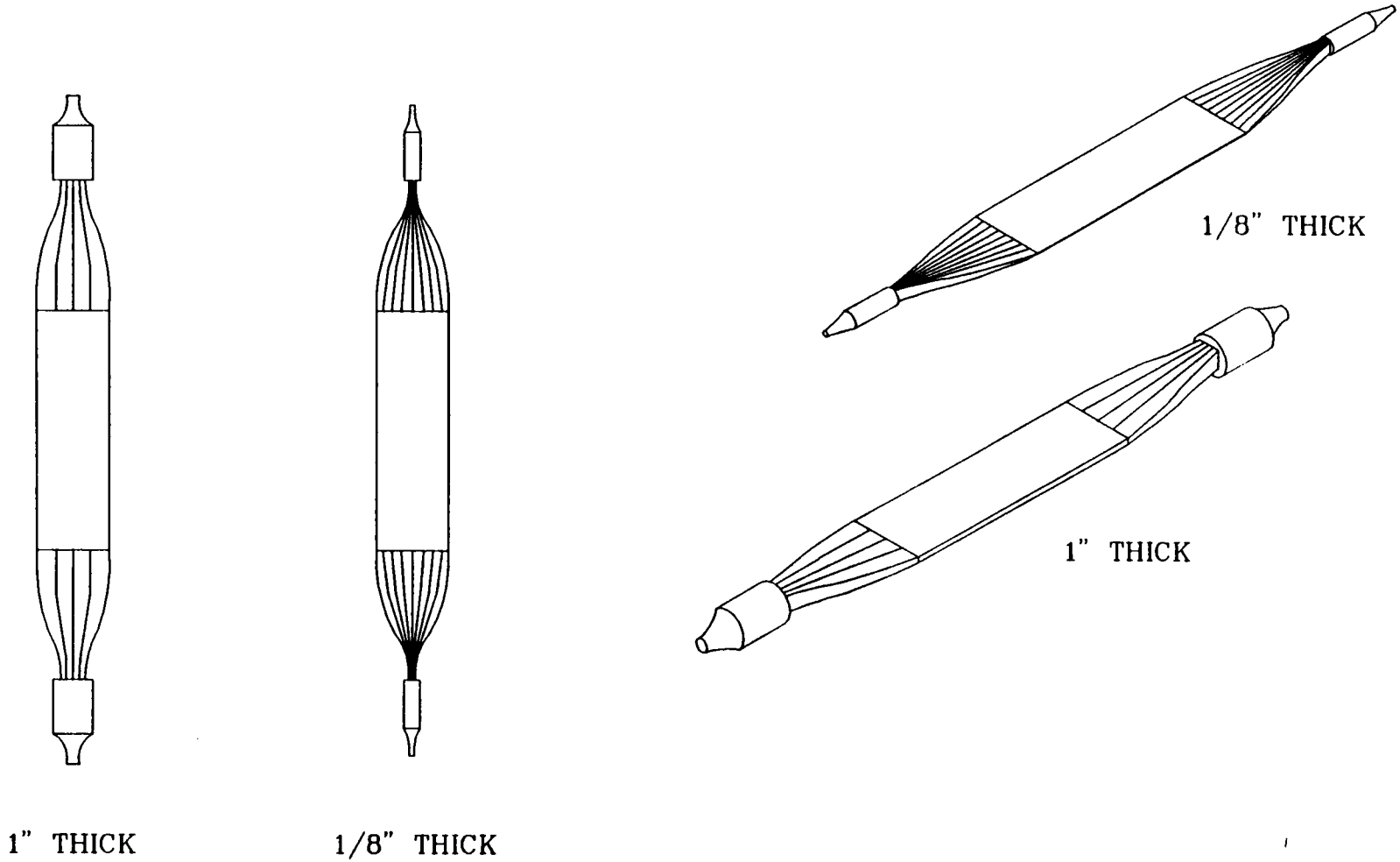

Figure 2.8: Drawing of the plastic scintillators

taking the difference between the pulse times from the two ends, a measurement of the z coordinate of the hit along the scintillator length can be obtained. The sum of the times may be taken as a position-independent measurement of the instant that the charged particle was incident on the scintillator.

The amplitude of the light pulse inside the plastic scintillator is attenuated on its journey to the phototube. Since the path length depends upon the location of the hit, the amplitude measured at the ends must be corrected for attenuation. This correction is described in detail in Chap. 4. Once a position-independent light amplitude is obtained, it must be transformed into particle energy or energy loss. This transformation requires a knowledge of both particle momentum and mass, neither of which are known until the later stages of analysis. Therefore plastic signal amplitude is expressed in units of electron-equivalent energy. An electron which drops a given amount of energy in a plastic scintillator generates a light pulse of a certain magnitude, regardless of its incident energy, thus providing a convenient unit for light amplitude. For minimum ionizing particles carrying one unit of charge, such as the muons found in cosmic rays, the conversion factor from electron-equivalent MeV to MeV of energy loss is 1. The conversion factor for slow particles is given by an empirical formula [76] with coefficients which must be measured for each type of scintillator. The response curves for the plastic used in the LASA detector are given in Chap. 4.

Chapter 3

Data Acquisition

With the high multiplicity and complexity of the LASA detector, it was seen from the beginning that a sophisticated data acquisition design would be required. Relying heavily upon hardware and software designs from high energy physics, and with considerable original work, a flexible and extendable system has emerged. The hardware and software aspects of the system are discussed below under separate headings. A special section is devoted to the event trigger design since it proved to be so critical to the success of this experiment.

3.1 Hardware

The LASA detector is described in Chap. 2. The wire chamber contains three levels of 64, 128, and 192 wires respectively, each of which is read out on either end. The plastic annulus consists of eight ΔE and eight E scintillators, each of which is read out on both ends. This yields a sum of 768 wire signals and 32 plastic scintillator signals, as well as the 32 signals from the monochromator focal plane, which define an event in the LASA detector. The time scale of an event is fixed by the time of propagation of a typical photodisintegration fragment from the target to the plastic annulus, roughly 10 ns. Compared to this time, the speed of the wire chamber pulses is slow, with a rise time of about 50 ns. Therefore no timing information is derived from the wire pulses; only their amplitude is digitized. However the scintillator signals, both from the LASA annulus and the

monochromator focal plane, are fast compared to 10 ns, and time information is extracted from them. The pulse amplitudes from the LASA plastic paddles contain particle energy information, so these are digitized as well. The amplitudes of the focal plane signals are useful only as a diagnostic, and are not digitized. All together there are 800 ADC (analog-to-digital converter) and 64 TDC (time-to-digital converter) values that define one event.

An event is defined as a combination of hits in the detector that generates a trigger. The event trigger is a logic pulse whose leading edge defines $t = 0$ for the event. Due to unavoidable delays in the trigger logic, $t = 0$ occurs long after the event has taken place in the detector. The trigger generates a gate signal for all of the ADC and TDC modules to begin acquisition. The design of the event trigger is detailed below in Sec. 3.2. In Fig. 3.1 is shown a simplified event timing diagram. The instant of photodisintegration defines the time origin in this diagram. Note that the trigger is not formed until 250 ns later. For this reason, signals must be delayed in order to arrive at the ADC or TDC input synchronous with the gate. This delay is achieved by using appropriate lengths of coaxial cable between the detector and the electronics.

Since they are used to generate the trigger, the plastic scintillator signals are delivered to the electronics with minimum delay. The intrinsic propagation delay in the 5 in. phototubes on the thick scintillators is longer than that in the 2 in. tubes, so the signals from the thin plastics are delayed 15 ns to arrive synchronous with those from the thicks. All 32 signals then pass through a bank of switchable delays where timing differences between individual ends are corrected at the level of ± 1 ns. The signals are then split in a passive network between one path to the timing discriminators and the other path to the ADC. A diagram of this circuitry is shown in Fig. 3.2. On the path to the ADC, the pulses go through 200 ns of cable delay so that they arrive synchronous with the gate. A tap located along the way carries a small fraction of each signal to a high impedance network where the two

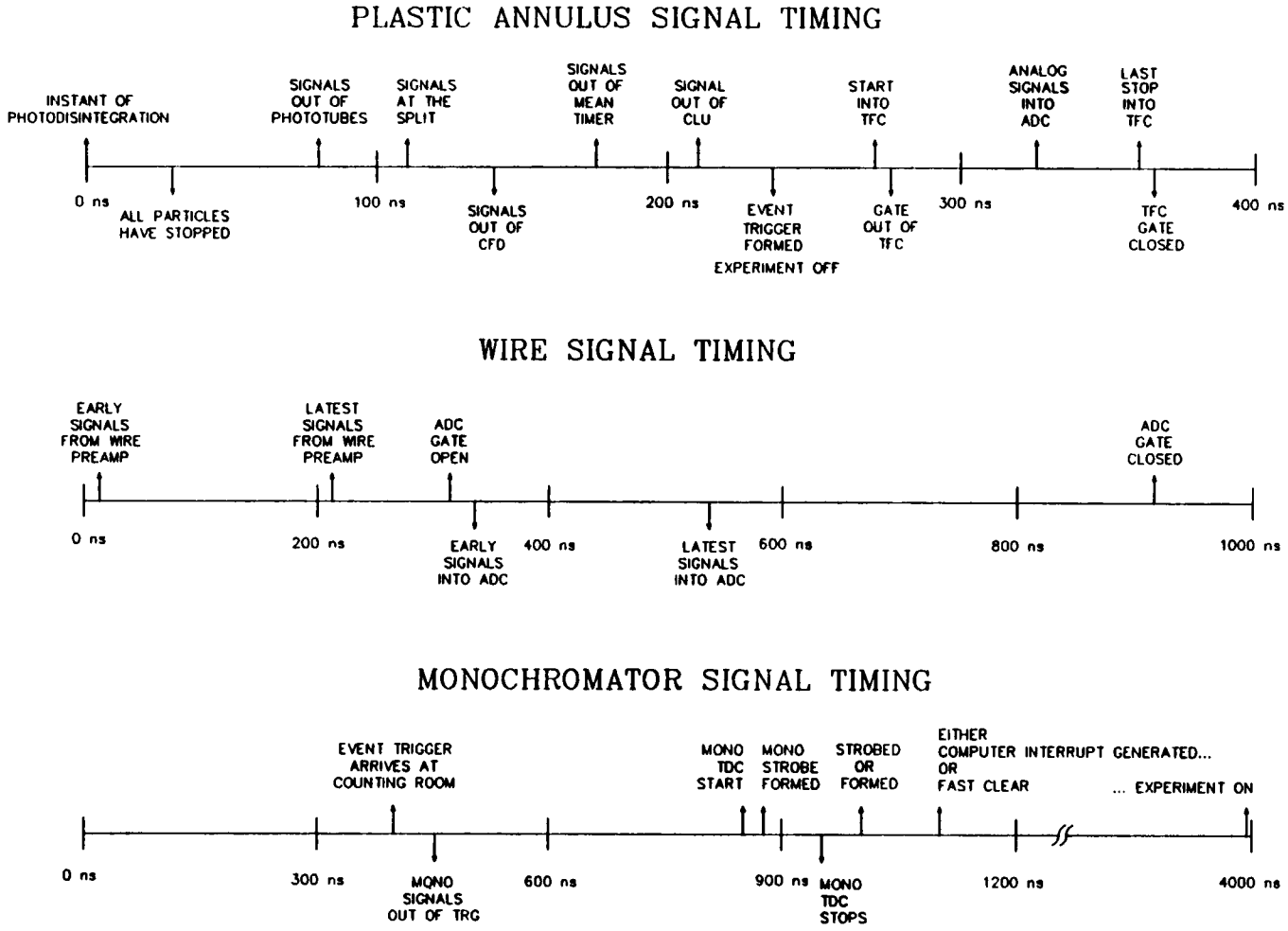

Figure 3.1: Abbreviated event timing diagram

ends of each thin paddle are summed. A level discriminator with high impedance input (not to be confused with the timing discriminators) on each of the eight sum signals provides one set of inputs to the trigger logic.

The timing discriminators used on the plastic signals are of the constant fraction type, NIM module 715 from Phillips Scientific. The time resolution of these devices for plastic scintillator signals is about 200 ps FWHM (full width at half maximum) using an inverter delay of 4 ns. These modules have been retrofitted with back panel inputs which are connected to DAC's (digital-to-analog converters) so that the discriminator thresholds can be adjusted by the computer. Each discriminator has three NIM logic outputs: one for the plastic TDC, one for the trigger, and the other is sent to a scaler.

All of the LASA detector signals are digitized in FASTBUS, a data acquisition standard widely used in high energy experiments. Faster and more compact than CAMAC, FASTBUS is designed to economically provide for large numbers of ADC and TDC channels. A single 1880 series ADC module from LeCroy Corporation contains 96 individual ADC's. The wire signals are digitized in a bank of eight 1885 ADC modules, the plastics in a ninth. The 1885 is a charge integrating ADC with 12 bits of resolution. The module supports two conversion gains: 50 fC/channel with a full scale of 200 pC, and 400 fC/channel with a full scale of 1600 pC. In experiments so far with the LASA detector, only the high range has been used.

Since a high resolution TDC is not yet available in FASTBUS, a LeCroy 4303 TFC module is used to convert the plastic time to a current pulse whose charge, when integrated in an ADC, is proportional to the time. The trigger provides a common start for all of the TFC channels, and each stops on the corresponding timing discriminator signal. Matched with a FASTBUS 1885 ADC operating in high range, the gain of the TFC is about 16 channels/ns, with a resolution on the order of 100 ps FWHM. Both the plastic amplitude and the timing pulses are digitized in the same 1885 ADC. The ADC gate is generated by the TFC to be

suitable for integrating the current pulses it produces. The delay on the amplitude signals is adjusted to fit them inside the same gate, since the 1885 uses a common gate for all 96 inputs. The gate width from the TFC, which also determines the full scale for the plastic timing, is adjusted to its minimum value of 100 ns. Although this gate is wider than optimum for the plastic analog signals, the rates in the scintillators under normal operation are not sufficient to present a problem.

The signals from the wire ends are fed directly into preamplifiers mounted on the chamber. There the signals are amplified by a factor of 150 and buffered to drive a 50 Ω load. The connection to the ADC inputs is made by ribbon coaxial cable, a specialty product from Belden. Each cable contains 24 individual 50 Ω coax lines and is mass terminated. The original plan to use twisted pair ribbon proved impossible due to rf pickup and problems with crosstalk between the pairs. As can be seen from Fig. 3.1, the wire signals require over 300 ns of delay, which translates to 200 feet of 50 Ω cable. At the chamber end, each cable splits into three parts, each one of which connects to one of the eight-channel preamps. The other ends of the cables connect to paddle cards which feed the ADC inputs.

Operating in proportional mode at modest wire gains, a typical proton track from a photodisintegration event produces a pulse height of about 50 mV on the preamp outputs, averaging between the two ends of the wire. This corresponds to a total charge of 1 pC collected on the wire. Such a pulse leads to an average of 100 pC delivered within the gate to the ADC connected to either end. The rms noise from the preamps for a gate width of 600 ns is at the level of 1 pC. This noise has been shown to be rf pickup, principally from a nearby AM radio station. While this noise makes a negligible contribution to the δE resolution of the wires, it limits the z resolution of the wires to 1.2 cm rms.

The pulses from the wires have a rise time of approximately 50 ns and a fall time of 200 ns. However the ADC gate must be somewhat wider than this in order to account for the time jitter of the wire pulses relative to the trigger. This

jitter is caused by the variation of electron drift delays with the distance from the particle track to the sense wire. The ionization electron drift velocity is a complex function of the electric field and chamber gas. For a chamber gas mixture of 90% argon, 10% CH_4, the electron drift speed is approximately 35 mm/μs [73], assuming LASA wire cell geometry with a nominal wire voltage of 2 kV. This yields a worst case drift delay of 200 ns from the cell corner to the center. For the helium-based chamber gas, the drift speeds are expected to be somewhat higher, reducing this effect. Since high rates in the wire chamber are not a problem, the gate width has been extended to 600 ns.

Actually the 1885 module only contains one ADC. The signals are integrated in individual S&H (sample-and-hold) circuits on the front end of the module; the integrated charge from each channel is later presented in sequence to the ADC for digitization. After the expiration of the gate, there is a 10 μs delay called the MPI (measure pause interval) before the conversion cycle begins. During this interval, if the higher level trigger logic decides to discard the event, the fast-clear pulse will restore the module to data acquisition mode. Fast clears during MPI complete in less than 1 μs. If a fast clear does not occur, the MPI expires, and the conversion cycle is entered.

The trigger logic and scalers for the LASA detector are distributed between CAMAC and Black Box. Black Box electronics, developed by the high energy group at University of Illinois during the 1970s, has a similar functionality to CAMAC, with somewhat lower cost. ECL logic, with its superior speed and noise immunity, is used wherever possible in the LASA electronics. ECL signals are transmitted differentially on twisted pair cable, which greatly simplifies the routing and reliability problem. Use of existing NIM modules required translation between ECL and NIM in many parts of the circuit.

3.2 Event Trigger

Since the signals from all eight plastic scintillator sandwiches enter symmetrically, only one set is shown in Fig. 3.2. Coming in from the left of the figure are the signals from the phototube bases. These run through fixed and variable delays, which adjust their relative timing, and then are split between one path, which leads to the ADC, and the other, which leads to the timing discriminator. A tap on the ADC leg couples the signals from either end of the thin paddle into the HI-Z summing discriminator which generates a pulse if the sum is over a preset threshold.

The output from the timing discriminator for either end of each paddle is delivered to a special device called a "mean timer." This device has two logic inputs and a single logic output. If pulses are received on the two inputs within 20 ns of one another, an output pulse is generated, whose leading edge is synchronized with the average time of the two input pulses. This way, the timing of the output pulse, and hence of the trigger formed from it, is independent of where along the length of the paddle the particle hit. The mean timer also serves to signal a coincidence between the two ends of each paddle. The status of all 16 mean timer outputs are latched in a LeCroy 4508 PLU (programmable logic unit) module, and together they form a trigger pattern for the event.

Loosely speaking, the mean timer outputs are the AND of the two ends of a paddle at a low discriminator threshold, and the HI-Z discriminator outputs are the OR of the two ends at a high threshold. When the two thresholds are set properly, together they provide for a minimum light pulse amplitude which is fairly uniform along the length of the paddle. The relative timing of the mean timer and HI-Z discriminator signals at the input to the CLU (coincidence logic unit) are adjusted so that the leading edge of the former follows that of the latter, with the result that the mean timer pulse defines the timing of the output of the AND between the two. The second level of coincidence in the CLU is not used, since only the

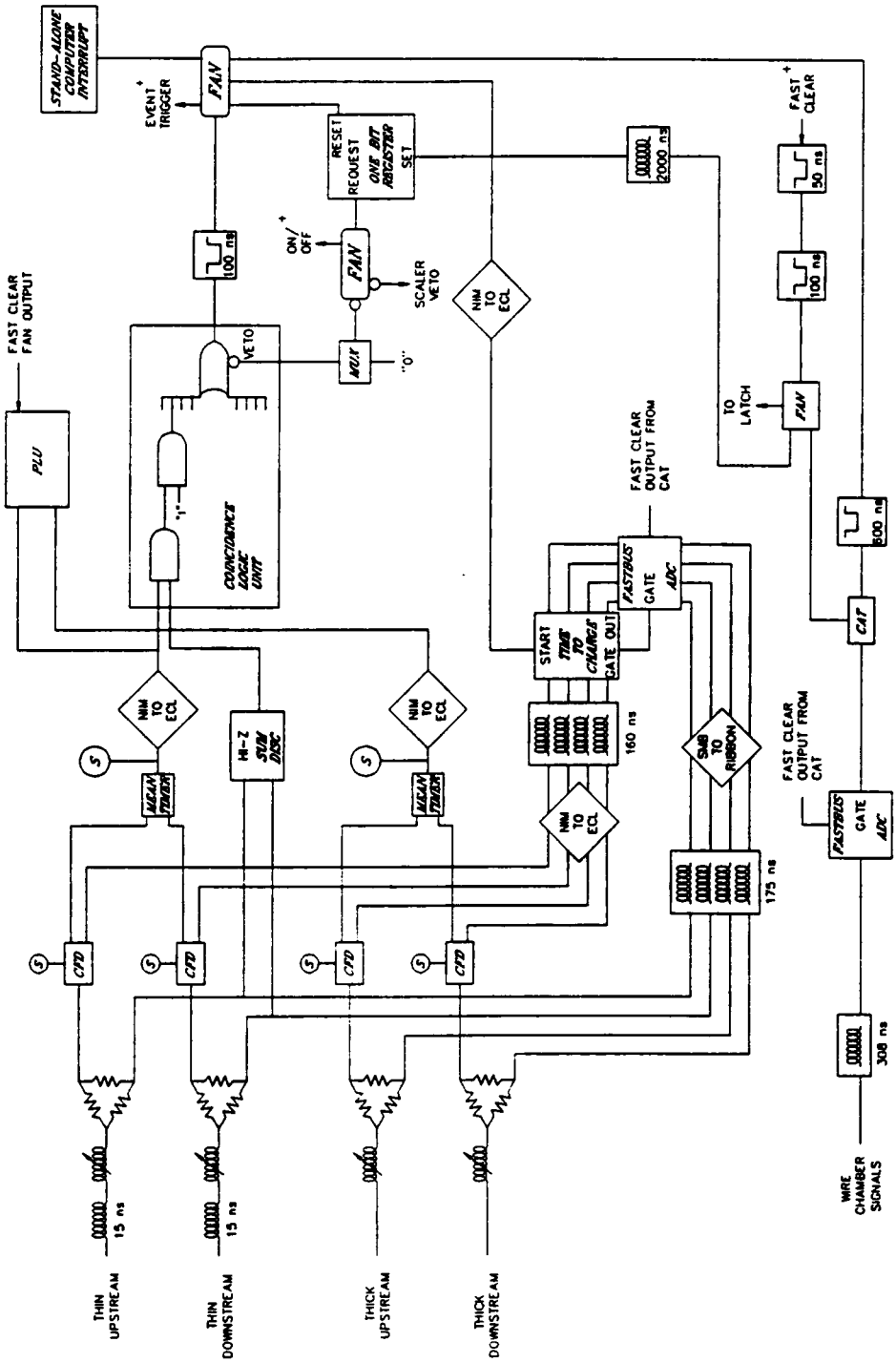

Figure 3.2: Schematic diagram of the LASA detector trigger electronics

thin paddles are involved in the trigger. The results from all eight thin paddles are then ORed together, and the result is called the event trigger.

The event trigger is fanned out to generate a gate for the ADC's and start the TDC's. It also resets a one-bit register known as the "G" bit, which contains the live/dead condition of the experiment. When the G-bit is off, the electronics are busy and no more triggers may be serviced; therefore the CLU is vetoed during this time. The fact that an event trigger has been received does not imply, in general, that the event will be read out. The "stand-alone" computer interrupt is used when no higher levels of trigger logic are enabled. When the monochromator is being used, a higher level circuit tests that the trigger came in coincidence with a hit in the focal plane. If this test fails, a fast clear signal is sent which resets the ADC's and turns the G-bit back on, enabling the CLU again. Otherwise the G-bit remains off and a computer interrupt is generated.

Since the monochromator is shared by several experimental projects, the tagger electronics are largely independent of the LASA detector. A diagram of the tagging system electronics is shown in Figs. 3.3 and 3.4. The event trigger signal enters the circuit from the detector room at the left of Fig. 3.3. It is fanned out to generate the "mono strobe" and the start signal for the tagger TDCs. The mono strobe is a logic signal which is ANDed with each of the tagging counter signals to gate out all focal plane hits which are outside of a preset coincidence timing window relative to the event trigger. This logic is shown in Fig. 3.4. The symbols $e_0 \ldots e_{31}$ label the analog signals from the tagging counters. After being shaped and amplified, these signals are converted to logic pulses in the TRG discriminators. These timing pulses are ANDed with the on/off gate and the mono strobe, then passed to the stop inputs of 32 individual TDCs. An OR of all 32 stop signals, called the "strobed OR", is formed and used to generate the computer interrupt.

In the case that none of the tagging counters was hit during the duration of the mono strobe, no strobed OR, and hence no computer interrupt, is generated. The

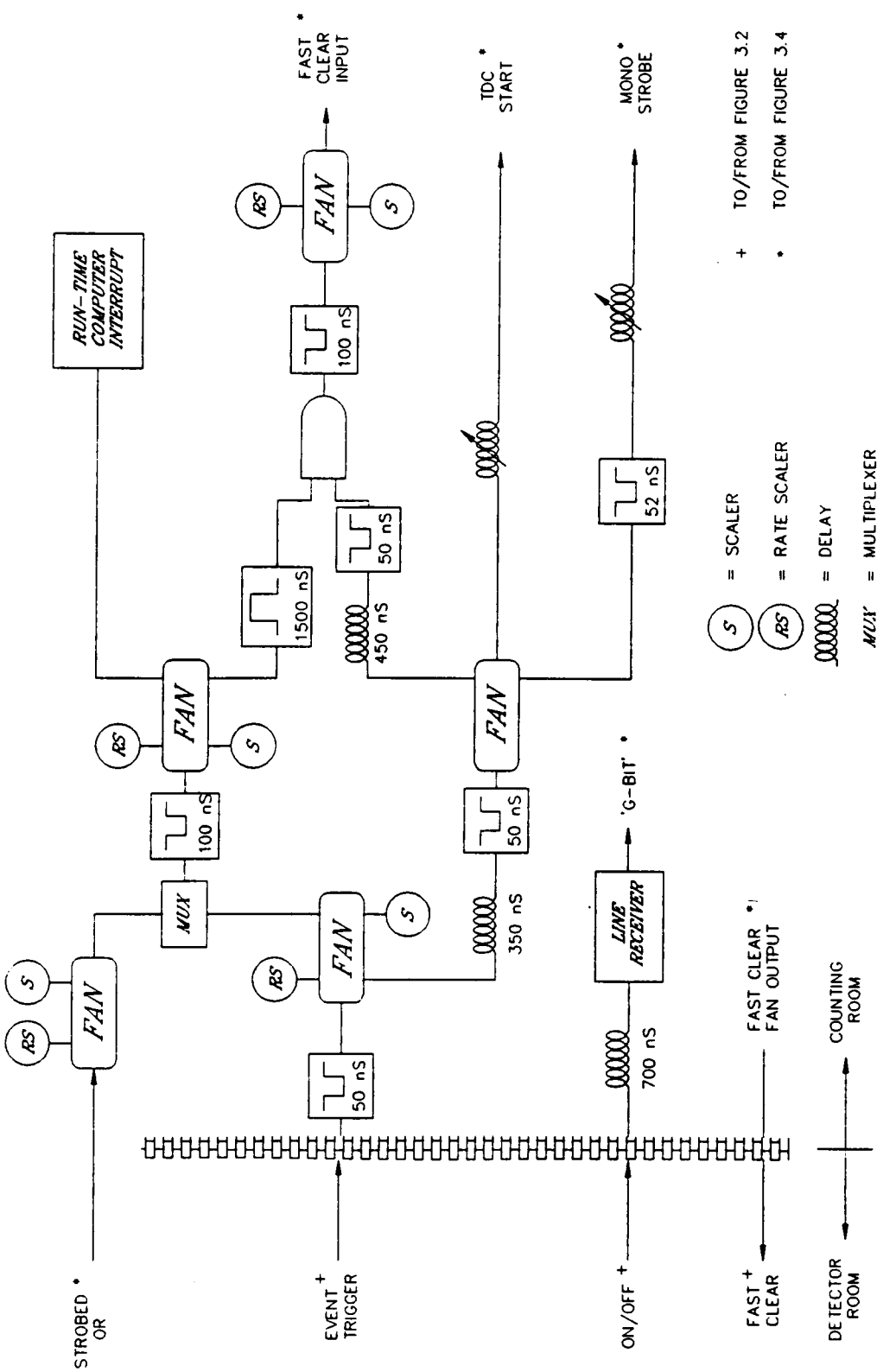

Figure 3.3: Schematic diagram of the monochromator coincidence electronics I

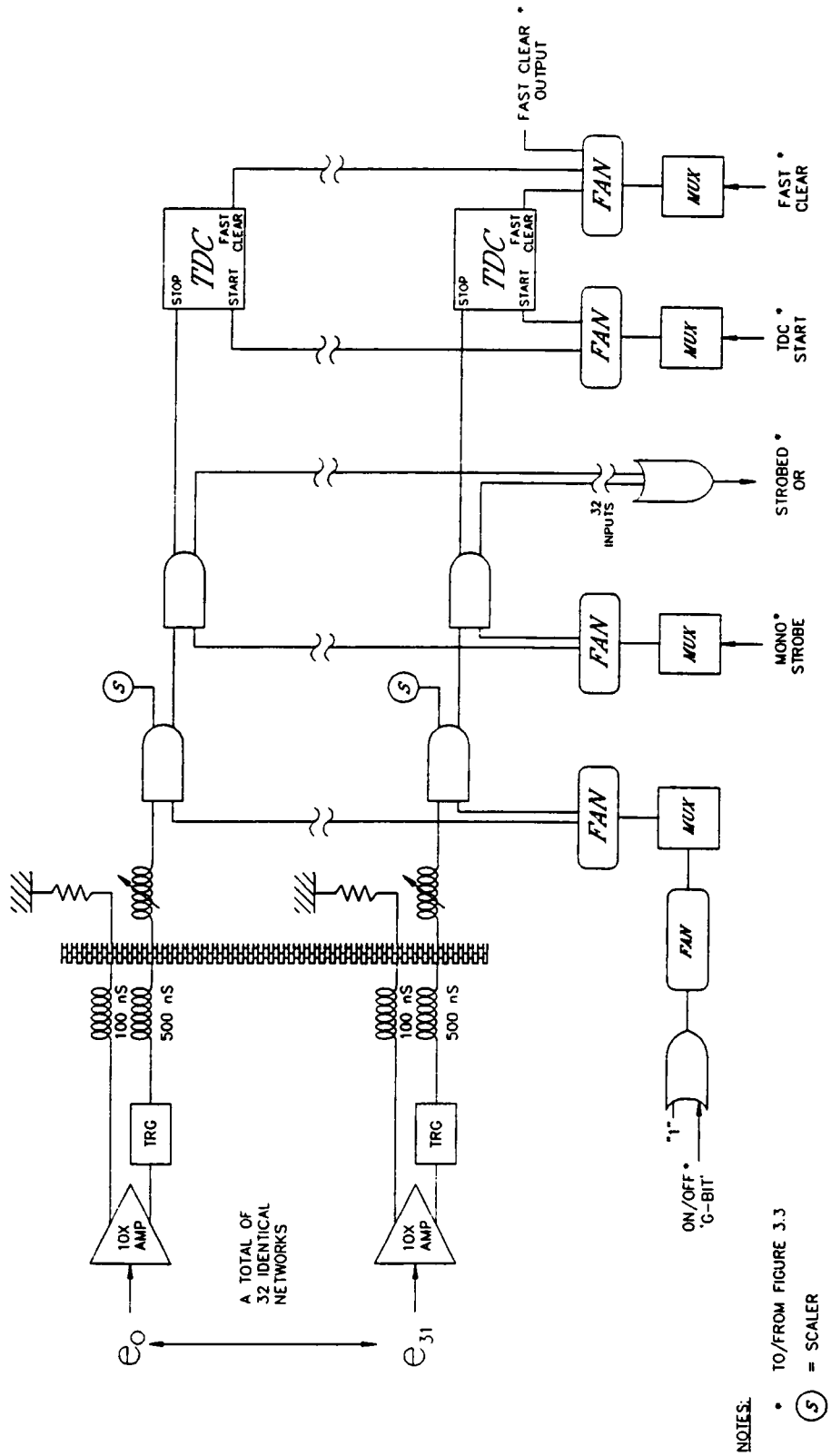

Figure 3.4: Schematic diagram of the monochromator coincidence electronics II

TDC's and other electronics then must be reset for the next trigger. This requires the generation of a fast-clear signal. The circuit for this is shown back in Fig. 3.3. A delayed event trigger pulse is ANDed with the inverse of the strobed OR signal and the result forms the fast-clear. The presence of a strobed OR signal inhibits the generation of a fast-clear; however if no strobed OR signal is present, the event trigger automatically generates the fast-clear, and the electronics are reset for the next event.

3.3 Online Computer Network

The fundamental job of the online experimental computer system is to read out the event data and record it on tape. In an experiment using a device as complex as the LASA detector, it is critical that the computer also provide automated experimental control, with instant and continuous feedback about detector performance. Singles rates in every part of the detector must be watched, high voltage and wire gains controlled, beam quality monitored etc. In order to be assured that the data being recorded on tape are meaningful, the experimenter needs to see some fraction of the incoming data carried through the entire analysis procedure. By examining the data at each stage as it proceeds through the analysis pipeline, the experimenter has a good chance of catching subtle faults. The appreciation of the need for extensive online software grew with experience throughout the development of the LASA detector.

The first attempt at data acquisition for the LASA detector involved the use of a Perkin Elmer, the online computer in use at NPL at the time. A rudimentary program was written and successfully used for the first test run with a prototype detector. Soon afterwards when it was decided to use FASTBUS, the Perkin Elmer was abandoned for a Q-bus based PDP-11, the LSI-11/73 from Digital Equipment Corporation (DEC). The LeCroy FASTBUS controller was provided with an adapter to interface to the Q-bus, and since Q-bus interfaces existed for both

CAMAC and Black Box, the LSI became the hub of data acquisition. Along with the LSI came the availability of a variety of online software packages, which had accumulated in the public domain during the previous decade. One such package of considerable capability is MULTI, developed at Fermilab during the 70s. RT-MULTI was taken and adapted for the LASA detector, and several test runs were taken successfully with this system. This experience, however, lead to the conclusion that a single job, single computer configuration was too limiting.

A diagram of the present online computer configuration is shown in Fig. 3.5. The horizontal bar across the middle of the diagram divides the components located in the monochromator hall with the LASA detector (bottom half) from those located in the counting room (top half). The data acquisition front end LSI-11, labelled FOUR-PI, is located next to the LASA detector, with parallel data connections to CAMAC, FASTBUS, and Black Box. The connection to the CAMAC crate containing the LASA trigger logic is via a memory-mapped Kinetic Systems 3912 controller. The FASTBUS crate is interfaced to the FOUR-PI computer through the LeCroy 1821 SMI (Segment Manager and computer Interface.) The SMI connects to the computer via a personality card called the 1821/DEC, which couples to the DR11-W parallel interface on the Q-bus.

The QMP (Q-bus multiport) interface provides access to the Multiport, the hub of a network of Black Box crates distributed between the experimental hall and the counting room. Using the Multiport, it is possible for more than one computer to access the same set of crates. For historical reasons, all access to the monochromator crates is via the Multiport. This includes the monochromator CAMAC crate which contains the tagger TDC's. A parallel CAMAC branch highway driver incorporated in a Black Box module provides access to this crate. The components of the trigger logic which reside in Black Box, both in the monochromator hall and the counting room, are also accessed through the Multiport.

As was discussed in Sec. 3.1, most of the event data comes in through FASTBUS.

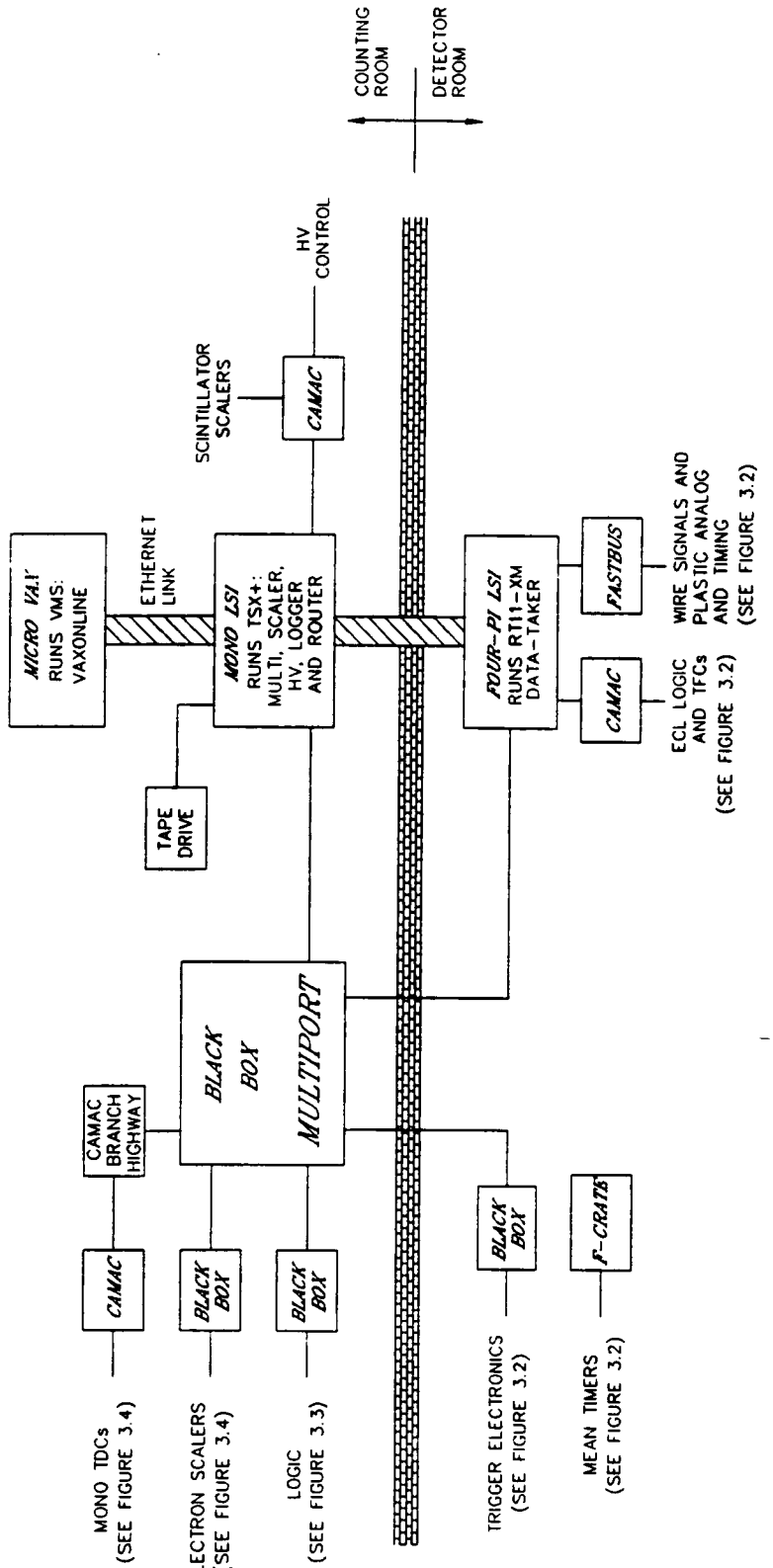

Figure 3.5: Diagram of the online computer configuration used with the LASA detector

The speed of FASTBUS data transfers coupled with the intelligence in the 1821 segment manager was the key to keeping the time required to service one event under 1.5 ms. The 1821 SMI is a dual-width FASTBUS module produced by LeCroy for use with their line of ADC's and TDC's. It contains a programmable sequencer featuring high speed FASTBUS readout with automatic pedestal subtraction and data compression.

The pedestal, the ADC value corresponding to zero pulse height, for each ADC channel is measured and downloaded by the host computer (FOUR-PI) into the 1821 pedestal memory. On subsequent readouts with automatic pedestal subtraction enabled, the ADC values piped from FASTBUS into the 1821 data buffer memory have this bias subtracted from them. With pedestals subtracted, the ADC values can all be compared with a common preset threshold to determine whether the corresponding detector element fired. With the SMI zero suppression feature enabled, only ADC values over some programmable threshold are stored in the data buffer. This data compression facility provides for the elimination in FASTBUS of the ADC values for all of the wires that were not hit in a particular event. By setting the software threshold just above the half-width of the pedestal peak, the number of wire ADC data words passed on from the 1821 to the FOUR-PI computer is reduced from 768 to an average of 25 per event. This does not eliminate the necessity of reading out all 768 wire end amplitudes in FASTBUS, but the speed of the 1821 is such that the readout of an entire ADC into the SMI data memory, requiring 96 32-bit transfers with pedestal subtraction and zero suppression, completes in 15 μs. By comparison, if all of the ADC data had to be transferred to the LSI for pedestal subtraction and zero suppression, it would take over 600 μs per ADC.

The FOUR-PI computer is devoted to the single task of servicing event interrupts. It reads out the trigger information and the ADC and TDC values from the data acquisition electronics and formats them into a variable length data structure

called the event record. Event records are packed together into a fixed length storage unit called a data buffer. Each time a data buffer is filled, it is passed by the FOUR-PI computer over an intercomputer data link to another LSI-11, labelled MONO in Fig. 3.5. The physical link, shown as a striped bar in Fig. 3.5, is an ethernet coaxial cable which interconnects all of the computers in the laboratory. The MONO computer is where the bulk of the data acquisition tasks are performed. There the data buffers received from the front end computer are logged to magnetic tape. Having its own connection to the Multiport, the MONO LSI has direct access to the experimental control hardware and scalers. The scalers are periodically read out by the MONO LSI, and formatted into scaler data buffers. These are interspersed with the event buffers on tape, providing a continuous record of normalization information. A multitude of data acquisition utilities are also run on the MONO machine, which regulate high voltages, adjust discriminator thresholds, monitor beam position, and a variety of other experimental control functions.

The MONO computer also performs a certain amount of diagnostic level analysis on the incoming data. The comprehensive analysis, however, is performed on the third computer in the online configuration, a VAXstation II. The fraction of data passed over ethernet to the μVAX is regulated in order not to bottleneck the primary data-acquisition, data-logging loop. Over the various stages of analysis on the μVAX, the analysis software maintains hundreds of updating histograms and scatter plots which provide the real test of the proper operation of the detector.

3.4 Online Software

The move away from a single computer configuration to a distributed environment was accompanied by a move to distributed software. An environment was created whereby many separate programs, each devoted to one particular aspect of data acquisition, can run concurrently and share data through a well defined interface. With the software thus segmented, the programs can be allocated at run

time between the available computers for the best performance. This also greatly simplifies the testing of new programs, and their integration into the whole, as the online software evolves. At the beginning, this necessitated a considerable amount of system programming to establish the interprogram interfaces. On the VAX this was already provided in the VAXONLINE package from the Fermilab Online Computing Department [77]. Using VAXONLINE as a model, a similar package was developed for the LSI-11's [78].

As shown in Fig. 3.5, the three online computers run three different operating systems. The FOUR-PI LSI runs RT-11, a single user operating system from DEC for the PDP-11. Designed for real time programming, RT-11 has virtually no operating system overhead associated with servicing interrupts, and provides the most unrestricted access to the machine at the hardware level. Hence it is well suited to the task of event service. In spite of the advantages of uniformity, it was not possible to run RT-11 on the MONO computer as well, because of the single-user limitations of RT-11. However with TSX-Plus, a multi-tasking extension to RT-11 from S&H Inc., it was possible to provide a similar programming environment between the two LSI-11's. In general, programs are interchangeable between the two operating systems. The VMS operating system is used on the VAXstation II.

The primary data acquisition program is DARTS. It runs on the FOUR-PI front end, servicing event interrupts and passing data buffers to the buffer stream as they are filled. The buffer stream is a pipeline of data buffers managed by the operating system, which flow from the source on FOUR-PI and end up on the μVAX. Programs can "attach" to the stream and intercept buffers to read and/or modify the data. The continuity of the stream between computers is provided by network master and server programs devoted to extracting buffers from the end of the stream on the server machine and placing them on the beginning of the stream on the master. On the LSI-11's, the network server is called DQUIET, and the

master program is ROUTER. On the μVAX, the VAXONLINE EB (event builder) program serves as network master.

As the data buffers proceed down the stream to the MONO computer, they are first intercepted by the LOGGER program, which records the data buffers on magnetic tape. There is one program on the MONO LSI upstream of LOGGER: the SCALER program, which periodically injects a buffer full of updated scaler information into the stream to be recorded on tape. After being logged to tape, the buffers proceed down the stream to a sequence of diagnostic programs devoted to checking the data for parts of the detector that have failed. Among these is the MULTI program, stripped of its data acquisition parts, and retrofitted for accepting buffers from the stream. With its flexible means for run-time definitions of histograms and simple calculations on the event data, MULTI is a useful diagnostic tool.

The buffer stream arrangements for these analysis programs are such that they cannot bottleneck the primary acquisition, logging loop. When LOGGER attaches to the data stream, it forces the condition that all data buffers coming down the stream must wait in its queue. If tape logging falls behind the data buffer rate, DARTS will be automatically suspended to let LOGGER catch up. Downstream of LOGGER, however, the buffer queues are regulated so that there is always a minimum number of free buffers. Thus the normal online situation is that only a fraction of the incoming data are seen by the analysis programs. This applies to VAXONLINE programs as well as to those on the MONO computer.

Several other programs run on the MONO computer, which are not attached to the buffer stream. One of these is the VIZRUN program, which is used to locate and align the incident electron beam. Since the electron beam currents used with the monochromator are too small to be sensed by conventional rf beam monitors, the electron beam position is determined by two pairs of revolving scintillating fibers, located at two positions along the straight section of the incoming beam line. As

each fiber rotates through the electron beam, it generates a pulse of light, which is picked up on a phototube. The VIZRUN program steps the fiber through an arc and reads out the light intensity profile, generating an updating two-dimensional picture on a CRT display of the beam spot at each location. This picture is used by the accelerator operator to align the beam on the bremsstrahlung converter.

A variety of utility programs are also used on the MONO LSI to diagnose and initialize the data acquisition hardware. The HV program controls and monitors all of the high voltages in the experiment. It generates an alarm whenever any of the high voltage supplies trips. The THRESH program is used to monitor and adjust the programmable thresholds on the CFD plastic scintillator discriminators. The MASTER program initializes FASTBUS and downloads program and pedestals to the 1821 SMI in preparation for data acquisition.

With the exception of the DARTS program, all of the online software is written in Fortran-77. The buffer management system is provided with a subroutine library to provide easy access to the data buffer stream from Fortran. Because of this, it was possible to import a great deal of useful software from other laboratories. The HV and SCALER programs both came from high energy experiments at CERN, and MULTI came from Fermilab. The greatest discovery, however, was VAXONLINE, a comprehensive online software framework still under development by the Fermilab online software group for high energy physics experiments. VAXONLINE provides a coherent way for multiple programs to access a common pool of event data, serialize sequential processing, and create and store histograms.

Provided with VAXONLINE are a set of utility programs which provide common services. The EB (event builder) program accepts data buffers from a variety of sources (ethernet, disk, tape ...) and outputs them to the VAXONLINE event pool as individual event records. The OUTPUT program logs selected events from the VAXONLINE pool to ethernet, tape, or disk. The DISPLAY program provides an interactive version of the CERN HBOOK histogram display/fitting package.

DISPLAY can access the histograms in the memory arrays of any other VAXONLINE program and display them as they are being filled. A uniform menu-driven user interface is provided for all VAXONLINE programs. While other languages are permitted, Fortran-77 is the standard for VAXONLINE programs. Fortran subroutine libraries are supplied for event record I/O (DAQ), delivery of warning messages to a common point (Courier), and maintenance of a common database about the status of all running programs (Status Manager).

These tools being present, the code which performs the actual data analysis must be written by the experimenter. These programs are shown in Table 3.1, along with the author and a summary of their function. The BREMS program is in a class by itself in that it does not analyse LASA event data, but rather data generated in the bremsstrahlung tagging efficiency calibration runs. These "brems runs" are described in Chap. 4. The TRANSLATOR program and the LASAxxx programs form the analysis pipeline for LASA events. The CALIBRATOR program is used to generate the calibration coefficients needed by TRANSLATOR to convert event data into physically meaningful quantities. These programs perform a predetermined sequence of operations on the event data. The SORTER program provides a more general way of looking at the data, permitting a set of histogram and analysis options to be selected at run time. CONSUMER, the example analysis program distributed with VAXONLINE, is also included in Table 3.1 because of its usefulness in capturing and displaying special events. These programs have accumulated since early test runs with the LASA detector, and continue to evolve. At the present they represent over 25,000 lines of Fortran code, not including the software distributed with VAXONLINE. All of these programs are used for both online and offline analysis.

As raw event records are read in by EB, either from tape or the online data acquisition system, they are picked up by TRANSLATOR. Here each TDC value is converted to ns and placed on a common time scale, each ADC value is converted

Table 3.1: LASA analysis programs under VAXONLINE

Program	Author	Function
BREMS	T. Sozen	Analyzes bremsstrahlung runs
TRANSLATOR	R. Jones	Converts LASA events to real format
CALIBRATOR	R. Jones	Calculates TRANSLATOR coefficients
LASAFIT	J. Knott	Fits particle tracks in LASA events
LASAHIST	J. Knott	Histograms results from LASAFIT
LASAPICT	J. Knott	Generates pictures of LASA events
LASANALYSE	R. Jones	Finds cross section from histograms
SORTER	R. Jones	Makes run-time histograms and cuts
CONSUMER		Displays events in general format

to eV of energy loss, and hit locations are transformed into detector coordinates in cm. The formulae for these conversions, detailed in Chap. 4, involve a large set of transformation coefficients. These constants depend on the detector response, and must be evaluated by examining the data itself. In an automatic feedback loop, TRANSLATOR keeps track of the spectra for each of the quantities it generates. CALIBRATOR uses these spectra to make adjustments to the coefficients used by TRANSLATOR. The event records that proceed from TRANSLATOR down the analysis pipeline contain only the translated data.

The events from TRANSLATOR are received by LASAFIT, whose job it is to search the event hit pattern for particle tracks and evaluate the track properties. This information is appended to the event record before it is passed on. LASAHIST, the next program in the chain, reads these events and accumulates the data in histograms. With all histograms and scatter plots enabled, there are over 500 spectra being recorded by LASAHIST. The data cuts are performed in LASAFIT, where programmable thresholds on χ^2 of track fit, dE/dx and total E are enforced. LASAHIST can tell VAXONLINE to only pass on from LASAFIT a certain class of events, such as those that satisfy two-body kinematics. This way LASAHIST can select events from the different photodisintegration channels. The spectra from LASAHIST contain all of the information necessary to extract a cross section. This is done in the LASANALYSE program. The contribution of random coincidences is subtracted from the angular distribution, the correction for detector acceptance applied, the normalization with the total photon beam flux performed, and a differential cross section is generated along with the associated statistical errors.

Of special use online is the LASAPICT program, which generates graphic pictures of events in the LASA detector. One such picture of an actual photodisintegration event is shown in Fig. 3.6. In the end view of the detector, each wire hit is marked by an asterisk. The amplitude of the hit is encoded in the color of the

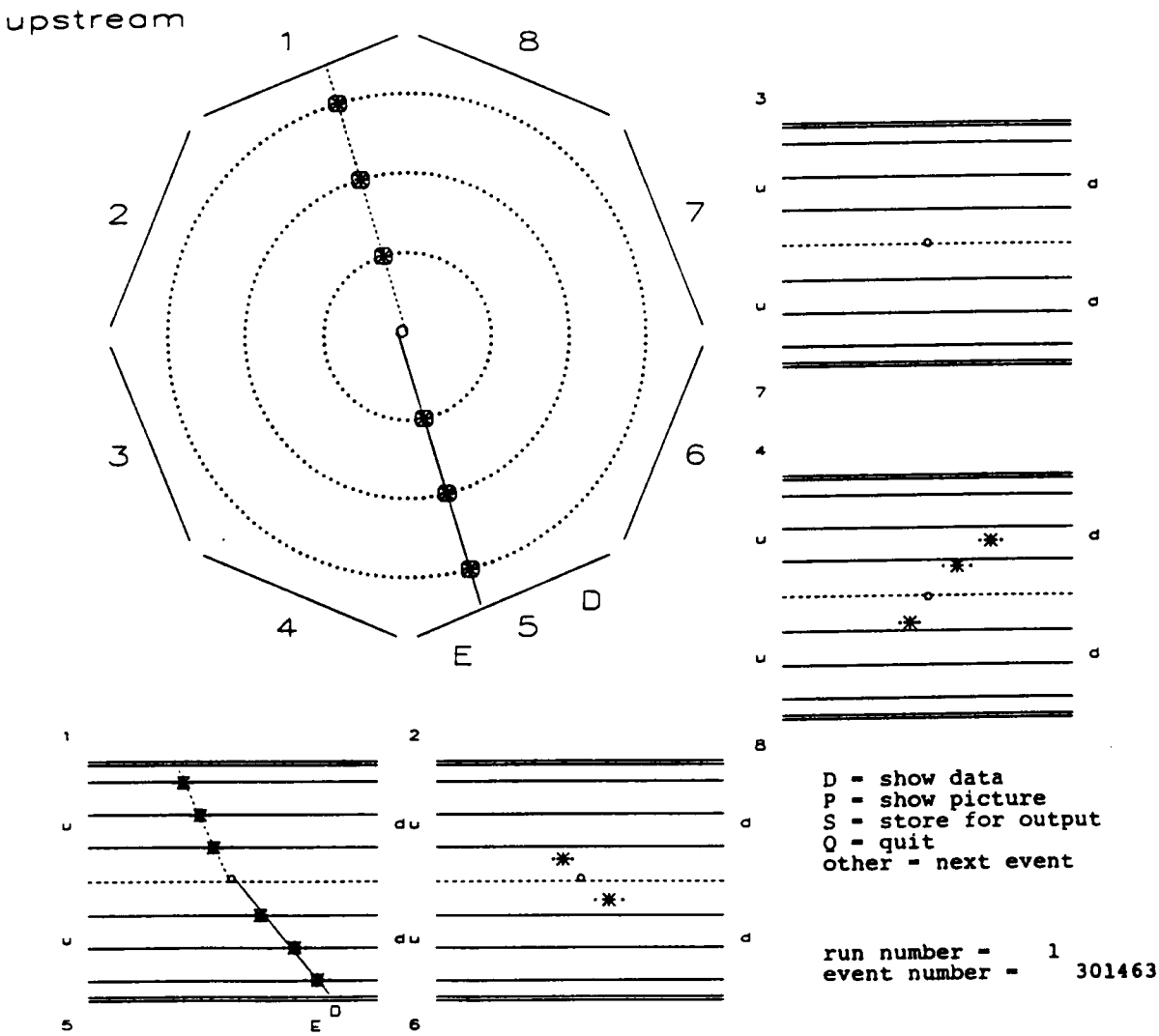

Figure 3.6: Example event picture by LASAPICT

asterisk. Those plastic sandwiches that received a hit are marked with the symbols D or E or both, indicating hits in the thin and thick paddles, respectively. Those hits which were determined to form a track are circled, and a line representing the best linear fit is drawn through the points. If the track connects to a hit in the plastic scintillator, the track is called a primary, otherwise it is a secondary track. Primary tracks are marked with a solid line, secondaries with a dashed line. The estimate for the vertex of the event is marked on the picture with a small hexagon.

To show the z projection of the hits, the detector is divided into eight azimuthal slices, one for each plastic sandwich. The eight side views around the bottom and right of the figure are projections onto the plane containing the detector axis and the midline of the corresponding plastic scintillator. The numbers around the perimeter of the end view label which side view corresponds to which segment of the annulus. Opposite plastic sandwiches are oriented in the side views opposing each other for better viewing of coplanar tracks. Any wire hit which, when viewed from the end of the chamber, could possibly form part of a track to a particular scintillator, is shown on the side view for that sandwich, with the result that a single wire hit may be included in two adjacent side views. The location of the symbols D and E along the length of the scintillator in the side views mark the z position of the scintillator hit. For events with fitted tracks, the track hits are circled, the track lines drawn, and the vertex marked on the side views as well as on the end view.

Chapter 4

Detector Calibration

Implicit in the detector design are the formulae which relate measured values to the underlying physical quantities, such as hit position, energy loss, and time of flight. In the process of calibration, these relations are tested, and amended if necessary, and the free parameters of the equations are evaluated. A separate set of these parameters is established for each individual detector element to correct for differences between similar channels. In the LASA detector, with its many duplicate elements, the overall detector resolution is limited, not only by the intrinsic precision of each element, but also by the quality of the calibration which places quantities from all similar elements on a common scale. The subsequent task of converting from arbitrary to physical units completes the calibration.

Calibration of the LASA detector occupied close to a year between detector construction and the first production experiment. It involved the use of electronic pulsers, radioactive sources and cosmic rays, gamma beam tests, and a trip to another laboratory for calibration with a proton beam. Some of the calibration coefficients depend upon static properties of the detector, and were measured just once and recorded. Others depend upon variables such as high voltage and gas purity, and required continuous adjustment throughout the experiment. In either case, the mechanism for calibration was established beforehand, and a reasonable operating range determined. With the electromagnetic background dominating the photodisintegration signal in the photon beam, a reasonable starting calibration

was necessary in order to set initial thresholds. This being done, the calibration was adjusted throughout the experiment, using the incoming data as a reference. Final refinements to the calibration were applied during off-line analysis.

4.1 Monochromator

4.1.1 tagging efficiency

The monochromator focal plane counters are small square rods of plastic scintillator. Since the post-bremsstrahlung electrons have varying path lengths inside the plastic, the analog signals from the focal plane have a broad range of amplitudes. The amplitude spectrum shows a broad bump, corresponding to electron pulses, situated on top of the tail of phototube noise which extends up from zero amplitude. The focal plane discriminator thresholds are set in the valley below the broad electron bump, as a compromise between electron efficiency and background rate. The fact that the analog gains and thresholds vary somewhat between counters does not require a correction. The calibration of the tagger depends only on the assumption that gains and thresholds are stable and independent of beam current within the operating range of the experiment.

Throughout the live time of a tagging experiment, scalers on each of the focal plane discriminators count the total number of times each fires. In the ideal limit of open geometry with no background in the focal plane, these are the counts of tagged photons incident on the target. However with photon beam collimation and the presence of focal plane background, these counts are somewhat inflated estimates of the flux of tagged photons. The conversion from electron scaler count to the true count of tagged photons on target is accomplished by a factor called tagging efficiency.

$$N_i^{(\gamma)} = \epsilon_i N_i^{(e^-)} \tag{4.1}$$

The tagging efficiency is measured independently for each of the focal plane counters. The calibration of the monochromator relies on the assumption that

tagging efficiency is independent of beam current. The maximum operating current which can be used with the tagger is the rate at which this assumption breaks down, on the order of $10^7\,s^{-1}$ per focal plane counter. The calibration is accomplished by reducing the beam current to about $20\,s^{-1}$ per focal plane counter, and positioning a large NaI crystal directly in the beam. Even at this low beam current, since the full bremsstrahlung photon spectrum strikes the crystal, the rate in the NaI is about $15 \times 10^3\,s^{-1}$, a moderate operating rate for a NaI crystal. The crystal is a cylinder with a diameter of 25.4 cm and length of 30.5 cm. It is positioned just behind the LASA detector at a distance of 6 m from the bremsstrahlung converter. At this distance, the rms diameter of the photon beam is 7 cm, indicating that the entire photon beam strikes well within the edges of the crystal. The attenuation length of a 70 MeV photon in NaI [79] is $0.059\,g/cm^2$, yielding a photon detection efficiency of 99.9%. The total attenuation of the photon beam from the center of the target to the front of the crystal is 0.3%, so that the beam sampled by the NaI is essentially that incident on the target.

The tagging efficiencies are measured periodically throughout the experiment by a series of these low current runs, called brems runs. In a brems run, the event trigger is derived from the NaI crystal, rather than from the LASA detector; essentially every tagged photon in the beam (during experimental live time) generates an event and is recorded on tape. The focal plane rate in a brems run being low relative to the bandwidth of the coincidence electronics, the chance of a random coincidence between the crystal and the focal plane is negligible. Therefore the number of tagged photons associated with a focal plane counter is given by the number of coincidence events in which the corresponding focal plane TDC received a hit. This count divided by the focal plane scaler count gives the tagging efficiency.

This simple procedure is complicated by the fact that the focal plane counters overlap their neighbors by about 10%. Thus in about 1/5 of the events in a brems run, two adjacent focal plane counters both record a hit. In this case, the event

is assigned to the counter in the focal plane position closest to the bremsstrahlung converter, because geometry dictates that the electron passed through that one first.

Brems runs are repeated throughout the experiment in order to confirm that tagging efficiencies are stable. In Fig. 4.1 is shown the record of tagging efficiencies for focal plane counter 16 throughout the ^{4}He experiment. The error bars shown represent the statistical error for each run. A series of eight runs were performed. As can be seen from Fig. 4.1, all of the runs are in agreement except numbers 2 and 3.

The first brems run was performed during detector setup, after which the accelerator broke down. When the beam returned several days later and a second brems run was taken, all of the tagging efficiencies had dropped by several percent. Investigation revealed that high electron beam current during the beam tuning procedure had activated material near the focal plane sufficiently to create a background of 1-2 s^{-1} per focal plane counter. Since the background was not in coincidence with the photon beam, it contributed to the focal plane scalers but not to the coincidence count, with the result that the measured efficiencies were too low. While this background was sufficient to distort the brems run results, it had negligible effect on an ordinary scattering run where the focal plane rate was 100 s^{-1} per counter. The experiment was permitted to proceed, in the hope that the background would decay with time. As can be seen from Fig. 4.1, this was the case. The accepted value for the efficiency, represented by the horizontal line on the figure, is the best fit to the data, excluding points 1-4.

4.1.2 timing calibration

The focal plane TDC's record the time between the event trigger and a hit in the corresponding tagging counter. The time slope of each has been measured off-line and recorded. The time delay on each focal plane signal is adjusted, using

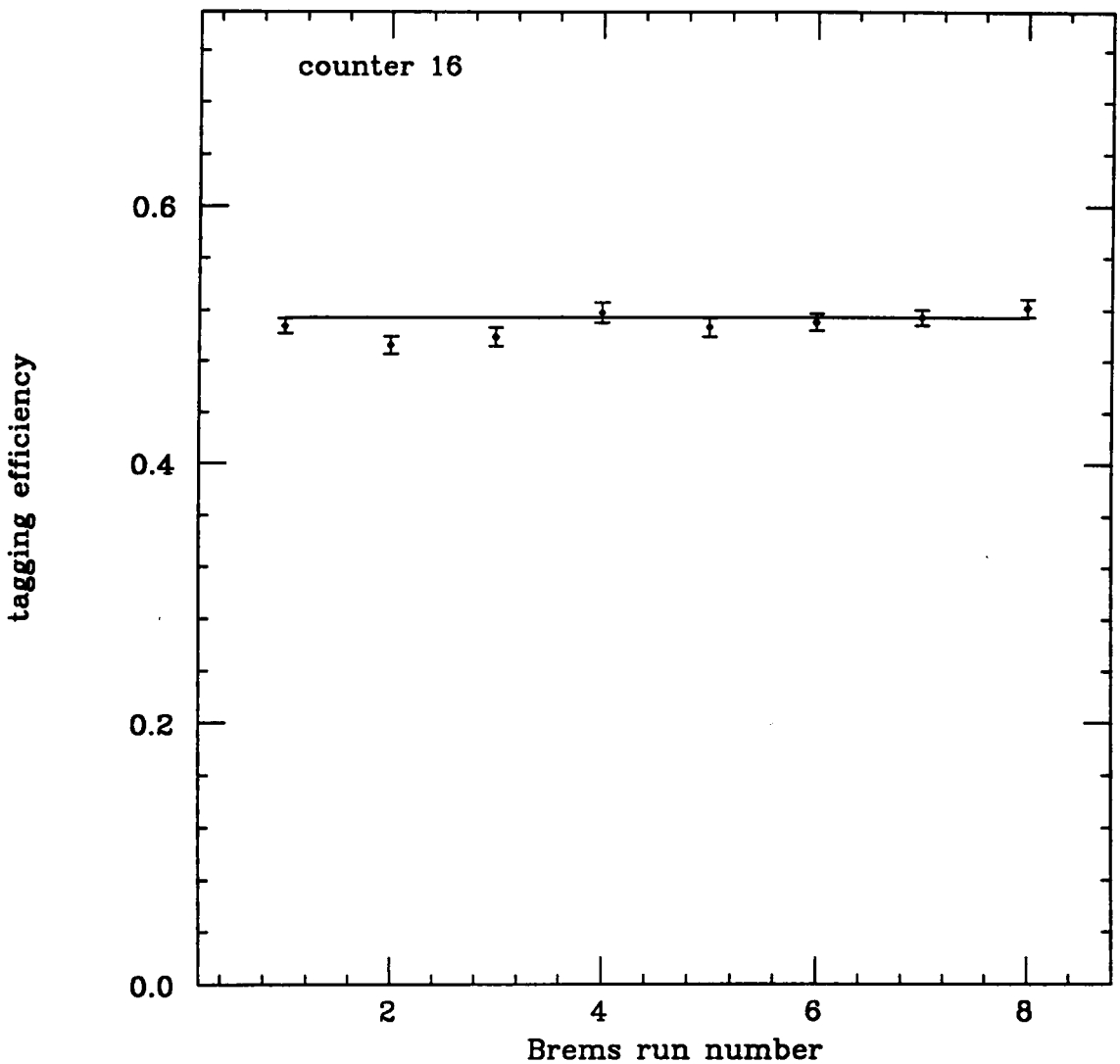

Figure 4.1: Measured values of tagging efficiency for focal plane counter 16 over a series of eight brems runs.

switchable delays, to align all of the tagging coincidences relative to the trigger, to within ±1 ns. The fine adjustment of the timing offsets is done in software. The equation which translates from TDC value to time is shown below. Raw numbers are represented in lower case, translated quantities in upper case, and calibration coefficients with Greek letters.

$$T_i = \alpha_i t_i + \beta_i + \delta_t \tag{4.2}$$

The subscript i labels the focal plane counter. The second offset factor δ_t corrects for skew in start times corresponding to different trigger sources. Each plastic sandwich in the LASA detector is a separate trigger source, with a slightly different trigger time delay. During calibration, a coincidence time spectrum is collected for each focal plane counter against a single trigger source, and for each trigger source against a single focal plane counter. The offsets are calculated so that the coincidence peaks in all of the timing spectra are aligned. There is an overall time offset which is undetermined by this procedure; this is chosen arbitrarily to align the peaks at 60 ns.

4.2 Wire Chamber

4.2.1 position calibration

Since the electric field within the volume of a wire cell is everywhere perpendicular to the wires, ionization electrons generated by a passing charged particle drift to the sense wire along paths of constant z. This means that the distribution in z of the charge deposited on the sense wire is confined to a small segment of length $\frac{1\text{ cm}}{\sin\theta}$, where θ is the polar angle of the particle track. In proportional mode, the spreading of the pulse at the amplification stage is small. In the following analysis, the current pulse is treated as a point source located at z. A more general treatment of an extended current source leads to the same formulae, with z representing the center-of-gravity of the current distribution.

The charge deposited on a sense wire flows in both directions down the wire to the amplifiers on each end, which provide a path to ground. The amount of the total charge that goes either way is determined by the total resistance to ground along each path. The equivalent circuit is shown in Fig. 4.2. Let the total charge collected on the upstream (downstream) end be denoted by Q_u (Q_d), and the charge of the pulse output by the amplifier, by q_u (q_d). Then,

$$q_u = g_u Q_u = g_u Q \left(\frac{\ell - z + r_d}{2\ell + r_u + r_d} \right) \tag{4.3}$$

$$q_d = g_d Q_d = g_d Q \left(\frac{\ell + z + r_u}{2\ell + r_u + r_d} \right) \tag{4.4}$$

where g_u and g_d represent the respective gains of the upstream and downstream amplifiers. The symbols r_u and r_d are the equivalent resistance, in cm of sense wire, of the amplifiers on the upstream and downstream ends, respectively, and ℓ is the half-length of the sense wire. Allowing for different amplifier gains on each end, there are four calibration coefficients (g_u, r_u, g_d, r_d) to be determined for each wire. An estimate for z can be derived from the quantity ξ defined as

$$\xi = \frac{q_d - q_u}{q_d + q_u} \quad . \tag{4.5}$$

In the case where $g_u = g_d$,

$$z = \frac{\mathcal{R}}{2}\xi + \frac{r_d - r_u}{2} \quad , \qquad \mathcal{R} = 2\ell + r_u + r_d \quad . \tag{4.6}$$

In the case where the two gains are not exactly matched, z may be expanded in a Taylor series in $\gamma = g_d/g_u$ about the point $\gamma = 1$ as

$$z = \left(\frac{\mathcal{R}}{2}\xi + \frac{r_d - r_u}{2} \right) + \left(\frac{\mathcal{R}}{4}(\xi^2 - 1) \right)(\gamma - 1) + \ldots \quad . \tag{4.7}$$

The gain factors of all of the amplifier cards were measured when they were first tested. According to these records, the gain varied between channels by about $\pm 5\%$, which justifies truncating the series at first order in $(\gamma - 1)$. Treating γ as a fixed parameter, Eq. 4.7 gives z as a quadratic function of ξ.

$$z = \left(\frac{\mathcal{R}(\gamma - 1)}{4} \right) \xi^2 + \left(\frac{\mathcal{R}}{2} \right) \xi + \left(\frac{2(r_d - r_u) - \mathcal{R}(\gamma - 1)}{4} \right) \tag{4.8}$$

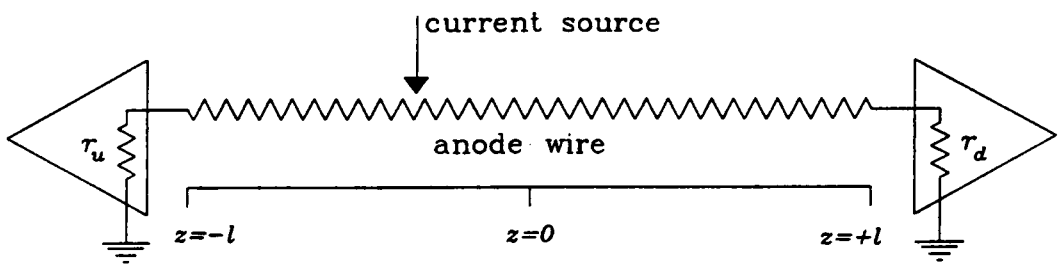

Figure 4.2: Equivalent circuit for resistive anode wire connected to amplifiers on either end. The current source is represented by the potentiometer tap which can move from $z = -\ell$ to $z = +\ell$.

To test this formula, an ^{55}Fe X-ray source was mounted on the axis of the chamber. The collimation confined the X-rays to a plane perpendicular to the chamber axis, so that even at wire level C, the distribution in z of X-rays was 3 mm wide. The test was done using a chamber gas mixture of 85% helium, 8% methane, 7% argon. The small admixture of argon was necessary to achieve good X-ray conversion efficiency, and to limit the range of the photoelectrons to 5 mm. Data were collected for each wire with the source set at $z = -40$, $z = 0$, and $z = +40$ cm. The ξ histograms were generated from these data, and the centroids and widths of the peaks were recorded. The three data points were sufficient to determine the three coefficients of the quadratic function $z(\xi)$. It was found that a least-squares linear fit to these points gave a reasonable χ^2, so the quadratic term was not required.

$$z = \alpha\xi + \beta \tag{4.9}$$

Values for α and β were extracted from the data for each wire by a least-squares fit.

The z resolution of the wires depends upon the size of the pulse, with larger pulses having better z precision. This is because the resolution is determined by the noise from the wire amplifiers, which enters as a fixed variance on the ADC values q_u, q_d, independent of their magnitude, whereas the uncertainty in z derives from the percent uncertainty in q_u, q_d. The best position resolution is therefore achieved with the highest possible chamber gain, within the limits of the ADC range and proper chamber operation. An optimum value for the chamber gain was determined by the process of trial and error, during a preliminary run in the photon beam. Analysis of these data showed that the proton pulse height distribution in the wires peaked at around 500 ADC channels. During the calibration with the ^{55}Fe source, the chamber high-voltage was adjusted to give the same average pulse height, so that the z resolution for these signals could be determined. The average value for all of the wires was $\sigma_z = 1.4$ cm.

4.2.2 energy calibration

In proportional mode, the ionization energy deposited in the volume of a wire cell is proportional to the total charge deposited on the wire.

$$\Delta E = \kappa(Q_u + Q_d) \simeq \frac{\kappa}{g}(q_u + q_d) \tag{4.10}$$

where κ is the proportionality constant, related to chamber geometry, gas composition and high voltage. Since the pulse height resolution of a proportional counter is no better than 20%, the amplifier gains may all be considered to be the same, represented by the factor g. The factor $\frac{\kappa}{g}$ is the net wire gain, which converts from ADC channels to keV of particle energy loss.

The wire chamber gain is the least-well understood characteristic of the LASA detector. Several studies were done, using a prototype chamber, with different gas mixtures to determine the dependence of gain upon high voltage. The results for the 90% helium, 10% methane gas mixture, using a beta source, are shown in Fig. 4.3. Repetition of this measurement, with the same apparatus and the same gas supply, reproduced the gain curve with the voltage scale shifted by as much as 20 V. Observation at a fixed value of high voltage revealed large drifts in the gain over a period of several days. As expected, any appreciable leakage of air into the chamber quenched the gain, but care was taken to insure that the gain shifts were not simply the result of faulty seals. Anomalous gain behavior in chambers operating with helium chamber gas has been observed elsewhere [80].

At any given value of high voltage, the gains on the three wire levels are different. This is expected, due to the proximity of layer A to the conducting surface of the target window, and of layer C to the conducting surface of the outer chamber window, both of which are at ground potential. The gains of all of the wires on a particular level are expected to be the same, due to the azimuthal symmetry of the chamber. There is one exception: those eight wire cells on level C which are adjacent to the chamber support rods are depressed in gain by roughly a factor of two.

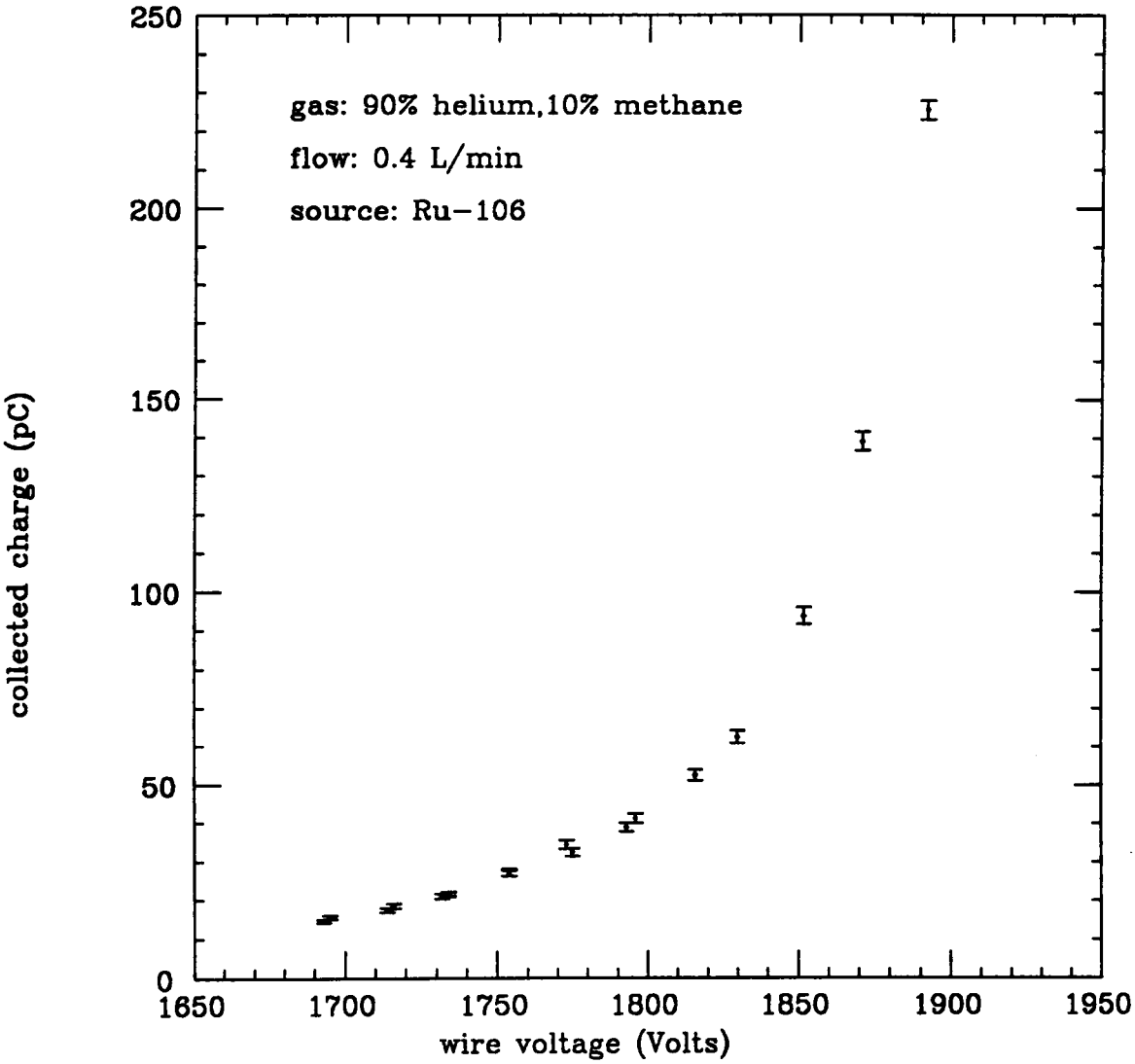

Figure 4.3: Gain of the wire chamber as a function of high voltage, with a chamber gas mixture of 90% helium, 10% methane. The measurement was performed with a test chamber and a Ru-106 beta source. The Y axis shows integrated charge after amplification (×200).

Since particles which go through those cells are stopped in the rod without making it to a scintillator, a special correction was not applied to them. In the analysis of the data from the experiment reported in this thesis, a significant systematic dependence of wire gain upon azimuthal angle was discovered. The description of this unexplained effect is given in Chap. 6.

Because the wire chamber gain was not reproducible, the energy calibration had to be done during analysis. During initial setup of the LASA detector, the pulse height spectrum from each of the three wire levels was generated, and the high voltages adjusted to match the gains. Throughout the run periodic adjustments were made to the high voltage to keep the gains near the initial setting. The gradual gain shifts which occurred took place on all three levels, so that they always stayed in the same relation to each other. This suggests that the cause of the shifts is related to subtle changes in the composition of the chamber gas. This rough gain adjustment was fine-tuned during off-line analysis.

The absolute energy scale is set by examining a histogram of the quantity $\Delta E \sin\theta$, where θ is the polar angle of the particle track associated with the hit. This quantity, also called dE/dx, is the energy lost by a particle in traversing 1 cm of gas. This spectrum contains a peak at low pulse height associated with minimum-ionizing particles (electrons and cosmic rays) and a peak at higher pulse height, associated with protons. Selecting only tracks whose θ falls within a narrow window, the dE/dx spectrum corresponds to a sample of monoenergetic protons. The energy scale is adjusted until the mean of the proton peak matches the value from the dE/dx tables for protons at the given energy.

4.3 Plastic Annulus

4.3.1 timing calibration

The LASA detector plastic annulus is composed of eight $\Delta E, E$ plastic scintillator sandwiches, each just over 1 m in length. The passage of an ionizing particle

creates a localized flash of scintillation light, which propagates both ways down the paddle to the phototube on each end. The timing of the pulses from either end are dependent both upon the time of the hit and the location of the hit along the paddle. The difference of the two, however, is only dependent on the hit position, and the sum is only dependent upon the time:

$$T_i = \frac{1}{2}(\tau_{ui} + \tau_{di}) + \delta_t \tag{4.11}$$

where δ_t is the trigger timing correction from Eq. 4.2, and the τ_{ui}, τ_{di} are the corrected times of the pulses on the upstream and downstream ends, respectively, of scintillator paddle i.

$$\begin{aligned} \tau_{ui} &= \alpha_{ui} t_{ui} + \beta_{ui} \\ \tau_{di} &= \alpha_{di} t_{di} + \beta_{di} \end{aligned} \tag{4.12}$$

The coefficient $\alpha_{\lambda i}$ is the effective time gain of the corresponding TDC channel. These are measured once and recorded. The $\beta_{\lambda i}$ coefficients correct for the different delays on each paddle end. With a pulse time resolution better than 500 ps FWHM, these offsets are sensitive to the details of the cabling, and must be adjusted each time the detector is set up. The definition of a properly adjusted set of offsets is that a hit which occurred simultaneously at the center of all 16 paddles would yield 16 equal values of $\tau_{\lambda i}$.

The rough timing alignment is done with an LED pulser. Each end of each paddle is equipped with a fast LED attached to the light guide near the phototube. All 32 paddle ends are pulsed simultaneously, and the timing is adjusted on each channel, by use of switchable delays, to be aligned to within ± 1 ns. The $\beta_{\lambda i}$ offsets are then determined in order to complete the alignment. The timing calibration procedure makes use of the dominant electron background in the photon beam. These electrons are created by photon conversion in the air upstream of the detector, and follow paths of low polar angle into the plastic scintillators. A histogram of $\tau_u - \tau_d$ for each paddle reveals a distribution, which corresponds to

the distribution of hits along the length of the paddle. These distributions have sharp edges, corresponding to the ends of the scintillator. The values of β_{ui} relative to β_{di} for each paddle are adjusted so that the center of the distribution falls at zero.

The timing of the paddles relative to each other is established by noting that the distribution of electron tracks about the photon beam is azimuthally symmetric. This means that a histogram of time-of-flight, given by $T_i - T_{mono}$ should be the same for each paddle i. The values of β_{ui}, β_{di} are increased or decreased for each paddle, keeping their relative value fixed, until all of the time-of-flight spectra are aligned. This procedure leaves one overall time offset undetermined; this is chosen arbitrarily so that the peaks in the T_i spectra are centered at 15 ns.

4.3.2 position calibration

The location of a hit in a scintillator paddle is specified by the coordinates (v, z), where v is the transverse coordinate and z is the longitudinal coordinate. The timing of the pulses at the ends of the scintillator is independent of the v coordinate, but reflects the z of the hit through the timing difference between the two ends.

$$z_i = \frac{1}{2}(\tau_{ui} - \tau_{di})S \quad , \tag{4.13}$$

where S is the propagation speed of the light pulse inside the plastic, and the $\tau_{\lambda i}$ were defined in the previous section. Assuming that the timing calibration is complete, the only remaining parameter is S, which is adjusted until the width of the z distribution is equal to the length of the paddles, 101.6 cm. The theoretical value for S is given by c/n where n is the index of refraction for plastic scintillator, yielding $S = 19.0$ cm/ns. The empirical value is somewhat less than this. This is because most of the light delivered to the phototube is not direct, but travels a longer path as it reflects between the two surfaces of the paddle along the way. Slightly different values were found for the thin (1/8 in.) and thick (1 in.) paddles: $S_{thin} = 16.8$, $S_{thick} = 16.0$ cm/ns.

4.3.3 energy calibration

The amplitude of the light pulse is attenuated as it propagates down the scintillator. Therefore the pulse amplitudes at the two ends of a paddle are dependent not only upon the amount of light produced, but also on where the hit occurred. To a first approximation, the attenuation is exponential, so that

$$\begin{aligned} A_u &= A_0\, e^{-\alpha z} \\ A_d &= A_0\, e^{+\alpha z} \quad , \end{aligned} \tag{4.14}$$

where α is the light attenuation length in plastic scintillator. The A_{ui}, A_{di} amplitudes are the pulse heights from the upstream and downstream end, respectively, of paddle i, after they have been corrected for phototube gain differences. They serve as two independent measurements of A_0, which is seen to be the amplitude of the light pulse as if it had occurred in the center of the paddle.

The amplitude attenuation correction is a function of z only. Actually the amplitude response depends upon v as well as z, resulting from variation in the light collection efficiency across the face of the light guide. Using a localized radioactive source, a scan was done of a typical thin and thick paddle to quantify this effect. The result was that in the region close to the light-guide joint at the end of the paddle nearest the phototube being observed, the response varied by as much as 20%, as the source was moved across the scintillator at constant z. The thin scintillator response was more uniform than that of the thick. This was attributed to the inferior uniformity in the response of the photocathode in a 5-in. phototube, compared with that of a 2-in. tube. As the source was scanned further away from the light guide, the dependence of the response upon v decreased rapidly until, at distances over 30 cm from the end under study, the response was uniform within the resolution of the measurement.

The best way to test the z dependence of the response was to use cosmic rays. Whenever the coincidence between the two ends of a paddle signaled a hit, both

ends were read out. For each end of each paddle, a two-dimensional histogram of pulse height versus z was generated. Slicing this histogram into domains in z, 10 cm wide, 10 pulse-height spectra were obtained which showed the attenuation profile of the paddle. The middle slice was used as a line-shape to fit all of the other slices, varying the gain for best fit. The results of this test for the upstream end of one of the thin paddles is shown in Fig. 4.4. The curve on the figure is an exponential fit to the data points past $z = 0$. The data points in the region close to the upstream end rise much faster than expected from the hypothesis of exponential attenuation. The reason for this effect is the fact that near the light-guide joint, a significant amount of direct light is collected. Direct light does not suffer the losses associated with multiple reflections from the scintillator surface, and so is much brighter.

The only way to obtain a position-independent amplitude without mapping the two-dimensional response function of every paddle is to only use the pulse height from the end furthest from the hit.

$$A_{0i} = \begin{cases} A_{di}e^{-\alpha_i z} & : \text{ if } z<0 \\ A_{ui}e^{+\alpha_i z} & : \text{ if } z>0 \end{cases} \tag{4.15}$$

The A_{ui}, A_{di} are as defined in Eq. 4.15, and A_{0i} is the amplitude of the hit on paddle i as if it had occurred at $z = 0$. The gain factors for each end of each scintillator are determined by collecting cosmic ray data. A two-dimensional histogram of plastic amplitude vs z has a discontinuity at $z = 0$ until the gains at the two ends of the paddle are properly corrected.

To set the absolute energy scale, a sample of cosmic rays which cross through the scintillators at normal incidence is needed. This may be obtained by setting the trigger logic to require a coincidence between thick paddles which are opposite from each other on the LASA detector assembly. This way only cosmic rays passing through the vicinity of the detector axis are accepted. Furthermore, accepting only events with a cosmic ray track which crosses the detector axis at roughly

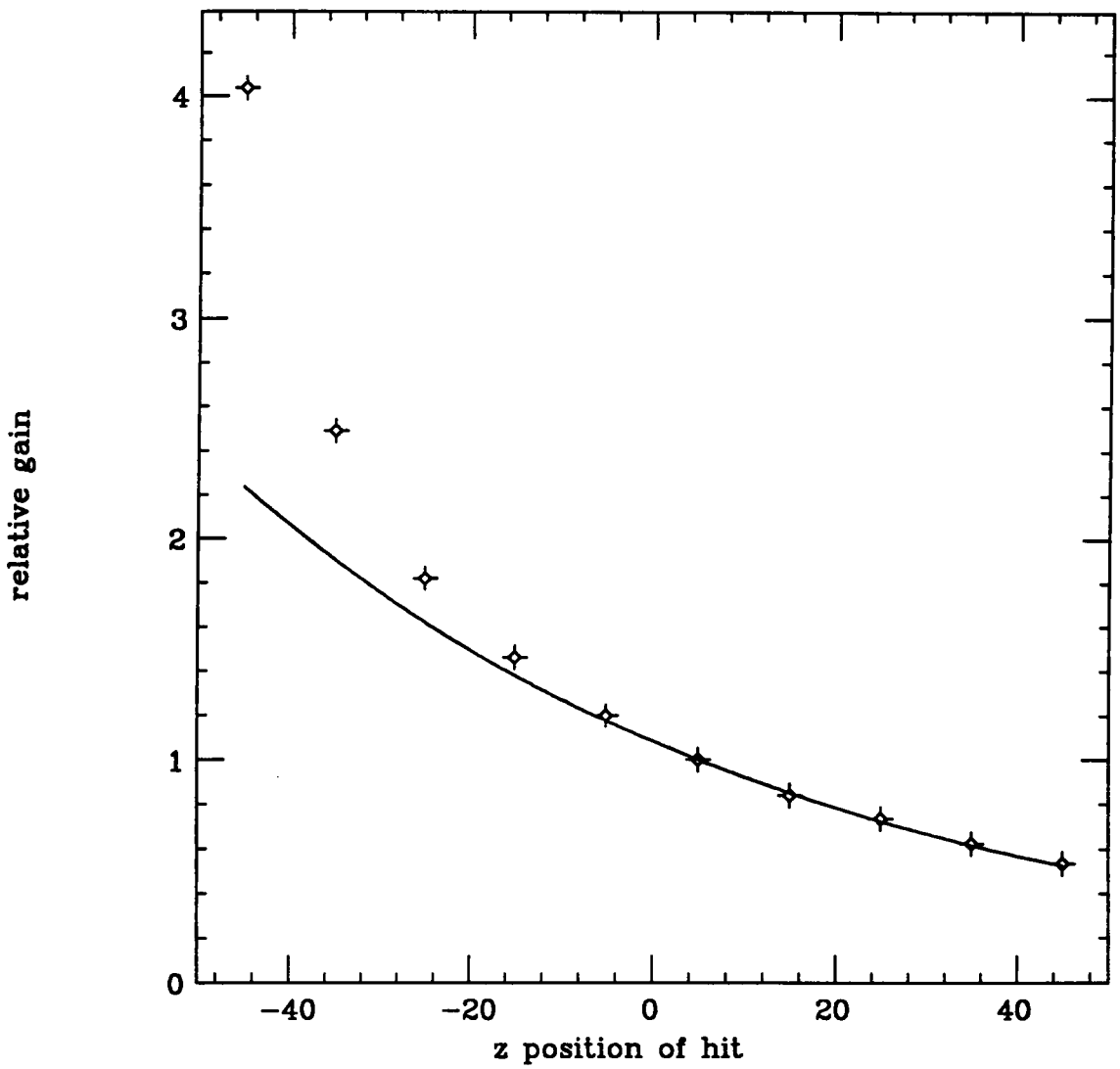

Figure 4.4: Amplitude response of a typical thin scintillator paddle, as a function of z. The vertical scale is the mean pulse-height from the upstream phototube, on a relative scale. These data were taken using cosmic rays.

90° , and rejecting multi-track shower events, the desired sample of cosmic ray events is obtained. A minimum-ionizing particle passing through 0.32 (1/8 in.) of scintillator drops 620 keV of energy by ionization. In 2.5 cm (1 in.) the loss is 5 MeV. The overall gain factor is adjusted for each paddle until the mean of the cosmic ray amplitude spectrum agrees with these values.

As was mentioned in Sec. 2.3.3, the relation between ionization energy loss and scintillation light output depends upon the velocity of the particle. For slow protons, the amount of light produced per MeV of energy loss is less than that of minimum-ionizing particles. This effect is called scintillator saturation, and response curves for different kinds of scintillator have been measured [76], and fitted to the following empirical formula.

$$T_e = a_1 \left(1 - \exp[a_2 (T_p)^{a_3}]\right) + a_4 T_p \quad , \tag{4.16}$$

where T_p is the proton kinetic energy, and T_e is the equivalent electron kinetic energy. The following values are reported in Ref. [76] in their fit to proton data in the energy range 2-20 MeV.

$$\begin{aligned} a_1 &= -8.0 \\ a_2 &= -0.10 \\ a_3 &= 0.90 \\ a_4 &= 0.95 \end{aligned}$$

This curve is shown in Fig. 4.5. The response to electrons of the same kinetic energy is also shown in the figure for comparison.

Since the photon energy is determined by the monochromator, the energy of the proton in the $^4\mathrm{He}(\gamma, \mathrm{p})^3\mathrm{H}$ is fixed by kinematics. Therefore the proton energy is known, and does not need to be derived from the plastic amplitude. The use for the plastic amplitude is to distinguish between protons and background (electrons and positrons). For this purpose it is sufficient to deal with the plastic light output

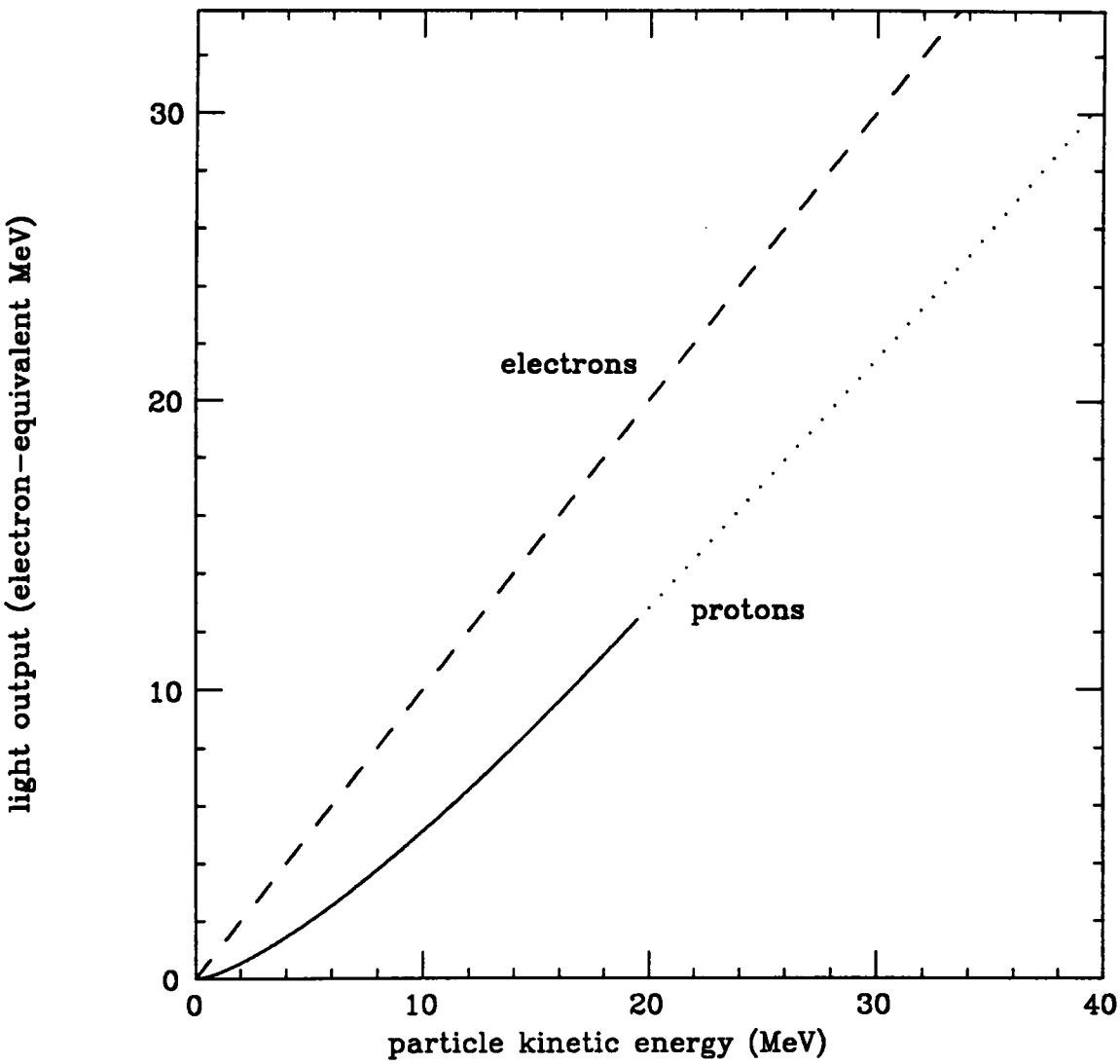

Figure 4.5: Light output response of NE102 plastic scintillator to incident electrons and protons of varying incident energy. The light output is given in units of electron-equivalent MeV. The scintillator is assumed to be thick enough to stop the particles.

directly, without having to convert to actual proton MeV. A convenient unit for plastic light output is electron-equivalent MeV, that is, the amount of energy loss sustained by an electron (or other minimum-ionizing particle) in generating a light pulse of that magnitude. On this scale, light output equals energy loss for cosmic rays and electrons, and is less, by a factor of 2-3, for slow protons. All plastic amplitude spectra in this thesis are given in units of electron equivalent MeV.

4.4 Indiana Run

The LASA detector was taken to the Indiana University Cyclotron Facility (IUCF) for tests in the proton beam. The purpose of the trip was to characterize the response of the LASA detector to protons, and to check the detector geometric acceptance function by measuring a well-known cross section, elastic p-p scattering. The energy of the proton beam was 45 MeV, and the LASA target was filled with hydrogen. With virtually no electromagnetic background present, the data recorded on tape were essentially 100% p-p scattering events.

The energy of the proton tracks depend upon the polar angle of the track, with forward going tracks having up to 40 MeV, and tracks close to 90° having only a few MeV. The kinematics forbid any tracks at angles further back than 90° in the lab. Choosing tracks whose polar angle θ lies within the range $25° < \theta < 30°$ selects a sample of protons of kinetic energy 35 ± 2 MeV, which is the median energy of the protons in the ^{4}He photodisintegration experiment. In Figs. 4.6 and 4.7 are shown the amplitude spectra of the plastic and the wires, respectively, for this sample of protons. These spectra were crucial for determining where to place the pulse-height cuts for the initial reduction passes on the photodisintegration data. Data reduction is described in Chap. 6.

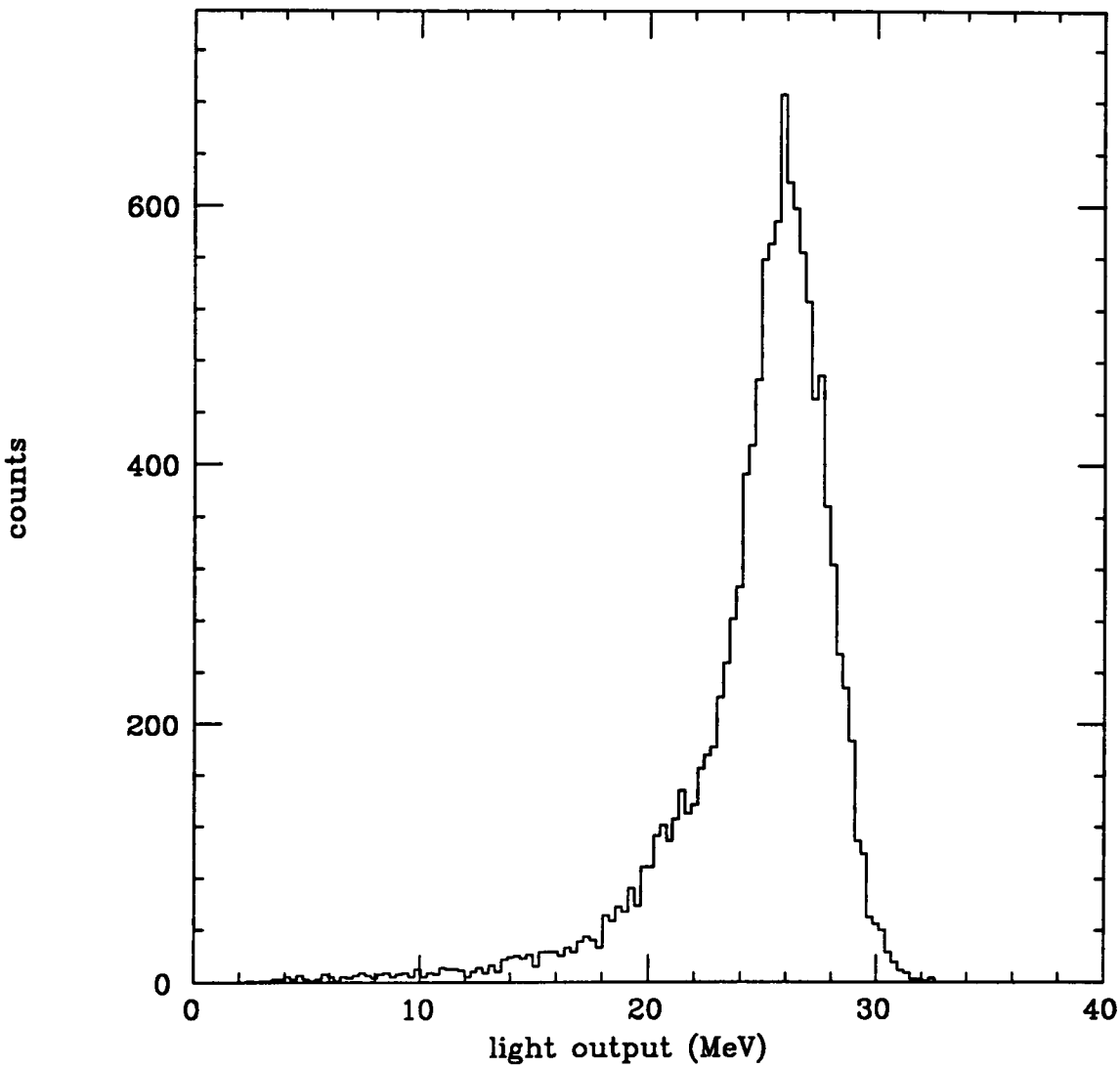

Figure 4.6: Pulse-height spectrum of plastic scintillator ($\Delta E + E$) for protons of energy 35 ± 2 MeV.

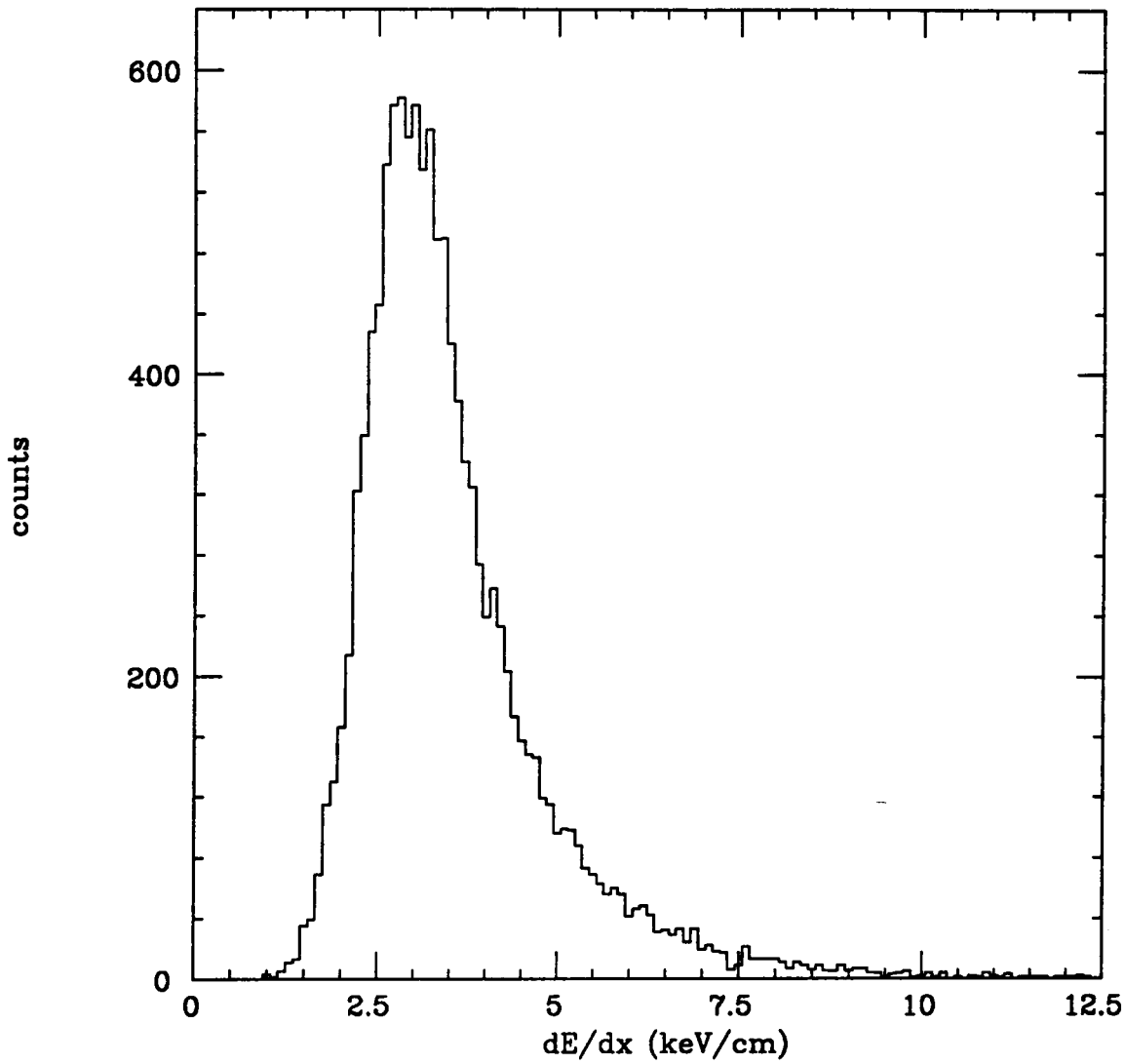

Figure 4.7: Spectrum of wire dE/dx for protons of energy 35 ± 2 MeV.

4.5 Geometric Acceptance

Before an experimental angular distribution can be normalized to a differential cross section, it must be corrected for detector efficiency. The most general efficiency function, written as $\varepsilon(\theta, \phi)$, measures the probability that an event which generates a track into the direction (θ, ϕ) will be counted by the detector. The total efficiency is a product of several efficiency functions, each of which accounts for loss of counts due to some effect. The leading contribution to the overall efficiency is the geometric acceptance, which accounts for the fact that the LASA detector does not subtend the full 4π sr around the target.

Fixing the track direction (θ, ϕ) defines a segment of the target which is "active". A volume element of target is said to be active at angle (θ, ϕ) if a track extending from the volume element, pointing in direction (θ, ϕ) passes through all three wire layers and penetrates both plastic scintillators. In the forward direction ($\theta = 0$), there is no active region of the target, which means that the acceptance is zero. At 90° , all of the target contained inside the bounds of the chamber is active. The geometric acceptance function, $\lambda(\theta, \phi)$ is defined as the length, in cm, of the active segment of target.

An approximation for λ can be obtained by assuming that the beam is confined to the detector axis. Ignoring the gaps between the scintillator paddles and modeling the plastic annulus as a cylinder, λ is independent of azimuthal angle ϕ. The dependence upon polar angle θ is obtained from simple trigonometry.

$$\lambda_1(\theta) = \max \left\{ \begin{array}{l} 2\ell - (r_p - r_a)|\cot\theta| \\ 0 \end{array} \right\} \tag{4.17}$$

where 2ℓ is the length of the wire chamber, r_p is the radius of the plastic annulus, and r_a is the radius of the inner wire level. This formula shows that λ_1 is symmetric about $\theta = 90°$. It is fairly uniform over the angular range $90° \pm 40°$, and then drops abruptly with a cutoff at about 16° .

A more precise calculation of the geometric acceptance must take into account

the fact that the plastic annulus is not a cylinder but is composed of flat segments, and that there are gaps between them. It must include effects from the finite diameter of the photon beam, and other subtle geometric corrections. The technique of Monte Carlo provides a way to account for all of these effects and obtain a result with arbitrary precision. A special Monte Carlo program called ACCEPT was written for this purpose. The function $\lambda(\theta, \phi)$ is calculated on a 1° grid in θ, ϕ, using a Gaussian beam intensity profile with a rms radius of 1.5 cm.

The geometric acceptance function described above is constructed with only a single-track requirement, that is, an event need only register one acceptable track to be counted. In the analysis of the experiment presented in this thesis, the particular channel $^4\mathrm{He}(\gamma, \mathrm{p})^3\mathrm{H}$ is separated from the three-body and four-body breakup channels by counting only events with both a proton and a triton track. The requirement of a second track was added to the Monte Carlo program, and a two-track geometric acceptance function, $\lambda_2(\theta, \phi)$ was calculated. A slice of this function in ϕ, $\lambda_2(\theta = 90°, \phi)$ is shown in in Fig. 4.8. Note that the finite extent of the beam tends to fill in the gaps between the scintillators.

Since the photon beam and target are unpolarized, there is no azimuthal dependence in the cross section, and events are summed over ϕ. Hence the geometric acceptance must be averaged over ϕ to form the univariate function $\lambda_2(\theta)$.

$$\lambda(\theta) = \frac{1}{2\pi} \int_0^{2\pi} \lambda(\theta, \phi)\, d\phi \tag{4.18}$$

Furthermore, the function $\lambda_2(\theta)$ must be transformed into the c.m. frame, because the acceptance correction is to be applied to a c.m. angular distribution. The function λ_2 measures a target thickness in cm, and hence must be length-contracted under the Lorentz boost from the lab into the c.m. frame. However, the geometric acceptance enters the differential cross section in the product $\lambda_2(\theta)\varrho$. The target density ϱ is multiplied by the reciprocal of the boost length-contraction factor under the lab-to-c.m. transformation, so that the product is a Lorentz scaler. Hence the length-contraction can be ignored, and the c.m. acceptance can

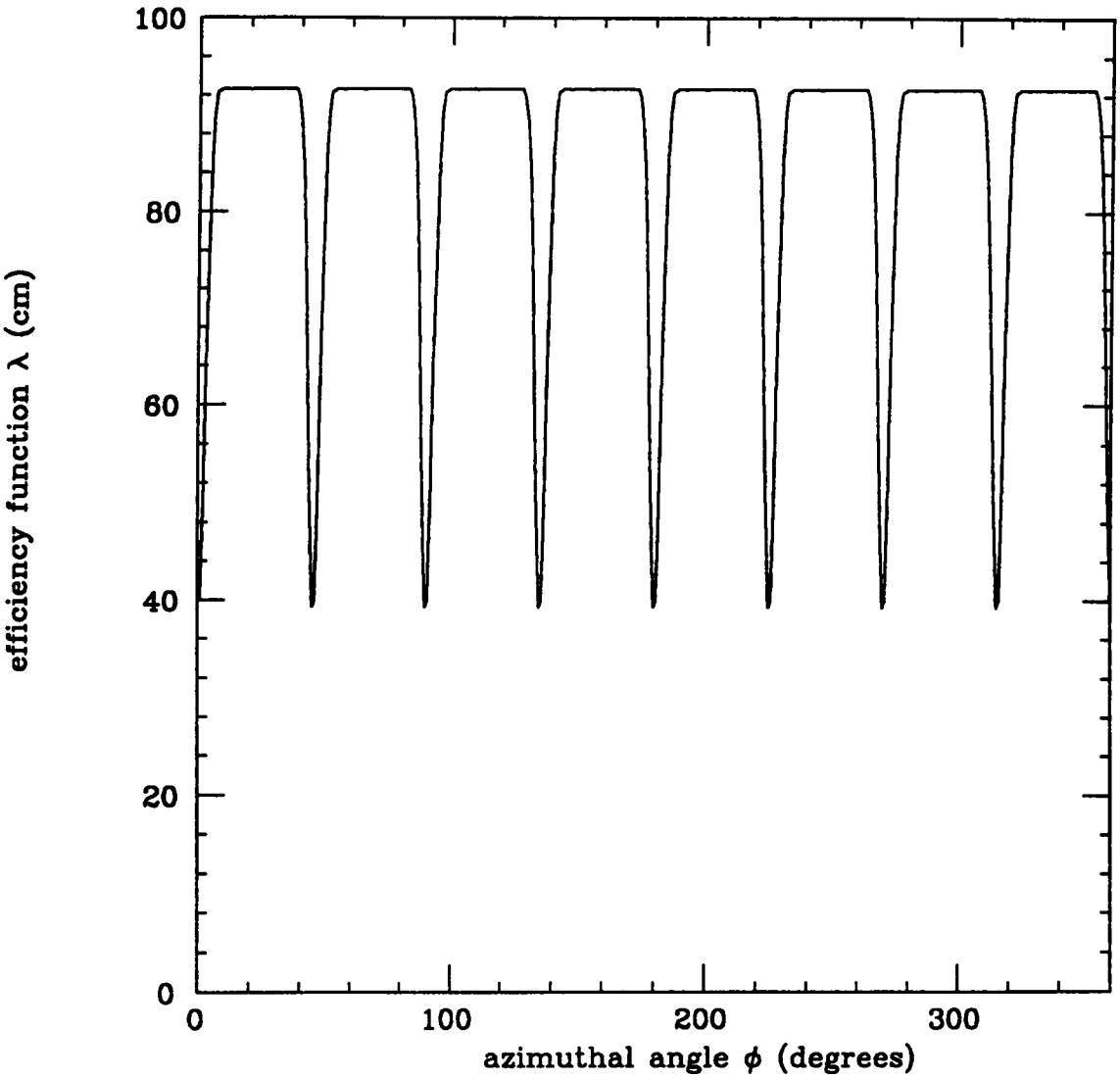

Figure 4.8: A ϕ-slice through the geometric acceptance function $\lambda_2(\theta, \phi)$ at $\theta = 90°$.

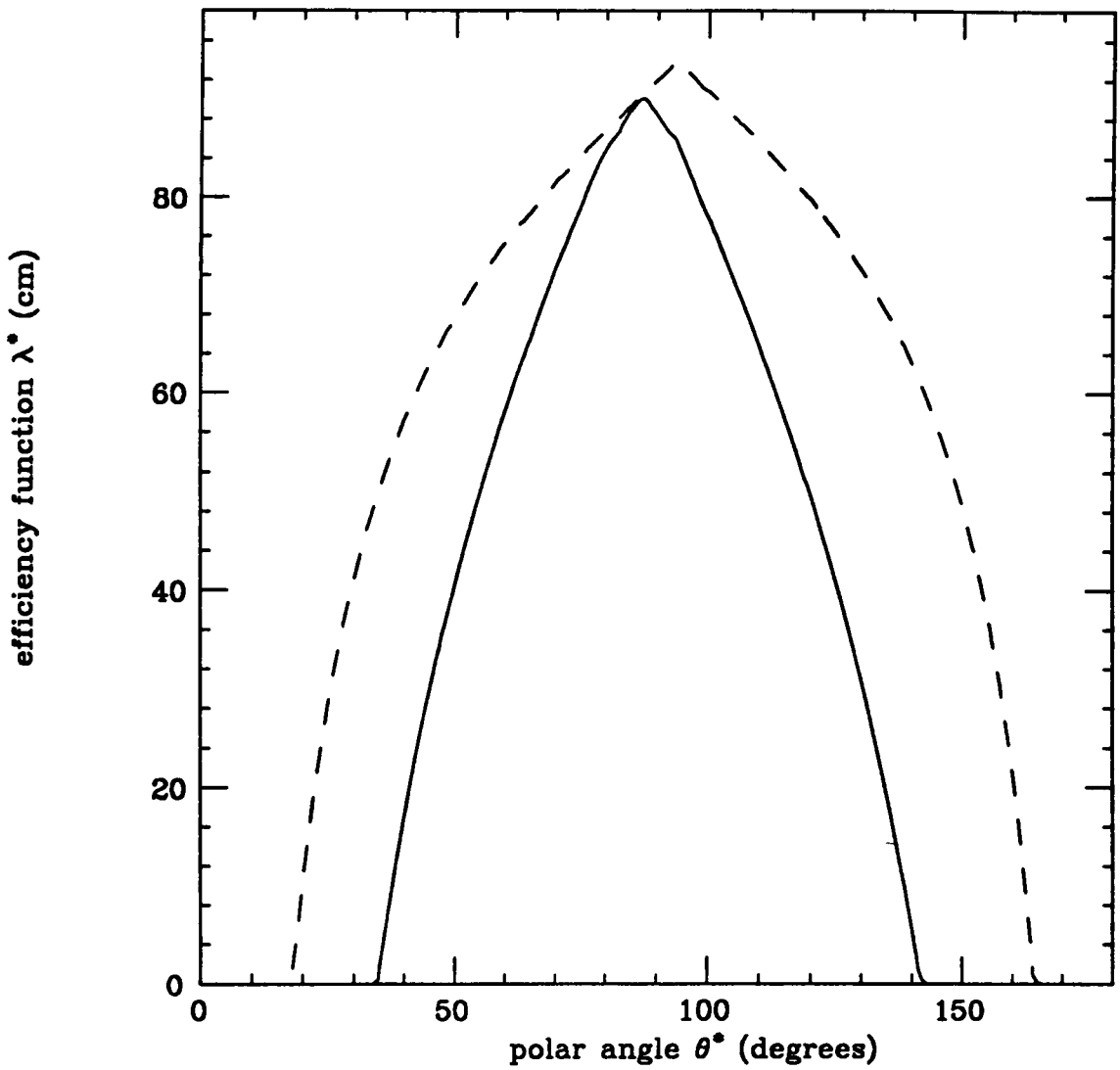

Figure 4.9: LASA detector geometric acceptance function as a function of c.m. polar angle. The curve dashed curve is the one-track function λ_1, and the solid curve is the two-track function λ_2.

be written as

$$\lambda_2^*(\theta^*) = \lambda_2(\theta) \tag{4.19}$$

with the condition that θ^* and θ are the polar angle of the same track in the c.m. frame and in the lab, respectively. The function $\lambda_2^*(\theta^*)$ is shown in Fig. 4.9. The function $\lambda_1^*(\theta^*)$ is also included in the figure for comparison. Note that the two-track requirement considerably contracts the range of angles which are accessible to the measurement. Henceforth the superscript * will be dropped, and $\lambda_2(\theta)$ should be interpreted as the c.m. acceptance function.

4.6 Monte Carlo Simulation

With the advent of larger and more complex detection systems, nuclear and high energy experimenters have come to rely increasingly upon computer simulations to characterize detector response. The GEANT program [81] from CERN is a general-purpose Monte Carlo simulator. Designed for modeling high energy physics detectors, GEANT simulates all important processes spanning the energy scale from 10 keV to 100 GeV, including the following electromagnetic processes which are important below 100 MeV: electronic and nuclear pair-production, photoelectric photon absorption, Compton scattering, bremsstrahlung, ionization energy loss and multiple scattering, and photofission. The cross sections for these processes, contained in a large database within the program, are said to be accurate to $\pm 2\%$.

A general facility is provided in GEANT for specifying the detector geometry. The entire LASA detector was entered into the program. The dimensions and material of every part was specified, including all of the wires, the chamber windows, and the entire support structure. The purpose of the simulation was to answer several questions about the response of the detector to slow, heavy particles. One concern was regarding what happens to particles which strike the wires in the chamber. A rough calculation shows that about 30% of the particles which pass through the chamber hit one of the wires. If energy loss or multiple scattering

cause these tracks to be lost, an efficiency correction will be necessary.

A simulation run was done with an artificial source of protons in the target. The azimuthal angle ϕ was chosen randomly, and the proton energy was a function of polar angle θ, simulating the protons from photodisintegration at a gamma ray energy of 68 MeV. The event vertex was distributed as a Gaussian about the chamber axis, with a diameter of 2 cm. It was found that $32.0 \pm 1.5\%$ of the protons hit at least one wire, but that the energy loss and multiple scattering were small. In Fig. 4.10 is shown the spectrum of kinetic energy remaining when a proton emitted at 150° in the lab reaches the front surface of the plastic scintillator. The initial kinetic energy at that angle was 31 MeV. The protons which hit wires show up as a broad peak below the main peak at 30 MeV. This shows that the energy loss in the wires in the worst case of a steep backward angle is only a few MeV.

The effects of multiple scattering are shown in Fig. 4.11. If a ray is drawn from the event vertex to the intersection of the proton track with the front surface of the thin plastic scintillator, the angle between that ray and the initial momentum vector is what is meant by $\Delta\theta$. Again, the worst case was tested, that of a 31 MeV proton at initial $\theta = 150°$. Note that the spectrum of $\Delta\theta$ looks like a narrow peak situated upon a broader one. The broad peak contains the protons which hit wires. Note that the multiple scattering of protons that hit wires does not contribute appreciably to the experimental θ uncertainty of $\sigma_\theta \simeq 2°$ at $\theta = 150°$.

These results show that the detector is essentially transparent to 30 MeV protons. The same is not the case for 10 MeV tritons, which are also tracked in the analysis of this experiment. The slow tritons are, in fact, largely stopped when they hit a wire. The associated triton efficiency function was calculated using GEANT, and checked by comparison with intermediate results from analysis of real data. The excellent agreement between the two justifies confidence in the fidelity of the GEANT Monte Carlo. The results are given in Chap. 6.

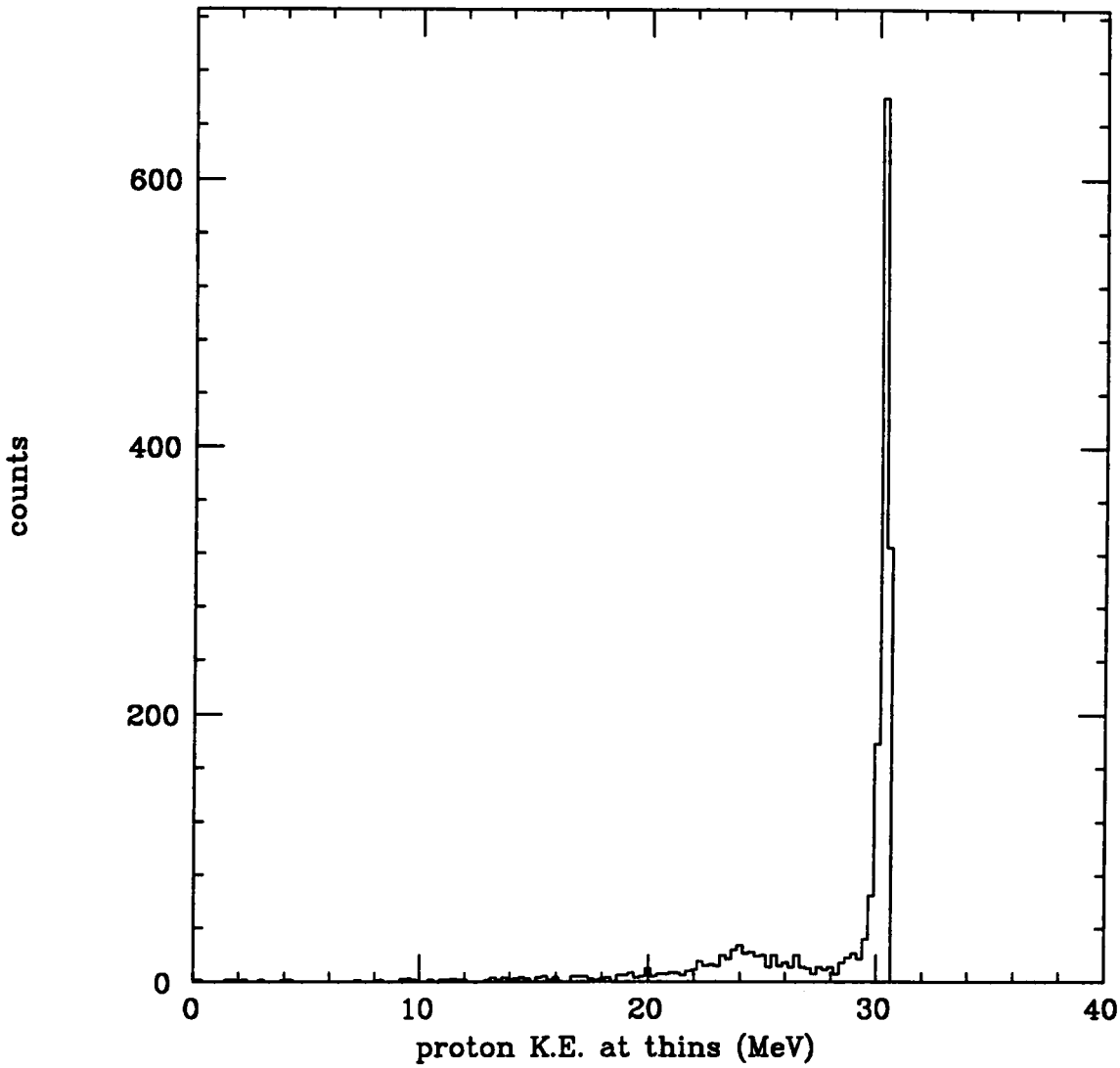

Figure 4.10: Distribution of kinetic energy remaining when a proton reaches the front surface of the thin plastic scintillator. The proton started on the detector axis at a polar angle of 150° and an energy of 31 MeV.

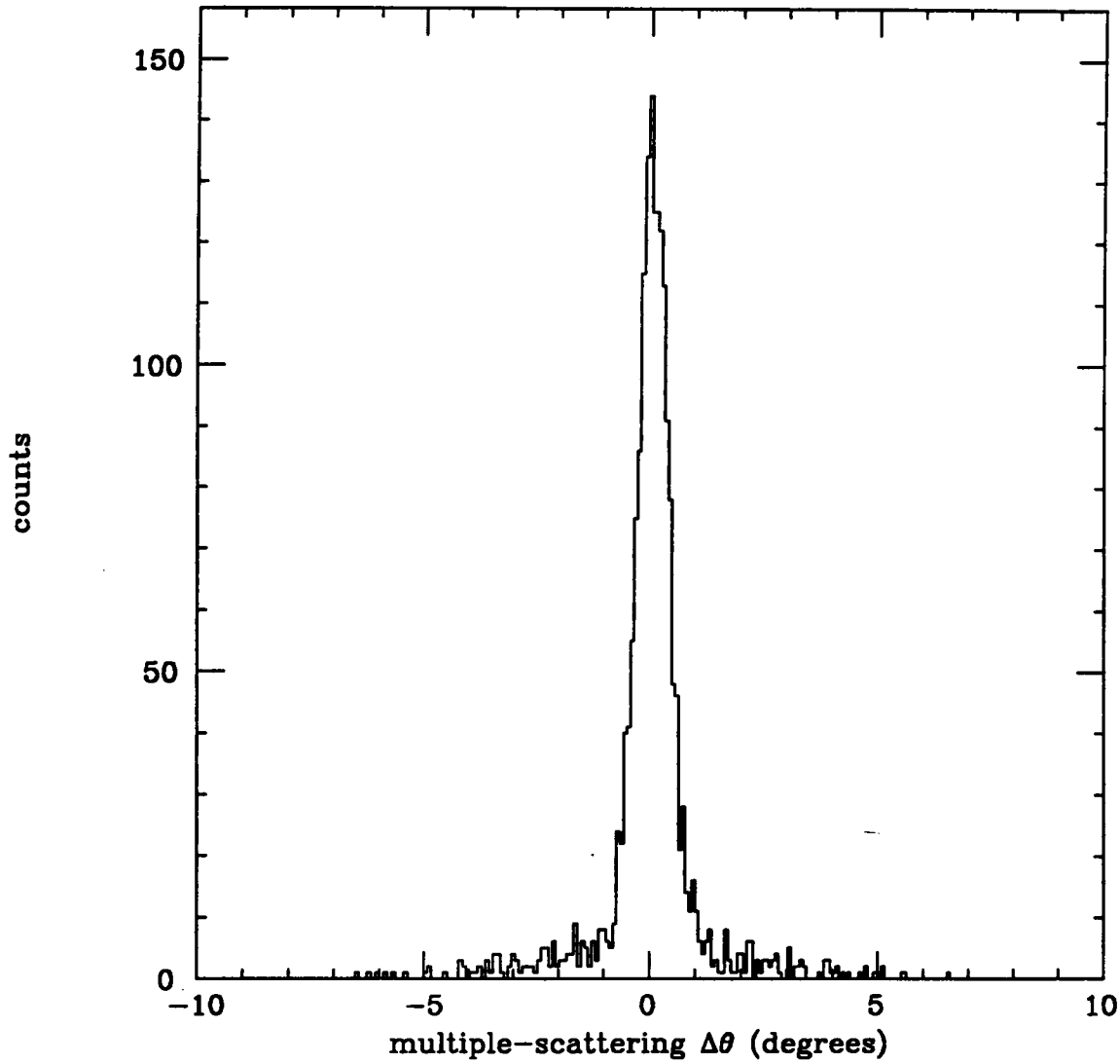

Figure 4.11: Distribution of $\Delta\theta$ of proton track, due to multiple scattering, at the front surface of the thin scintillator. The proton started near the detector axis at an initial angle $\theta = 150°$ and an energy of 31 MeV

Chapter 5

The Experiment

The electron beam energy chosen for the ^{4}He photodisintegration experiment was 88 MeV. The tagging spectrometer magnetic field was set to tag gammas within the energy range 63.3-71.1 MeV. In Fig. 5.1 is shown a cross section of the photon beam line. The vacuum exit port, just behind the brass collimator, is a 5 mil kapton window. The brass collimator is a 20.3 cm-long brass cylinder with an outer diameter of 12.6 cm and an inner diameter of 3.1 cm. The inner bore is tapered to subtend a constant opening angle of 33 mr with respect to a point in the middle of the bremsstrahlung converter. The FWHM opening angle of the bremsstrahlung cone, for a beam energy of 88 MeV, is roughly $m/E \simeq 12$ mr. In the Gaussian approximation, only 2% of the photon beam hits the brass collimator. Projecting from a point at the middle of the bremsstrahlung converter through the brass collimator, the photon beam is entirely contained within a radius of 8 cm at the downstream end of the LASA target chamber.

The fraction of the photon beam which scrapes the brass collimator produces a shower of electrons which is sharply forward-peaked. To prevent these particles from creating background in the detector, a secondary lead collimator was set up downstream of the brass. The second collimator is a tunnel built of lead bricks, 5 cm thick, which completely surrounds the photon beam. The downstream end of the tunnel is blocked by a 10 cm lead wall, with an aperture 7.6 cm in diameter. The photon beam is entirely contained within the secondary collimator; it only

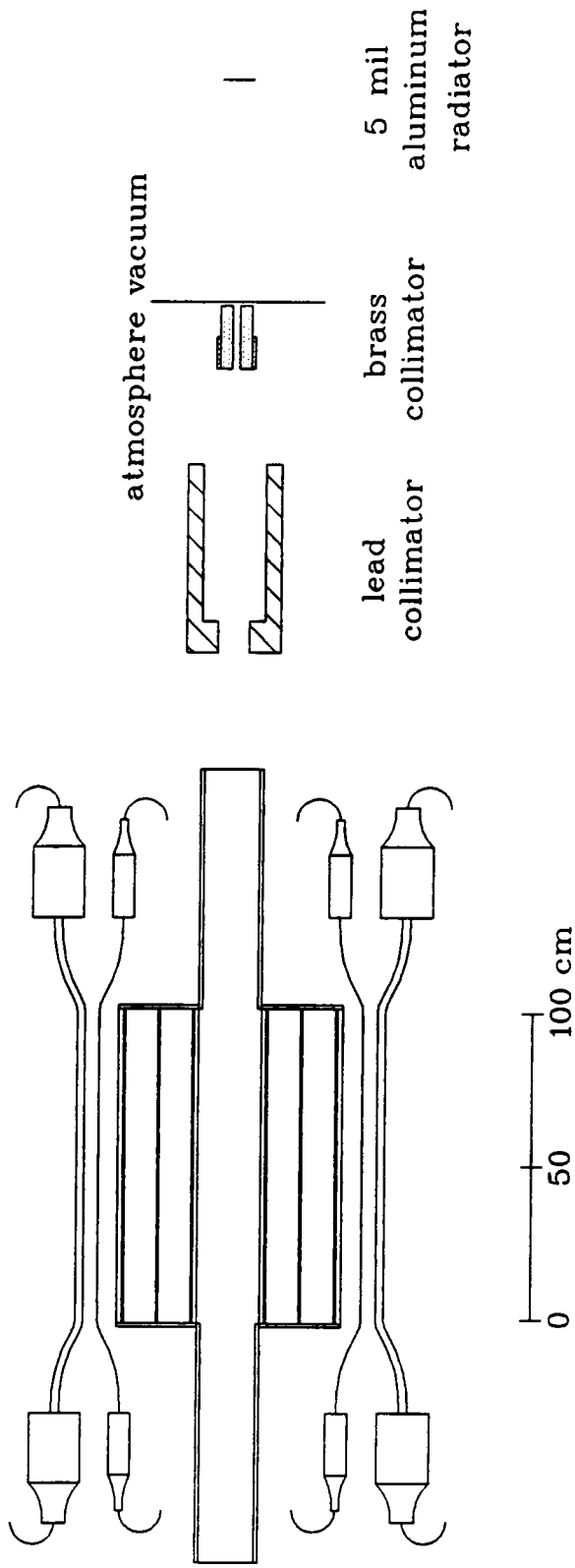

Figure 5.1: Cross section of the photon beam line, showing the collimators on the same scale as the detector.

serves to shield the detector from charged particles in the halo around the beam. The detector was positioned as close as possible behind the secondary collimator.

5.1 Background

The major obstacle to the success of this measurement was the elimination of the charged-particle background in the LASA detector. During early test runs before the secondary collimator was added to the setup, the electron background was so high that the photodisintegration signal was missed altogether. Examination of the data revealed that the events arose from light minimum-ionizing particles originating upstream of the LASA target. The addition of the secondary collimator reduced the overall event trigger rate by a factor of 5, and a small bump appeared in the time-of-flight spectrum, indicating a few slow, heavy particles in coincidence with the beam. Subsequent tuning of the event trigger enhanced the signal-to-noise ratio to the level of 0.3%: one out of 300 event triggers corresponds to a coincident photodisintegration event.

5.1.1 elementary estimates

The dominance of the electron background was not anticipated during the design of the LASA detector. Calculated estimates of the background rate were performed, taking into account the most important photon processes at intermediate energies: Compton scattering and electron-positron pair production. The cross section for Compton scattering is given by the Klein-Nishina formula [79]. Pair production is divided into nuclear pair production, which involves the conversion of a photon to an electron-positron pair in the field of a nucleus, and electronic pair production (or triplet production), which involves conversion in the field of an atomic electron.

The total cross section for Compton scattering of a 70 MeV gamma ray on helium is 22 mb. While this is large compared with the total ^{4}He photodisintegration cross section of about 0.2 mb, the cross section is extremely forward-peaked,

with the rms scattering angle of the Compton electron being 7° . Integrating only over angles greater than 15° , the total cross section is only 1.2 mb. Moreover the energy of the Compton electron decreases with increasing scattering angle, so that beyond 30° , the electron energy is under 4 MeV. Assuming a low-angle cutoff of 15° implied by the detector acceptance (see Fig. 4.9), and a threshold of 2 MeV on the 1/8 in. plastic scintillator, the effective total cross section for Compton background in the LASA detector is approximately 1 mb.

Several expressions for the nuclear pair production cross section have been published [82,83,84]. Integration of these formulae over the direction of one of the pair gives the doubly differential cross section $d^2\sigma/d\Omega dE$ in terms of the angle and energy of the other. Integration over E, above some energy threshold, yields an effective differential cross section for generation of electron background by this process. Similar expressions also exist for triplet production [85,86], which can similarly be reduced to an effective cross section.

The total cross section for nuclear pair conversion of a 70 MeV gamma ray on helium is 21 mb. The angular distribution of the electron (or positron) is forward-peaked, with a rms scattering angle similar to that of the Compton electron. Whereas the energy of a Compton electron can only have a single value at a given scattering angle, the energy of the pair electron (or positron) has a broad distribution of energies, for any scattering angle. This distribution depends upon scattering angle, with the general rule that electrons at larger scattering angles have lower typical energies. For angles greater than 10° , the distribution is peaked below 3 MeV, and has a long tail to higher energy.

In the Born approximation, the electron and positron of the pair have the same distribution, so it is sufficient to study only the electron. At 20° , the most probable electron energy is 2 MeV, with only 5% of the electrons having energies over 10 MeV. The effective total cross section for nuclear pair background can be obtained by integrating the differential cross section in the Bethe-Heitler formula [82],

excluding the region where both the electron and positron angles are below the 15° cutoff of the LASA detector. The result on helium, for a gamma energy of 70 MeV, is 0.8 mb. At most, only 50% of these electrons (or positrons) can exceed the 2 MeV energy threshold in the 1/8 in. scintillator.

The total cross section for triplet production on helium is less than half that for nuclear pair production. In addition, a triplet electron (or positron) which scatters at a large angle (> 15°) from the incident photon direction has a lower typical energy than in the case of nuclear pair production. Thus triplet production is less important than pair production, as a background in the LASA detector. Simply taking the sum, the effective total cross sections for background from Compton scattering and pair production is estimated to be 1.8 mb. Comparing this figure with the ^{4}He photodisintegration cross section, the ratio of background to photonuclear events should be no worse than 10.

5.1.2 empirical rates

The counting rates established for this experiment are listed in Table 5.1. The raw event trigger rate is the frequency of the triggers from the plastic annulus. An event interrupt is not generated unless the raw trigger is in coincidence with a hit in the monochromator focal plane. Hence the rate of events being recorded to tape is given by the coincidence event rate. The raw trigger rate with the photon beam off was measured by simply removing the bremsstrahlung converter from the electron beam. Most of this room background is from cosmic rays, with about 10% associated with the presence of the electron beam in the room. Since the raw trigger is only enabled when the computer is not dead, the event rate should be corrected for computer dead time before it is interpreted as an instantaneous rate.

The observed ratio of total to photodisintegration event rate is approximately 300:1, in distinction to the expected ratio close to 10:1. Investigation of the source of the background revealed that the dominant part was electrons coming from

Table 5.1: Summary of counting rates for this experiment

electron beam current	2.5 nA
average rate per focal plane counter	10^5 s^{-1}
raw event trigger rate	1200 s^{-1}
coincidence event rate	200 s^{-1}
raw trigger rate with photon beam off	75 s^{-1}
rate of coincident (γ, p) events	0.7 s^{-1}
computer dead time with beam on	40%

upstream of the detector, and passing at very low angles through the scintillators. The calculation outlined above was done with the assumption that particle tracks at lower angles than 15° would be excluded by geometry. The fact is, however, that electrons only lose about 5 MeV passing through the aluminum end-plate of the wire chamber [87]. This means that 20 MeV Compton electrons scattered at 11° , from the vicinity of the lead collimator, easily punch through the aluminum end-plate, and hit the thin scintillator toward the downstream end.

Noting that the Compton scattering cross section for air is 7 times that of helium, and the pair production cross section is larger by a factor of 25, it is clear why just 50 cm of air between the front of the target, and the region shielded by the secondary collimator can make such a big difference. Mechanical problems prevented moving the secondary collimator any closer to the front of the target. At the present, plans are being made to install a pipe which extends the monochromator vacuum up to the front window of the target.

5.2 Trigger Threshold

The kinetic energy in the lab of the proton and triton from the reaction $^4He(\gamma,p)^3H$ at a gamma energy of 70 MeV is shown in Fig. 5.2(a). When the particles arrive at the plastic annulus, they have somewhat less energy due to losses in the gas and windows. In Fig. 5.2(b) is shown the remaining kinetic energy of the proton and triton when they reach the front surface of the 1/8 in. plastic scintillator. The losses at forward and backward angles are larger than at angles close to 90° , due to the longer path length in the windows and gas. The energy loss sustained when a particle hits a wire in the chamber is not taken into account. The correction for these effects is discussed in Chap. 6.

The summed light output from the thin (1/8 in.) and thick (1 in.) plastic scintillator for the proton and triton is shown in Fig. 5.3(a). The light output is measured in units of electron-equivalent MeV, and shows the effects of scintillator

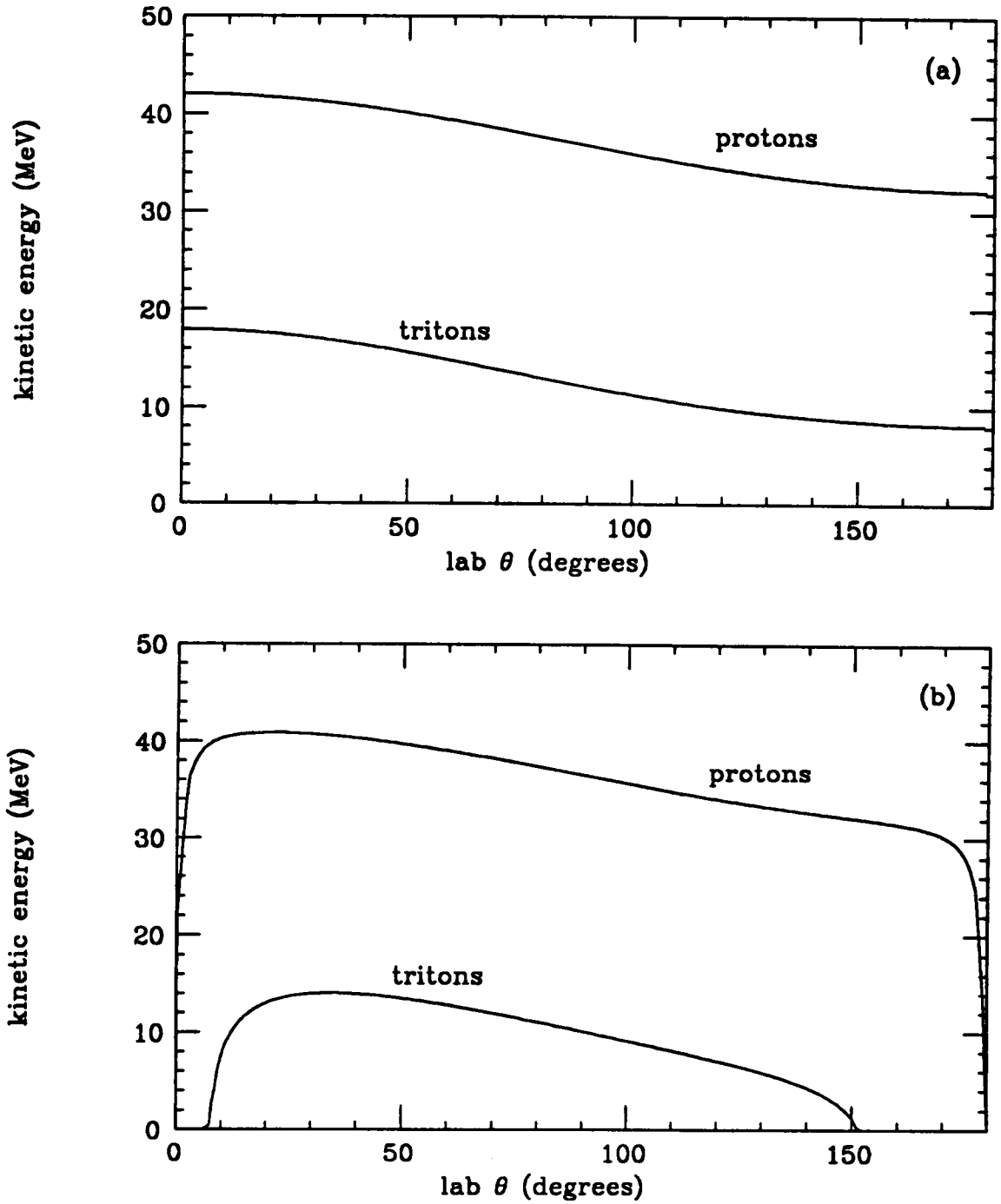

Figure 5.2: Kinetic energy in the lab, as a function of lab scattering angle, of the proton and triton from the reaction ^{4}He$(\gamma, \mathrm{p})^3$H. The incident gamma energy is 70 MeV. (a) The kinetic energy at the photodisintegration vertex. (b) The kinetic energy remaining when the particles reach the front surface of the plastic scintillator. Energy loss is calculated from the tables of Ref. [88].

saturation. The pulse height in the thin scintillator alone is shown in Fig. 5.3(b). The depression in the pulse height of the proton signal in Fig. 5.3(b) at angles around 90° is due to the fact that the protons are punching through the thin into the thick scintillator.

Since the proton has much more energy than the triton, the trigger is designed for maximum efficiency for detecting protons. As discussed in Chap. 3, the raw trigger is formed out of a logical combination of the signal from the thin and thick scintillators. The trigger logic is performed individually for each scintillator pair, and the results from all of the pairs are ORed together to form the raw trigger. The four possibilities for the trigger logic are (a) AND of thick and thin, (b) OR of thick and thin, (c) thin only, and (d) thick only. As can be seen from Fig. 5.3, protons at forward and backward angles stop in the thin scintillator. Thus, if these events are not to be excluded, trigger choices (a) and (d) are disallowed. Since trigger option (c) is capable of accepting all desired events, the inclusion of the thick scintillator in option (b) only adds background triggers. Hence the choice was made to simply place the trigger on the thin scintillator.

A raw trigger is generated every time a coincidence occurs between the two ends of a thin scintillator. Since the pulse height at the ends depends upon the location of the hit along the length of the paddle, the effective threshold for firing the trigger depends upon z. The effective threshold is highest near either end of the paddle, and lowest at z=0. At the end of the paddle, the signal on the near phototube is large, but the phototube on the far end sees the light pulse attenuated by the full length of the scintillator. Because the discriminators on both ends are required to fire in order for there to be a coincidence, this leads to a high effective threshold near the ends of the paddle compared to the middle.

The magnitude of the difference in the effective threshold between the ends and the middle of the thin scintillator is determined by the attenuation length of the plastic. For the thin scintillators, the measured attenuation length averaged

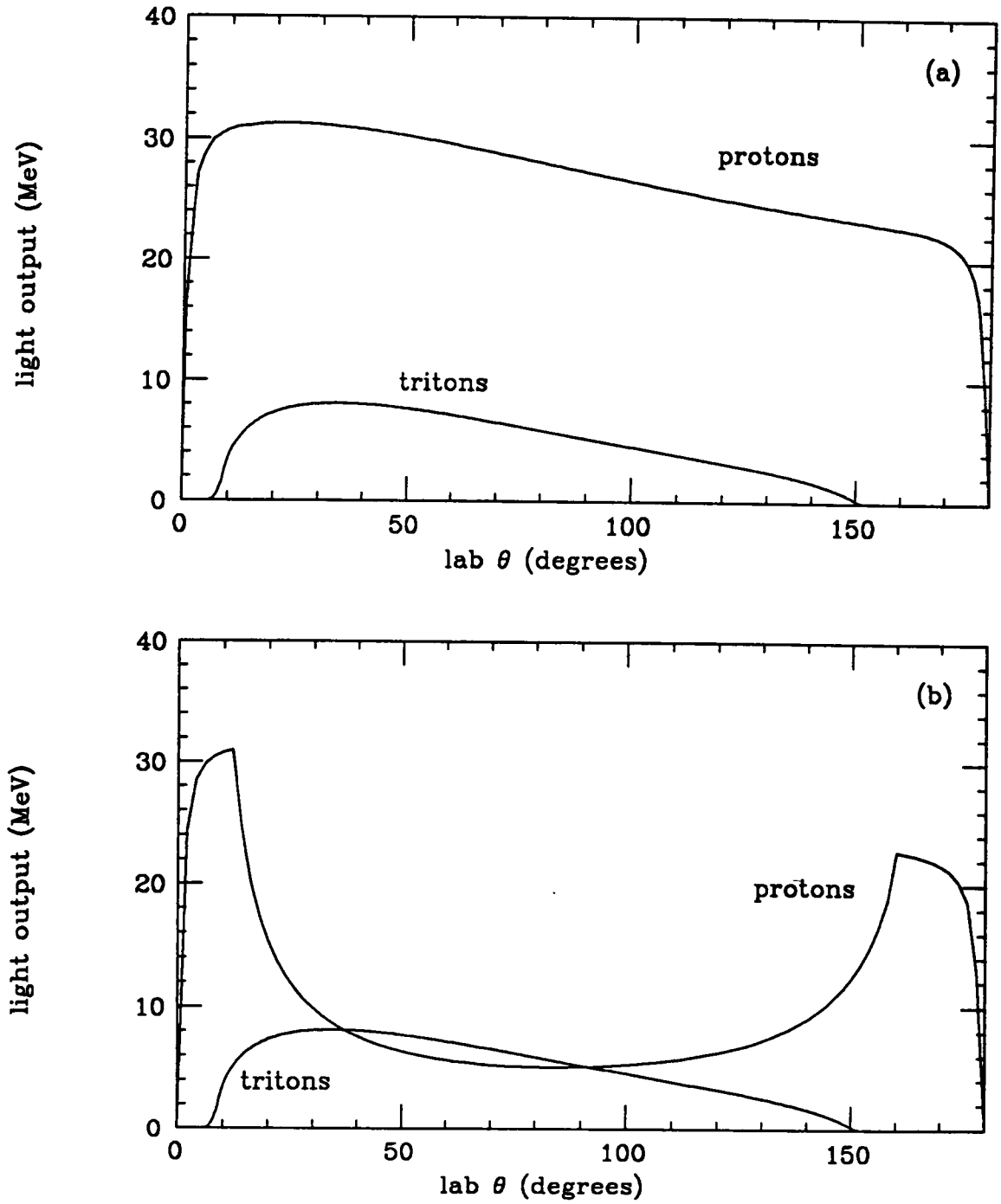

Figure 5.3: Light output from plastic scintillator, as a function of scattering angle, in response to photodisintegration protons and tritons. (a) The summed light output from thin and thick scintillators. (b) the light output from the thin scintillator alone. Light output is measured in units of equivalent-electron MeV.

75 cm, leading to a ratio of nearly 2. Lowering the discriminator thresholds to achieve good efficiency for protons near the ends of the paddles creates a region in the center of the paddle which is unnecessarily sensitive to background.

To alleviate this problem, the HI-Z discriminator was added to the trigger. This device performs an analog sum of the pulses from the two ends of the thin scintillator, and discriminates the sum. The effective threshold of this arrangement exhibits the opposite z dependence, being high in the middle and low toward the ends. This is the result of the fact that the attenuation function is not a straight line. The relative thresholds on the HI-Z and the timing (individual-end) discriminators can be adjusted so that the AND of the two generates a fairly flat effective threshold.

The effective threshold is exhibited in the profile of thin plastic pulse height, shown in Fig. 5.4, for different sections of the scintillator. Each curve corresponds to a section of scintillator 10 cm long in z, with the upstream end in the foreground. The curves on either end are nearly empty because they correspond to hits with a z beyond the ends of the paddle. These spectra were made from the ^{4}He photodisintegration data. Note that most of the hits fall toward the downstream end of the paddle, as explained above in Sec. 5.1.

The discriminators were adjusted for this experiment to produce an effective threshold that was nowhere higher than 2 MeV thin light output. As can be seen from Fig. 5.3, protons at 90° produce an average of 5 MeV of light in the thin plastic. The choice of 2 MeV was made, based upon a pessimistic estimate of the plastic pulse-height resolution, to insure that the trigger efficiency for 90° protons was near unity. The analysis of the data showed that this could have been raised as high as 3 MeV without significant loss of efficiency.

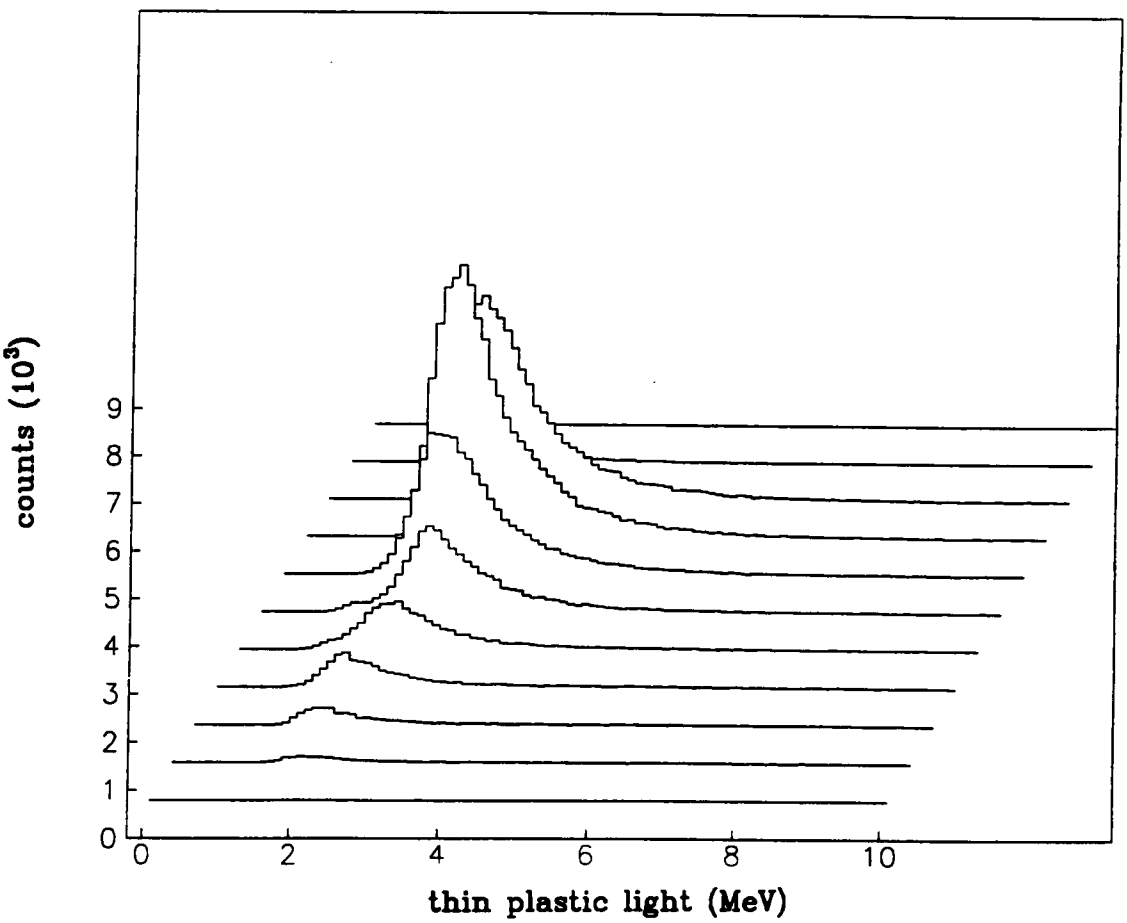

Figure 5.4: Amplitude spectra for one of the thin plastic scintillators, sliced into 10-cm sections along z. The low edge of the peaks is the discriminator cutoff, which falls at about the same place for each of the slices.

5.3 The Run

The data for this experiment were taken over a period of 116 h. There were 107 reels of magnetic tape filled at a density of 1600 bpi (bits per inch). Of these, seven hold tagging efficiency calibration runs (Brems runs), and the rest contain photodisintegration data. A total of eight Brems runs were performed, one at the beginning and at the end of the experiment, and the others dispersed throughout. The Brems runs were typically stopped when the focal plane scalers reached 10^4 counts, after about 1/2 h. It took about 40 min to fill a tape during a photodisintegration run, each tape holding about 450 000 events.

The electron beam was extremely stable throughout the course of the experiment. The current was monitored by a Faraday cup in the electron beam dump, and was kept within $\pm 10\%$ of the nominal value listed in Table 5.1. The electron beam alignment was monitored by the visualization system, described in Sec. 3.1. Alignment of the LASA detector and NaI crystal was performed with the aid of a laser, which defines the photon beam axis. The same laser is used to calibrate the visualization system. A check of the beam alignment was made at the beginning of each run, and steering corrections were made if necessary. The center of the photon beam was kept within a radius of 1.5 cm of the LASA detector axis, at $z = 0$. This figure is less than the rms radius of the photon beam.

Several hardware problems were discovered throughout the course of the experiment. At the end of tape 52, it was discovered that the upstream end of thin scintillator 6 had a bad connection. This problem, which had existed since tape 29, was fixed before tape 53 was started. Then at tape 71, it was discovered that 1/3 of the wires on level C were giving bad z values. The problem turned out to be a bad connection on the power distribution cable to the upstream wire amplifiers. This problem was fixed before the experiment continued. It turns out that this problem existed from the beginning, but had escaped notice.

At tape 86, it was discovered that focal plane counter 23 was counting more

slowly than its neighbors. The fault was diagnosed and repaired, and the experiment continued. Several times throughout the experiment, the wire chamber high voltage shut down due to electrostatic discharge in the chamber. This was understood to be due to the slowly drifting wire gain and so was not a problem. The voltage was adjusted, and turned back on again. There were no problems with the phototube high voltage supplies, either on the focal plane or the LASA detector.

The problem with the wire amplifiers on level C rendered the early 2/3 of the data tapes difficult to analyze. With one third of one layer vetoed in the analysis, only 1/3 of the photodisintegration events would be accepted; the others have either a proton track or a triton track in the veto zone. Furthermore, half of these tapes have the additional problem that scintillator 6 is out, which means that only 1/6 of the events on these tapes are analyzable. With part of the chamber disabled, a different geometric acceptance function would have to be used. For these reasons, the results presented in this thesis are derived entirely from the tapes 73-107.

Chapter 6

Data Analysis

The trigger threshold, discussed in Chap. 5, was set to accept any event with a hit in one of the thin scintillators with an energy deposit over 2 MeV. Due to the short range of the ^{3}He particle from the ^{4}He$(\gamma, \mathrm{n})^3$He reaction, the trigger was not sensitive to this channel. However, events from the other two-body channels ^{4}He$(\gamma, \mathrm{p})^3$H and ^{4}He$(\gamma, ^2\mathrm{H})^2$H were accepted, along with any events from the reactions ^{4}He$(\gamma, \mathrm{pn})^2$H and ^{4}He(γ, ppnn) with protons of sufficient energy to fire the trigger. The analysis reported in this thesis pertains only to the ^{4}He$(\gamma, \mathrm{p})^3$H component of this experiment.

The analysis is described as follows. First, the 107 tapes of raw data were read in and reduced to disk files. In the reduction, a few elementary data cuts were made, which rejected about 98% of the events, and made it possible to store the data all in one place. The reduction is described below in Sec. 6.2. Repeated analysis passes were then made over the reduced data, to find the best thresholds for the final cuts, and to estimate the associated uncertainty. The events were then accumulated into histograms. The contribution to these histograms from random coincidences was subtracted, by the procedure described below in Sec. 6.4. The efficiency correction and the overall normalization, discussed in Secs. 6.5-6.6, were applied to obtain the differential cross section.

6.1 Track Analysis

The fundamental task of analyzing an event from the LASA detector is to identify and analyze the tracks of photodisintegration fragments. For the reaction under study, the fragments of interest are protons and tritons. The data record for each event includes a list of the locations and amplitudes of all the hits in the wire chamber. From these, a table of all hit-combinations which could possibly be tracks is assembled. This is called track finding. The task of track fitting follows, in which the track candidates are analyzed and subjected to consistency tests.

6.1.1 track finding

The search for track candidates involves identifying all the sets of three wire chamber hits which lie reasonably close to a straight line intersecting the target region. The collinearity of the hits is first examined by projecting them onto the xy plane, taking an end-view of the wire chamber. In this view, the hit pattern is contained simply in the list of the wires that fired; the z position of the hits is projected out. The assembly of hits into track candidates is performed by the following procedure. The wire hits are separated according to wire level, the inner level being labeled A, the middle B, and the outer C. For each hit on level C, a scan is done of hits on level B, asking the following question: does a line containing hits C and B intersect, or pass sufficiently close to, level A? Note that this question can be answered by simply examining the hit pattern in the xy plane. For all pairs C,B which pass this test, a scan of level A is done for any hits on the same side of the target as hits B and C. All A,B,C hit combinations which pass these tests are entered into the table of track candidates.

The job of track finding is not to make the final determination of which combinations are valid tracks, but to isolate a reasonable number to be examined further at the track fitting stage. If the track finder assembles too few candidates then tracks are missed, and if it finds too many, the track fitter spends too much time

analyzing worthless tracks. A track-finding procedure is characterized by its type-I and type-II error frequencies. A type-I error occurs when a valid track is not found. A type-II error occurs when an invalid track is found by the finder, and must be rejected by the fitter. The best algorithm is one which minimizes the type-II error frequency, while keeping the type-I error probability essentially zero.

The method outlined above is called a modified exhaustive-search algorithm. An exhaustive search algorithm has a type-I error probability of exactly zero, because it enters every A,B,C combination into the table of candidates. This method is all right for simple events, but when the average number of hits per level increases much above 1, the number of track candidates to be evaluated by the fitter becomes very large. The modification to this algorithm, outlined above, eliminates the combinations which are far from forming a straight line, looking at the pattern on the end-view of the chamber. Since the great majority of random combinations are far from collinear in the xy plane, the type-II error frequency is much less than unity. For those tracks which originate in the target, the type-I error probability remains zero.

One disadvantage of this finding algorithm is that a single hit often appears more than once in the candidate table. This is because more than one candidate track can claim the same wire hit. A more sophisticated algorithm is required if these are to be excluded from the candidate table at the track-finding stage, without introducing type-I errors. With the present algorithm, it is up to the track fitter to decide which of the tracks can best own the shared hit, since in the end, only one track may keep it (tracks do not intersect). The chief advantage of this finding algorithm is its speed. Each test is simply a check if an angle is between two limits. For the relatively simple events in this experiment, only a few percent of the track candidates approved by the finder were rejected by the fitter.

Note that with this algorithm, any particles which fail to make a hit in all three wire levels are lost to the analysis. This means that a correction must be applied

in the end, to account for the tracks which have been missed for this reason. The general subject of tracking efficiency is discussed in Sec. 6.5.

6.1.2 track fitting

The task of finding the best-fit straight line for a set of hits in three dimensions may be divided into two separate fits in 2 two-dimensional projections. The first projection is onto the xy plane, discussed above. The (x, y) coordinates of each hit are determined, and a linear least-squares fit is performed. The χ^2 of the linear fit is checked, and if it is within preset bounds, the candidate passes on to be fitted in the other projection, otherwise it is struck from the table. An example is shown in Fig. 6.1. The xy projection of the event is shown in the upper half of the figure. The wire hits which form the track candidate are circled, and the best-fit straight line is drawn through them.

The fit in the xy plane yields an azimuthal angle ϕ for the track. A vector from the origin in the xy plane may be drawn at the same azimuthal angle, labeled r in the upper half of Fig. 6.1. In the lower half of the figure, the same track candidate is shown projected onto the zr plane. This choice of geometry for the second projection has the advantage that the slope of the best-fit line in the zr projection gives the polar angle θ of the track by $\tan\theta = slope$. The least-squares fit is performed in this projection, and an upper bound is imposed on the resulting χ^2. The sum $\chi^2_{sum} = \chi^2_{xy} + \chi^2_{zr}$ is also formed, and an upper bound is enforced on it.

Only tracks which pass this linear-fit test remain in the track table. Next, any tracks which share wire hits must be reduced. Given a set of tracks which share a hit, only the track with the lowest value of χ^2_{sum} is accepted, and the rest are eliminated from the table. The next step is to determine which wire chamber tracks are associated with hits in the plastic annulus. For each scintillator that fired, a list of the wire chamber tracks that intersect that scintillator is assembled. For

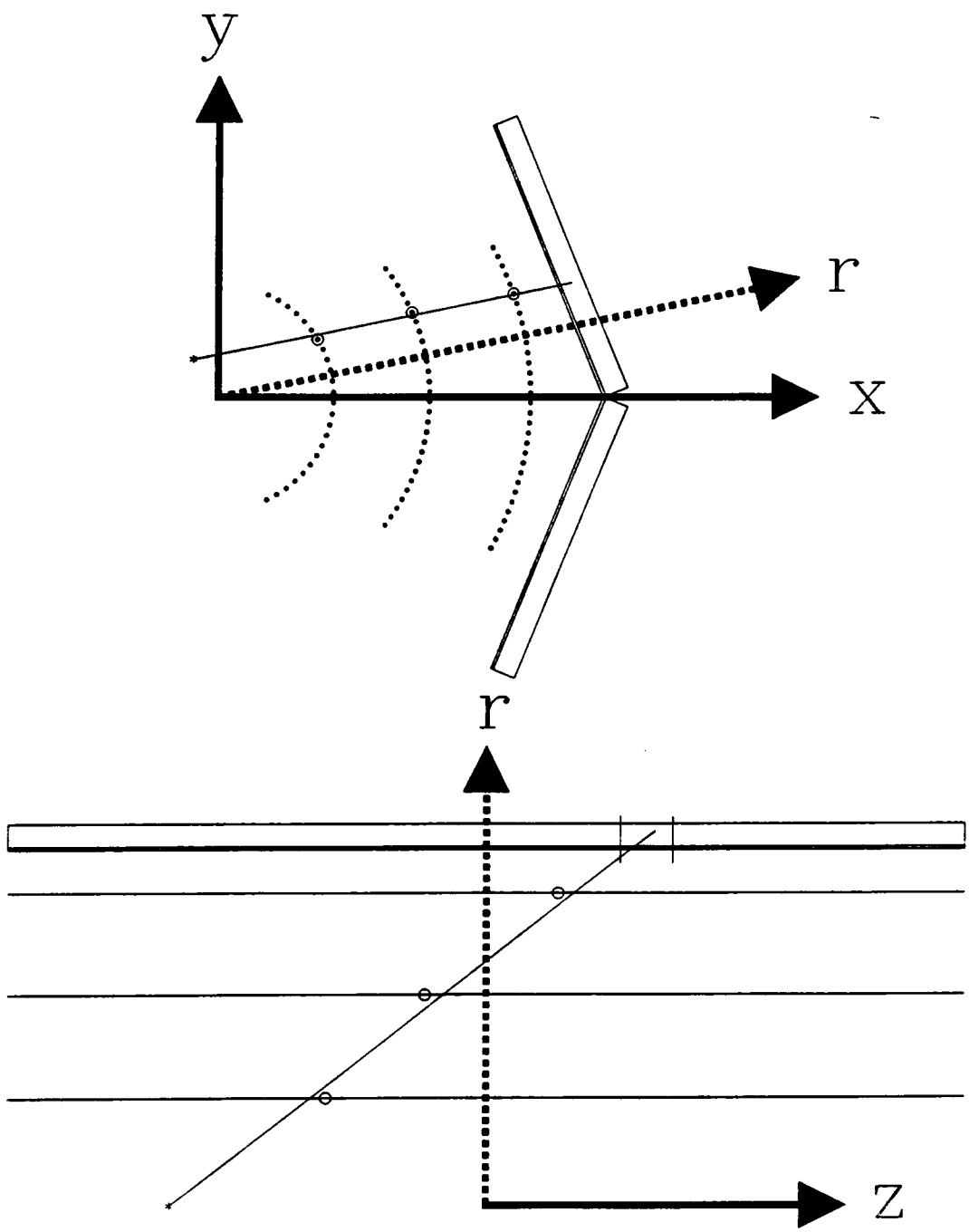

Figure 6.1: Linear fit to a typical particle track in the wire chamber, showing the coordinate systems used. The upper picture shows the xy projection, and the lower shows the zr projection of the track.

each track in the list, the fit in the zr plane is performed again, this time including the z coordinate of the plastic hit in the fit. If the χ^2 of the new fit is within limits, the entry in the track tables for this track is amended to include the plastic information. If more than one track claims the same plastic hit, the one with the lowest χ^2_{zr} takes it, and the others are restored to their previous fit, which used the wire chamber hits only. The tracks which end up owning a plastic hit are called *primary* tracks, and those which have only the three wire chamber hits are called *secondary* tracks.

Note that the initial track fitting is done with the wire hits only, and that plastic hits are included only on the tracks which passed the initial fit. This means that some candidate tracks are eliminated before they are tested against the plastic hits. This procedure was implemented because the tracking resolution in the wire chamber is much better than in the plastic annulus. In the case where the wire chamber track fails to pass the test, a good agreement between this ill-fit track and a plastic hit does not change the conclusion that the track should be rejected. The inclusion of the plastic hit in the linear fit does not appreciably improve the angular resolution of the track; it merely serves to distinguish which track belongs to which plastic hit.

6.1.3 vertex fitting

In the final stage of track analysis, an attempt is made to determine the location of the photodisintegration vertex. If only one track was found for the event, the best estimate for the vertex is the point of closest approach of the track to the detector axis. In the case where more than one track was found, a better estimate may be obtained by locating the "intersection" of the tracks. Because of tracking errors, the likelihood of obtaining two tracks which intersect exactly in three-dimensions is zero. However there is a point which minimizes the sum of squares of the distances to an arbitrary number of lines. This point is used as an estimate of the vertex.

In the case of only one track, or of two tracks which are collinear, this point is not unique (the vertex could be anywhere along the tracks), so a weak bias was added to the equations which favors the point closest to the detector axis.

Having an estimate of the vertex is useful for making background cuts, and investigating the variation of the detector response for events originating in different regions of the target. A histogram of the distribution of the vertex in the xy plane showed a much broader beam profile for the electron background than for photodisintegration events. This was attributed to greater tracking uncertainty for electrons, due to their large multiple scattering. Setting an upper limit on the distance of the vertex from the beam axis was one means of suppressing electron background relative to photonuclear events.

6.2 Data Reduction

Due to the large quantity of the raw data, it is inefficient to make multiple analysis passes through the whole set of tapes. Several passes through just a few tapes show what cuts can be used to reject most of the background, and still keep all of the photonuclear events. The definition of a cut is the elimination of events from analysis based upon the value of an event variable; that is, whenever the variable is outside of the limits imposed by the cut, the event is eliminated from further analysis. A cut is defined by specifying the variable being tested, and the allowed range of the variable.

Data reduction involves three distinct tasks: (a) the raw event numbers must be *translated* into physical quantities, (b) the translated quantities must be *diagnosed* to make sure that the detector was working properly, and (c) the *cuts* must be imposed. Those events which pass the cuts are recorded in translated form on disk, to be further analyzed later. Recording them in translated form means that the translation needs to be done only once, during reduction. The cuts made at reduction time are deliberately loose, to give as much freedom in the choice of final

cuts later on. With the data in reduced form on disk, multiple passes over the entire data set can be made to determine the best placement for the final cuts to be made on the data.

The main task of event translation is to convert ADC and TDC numbers in the raw event record into the properly corrected time (ns), position (cm), and pulse-amplitude (MeV) values which they represent. The formulae for this translation have been discussed in Chap. 4. Also included with event translation is the reduction of hit clusters. Frequently a particle track passing through a wire layer deposits energy in more than one wire cell. Cluster reduction involves finding these compound hits, and summing the amplitudes to form a single entry in the hit tables. The summed hit is assigned the wire number closest to the center-of-gravity of the pulse amplitudes, and the z of the hit is calculated as the average of the individual z's, weighted by the respective hit amplitudes. Any contiguous sequence of hits within a wire level was assumed to be a cluster, and was compacted to a single hit.

Multiple-hit clusters also occur in the monochromator focal plane. Since the focal plane counters overlap one another by about 10%, about 20% of the electrons fire more than one counter. These must be reduced to prevent double-counting of coincidences. To prevent the reduction of independent hits which are accidentally contiguous, the time difference of adjacent hits is required to be less than 5 ns, or else they are treated as separate hits. Sequences of three or more adjacent hits rarely occur, and are reduced pair-wise, with any singles left over treated as separate hits. The same cluster reduction was used in analysing Brems runs, since it affects the numbers obtained for the tagging efficiency.

Histograms of every translated datum are accumulated, for a diagnostic monitor of detector operation. With the large number of similar elements in the system, a reliable diagnostic is found in a comparison between similar spectra. The number of counts in each, the location and relative heights of peaks in timing spectra, and

the relative gain in amplitude spectra are periodically checked during reduction, to look for inconsistencies. The translation and diagnostic tasks are combined into a single VAXONLINE program, TRANSLATOR.

6.2.1 wire gain anomaly

One very surprising anomaly was uncovered by the diagnostic monitor during data reduction, regarding the relative gain of wires within a given level. Up to that point, it had been assumed, due to the azimuthal symmetry of the chamber and the fact that a single high voltage was delivered to each level, that all of the wires on a single level had the same gain. The discovery was that the gain varied within a level by as much as a factor of 2. The systematic nature of the variation is apparent from Fig. 6.2, which shows the relative gain of wires on level C. The wires are grouped into sets of eight. The curve through the points is a fit, using the function

$$f(x) = ax + b \quad ,$$

where x is the vertical displacement (altitude) of the wire in the chamber, given by $x = r\cos\phi$ with r being the radial coordinate of the wire, and ϕ its azimuth.

The choice of this formula was motivated solely by the shape of the data. At present there is no explanation for the effect. Apparently it is related to the chamber gas composition, since the data from another experiment performed a few days after this one, in which an argon chamber gas mixture was used, do not show this effect. The helium and methane components of the gas mixture were premixed by the manufacturer, and a mechanism for how the gas composition could vary appreciably with altitude inside the chamber is hard to imagine. The fact that all three levels show the effect, and that the fits all have roughly the same a value are evidence that the effect is caused by an inhomogeneity in the chamber gas. Investigation of this effect is still underway.

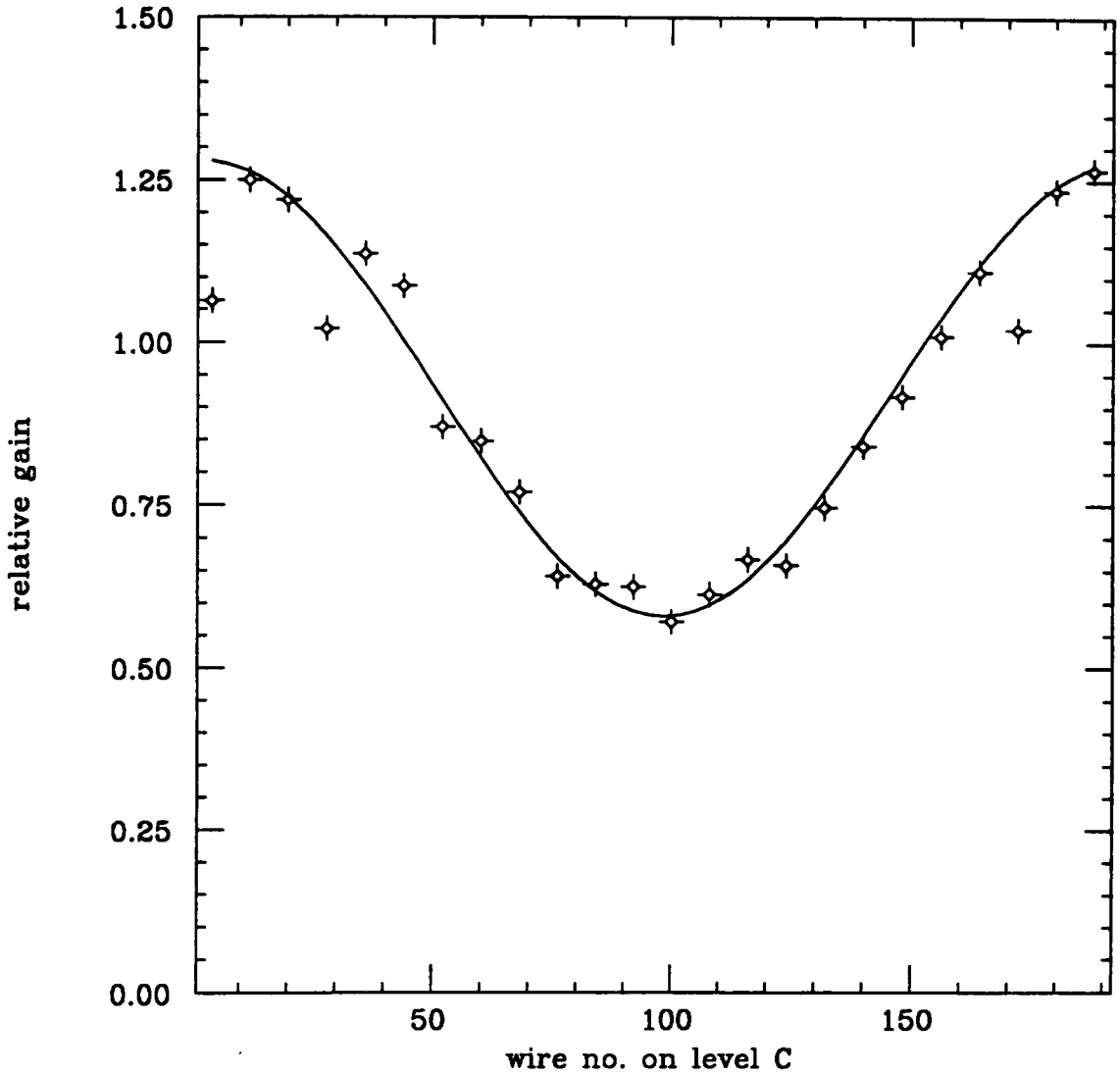

Figure 6.2: Profile of relative wire gain on level C. The data points each represent eight adjacent wires. The curve is a fit to an empirical function.

6.2.2 reduction cuts

Several different cuts were investigated for use at reduction time. The goal is to use as few and as loose cuts as possible, and still achieve the desired reduction factor. A cut on the thin scintillator pulse amplitude at about 2 MeV has already been imposed by the trigger hardware. Imposing this 2 MeV cut in software gets rid of a few events with plastic hits below 2 MeV, which leaked through the trigger. Greater reduction can be achieved by raising this cut, but in the interest of later analyzing three-body and four-body breakup events from the same reduced data set, this was not done.

The wire chamber pulse height information, on the other hand, has great potential for background discrimination. In order to exploit this information, track fitting must be performed first. This is because the electrons pass through the wire chamber at low angles, making long tracks in each of the wire levels. Thus, the low specific ionization of the electron is offset by the long path length in the wire cell, producing pulses similar in magnitude to those from heavy-ionizing protons passing through at 90° . Once the track fitting is performed, the pulse amplitude δE can be multiplied by $\sin\theta$ of the track to obtain dE/dx, which is independent of angle.

The reduction cuts may be summarized as the requirement that a *primary* track be found whose plastic hit amplitude exceeds 2 MeV, and whose wire dE/dx is over some threshold. The achieved reduction factor depends critically upon the choice of the dE/dx threshold. Since the amplitudes of the wire hits on all three levels are independent measurements of dE/dx, there are actually three wire dE/dx values. A variety of statistics may be derived from these three, such as the lowest, the highest, the mean, the average of the lowest two, etc. The simplest cut is simply to require all three values to be over some threshold. This is the same as placing a threshold cut on the lowest of the three. It was a surprise to discover that the minimum is a more powerful statistic than the mean, in this case. Henceforth the

minimum wire dE/dx will be referred to simply as the wire dE/dx.

In Fig. 6.3 is shown the wire dE/dx of the primary track for all events from one data tape, prior to reduction. The large peak below 0.5 keV/cm corresponds to electrons, and the peak at larger dE/dx corresponds to protons. The goal at reduction time was to pick a threshold which would reject most of the electrons, but still allow freedom in the choice of a final cut during later analysis. The arrow in the figure marks 0.7 keV/cm, which was the threshold chosen for reduction. The average number of raw events per tape was 460 000. This number was reduced to about 11 000 by the reduction cut, giving a reduction factor of 42.

6.3 Final Cuts

The complete set of cuts used in the analysis of the data is discussed in this section. The final cuts mask all earlier cuts, both those imposed by the hardware trigger, and those imposed during reduction; hence the justification of cut limits has been deferred until now. The cuts are incremental, in that a subsequent cut is imposed only upon the set of events which passed all previous cuts. Therefore the order of cuts is significant.

The goal of the cuts is to isolate those events which belong to the reaction $^4\mathrm{He}(\gamma,\mathrm{p})^3\mathrm{H}$. The signature of these events is the presence of two heavily-ionizing tracks with the proper angular correlation. The first cut is the implicit requirement that the tracks of both proton and triton fall within the geometric limits of the chamber, that the proton gets all the way to the plastic annulus, and that the triton penetrates at least as far as wire level C. This cut is implicit in that it is not adjustable, and its effects must be estimated from Monte Carlo.

The first explicit cut is the upper bound on the χ^2 of the linear fit to the proton and triton tracks. Shown in Fig. 6.4 is the distribution of χ^2_{xy} and χ^2_{xr} for primary tracks. The χ^2_{xy} spectrum is discrete because the (x,y) coordinates of wire hits are simply the locations of the wires that fired. Sometimes the wire hits line up exactly,

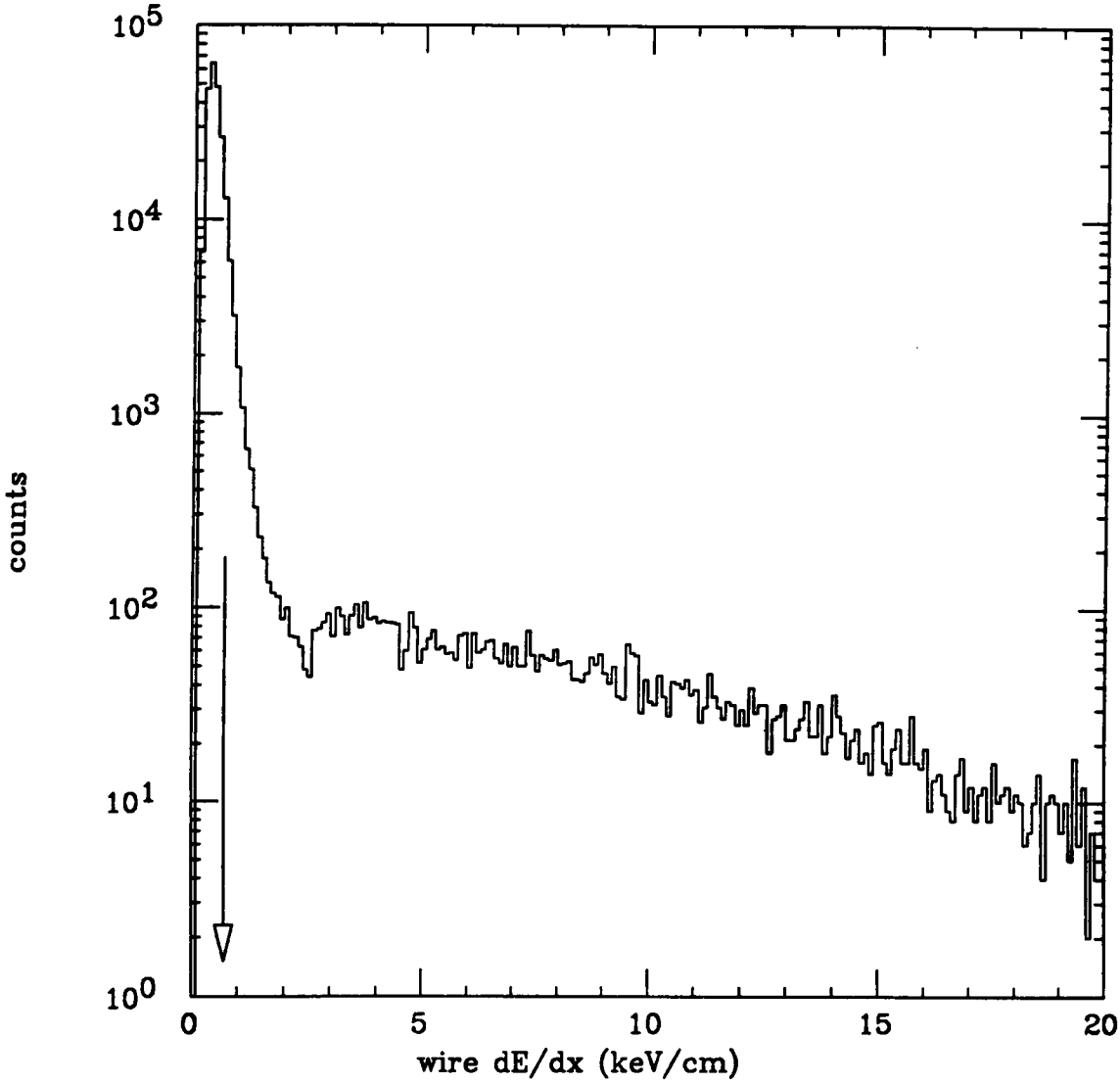

Figure 6.3: Spectrum of wire dE/dx of the primary track for all events from one tape. The large peak at low dE/dx is electrons. Protons (and other nuclear particles) are in the bump at higher dE/dx. The arrow shows where the cut was placed at reduction time.

sometimes one of the hits is one wire off, and so on. The standard deviations of the hit coordinates which are passed to the track-fitting algorithm were adjusted until the χ^2_{xy} spectrum was consistent with the χ^2 distribution with one degree of freedom, and the χ^2_{zr} spectrum was consistent with a χ^2 with two degrees of freedom. The additional degree of freedom in the zr fit is introduced by including the z of the plastic hit in the fit. The final choices were as follows:

$$\begin{aligned} \text{wire coordinates:} \qquad \sigma_x = \sigma_y &= 0.4 \text{ cm} \\ \sigma_z &= 1 + \left(\frac{1 \text{ keV}}{\delta E}\right) \text{ cm} \quad , \\ \text{plastic coordinate:} \qquad \sigma_z &= 3 \text{ cm} \quad . \end{aligned}$$

To test the track acceptance efficiency of the χ^2 cut, a series of analysis passes were done, varying the upper limit. The χ^2_{xy} and χ^2_{zr} limits were varied together, with the limit on the sum kept a factor of 3/2 higher. The data obtained in the elastic p-p scattering experiment at IUCF were used for this study because they provided a sample of protons uncontaminated with electron background. The results are plotted in Fig. 6.5. The number of tracks saturates in the limit of a large cutoff, indicating that 100% of the tracks are being accepted. The arrow in the figure indicates the placement of the final cut. A similar graph including electron tracks would not exhibit the saturation seen with protons, since multiple scattering makes the electron tracks rather crooked. The choice of a χ^2 cutoff as low as possible helps the analysis by rejecting a certain fraction of electron tracks.

A plot of the primary track angle for all events which passed the track-fit cut is shown in Fig. 6.6. The large peak at forward angles is the signature of electron background. The photodisintegration events give a broad distribution in track angle, centered somewhat forward of 90° . It is interesting to note that the requirement of a primary track below the χ^2 limits only gets rid of about 30% of the electromagnetic background events.

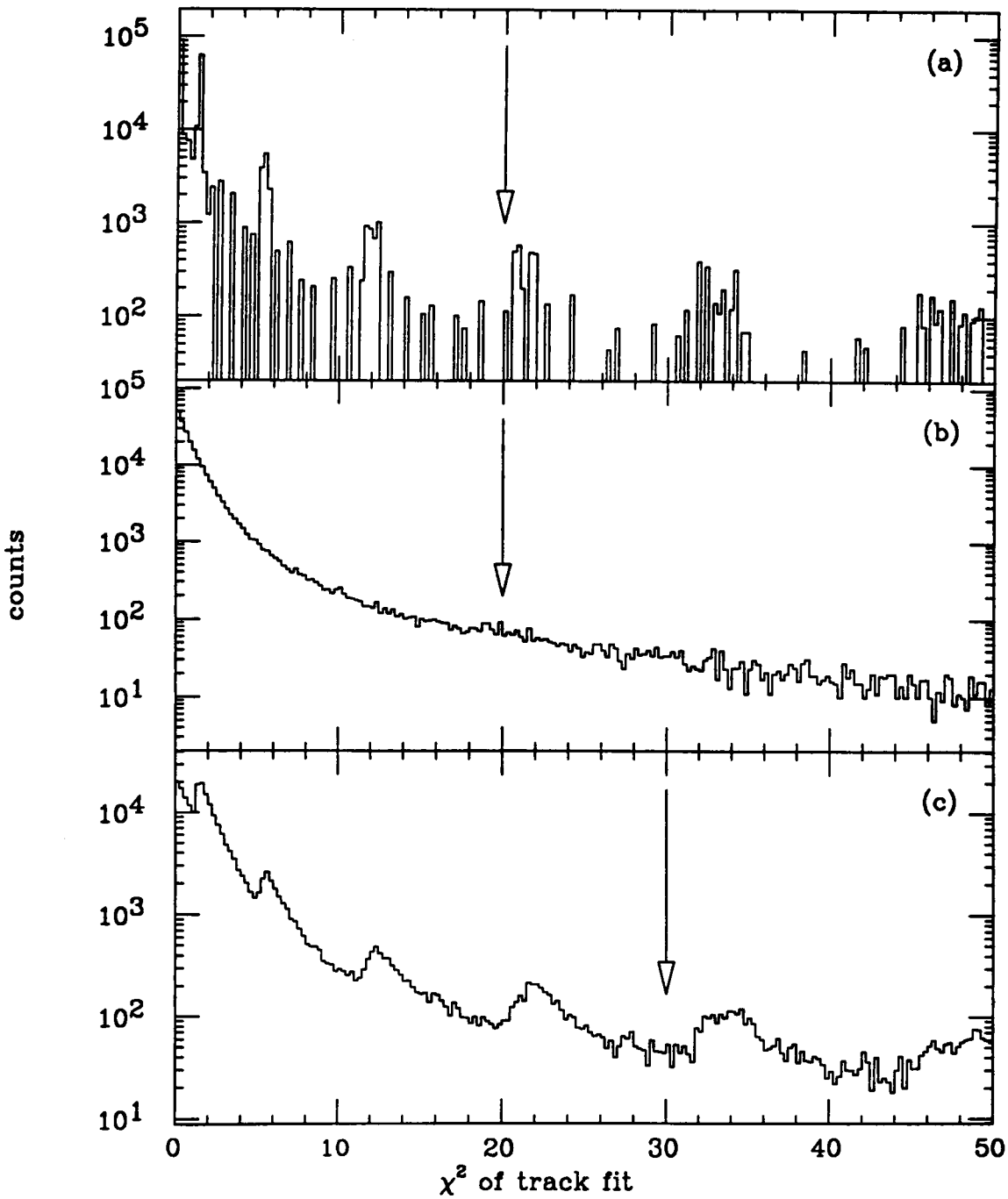

Figure 6.4: χ^2 of least-squares fit to primary tracks. (a) χ^2_{xy} of linear fit in the xy plane. (b) χ^2_{zr} of linear fit in the zr plane. (c) χ^2_{sum} of 2 two-dimensional fits. The arrows indicate where the final cuts were placed.

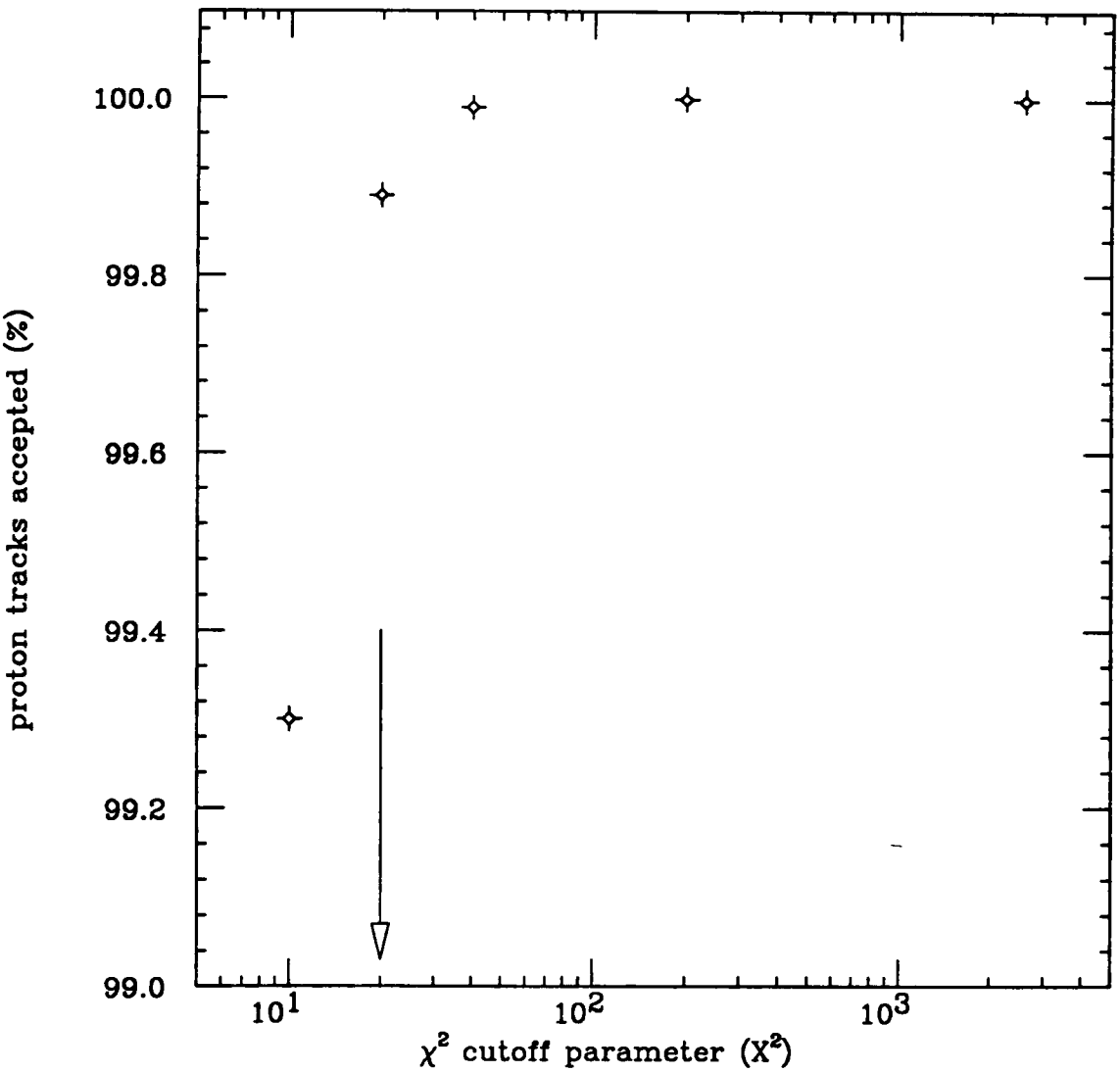

Figure 6.5: Efficiency for accepting proton tracks versus χ^2 cutoff. The χ^2 cuts required $\chi^2_{xy} < X^2$, $\chi^2_{zr} < X^2$, and $\chi^2_{xy} + \chi^2_{zr} < \frac{3}{2}X^2$. The arrow indicates the placement of the final cut.

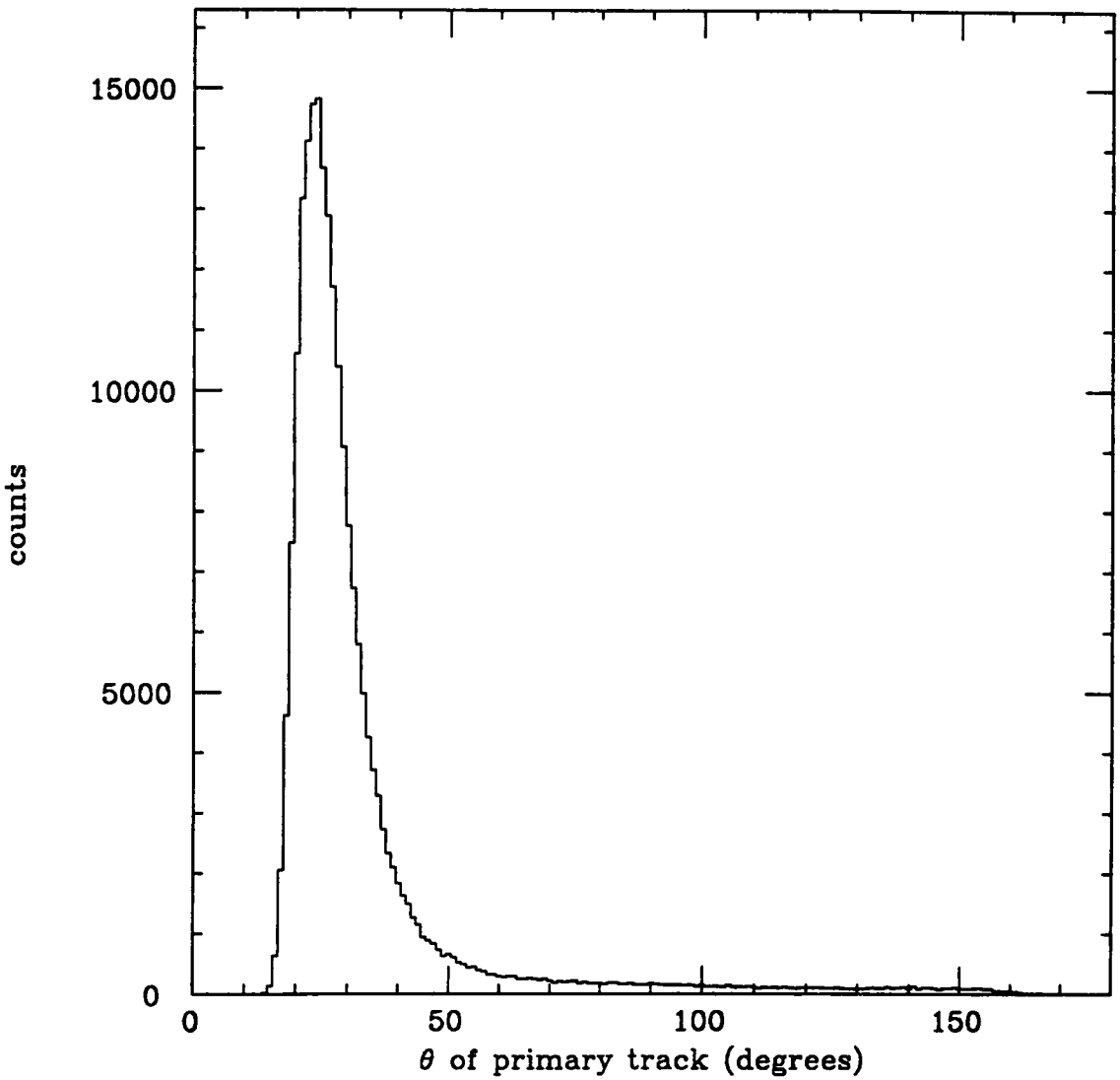

Figure 6.6: Theta (polar angle) spectrum of all primary tracks which passed the χ^2 track-fit cut. Most of the tracks are at very shallow angles, indicating that they are electrons.

Along with the parameters of the particle tracks, the track fitter also calculates an estimate for the event vertex. Since the beam is confined to the region near the detector axis, a cut on the radial coordinate of the vertex can be made without losing photonuclear events. This cut is very efficient for eliminating cosmic ray events, and a certain percentage of electrons are eliminated as well. In Fig. 6.7(a) is shown the distribution in x of the vertex for all events. After imposing all of the cuts to be discussed below, which eliminate background electrons, another histogram of the x of the event vertex was formed. This histogram, shown in Fig. 6.7(b), contains mainly protons from photodisintegration. The arrows in the figure show the placement of the final cut at 6 cm on the vertex radius.

To check how many photodisintegration events are being eliminated by the vertex radius cut, several analysis passes were performed, varying the cut. The results are shown by the points in Fig. 6.8. The curve in Fig. 6.8 is the result obtained using a Gaussian beam profile, with a rms radius of 2 cm. More photodisintegration events fall outside the radius cut than predicted by the curve. This is explained by assuming some error on the vertex estimate obtained from the track fitter. It is clear from Fig. 6.7 that this cut rejects a significant number of background electron events.

The next cut to be imposed is the threshold on the wire dE/dx. In Fig. 6.9(a) is shown the wire dE/dx for primary tracks (electrons + protons.) Just below in Fig. 6.9(b) is shown the same for secondary tracks (electrons + tritons.) Note that the combination of larger mass and lower energy make the tritons about 7 times as heavily-ionizing as the protons. For a wire dE/dx spectrum free from electron background, see Fig. 4.7, which contains 35 MeV protons from the IUCF data. The arrows in Fig. 6.9 indicate where the final dE/dx cut was placed, at 1.0 keV/cm. Note that this cut masks the reduction cut, which was 0.7 keV/cm.

In order to determine the best place for the wire dE/dx cut, a series of analysis passes was done using different thresholds. The results are shown in Fig. 6.10.

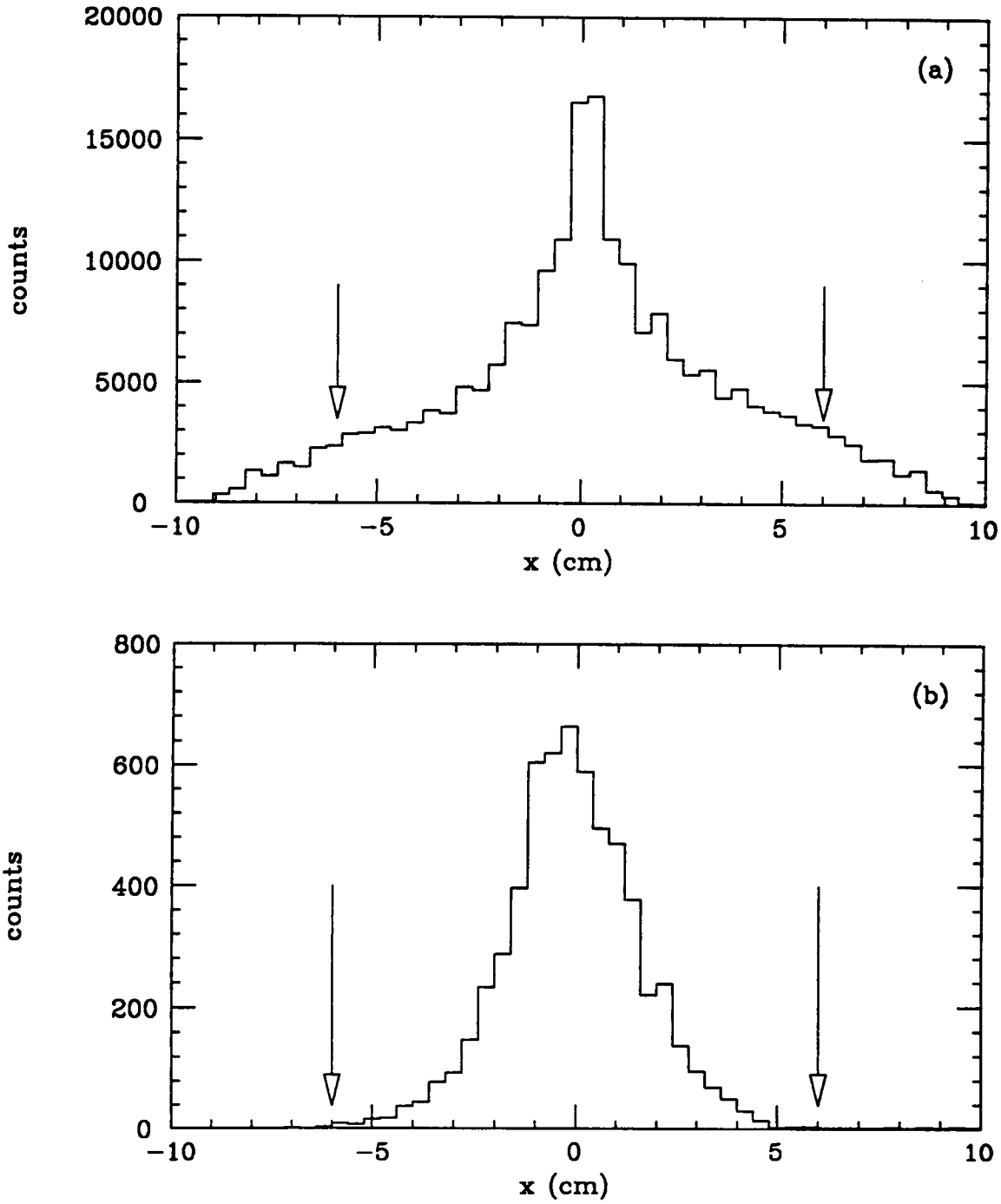

Figure 6.7: Profile of photon beam along x axis, obtained by histogramming the x coordinate of the track vertex. (a) All events with tracks are included. (b) Only proton events are included. The arrows indicate the placement of the final cut.

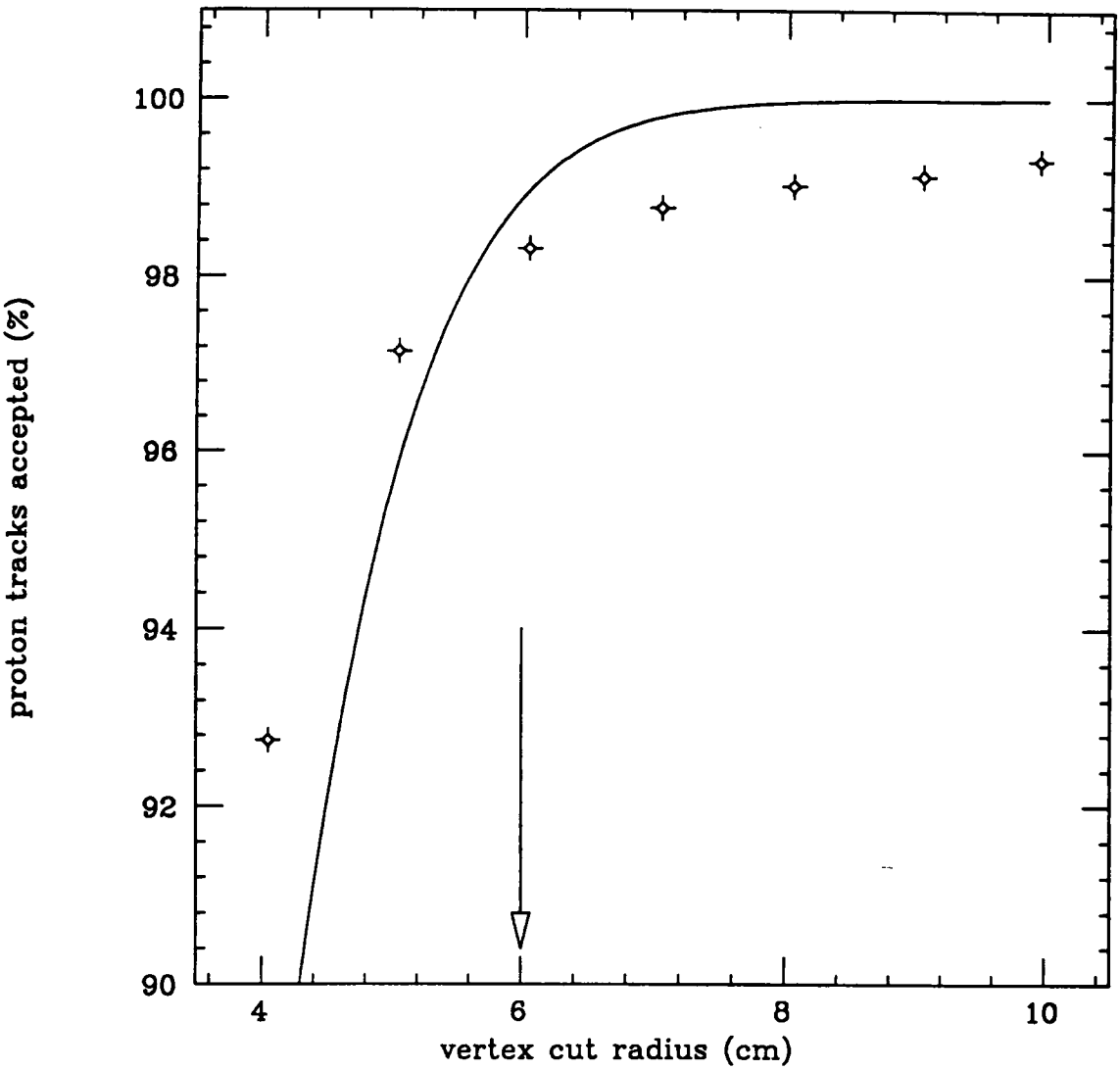

Figure 6.8: Efficiency for accepting proton events versus vertex cut radius. The points were obtained from the data, using cuts to eliminate background electrons from the sample. The curve is the expected behavior, assuming a Gaussian beam with a rms radius of 2 cm. The arrows indicate the placement of the final cut.

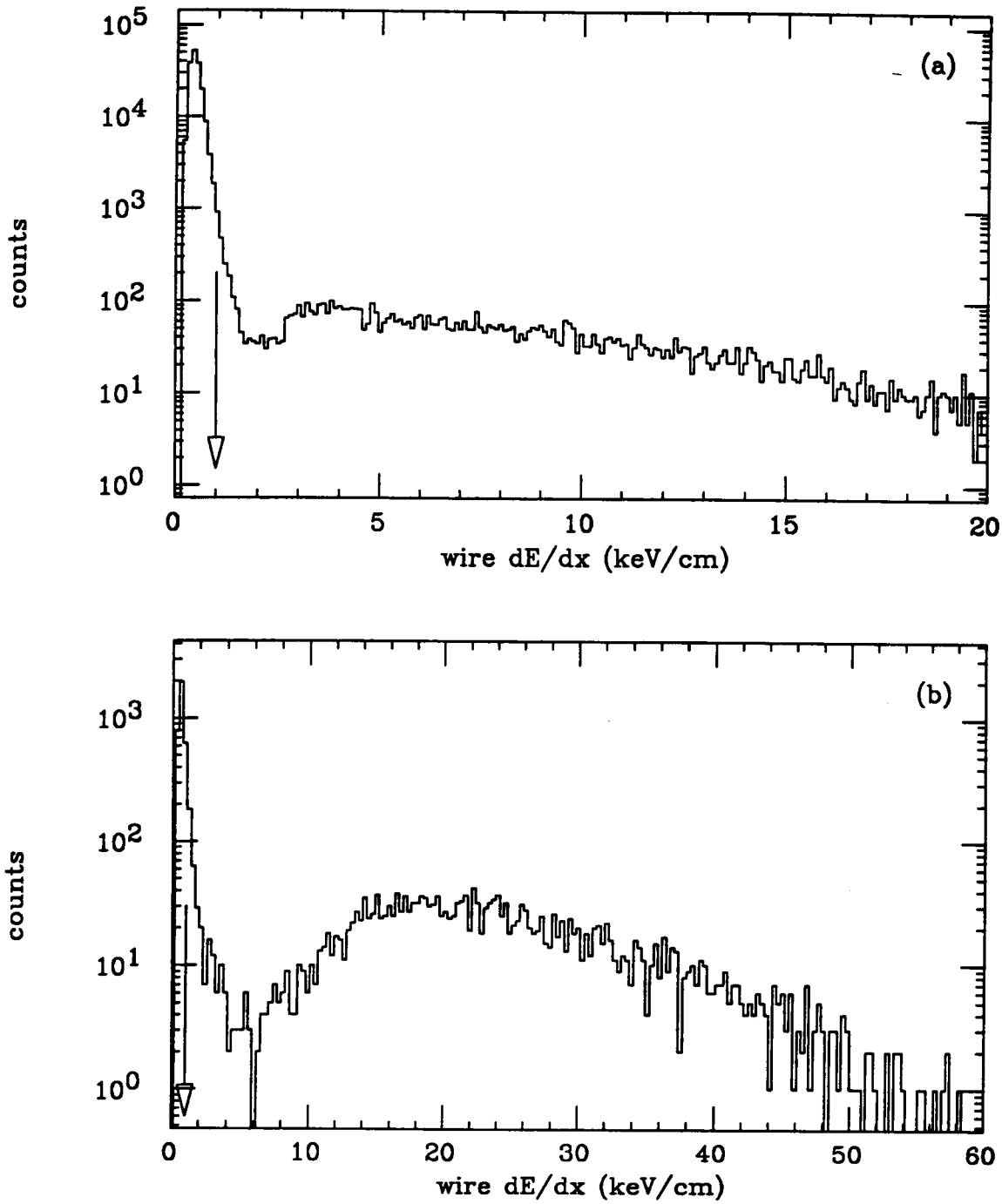

Figure 6.9: Wire dE/dx for all events which passed the track and vertex cuts. (a) The dE/dx spectrum of primary tracks (electrons + protons). (b) The dE/dx spectrum of secondary tracks (electrons + tritons). The arrow indicates the placement of the final cut.

This scan was done using the IUCF data, since it provided a sample of protons uncontaminated with electrons. The same cut was applied to all tracks, both primaries and secondaries. Figure 6.10 provides for this cut for the case of protons. Since the tritons are so much more heavily-ionizing than the protons, a justification for imposing the same threshold on the triton tracks was not necessary.

The next cut to be imposed is a threshold on the plastic pulse amplitude. This is divided into two cuts: one on the plastic dE/dx, and one on the total E. The plastic dE/dx is defined as the light amplitude (in electron-equivalent MeV) $\times \left(\frac{\sin\theta}{0.318\ \mathrm{cm}}\right)$. This quantity is only meaningful if the particle penetrated through the thin into the thick scintillator before it stopped. As can be seen from Fig. 5.3, this is true for most of the protons, and can be used in a similar way as the wire dE/dx to reject electrons. A plot of plastic dE/dx is shown in Fig. 6.11, including all events which passed the previous cuts. Plastic dE/dx is not available for tritons, since they do not make it through the thin scintillator.

The arrow in Fig. 6.11 indicates where the final cut was placed. The justification for this cut is shown in Fig. 6.12. Similar to the case of wire dE/dx, this data was derived from a study of proton tracks in the IUCF experimental data. The cut threshold at 8 MeV/cm was chosen, the point where a significant number of protons began to be lost. This cut is powerful for rejecting background events in which the electron left signal in both the thin and thick scintillators.

The plastic total pulse amplitude is shown in Fig. 6.13(a), for all events which passed previous cuts. The total E was taken from the sum of the amplitudes in the thin and thick. In the case where an event had more than one primary track, as when both the proton and the triton make pulses in the plastic, only the one with the larger total is histogrammed. Thus Fig. 6.13 can be considered as a sum spectrum of protons from photodisintegration, plus miscellaneous tracks from background events. The peak centered at 25 MeV (light output) is identified as the two-body (γ, p) peak. The rest is from protons and deuterons from other channels,

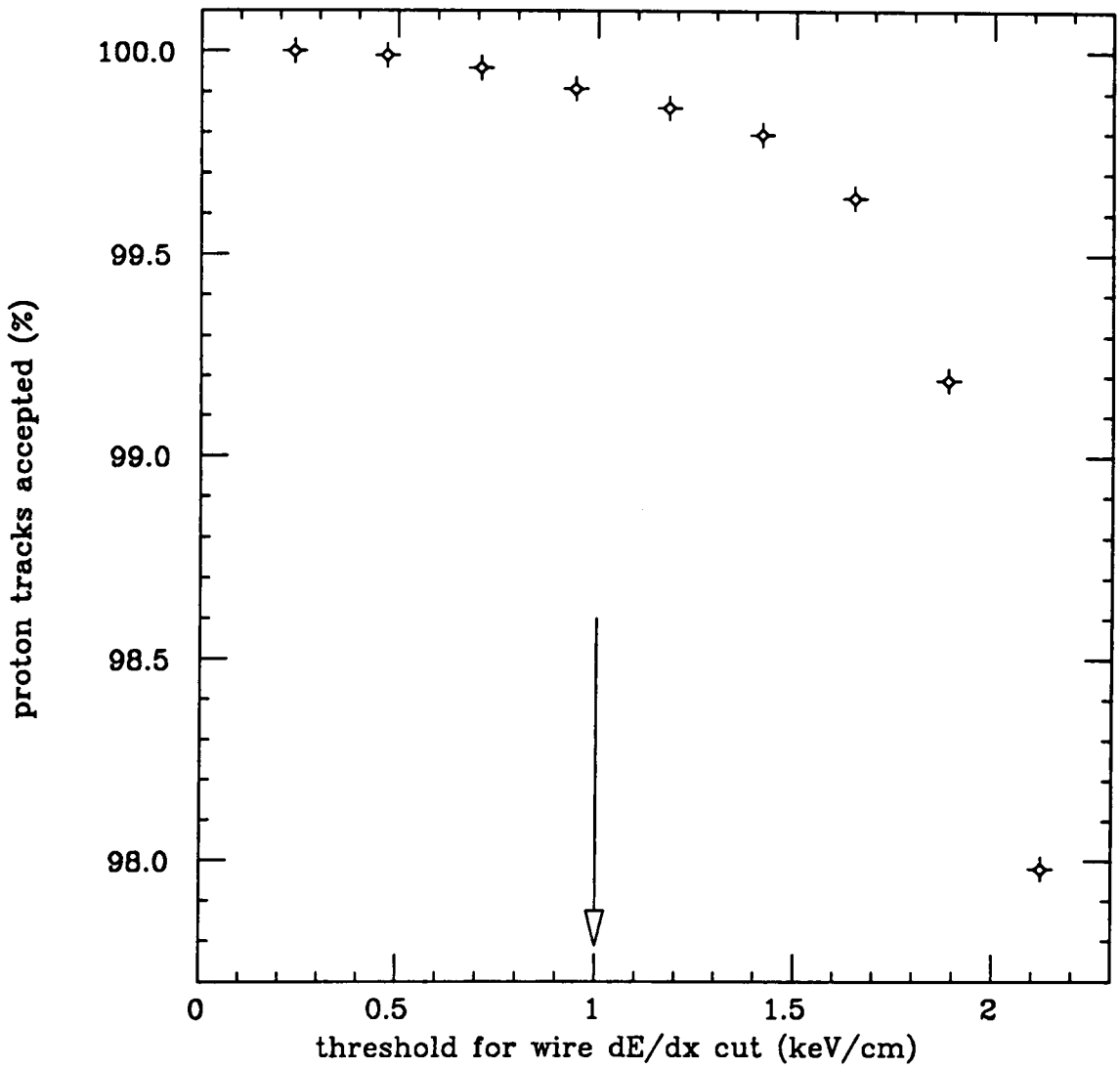

Figure 6.10: Efficiency for accepting proton tracks versus threshold for the wire dE/dx cut. The arrow indicates where the final cut was placed.

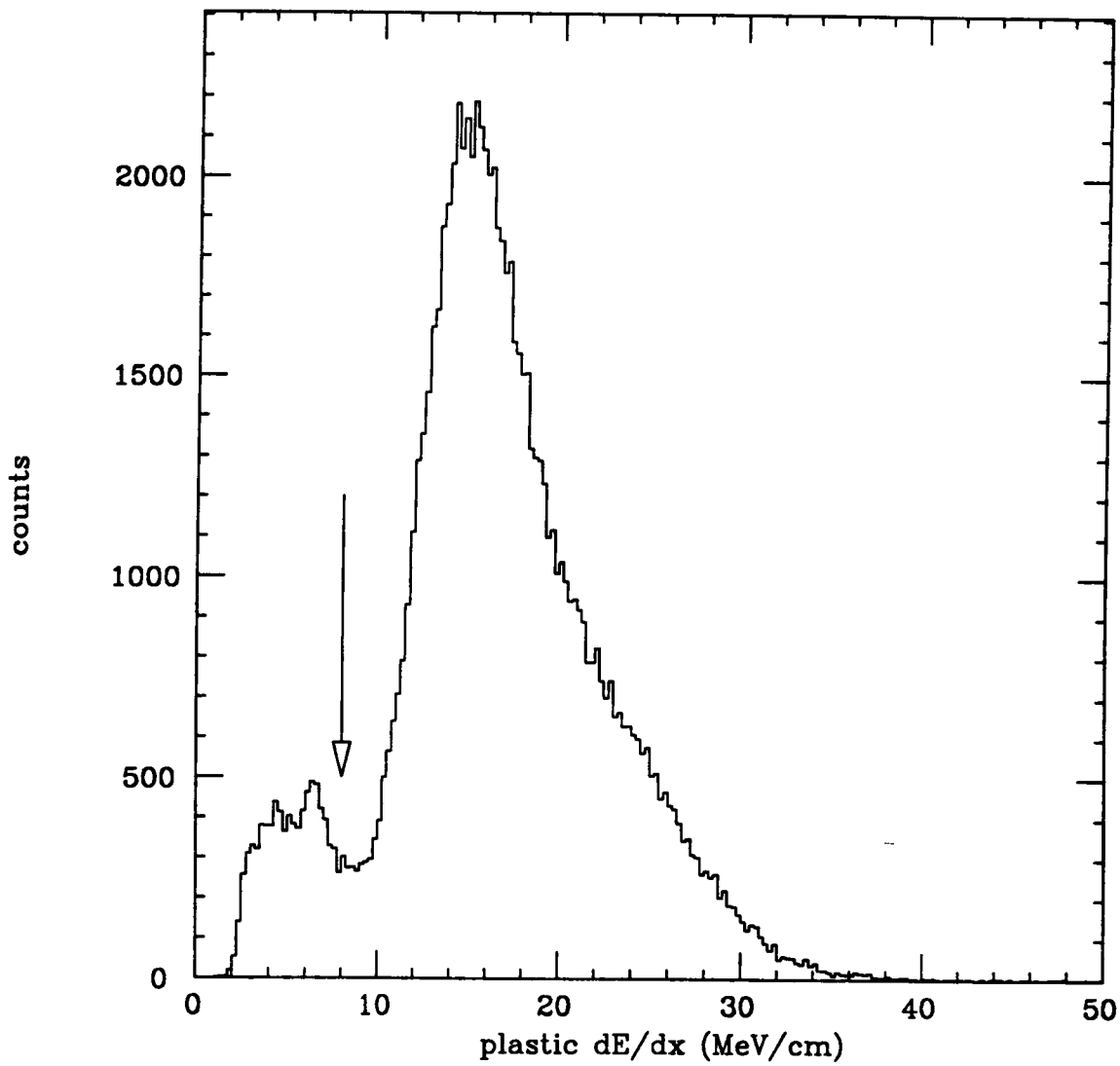

Figure 6.11: Plastic dE/dx of primary track for all events which passed earlier cuts. The main peak is protons. Electrons fall at lower dE/dx. The arrow indicates where the final cut was placed.

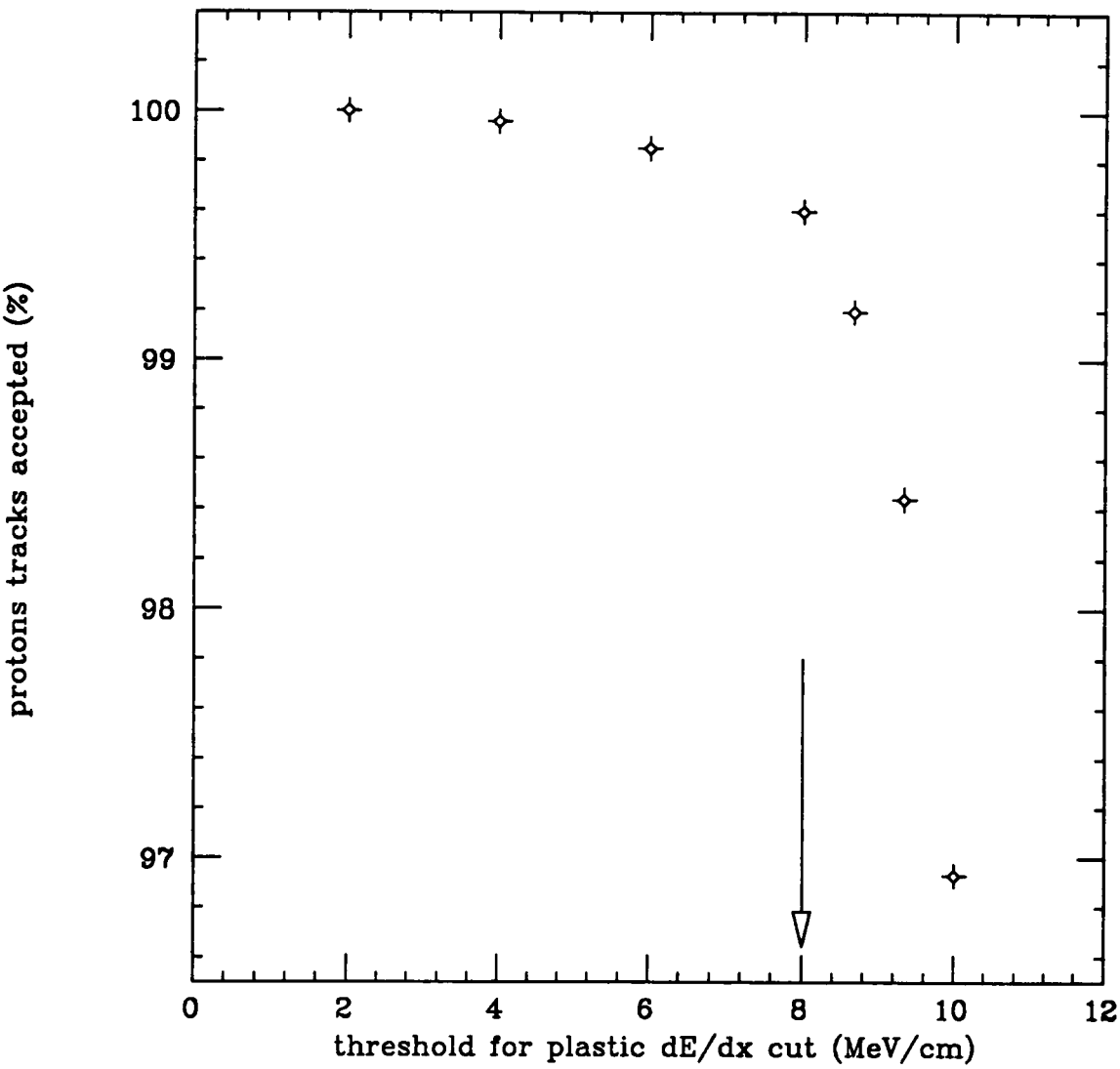

Figure 6.12: Efficiency for accepting proton tracks versus threshold of plastic dE/dx cut. The arrow shows the placement of the final cut.

and the remains of the electron background.

The plastic total E for 35 MeV protons, from Fig. 4.6, is shown for comparison in Fig. 6.13(b). The choice of a threshold cut for this quantity is rendered ambiguous by the long tail on the low side of the peak. This tail is due to the fact that some protons escape through the sides or ends of the scintillator, before they deposit all of their energy there. This problem is encountered in the calculation of the geometric acceptance of the detector (see Sec. 4.5.) There the question is how far the particle track must penetrate into a plastic scintillator without leaking out the side, before the track may be said to be within the geometric limits of the detector.

The choice was made, in the calculation of the geometric acceptance, to require that a particle track must have at least 0.8 cm of path length in the scintillator before it escapes, if it is to be accepted as within the detector geometric limits. For a proton of 35 MeV incident energy, this implies a minimum energy loss of 15 MeV in the plastic, corresponding to 13 MeV of light output. Therefore the plastic total E cut threshold was placed at 13 MeV. The resolution of the plastic total E, taken as the FWHM of the peak in Fig. 6.13(b) is 15% FWHM.

The cuts discussed so far are designed to select photodisintegration events over background. The task of separating the ^{4}He$(\gamma,\mathrm{p})^3$H events from those from other channels remains to be done. Since the ^{3}He particle from the reaction ^{4}He$(\gamma,\mathrm{n})^3$He cannot make the plastic total E cut, and the cross section for the reaction ^{4}He$(\gamma,{}^2\mathrm{H})^2$H is a factor of nearly 500 (see Table 1.2) smaller, the reaction ^{4}He$(\gamma,\mathrm{p})^3$H is the only two-body photodisintegration channel observable within the statistics of this experiment. Thus two-body kinematics may be exploited to eliminate events from the reactions ^{4}He$(\gamma,\mathrm{pn})^2$H and ^{4}He(γ,ppnn).

In order to exploit cuts based upon two-body kinematics, it is necessary to only analyze events with two tracks. The first track must be a primary, and must pass all of the cuts described above. The second track may be a primary or a secondary.

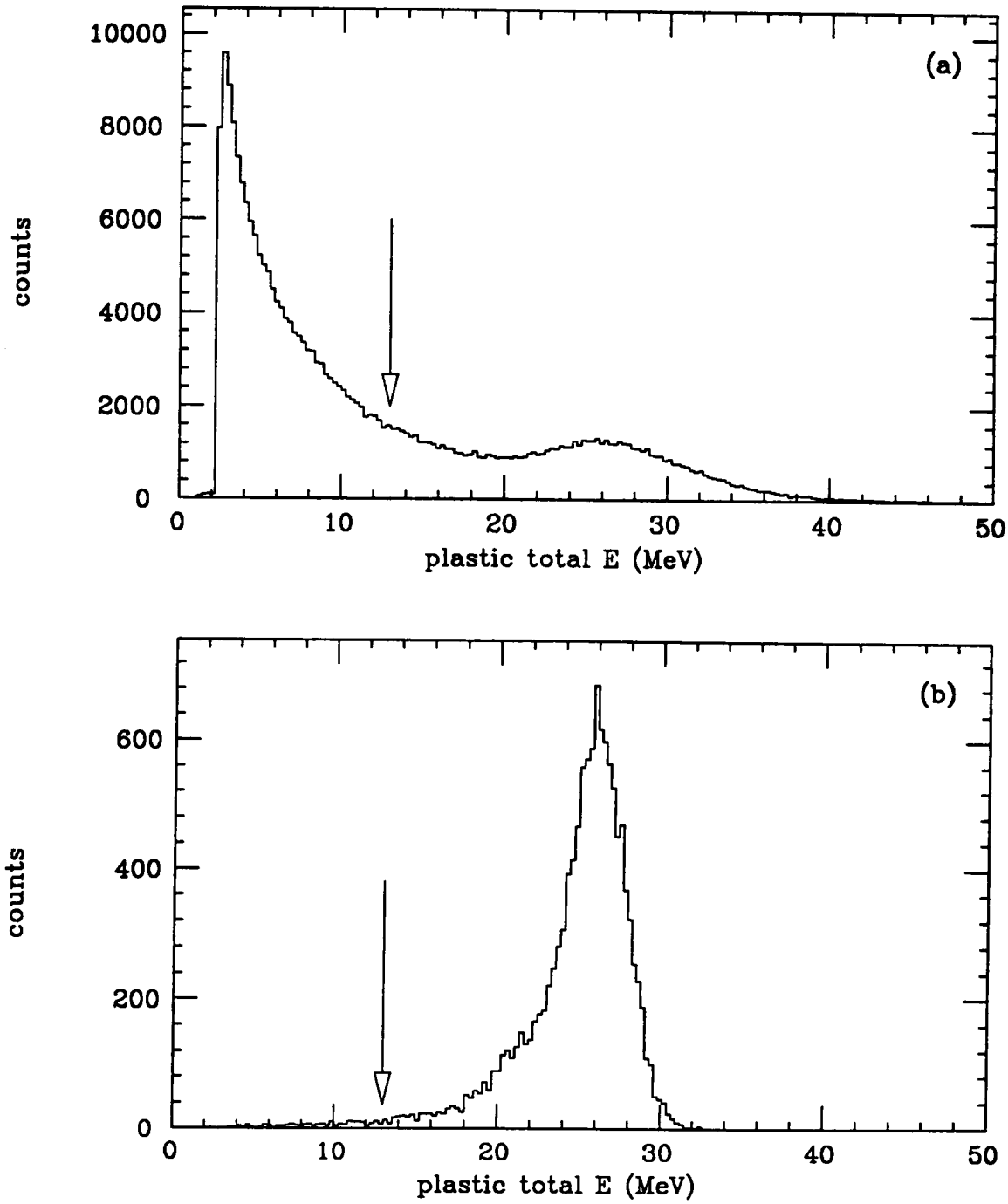

Figure 6.13: Spectrum of plastic total amplitude $\Delta E + E$. (a) Plastic total E of primary tracks from all events which passed earlier cuts. The bump at 25 MeV is protons from the ^{4}He$(\gamma, \mathrm{p})^3$H reaction, the rest is protons from other channels and miscellaneous background. (b) Spectrum from Fig. 4.6, included for comparison. The arrow shows where the final cut was placed.

It is subjected to all but the plastic dE/dx and total E cuts. In Fig. 6.14(a) is shown the difference $\phi_1 - \phi_2$ in the azimuthal angle ϕ between the first and the second track. The peak at 180° contains all of the two-body events, since kinematics requires the tracks to be back-to-back in the xy plane. This peak sits upon the broad distribution of three-body and four-body events, whose tracks are not kinematically confined to a plane.

Figure 6.14(b) shows $\phi_1 - \phi_2$ from the IUCF p-p scattering data. This sample contains only two-body events, and shows the ϕ resolution of the detector. The arrows show where the two-body cut is made on $\phi_1 - \phi_2$. A similar cut can also be made on the relative polar angle between the two tracks, $\theta_1 + \theta_2$. Due to the motion of the center of mass, this quantity peaks somewhat lower than 180° . In Fig. 6.15(a) is shown the $\theta_1 + \theta_2$ spectrum prior to the ϕ cut. Figure 6.15(b) shows the same spectrum after the ϕ cut. The arrows indicate where the final $\theta_1 + \theta_2$ cut was placed.

To investigate the best placement for the cuts on $\theta_1 + \theta_2$ and $\phi_1 - \phi_2$, a series of analysis passes were taken with varying window widths. The results are shown in Fig. 6.16. The two-body event acceptance efficiency for the ϕ cut, shown in Fig. 6.16(a), was determined using the p-p scattering data from IUCF. This data was not suitable for evaluating the θ cut, however, because the $\theta_1 + \theta_2$ for p-p events peaks at 90° . Therefore, it was necessary to use the photodisintegration data itself. The $\phi_1 - \phi_2$ cut window was temporarily narrowed to 180° ± 2°, and the width of the $\theta_1 + \theta_2$ window was varied to find the best place for the cut. The results of this scan are shown in Fig. 6.16(b).

Up to this point, no use has been made of the information available from the monochromator. For those events arising from a photon in true coincidence (as opposed to random coincidence) with the tagger, the focal plane timing measures particle time-of-flight for all primary tracks. The monochromator timing spectrum is a histogram of the time difference $t_{mono} - t_{trigger}$. The shorter particle time-of-

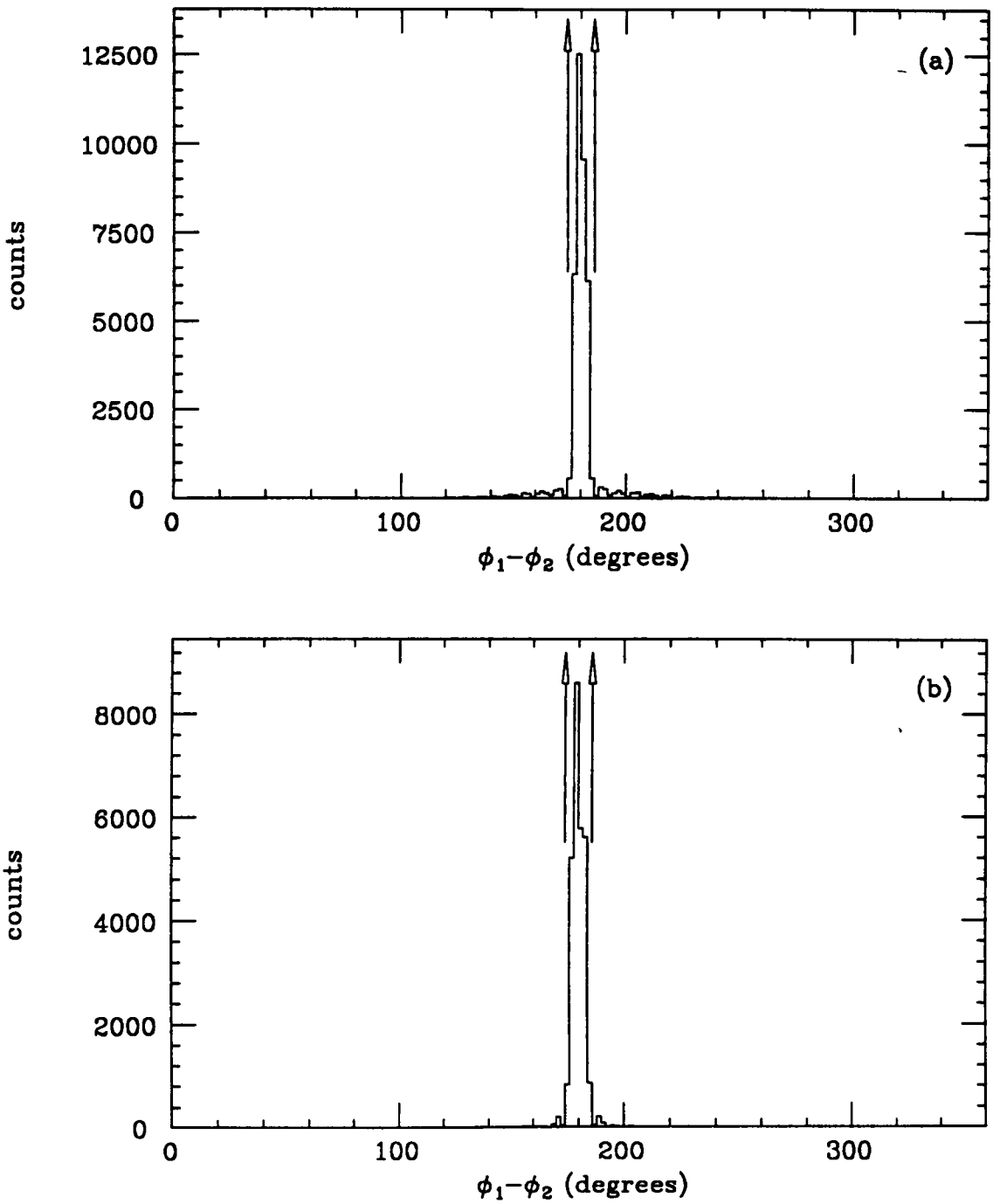

Figure 6.14: Spectrum of $\phi_1 - \phi_2$ for two-track events which passed earlier cuts. (a) The full spectrum of $\phi_1 - \phi_2$, showing two-body peak sitting on the continuum from three-body and four-body events. (b) The spectrum from p-p scattering,taken from the IUCF data. The arrows indicate the placement of the final cut.

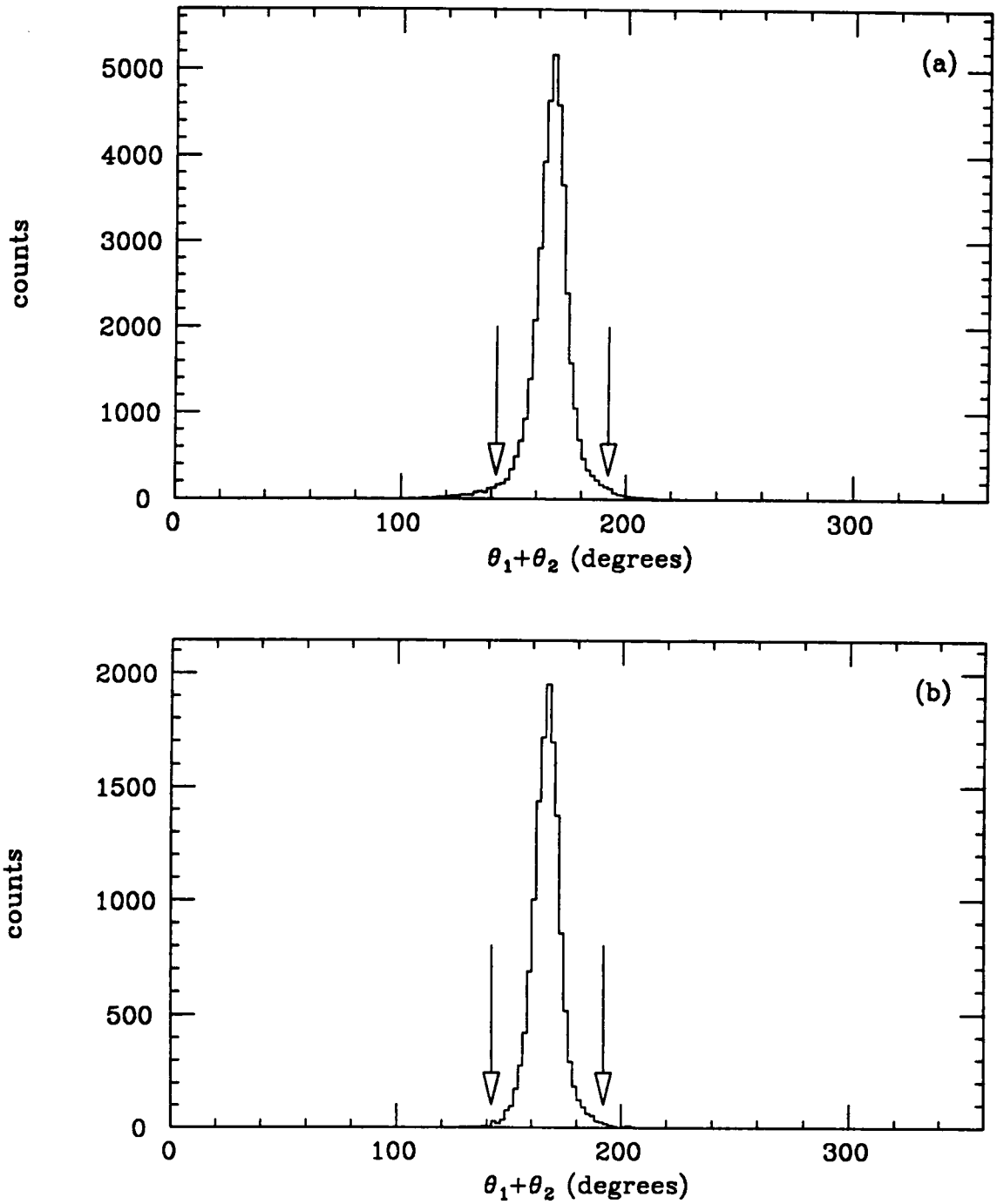

Figure 6.15: Spectrum of $\theta_1 + \theta_2$ for two-track events. (a) The full spectrum of $\theta_1 + \theta_2$, prior to the cut on $\phi_1 - \phi_2$. (b) The spectrum of $\theta_1 + \theta_2$ after the $\phi_1 - \phi_2$ cut has been imposed. The arrows indicate the placement of the final cut on $\theta_1 + \theta_2$.

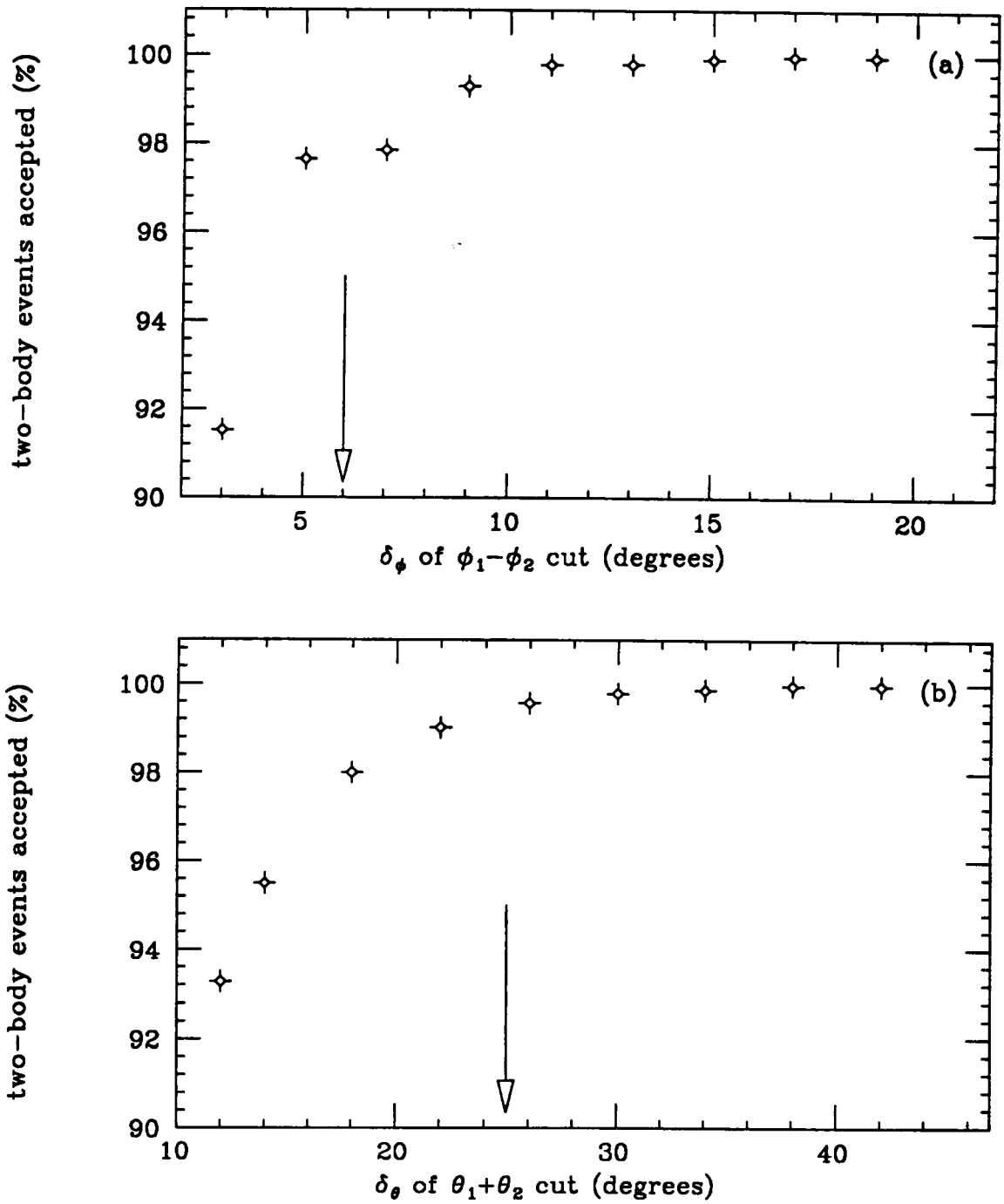

Figure 6.16: Efficiency for accepting p,^{3}H photodisintegration events versus window widths for the two-body angular correlation cuts. (a) Efficiency for the $\phi_1 - \phi_2$ cut: $(180° - \delta_\phi) \leq (\phi_1 - \phi_2) \leq (180° + \delta_\phi)$. (b) Efficiency for the $\theta_1 + \theta_2$ cut: $(167° - \delta_\theta) \leq (\theta_1 + \theta_2) \leq (167° + \delta_\theta)$. The arrows show the placement of the final cuts.

flights appear to the right in the monochromator timing spectrum, time-of-flight being measured from the instant of bremsstrahlung in the photon converter until the instant of the hit in the plastic scintillator. With the large difference in speed between electrons and protons, this spectrum provides an instant count of the different types of events.

In Fig. 6.17 is shown the monochromator timing spectrum at different stages along the cuts pipeline. Figure 6.17(a) shows the raw spectrum, including all events from a single tape. The large peak is identified as electrons. The flat background is due to random coincidences. The monochromator timing spectrum reveals nothing about the nature of the random events, and an event-by-event separation between true coincidences and randoms is not possible. The cuts discussed above eliminate background events without regard to whether they are true coincidences or randoms. The elimination of randoms must be put off until the last step (see Sec. 6.4.)

Figure 6.17(b) shows the monochromator timing spectrum after the track-fit and wire dE/dx requirement are imposed. Note that a second peak, corresponding to protons, has emerged from the background after these cuts. Since the statistics on a single tape are poor after these cuts are imposed, the full set of 34 tapes have been added together. The results after the plastic dE/dx and total E cut are shown in Fig. 6.17(c). The final monochromator timing spectrum, after the two-body cuts are imposed as well, is shown in Fig. 6.18. Note that the coincident electron background has been effectively suppressed.

Virtually all of the events remaining in the analysis pipeline after the above cuts have been performed are p,^{3}H photodisintegration events. However not all of these correspond to gammas within the energy range of the tagger. The photon beam contains gammas of a continuum of energies, and many of the photodisintegrations involving lower energy gammas generate random coincidences with the monochromator, and so get into the data set. These are the dominant component of the

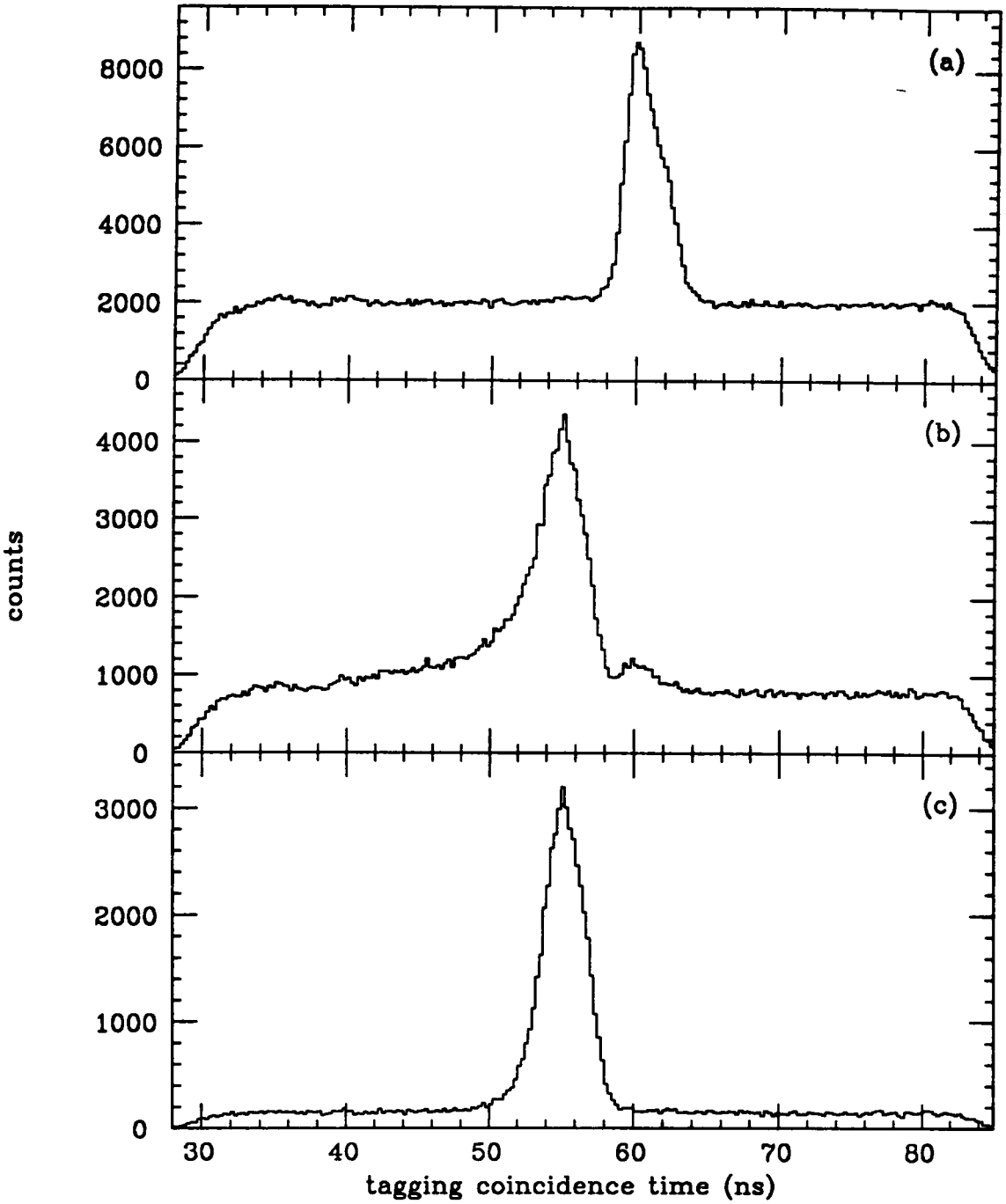

Figure 6.17: Monochromator timing spectrum obtained at various stages along the analysis pipeline. (a) Raw timing spectrum, with all events included. (b) Timing spectrum after track-fit and wire dE/dx cut. (c) Timing spectrum after plastic dE/dx and total E cuts.

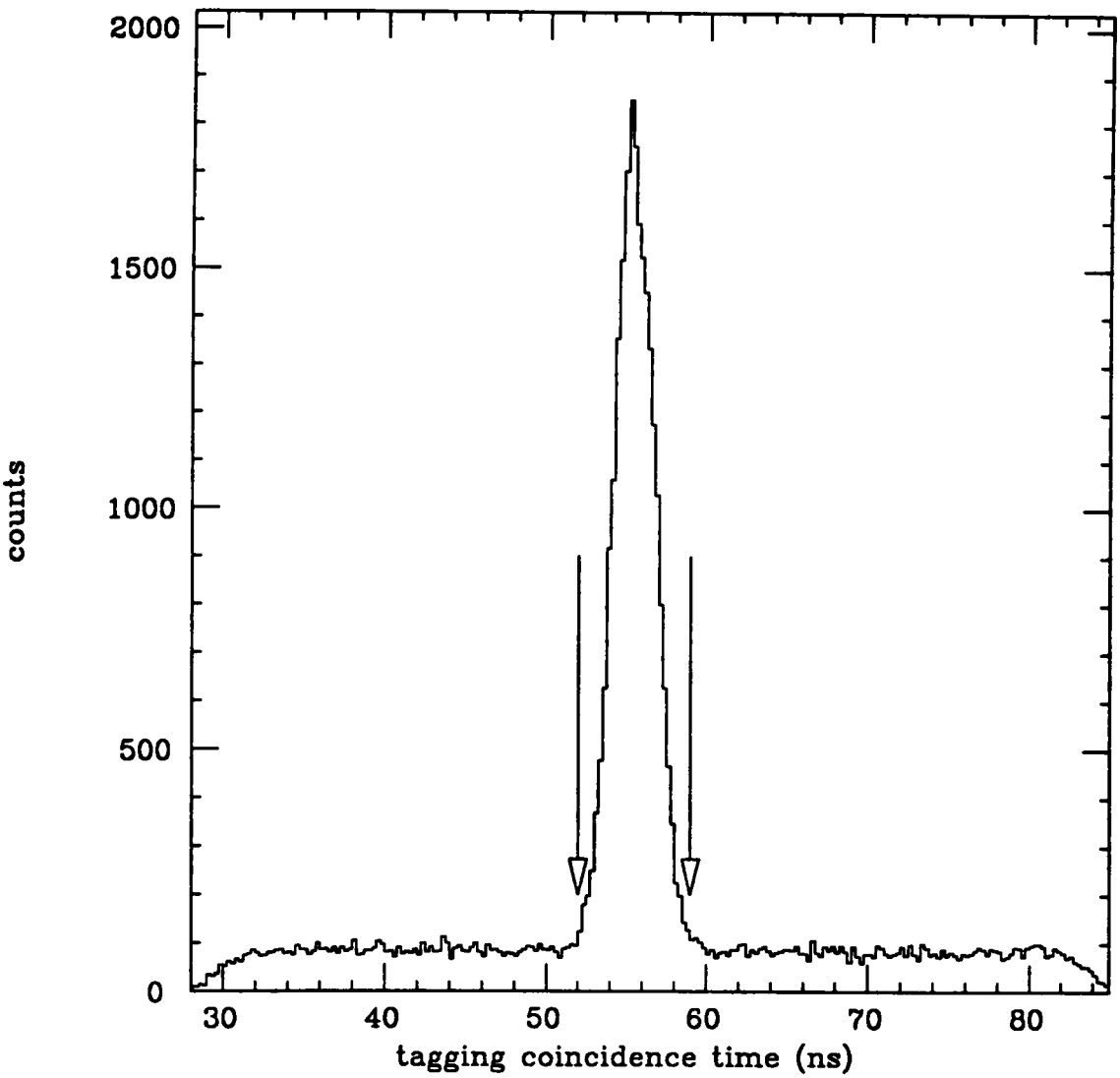

Figure 6.18: Monochromator timing spectrum after the full set of track cuts and the two-body cuts are imposed. The arrows show where the final cut was placed around the coincident proton peak.

flat background in Fig. 6.18. The sample of true coincidences can be enriched by excluding all events outside of the region of the coincidence peak.

The arrows in Fig. 6.18 indicate the boundaries of the window placed around the true coincidence peak. The width of the window was chosen so that just over 99% of the p,^{3}H events fall inside. In Fig. 6.19 is shown the percentage of p,^{3}H events contained within the coincidence window for various window widths. While there is nothing to prevent using a wider window and including the last 1%, the three-body and four-body events tend to fall on the left side of the peak (see Fig. 6.17(b)), so this cut helps to suppress them.

With all of the cuts in place, the amount of background which remains in the spectra can be ascertained. In the sequence of spectra in Fig. 6.17, the electron background which dominates the raw spectrum has nearly vanished after the cuts on plastic amplitude. After the two-body cuts, the bump from coincident electrons is not statistically significant, as can be seen from Fig. 6.18. To check for any remaining contamination from three-body and four-body photodisintegrations, an analysis pass was done with the $\phi_1 - \phi_2$ cut turned off. Three and four-body events will show up as a broad distribution in $\phi_1 - \phi_2$. The result is shown in Fig. 6.20 on a log scale, to highlight the tails of the distribution. The curve is a Gaussian fit, excluding the points inside the two-body peak. Of the 20 000 events within the two-body ϕ-cut window, about 560 are under the curve which estimates the contribution from three-body and four-body events. This leads to a contamination of 2.8% in the final spectra from competing photodisintegration channels.

In Fig. 6.21 is shown the angular distribution of proton tracks from all events within the true coincidence window. This spectrum still contains a few randoms; the amount of the flat background in Fig. 6.18 which extends under the true coincidence peak remains. In the next section is discussed the procedure for subtracting the contribution of randoms from Fig. 6.21. The following sections describe the detector efficiency correction, and the normalization, by which the angular distri-

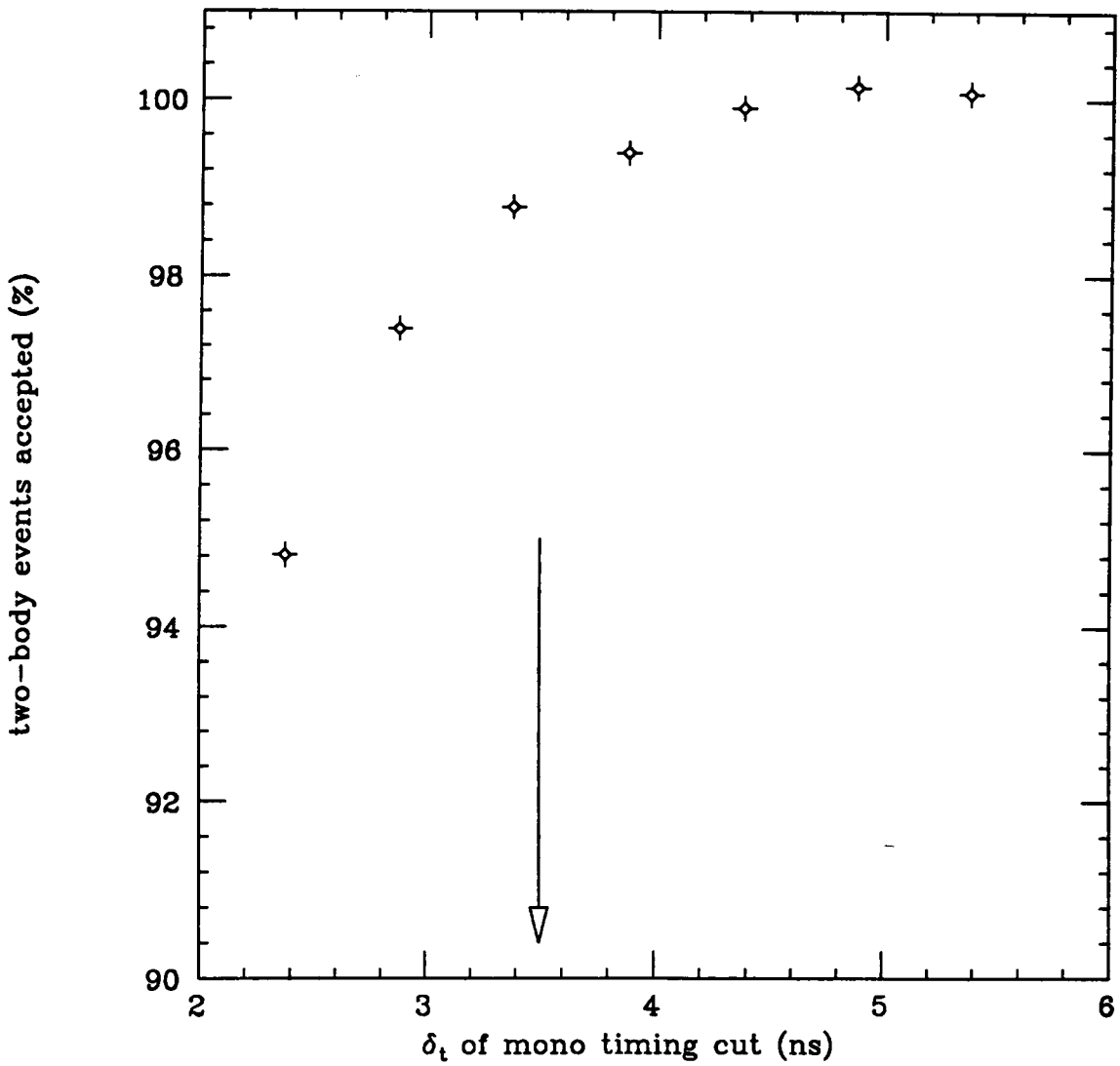

Figure 6.19: Efficiency for accepting p,^{3}H coincidence events versus the width of the coincidence window on the monochromator timing spectrum. The cut is defined as $(55 - \delta_t) \leq t_{mono} \leq (55 + \delta_t)$.

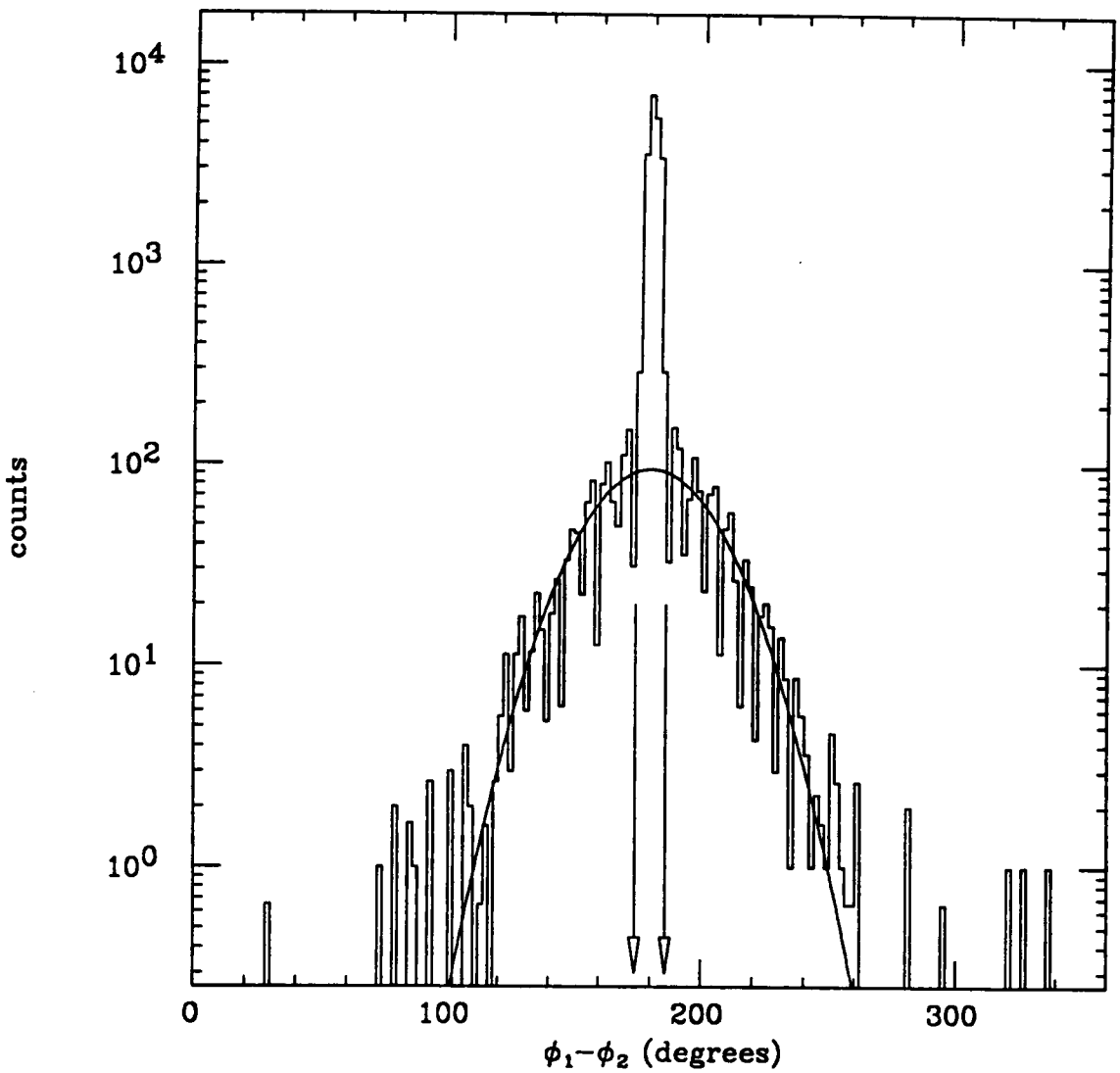

Figure 6.20: Contamination from three-body and four-body photodisintegrations, examined by loosening the $\phi_1 - \phi_2$ cut, and displaying the distribution of events outside the two-body peak. The curve is a Gaussian fit, excluding the points inside the cut-window, delimited by the arrows.

bution is transformed into a differential cross section. Henceforth, when an angular distribution or differential cross section is presented, it is given as a function of the polar angle θ of the *proton* track in the c.m. frame.

6.4 Random Subtraction

Discarding all of the events in Fig. 6.18 which lie outside of the window around the coincidence peak does not get rid of all of the random coincidences. The ones which lie inside the coincidence window remain, and are indisinguishable from true coincidences. Therefore, all of the events within the coincidence window must be included in the analysis up to the end, and then, as a last step, the contribution from the randoms can be subtracted from the spectra.

From the nature of randoms, their time distribution is exponential. The decay constant of the exponential is given by the reciprocal of the singles rate in the focal plane. With a singles rate per focal plane counter of 10^5 s^{-1}, the decay constant is 10^4 ns. Since the entire monochromator timing spectrum is only 50 ns wide, the distribution of randoms therein is essentially constant. Therefore, the number of randoms within the coincidence window may be calculated by multiplying the width of the window by the average height of the random background in the flat region outside of the coincidence peak. This is equivalent to drawing a line at the level of the flat background across the entire timing spectrum, and integrating the coincidence peak above the line.

This gives a random-subtracted count of the total number of coincident p,^{3}H photodisintegration events. However, it is the angular distribution which is desired, and not simply the total count. The procedure for subtracting randoms from the angular distribution, shown in Fig. 6.21, (or any other spectrum) depends upon the fact that a sample of random-coincidence events has the same composition, no matter where it is drawn from the monochromator timing spectrum. In the region to the right of the coincidence timing window, in Fig. 6.18, is placed a second

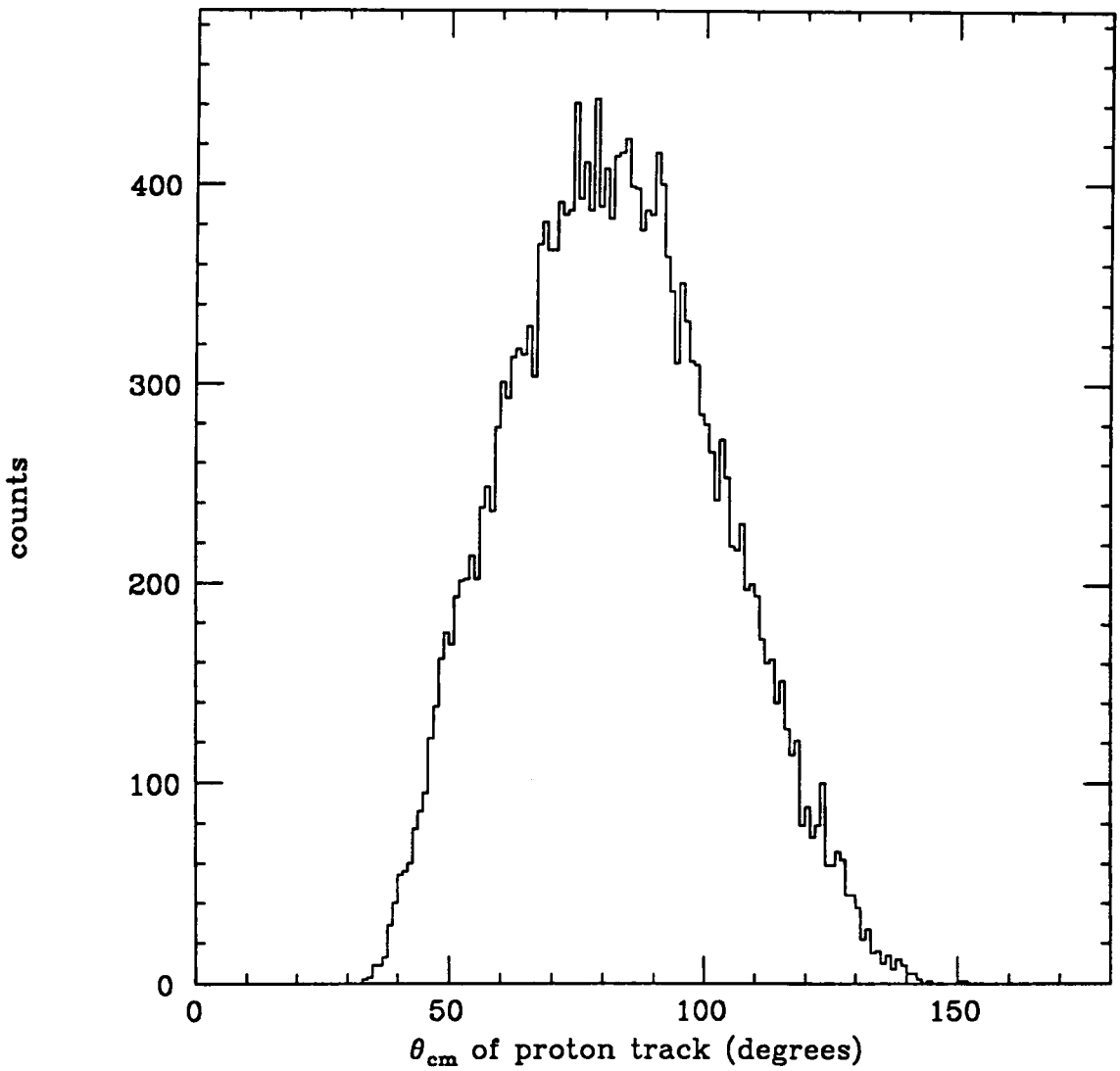

Figure 6.21: Angular distribution of proton tracks in the c.m. frame, from all events within the true coincidence window of the monochromator timing spectrum. The entire data set for this experiment is included in this spectrum.

window, called the randoms window. The angular distribution of events within this window is shown in Fig. 6.22. Properly scaling this spectrum by the ratio of the width of the coincidence window to that of the randoms window, and subtracting it from the coincidence angular distribution of Fig. 6.18 gives the random-subtracted coincidence angular distribution, shown in Fig. 6.23.

Up until the point of random subtraction, no calculation of the statistical error has been necessary, because all of the spectra contained a simple sum of counts. This is no longer true after random subtraction. Now the spectra are differences between sums of counts. Therefore when the randoms are subtracted, the statistical error on the difference is calculated from the errors of the original spectra. This is why the errors are shown explicitly in Fig. 6.23. Poisson statistics dictate that the variance of a random variable n, where n is a sum of counts, is estimated by n itself. The variance on the difference is therefore given by

$$W = C - \alpha R \quad \Rightarrow \quad V_W = V_C + \alpha^2 V_R \quad , \tag{6.1}$$

where α represents the ratio of coincidence to randoms window-widths. The width of the randoms window was chosen to be as wide as possible in order to minimize the statistical error introduced by the random subtraction.

6.5 Efficiency Correction

Throughout the analysis procedure, care was taken to quantify the acceptance efficiency of each cut for ^{4}He$(\gamma,\mathrm{p})^3$H events. This was done so that the final result can be corrected, and a reliable absolute cross section obtained. The efficiency correction is calculated under the assumption that the cuts are independent. This is equivalent to assuming that the losses are due to random fluctuations in the measurements, which is evidently the case. Under this assumption, the overall efficiency function is obtained as a product of the independent efficiencies. The total efficiency, represented by the function $\varepsilon(\theta)$, relates the measured angular

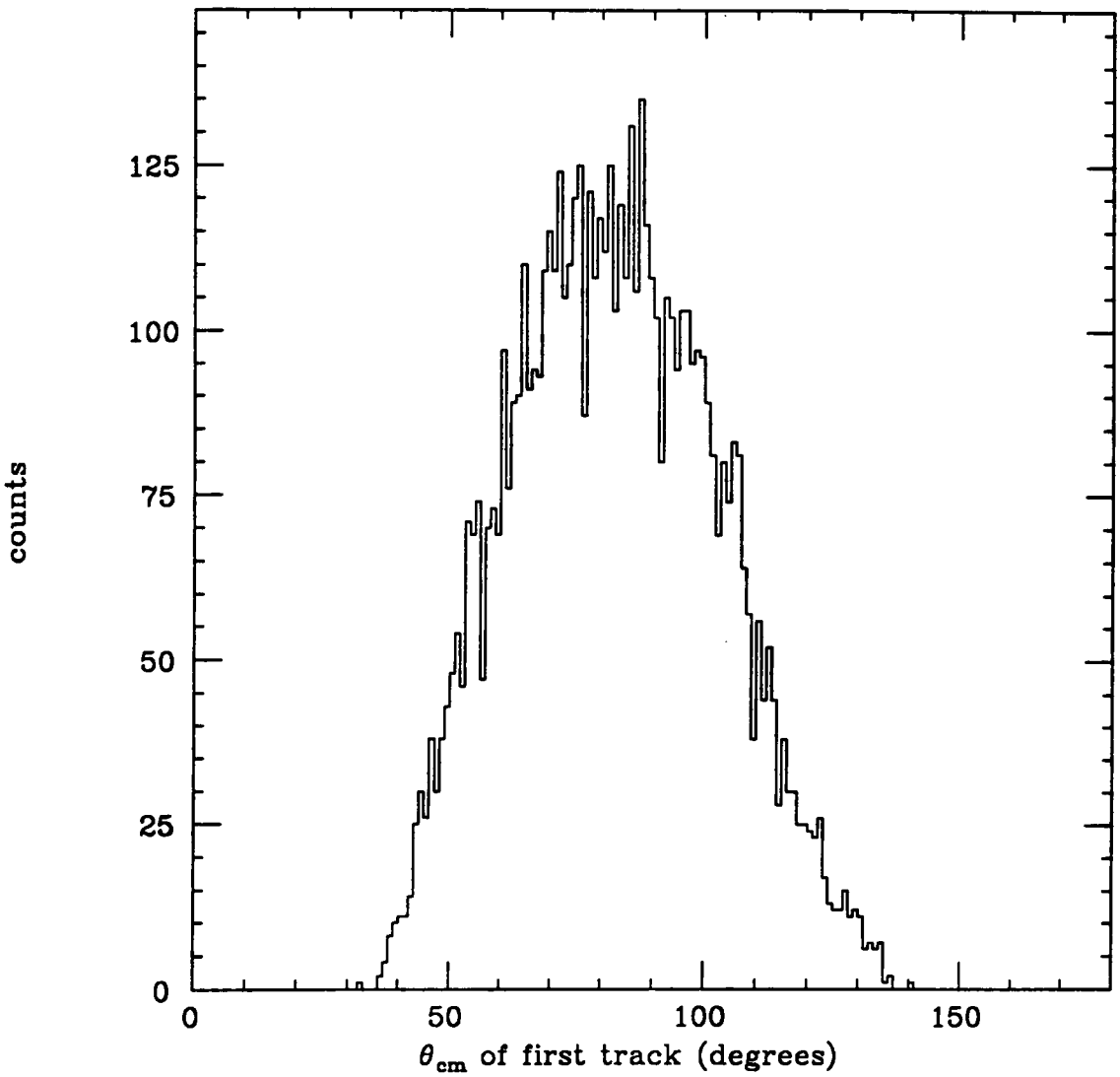

Figure 6.22: Angular distribution of events in random coincidence with the monochromator.

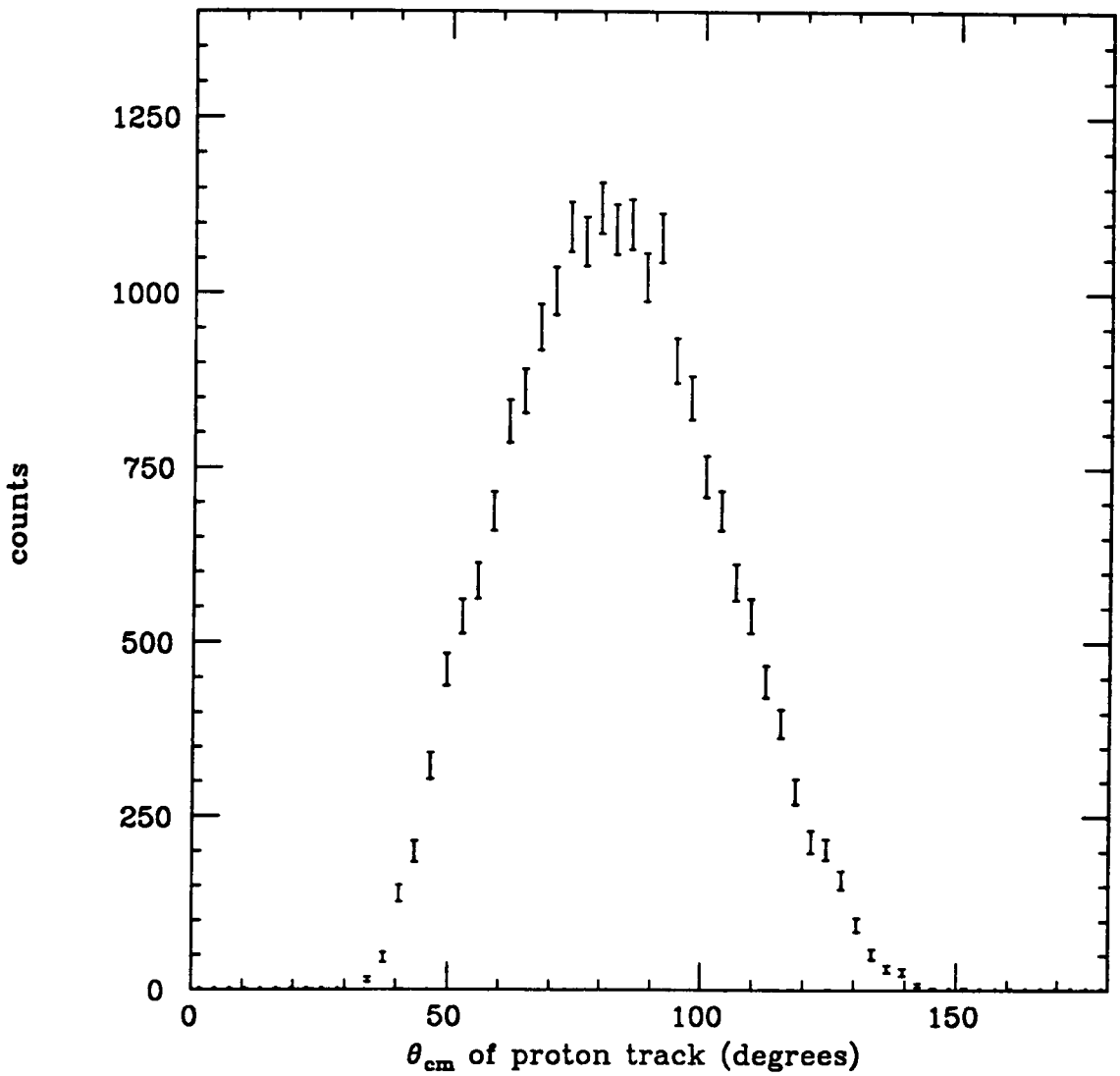

Figure 6.23: Angular distribution of coincident events, after the contribution from randoms has been subtracted. The error bars show the statistical error.

spectrum N_θ to the ideal spectrum $\mathcal{N}_\theta$, which would be obtained with a 100%-efficient device, as

$$N_\theta = \varepsilon(\theta)\mathcal{N}_\theta \quad . \tag{6.2}$$

This equation can be inverted to give $\mathcal{N}_\theta$ in terms of N_θ.

The total efficiency function is composed of a product of independent efficiencies as

$$\varepsilon(\theta) = \varepsilon_0(\theta)\, \varepsilon_1\, \varepsilon_2\, \varepsilon_3\, \cdots \quad . \tag{6.3}$$

Note that the geometric acceptance function $\lambda_2(\theta)$, introduced in Sec. 4.5 is not included in $\varepsilon(\theta)$. The geometric acceptance correction is included in the calculation of the target thickness, in Sec. 6.6.

The quantity $\varepsilon_0(\theta)$ in Eq. 6.3 represents the implicit requirement that both proton and triton must not be absorbed before they make complete tracks. To complete its track, a proton must reach the plastic annulus with enough remaining kinetic energy to pass the plastic total E cut. A triton is only required to penetrate wire level C to complete its track. Once these requirements are met, all losses are accounted for by the explicit cuts outlined in Sec. 6.3.

The function $\varepsilon_0(\theta)$ is evaluated by Monte Carlo. The general technique was discussed in Sec. 4.6, so only the results are presented here. Protons and tritons of the correct energy were injected (Monte Carlo simulation) into the LASA detector from the axis of the target, at a series of angles θ. The azimuth ϕ of the track was permitted to vary randomly. The percentage of protons and tritons which made complete tracks, as defined above, is plotted in Fig 6.24. The error bars on the points are statistical. Note that the great majority of the protons pass the test, as expected. However, a significant fraction of the tritons are lost in the wire chamber, mainly from hitting wires.

The magnitude of this correction warrants a careful check of the fidelity of the Monte Carlo simulation. For this purpose, a series of analysis passes were performed through the actual data, relaxing the requirement that the triton must reach level

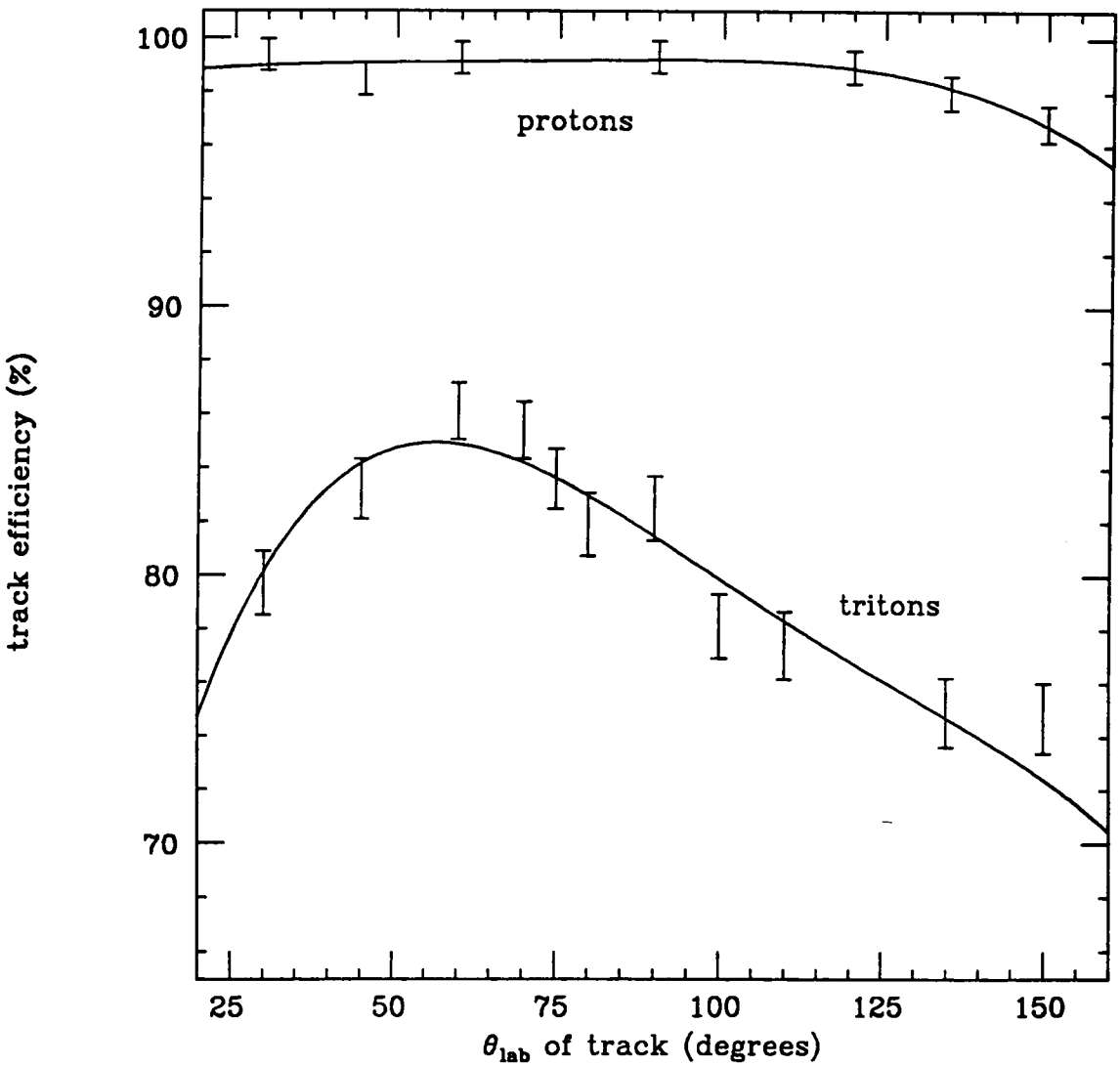

Figure 6.24: Percentage of protons and tritons which form complete tracks, as derived from Monte Carlo simulation.

C. It was observed that, as with the Monte Carlo results, several percent of the tritons which make it to level A do not reach level B, and likewise many which reach B do not arrive at level C. These results are shown in Fig. 6.25. Figure 6.25(a) plots the fraction of tritons that fired level B, given that they fired A, Fig. 6.25(b) plots the fraction that fired level C, given that they hit level B, and Fig. 6.25(c) plots the fraction that fired level C, given that they hit A. The data points show the results from the real data, and the curves are from Monte Carlo. The striking agreement induces confidence in the efficiency curves in Fig. 6.24.

The track efficiency $\varepsilon_0(\theta)$ must be calculated as a function of c.m. angle θ of the proton track. At each c.m. angle θ, the lab angle of the proton and triton track were calculated, and the product of their track efficiencies from Fig. 6.24 was taken. The result for $\varepsilon_0(\theta)$ is shown in Fig. 6.26.

The efficiencies $\varepsilon_1, \varepsilon_2 \ldots$ associated with the remaining cuts should *a priori* be treated as functions of θ, similar to ε_0. However, the cuts were imposed upon spectra which either had no angular dependence, or whose angular dependence had been removed, as in the case of the dE/dx cuts. Therefore they are treated as constants. The efficiency factors are given in Table 6.1 for each of the explicit cuts described in Sec. 6.3. The numbers are taken directly from the acceptance plots that were given for each cut. The product of the efficiencies from Table 6.1 is 93.9%.

6.6 Absolute Normalization

The differential cross section is related to the experimental angular distribution in the c.m. frame by

$$\frac{d\sigma}{d\Omega} = \frac{1}{f\tau}\frac{d\mathcal{N}}{d\Omega} \quad , \tag{6.4}$$

where f is the total number of *tagged* photons incident on the target throughout the experiment, τ is the effective target thickness in scatterers per cm^2, and $\mathcal{N}$ represents the efficiency-corrected experimental angular distribution of counts,

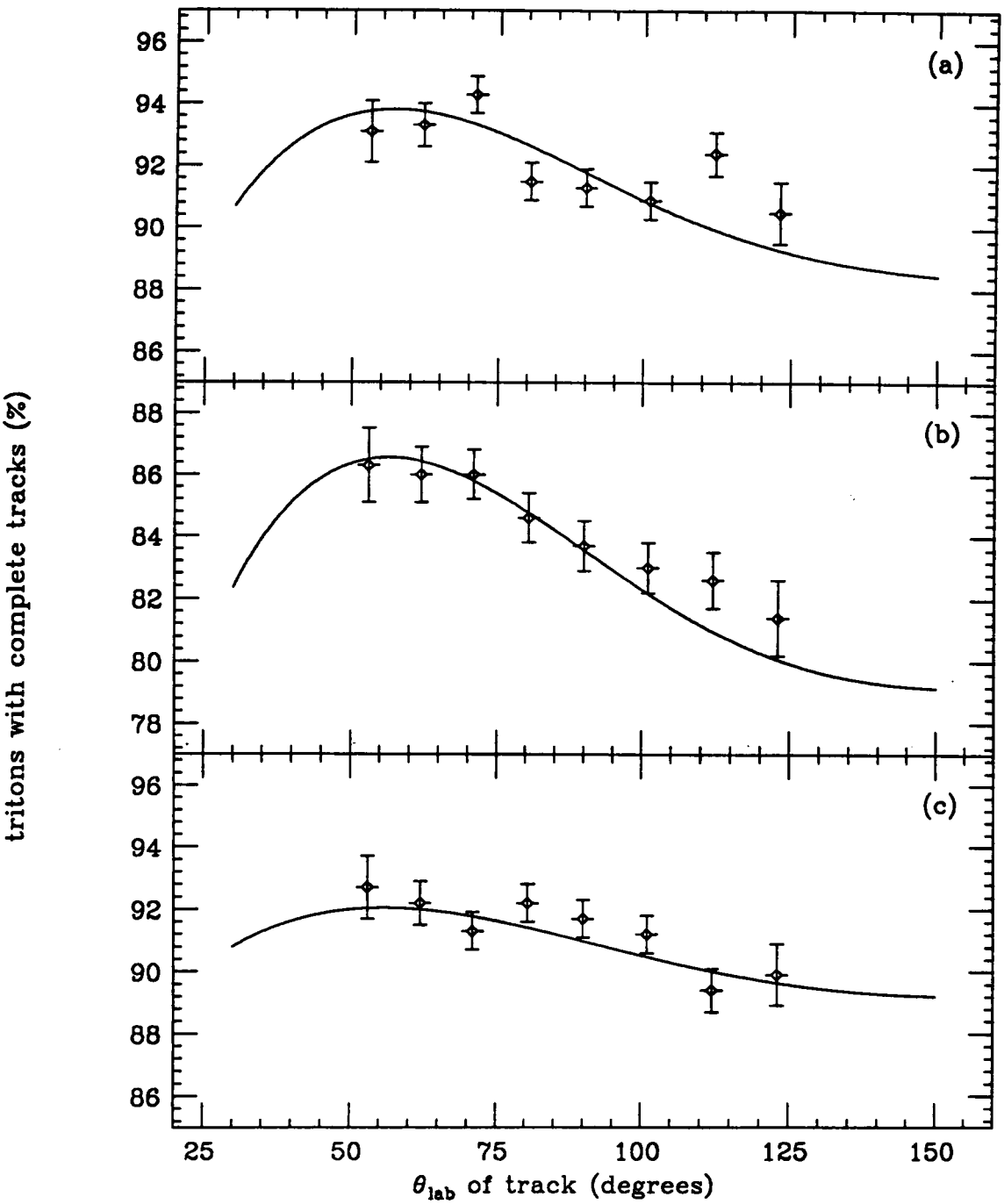

Figure 6.25: Test of Monte Carlo efficiency calculation. The points are derived from analysis of real data. The curves are from Monte Carlo. (a) Fraction of tritons that make it from level A to B. (b) Fraction of tritons that make it from level B to C. (c) Fraction of tritons that make it from level A all the way to level C.

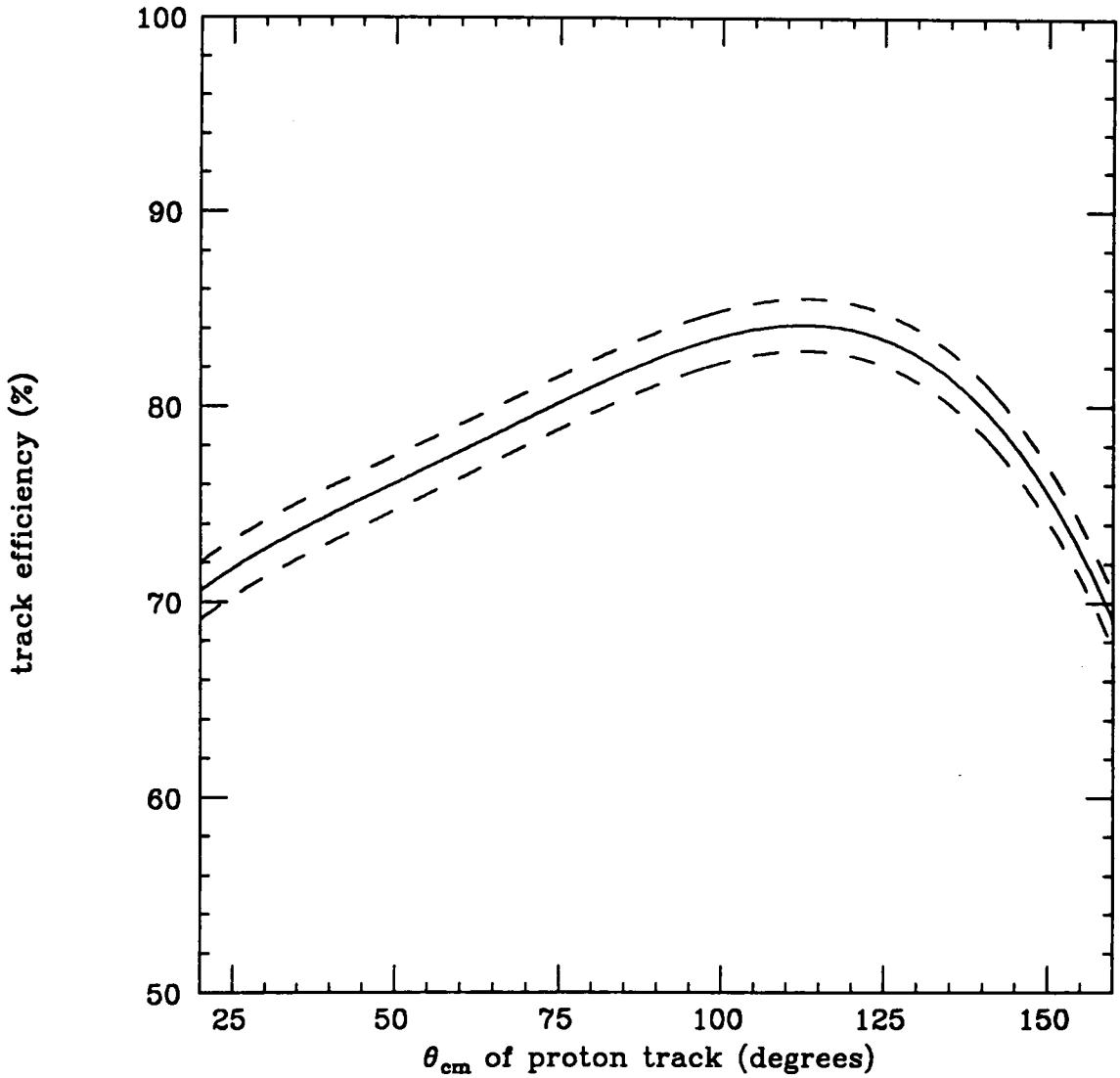

Figure 6.26: Track efficiency function $\varepsilon_0(\theta)$, obtained by combining the proton and triton track efficiencies. The error band represented by the dotted lines was obtained by summing in quadrature the individual errors on the proton and triton track efficiencies.

Table 6.1: Efficiency factors for each of the explicit cuts

Cut description	Efficiency (%)
χ^2 cut on track fit	99.9
cut on radius of vertex	98.3
cut on wire dE/dx	99.9
cut on plastic dE/dx	99.6
two-body $\phi_1 - \phi_2$ cut	97.7
two-body $\theta_1 + \theta_2$ cut	99.4
tagging coincidence cut	99.0

introduced in Eq. 6.2.

The monochromator timing spectrum in Fig. 6.18 is actually the sum of 32 individual timing spectra, one for each of the tagging counters. Likewise, the angular distribution in Fig. 6.23 contains coincidence events associated with all 32 counters, summed together. Since the differential cross section varies slowly over the tagged gamma energy range from 63 to 71 MeV [13], it is reasonable to gain the maximum statistical precision by using the summed spectra. The photon flux needed to normalize the summed spectra is the total count of tagged photons across the focal plane. Thus,

$$f = \sum_{i=1}^{32} f_i = \sum_{i=1}^{32} \epsilon_i N_i^{(e^-)} \quad , \tag{6.5}$$

where ϵ_i is the tagging efficiency of counter i, and $N_i^{(e^-)}$ is the corresponding tagging focal plane scaler (see Sec. 4.1.) The tagging efficiency and total scaler count for each of the 32 counters are given in Table 6.2. The scaler counts are the sum from the 34 tapes that were analyzed. Performing the sum leads to a value of $f = 8.82 \times 10^{10}$ tagged photons.

The effective target thickness is given by

$$\tau = \lambda_2(\theta) \left(\frac{\varrho N_A}{A} \right) \quad , \tag{6.6}$$

where N_A is Avogadro's number, ϱ is the density of the target in g/cm^3, and A is the gram-atomic weight of ^{4}He . The geometric acceptance function λ_2, introduced in Sec. 4.5, represents the length, in cm, of the target segment from which p,^{3}H events at proton angle θ are not excluded by the geometry of the LASA detector. Thus the function τ has units of scatterers per cm^2. The target density ϱ is calculated as

$$\varrho = \varrho_{STP} \left(\frac{T_0}{T} \right) \left(\frac{P}{P_0} \right) \quad , \tag{6.7}$$

where ϱ_{STP} is the tabulated density of ^{4}He at standard temperature T_0 and pressure P_0, and the actual temperature and pressure measured during the run are denoted by T and P, respectively.

Table 6.2: Tagging efficiency and total focal plane scaler counts. The tagging counters subtend photon energy bins of approximately equal width between 63.3 and 71.1 MeV.

counter no.	tagging efficiency	scaler (10^9 counts)	counter no.	tagging efficiency	scaler (10^9 counts)
1	0.603	6.51	17	0.564	5.03
2	0.515	6.47	18	0.424	5.08
3	0.488	6.36	19	0.661	5.04
4	0.544	6.33	20	0.446	4.83
5	0.415	6.29	21	0.567	4.78
6	0.470	5.92	22	0.543	4.77
7	0.494	6.10	23	0.575	3.56
8	0.584	6.25	24	0.582	4.73
9	0.439	5.72	25	0.480[a]	4.38
10	0.551	5.76	26	0.581	4.48
11	0.596	5.30	27	0.505	4.40
12	0.417	5.29	28	0.651	4.41
13	0.633	5.25	29	0.495	4.02
14	0.452	5.41	30	0.589[a]	4.22
15	0.580	5.16	31	0.677	4.06
16	0.514	5.39	32	0.580	3.73

[a]The tagging efficiency for this counter fluctuated beyond the limits of statistics, between tagging efficiency runs.

The continuous function $d\mathcal{N}/d\Omega$ is represented by the discrete spectrum $\mathcal{N}_\theta$ as

$$\frac{d\mathcal{N}}{d\Omega} \simeq \frac{\mathcal{N}_\theta}{2\pi \sin\theta \Delta\theta} \quad , \tag{6.8}$$

where $\Delta\theta$ is the bin width, in radians, of the angular spectrum. The angular distribution prior to the efficiency correction, denoted by N_θ in Eq. 6.2, may be substituted for $\mathcal{N}_\theta$ to obtain

$$\frac{d\mathcal{N}}{d\Omega} \simeq \frac{N_\theta}{2\pi \sin\theta \Delta\theta\, \varepsilon(\theta)} \quad . \tag{6.9}$$

The spectrum N_θ is shown in Fig. 6.23.

The efficiency correction and the normalization can be combined into a single expression which transforms the random-subtracted angular distribution N_θ into the differential cross section, as

$$\frac{d\sigma}{d\Omega} = \left(\frac{A}{f\varrho N_A}\right) \frac{N_\theta}{2\pi \sin\theta \Delta\theta\, \varepsilon(\theta)\lambda_2(\theta)} \quad . \tag{6.10}$$

The units on this expression are $\mathrm{cm}^2/\mathrm{sr}$. Recall that the angle θ is the polar angle of the proton track in the c.m. frame. This demands that the functions ε and λ_2 be evaluated in the c.m. frame. The superscript * on the c.m.-corrected λ_2, defined in Eq. 4.19, has been dropped for simplicity.

The result is shown in Fig. 6.27, expressed in the more convenient units of $\mu\mathrm{b}/\mathrm{sr}$. The curve superimposed upon the data in Fig. 6.27 is a fit in the Legendre polynomial expansion of Eq. 1.37, truncated to four terms.

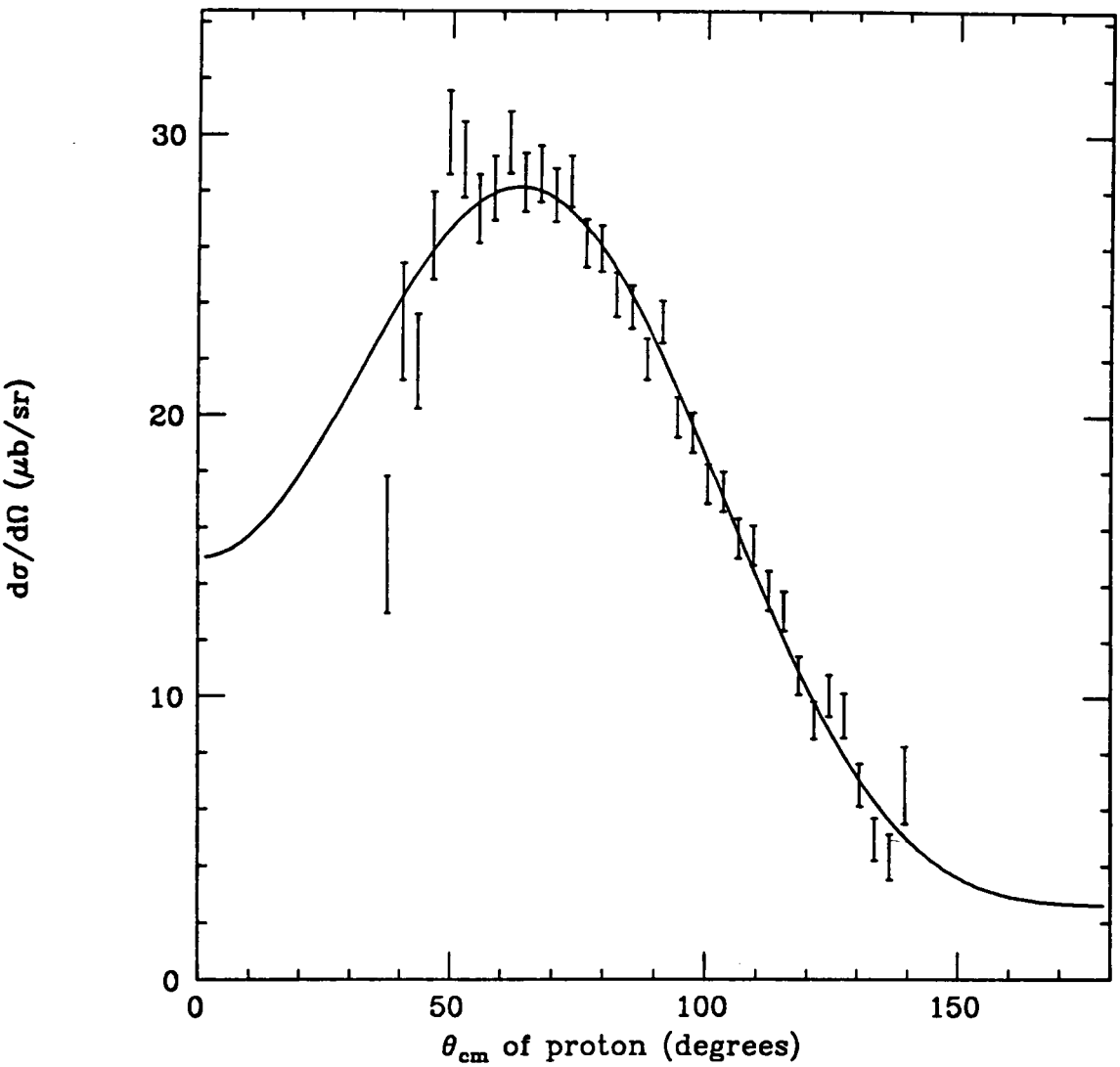

Figure 6.27: Final differential cross section, averaged over the photon energy range 63-71 MeV. The errors are statistical only. The curve through the data is a fit using a Legendre expansion in $\cos\theta$, truncated to 4 terms.

Chapter 7

Results and Discussion

In Chap. 6 the procedure for extracting a differential cross section for the reaction ^{4}He$(\gamma,\mathrm{p})^3$H from data taken with the LASA detector has been described. In this chapter, the final results are presented, along with a discussion of the statistical and systematic errors. A comparison with previous experiments and theoretical calculations is also given.

7.1 The Fit

The general form being used to fit the differential cross section is

$$f(\theta) = A_0 \left(1 + \sum_{n=1}^{N} a_n P_n(\cos\theta)\right)$$

where θ is the polar angle of the proton track in the c.m. frame, P_n is the Legendre polynomial of order n, and the coefficients A_0, a_n are determined by a fit to the data. This expansion contains no model-dependence, since the $P_n(\cos\theta)$ form a complete set of functions on the interval $0 \leq \theta \leq \pi$. The usefulness of this series lies in the fact that the magnitude of successive terms decreases rapidly, as discussed in Sec. 1.2, so that a truncation can be performed after just a few terms. In the analysis of this data, only terms up to $n = 5$ were used. The forms of the lowest-order Legendre polynomials are listed below.

$$P_0(x) = 1 \tag{7.1}$$

$$
\begin{aligned}
P_1(x) &= x \\
P_2(x) &= \frac{1}{2}(3x^2 - 1) \\
P_3(x) &= \frac{1}{2}(5x^3 - 3x) \\
P_4(x) &= \frac{1}{8}(35x^4 - 30x^2 + 3) \\
P_5(x) &= \frac{1}{8}(63x^5 - 70x^3 + 15x)
\end{aligned}
$$

To investigate the best place to truncate the Legendre expansion, a sequence of fits was performed, each one allowing an additional coefficient in the series to vary. The data, as shown in Fig. 6.27, were arranged in 35 bins of 3° width, between the angles 36° and 141° . The fitting procedure determined the values of the free parameters which minimized the value of χ^2, defined as

$$\chi^2 = \sum_\theta \left(\frac{D_\theta - f(\theta)}{S_\theta} \right)^2 \tag{7.2}$$

where D_θ is the differential cross section data point centered at θ and S_θ is the one-standard-deviation error on that point, due to statistics.

The quality of the fit is judged by the value of χ^2 obtained after minimization. The range of acceptable values for χ^2 is characterized by the number of degrees of freedom, which is defined as the number of data points used in the fit, minus the number of fit parameters. The expected value of χ^2 for a good fit is equal to the number of degrees of freedom, and values much larger than this indicate a bad fit. The probability density X_{30}, for 30 degrees of freedom, is shown in Fig. 7.1(a). The quantity plotted in Fig. 7.1(b) is

$$\int_{\chi^2}^{\infty} X_{30}(x)\, dx \quad .$$

This represents the probability that, if f were the true distribution, the fit would be no better than it is, and is henceforth denoted by the symbol $\mathcal{P}$.

The results of a sequence of fits, each including one additional term in the Legendre series, are shown in Table 7.1. The fourth column, labeled $\chi^2_{\rm red}$, contains

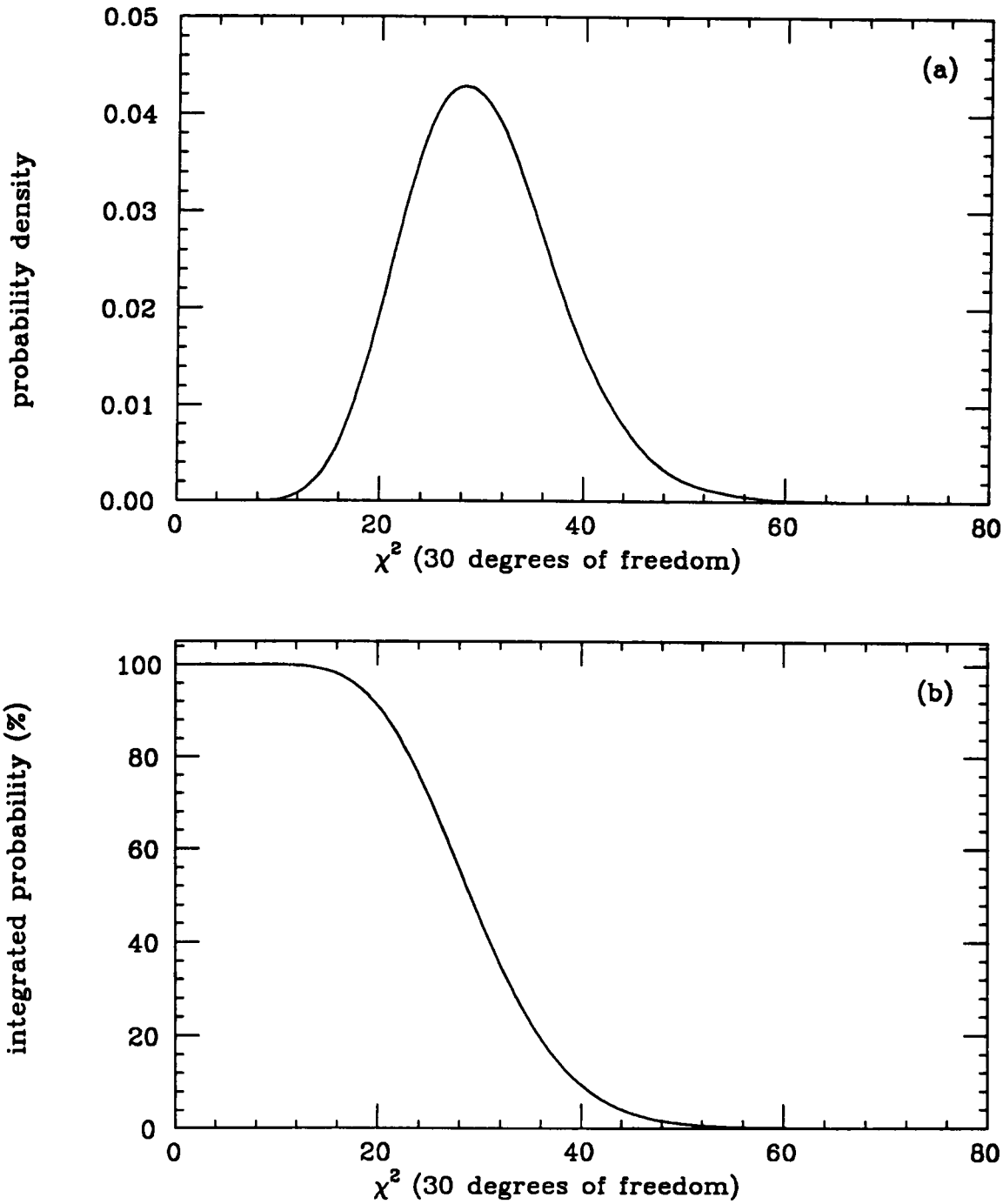

Figure 7.1: χ^2 distribution with 30 degrees of freedom. (a) The probability density. (b) The probability $\mathcal{P}$ (ordinate) of getting χ^2_{30} at or above any given value of χ^2 (abscissa).

the *reduced* χ^2, defined as the χ^2 of the fit divided by the number of degrees of freedom. For a good fit, the $\chi^2_{\rm red}$ value should be close to 1. These fits were all performed on the differential cross section obtained by summing all 32 photon energy bins.

The large values of $\chi^2_{\rm red}$ for $N<3$ indicate that terms up to third order are required in order to get a reasonable fit to the data. As can be seen in Fig. 6.27, the fit for $N = 3$ is qualitatively good. Quantitatively, however, the value of $\mathcal{P}$ from Table 7.1 indicates that some improvement in the fit function should still be expected, assuming the conventional cutoff of $\mathcal{P} = 5\%$ as the limit of significant deviation [89]. When the $n = 4$ term is included, some improvement in the quality of the fit is obtained. However, the problem occurs that the fit function dips below zero in the region $\theta>150°$. This is inconsistent with the definition of a differential cross section.

To correct this problem, a constraint was added to the fit, requiring that the cross section be positive at $\theta = 180°$. This was done by adding a dummy data point of 0.2 ± 1.0 μb/sr at 180° . The χ^2 of the overall fit increased by less than 1 when this constraint was imposed, and the net improvement in the goodness-of-fit was sufficient to justify the inclusion of the $n = 4$ term. Including the $n = 5$ term produced a further decrease of about 10 in the fit χ^2. However, the same problem as before was encountered in the forward direction: the fit function went negative for $\theta<30°$. Another dummy data point was added at 0° , with a value of 0.3 ± 1.0 μb/sr. The addition of this constraint increased the χ^2 of the overall fit by only 2.5. The χ^2 values in Table 7.1 are those obtained with the constraints in place.

Including $n = 4, 5$ terms in the fit gives a significant improvement in the value of $\mathcal{P}$. Adding terms beyond $n = 5$ brings about very small improvement in the fit, and the $\chi^2_{\rm red}$ value actually increases, indicating that the parameters are not statistically significant. The fit using $N = 5$ is shown in Fig. 7.2. Note the marked difference

Table 7.1: χ^2 of best fit to the differential cross section, using the Legendre series truncated after term N. The abbreviation DOF stands for degrees of freedom, χ^2_{red} is χ^2 per degree of freedom, and $\mathcal{P}$ is the probability function, like that for 30 DOF in Fig. 7.1(b).

N	DOF	χ^2	χ^2_{red}	$\mathcal{P}$ (%)
0	34	2764.9	81.32	0
1	33	282.9	8.57	0
2	32	101.1	3.16	0
3	31	56.0	1.81	1
4	30	48.6	1.62	2
5	29	40.2	1.39	9
6	28	39.7	1.42	7
7	27	39.2	1.45	6
8	26	38.3	1.47	6

between the extrapolation of the cross section toward forward and backward angles between the $N = 3$ fit in Fig. 6.27 and the $N = 5$ fit in Fig. 7.2.

One way to estimate the uncertainty in the 0° and 180° cross section derived from this data is to raise the dummy data points at 0° and 180° one at a time, until the χ^2 of the overall fit increases by 1. The dotted curves in Fig 7.2 represent the one-sigma limits, thus defined. Note that this estimate takes into account only the statistical errors on the data points. While the systematic error on any one data point is much smaller than its statistical error, a systematic shift of several points by a few percent can cause a large change in the behavior of the extrapolated differential cross section. Therefore these statistical limits should be taken with caution.

The values of the parameters which produced the fit in Fig. 7.2 are listed in Table 7.2. The statistical errors listed in the table contain the influence of the constraints which were imposed on the fit at 0° and 180° , and are smaller than is warranted by the data itself. When the constraints are removed from the fit so that the parameters are permitted to vary freely, the statistical uncertainties on the resulting fit parameters are larger than those from the constrained fit by about a factor of 2. This demonstrates the fact that any knowledge of the cross section at the forward and backward angles would greatly improve the precision of the Legendre coefficients derived from this data.

Since the data in Fig. 7.2 contains the sum from all of the focal plane counters, the parameters in Table 7.2 are an average over the photon energy range 63-71 MeV. To examine the energy dependence of the coefficients, angular distributions may be generated for each individual focal plane counter. The statistics in these spectra are not sufficient to justify extracting a full set of Legendre coefficients for each. However, the dependence of the total cross section on energy can be ascertained by fixing the shape of the angular distribution, and permitting the magnitude to vary for best fit on each individual spectrum. This is equivalent to fixing parameters

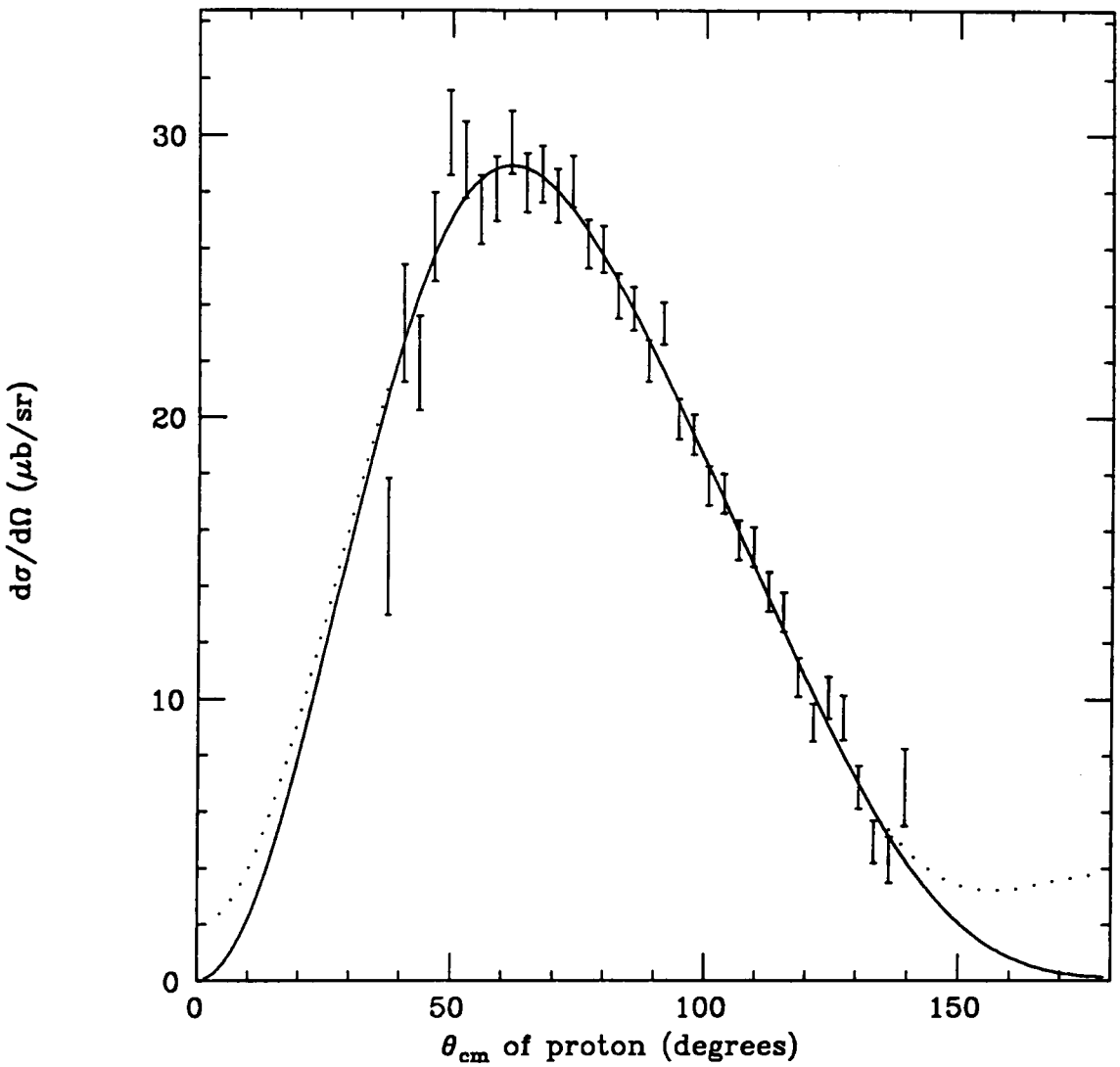

Figure 7.2: Differential cross section with best fit using terms in the Legendre sum up to $n = 5$. The fit was constrained to keep the cross section non-negative everywhere. The dotted lines indicate the statistical uncertainty in the extrapolation.

Table 7.2: Parameters of the best fit with $N = 5$

Parameter	Value ± statistical error[a]	
A_0	17.06	± 0.17
a_1	0.623	± 0.022
a_2	−0.771	± 0.030
a_3	−0.525	± 0.025
a_4	−0.224	± 0.025
a_5	−0.101	± 0.029

[a]These errors contain the influence of the constraints used in the fit. The statistical uncertainty on these parameters is approximately a factor of 2 larger when the constraints are removed.

$a_1 \ldots a_5$ and varying A_0. The results are shown in Fig. 7.3. The values of $a_1 \ldots a_5$ from Table 7.2 were used. The total cross section is given by $4\pi A_0$. There is a 30% decrease in the total cross section with energy between 63 and 71 MeV.

The error bars on the points in Fig. 7.3 are statistical only. There is an additional uncertainty on A_0 resulting from the error in the $a_1 \ldots a_5$ coefficients which are used in the fit. This uncertainty is not included in the error bars in Fig. 7.3 since it affects all of the points in the same way, and should be viewed as a systematic error arising from the fitting procedure. The magnitude of this systematic uncertainty can be estimated by

$$V(A_0) = \sum_{i=1}^{5} \left(\frac{\partial A_0}{\partial a_i} \right)^2 V(a_i) + \sum_{i \neq j} \left(\frac{\partial A_0}{\partial a_i} \right) \left(\frac{\partial A_0}{\partial a_j} \right) C(a_i a_j) \qquad (7.3)$$

where $V(a_i)$ represents the variance on coefficient a_i and $C(a_i a_j)$ is the covariance between a_i and a_j. The partial derivatives were evaluated by varying the a_i coefficients and noting the shift in A_0 when the fit was repeated. The result is a systematic error of 0.25 μb/sr. While this is only about half of the statistical error on a single point in Fig. 7.3, it presents a limit on the precision which may be obtained by averaging adjacent points. The general topic of systematic error is addressed in Sec. 7.2.

Any attempt to quantify the statistical error on the Legendre coefficients for a fit of order $N = 4$ or $N = 5$ is clouded by the influence of the constraints, which prevent the fit from producing a negative differential cross section in the angular region outside of the range of the measurement. One approach would be to simply ignore the problem, since it is outside of the angular range of the measurement, and just report the differential cross section between the angles 40° and 140° . However, it is the Legendre coefficients which are directly related to the underlying physics (see Eq. 1.33), and their extraction is necessary to unravel the contributions from the various terms in Table 1.3.

Since the leading term in each polynomial $P_n(\theta)$ is of order $\cos^n \theta$, the $n = 4$

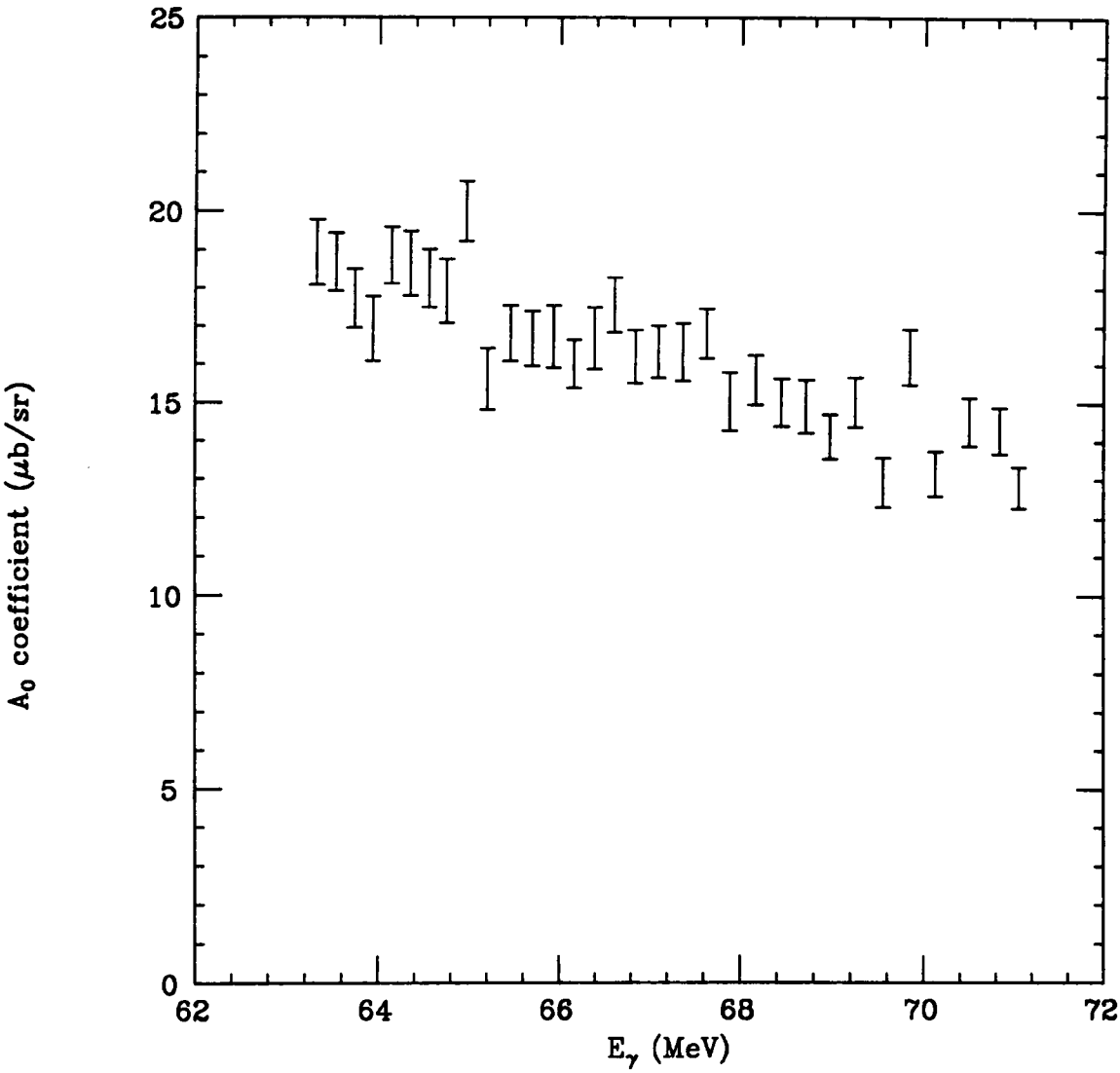

Figure 7.3: A_0 coefficient for 32 individual energy bins, taken separately. The fit was done fixing the shape of the angular distribution and letting the magnitude, specified entirely by A_0, vary. The error bars are statistical only.

and $n = 5$ terms make their largest contribution to $f(\theta)$ in the regions near 0° and 180° . This is apparent from the fact that a reasonable fit to the data can be obtained with a series truncated after $n = 3$ (see Fig. 6.27.) Since for up to $n = 3$, no constraints are needed to obtain a fit function which is positive everywhere, it is possible to present the four lowest-order coefficients with unambiguous values for the associated statistical error. In order to show the variation of the coefficients with energy, the 8-MeV band of photon energy was divided up into four bins of 2 MeV each. The results are shown in Figs. 7.4-7.7, and are listed in Table 7.3. The errors listed are statistical errors only.

7.2 Systematic Errors

In the analysis of errors, an account must be given of the precision with which each quantity is known that is used in the calculation of the cross section. In Eq. 6.10 each ingredient is shown separately:

$$\frac{d\sigma}{d\Omega} = \left(\frac{A}{f\varrho N_A}\right) \frac{N_\theta}{2\pi \sin\theta \Delta\theta\, \varepsilon(\theta)\lambda_2(\theta)} \quad .$$

The errors on N_θ are strictly statistical, and have been presented along with the data. The uncertainties on the photon flux f, the efficiency ε, and the geometric acceptance λ_2 are the sources of systematic error.

The total flux of tagged gammas is calculated by multiplying the focal plane scaler counts by the tagging efficiency. Since the scaler counts are on the order of 10^9, the fluctuations are negligible and no uncertainty is assigned to them. The tagging efficiency was measured a total of eight times throughout the course of the run. The results for focal plane counter 16 were shown in Fig. 4.1. The errors shown are derived from the statistics of the calibration runs, about 2%. Since the foregoing analysis was only carried out on the last third of the data tapes, only the last five calibration runs are included in the calculation of tagging efficiency.

The tagging efficiency calibration data are consistent with the hypothesis that

Table 7.3: Values of Legendre coefficients up to $n = 3$

Coefficient	Photon energy	Value ± statistical error	
A_0	64	19.80	± 0.49
	66	18.86	± 0.47
	68	17.70	± 0.43
	70	15.84	± 0.39
a_1	64	0.572	± 0.078
	66	0.538	± 0.080
	68	0.794	± 0.074
	70	0.772	± 0.075
a_2	64	−0.641	± 0.081
	66	−0.574	± 0.080
	68	−0.464	± 0.077
	70	−0.460	± 0.078
a_3	64	−0.403	± 0.102
	66	−0.477	± 0.100
	68	−0.182	± 0.104
	70	−0.390	± 0.103

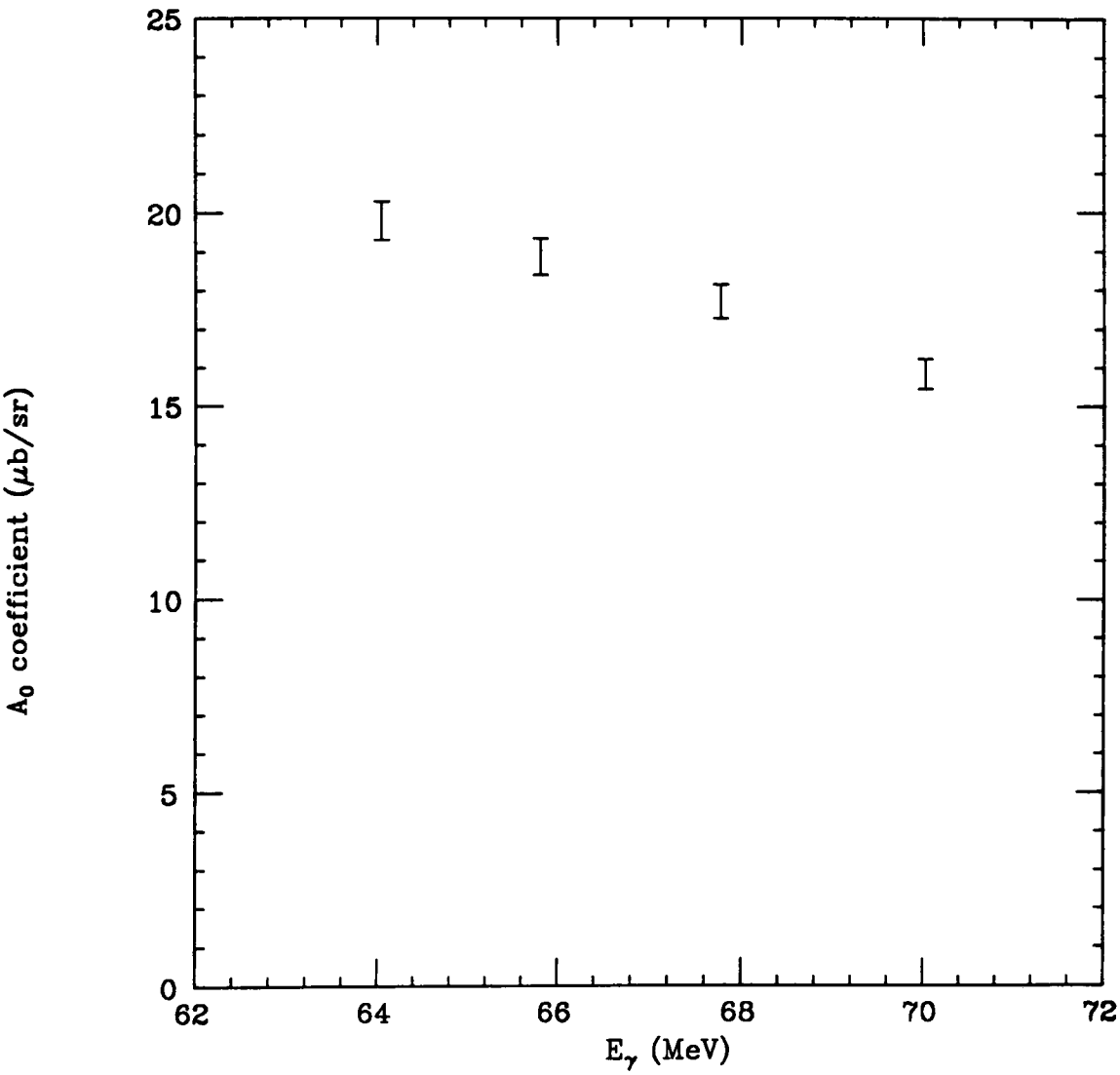

Figure 7.4: Legendre coefficient A_0 versus photon energy

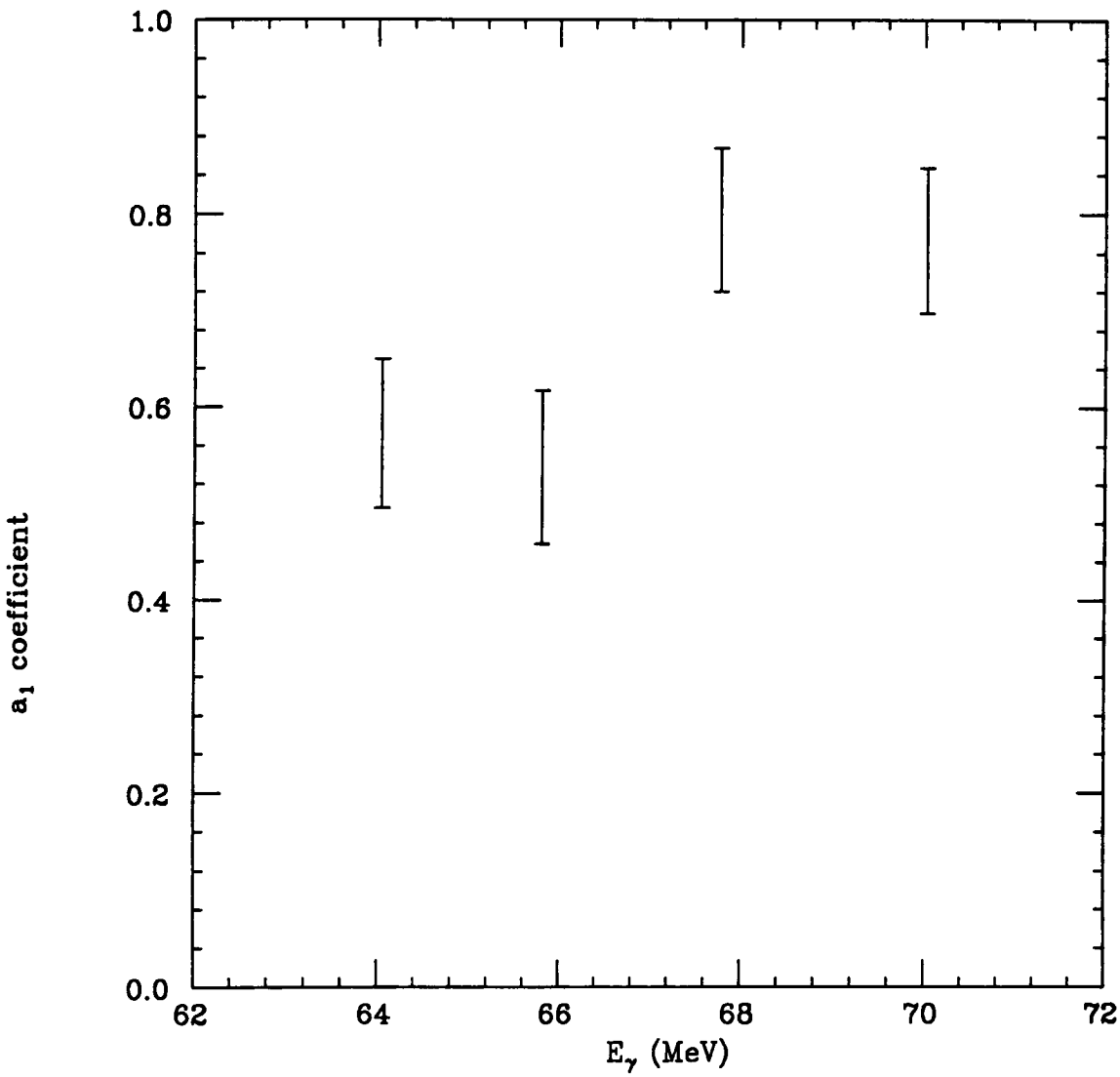

Figure 7.5: Legendre coefficient a_1 versus photon energy

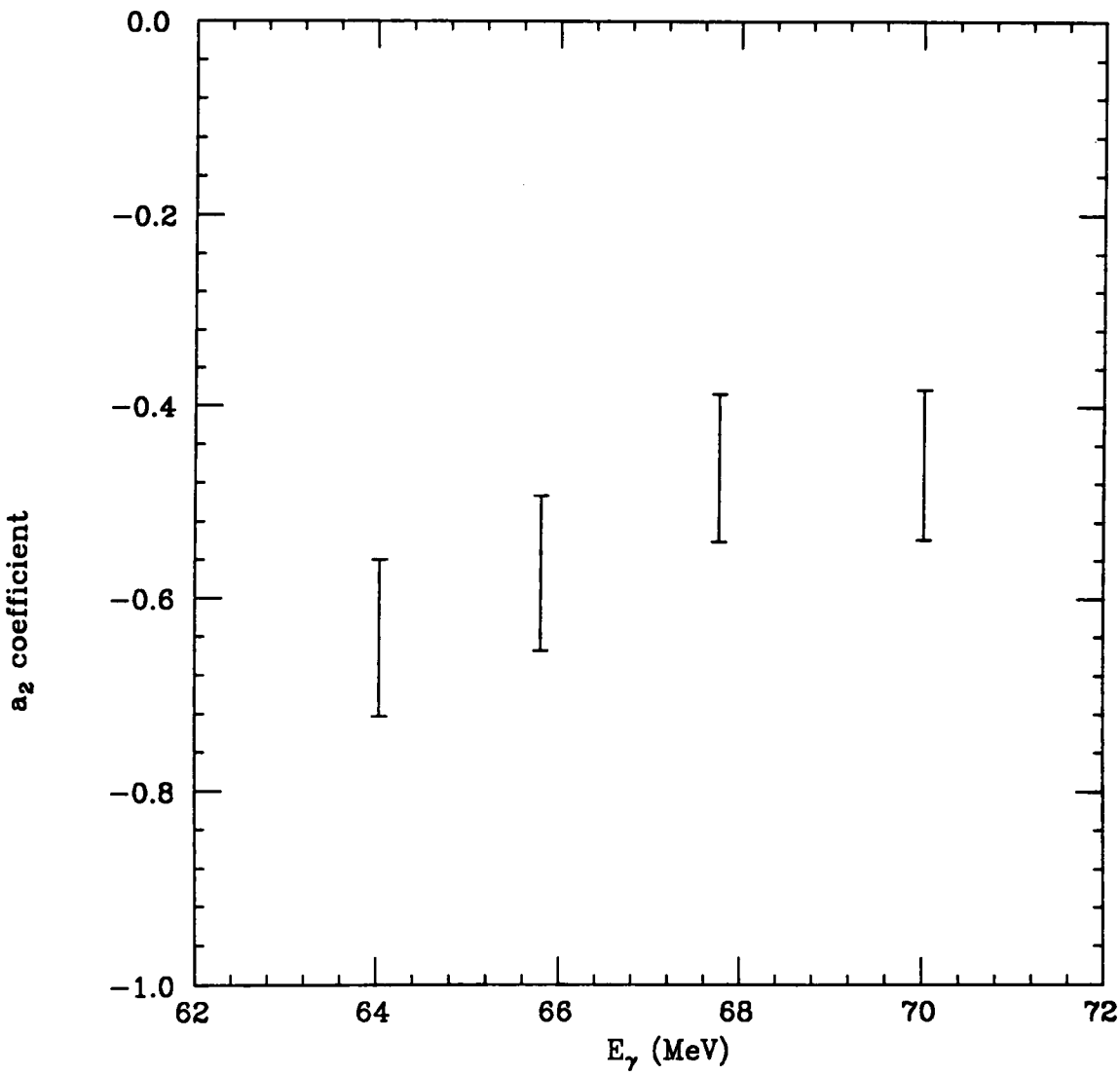

Figure 7.6: Legendre coefficient a_2 versus photon energy

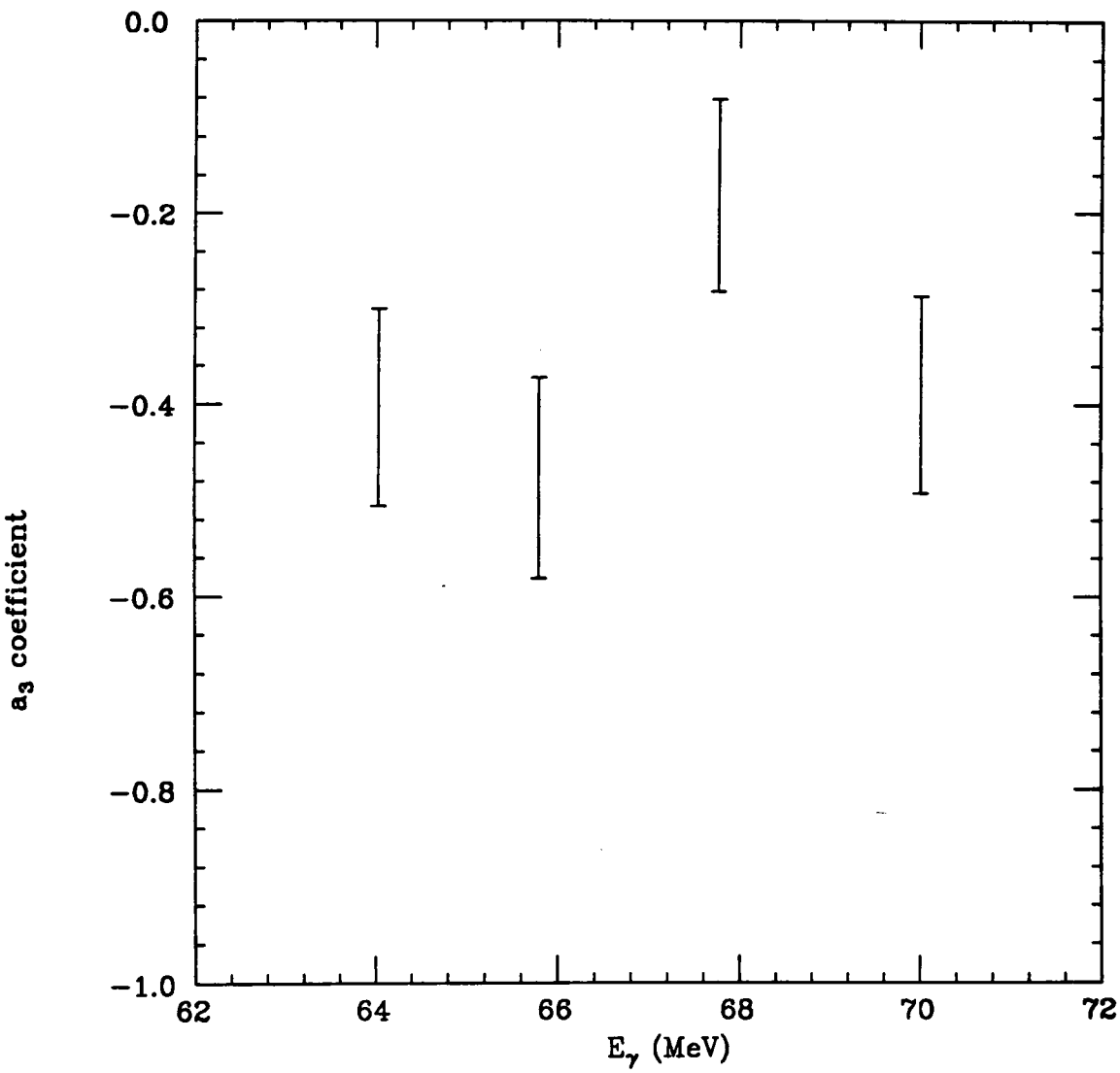

Figure 7.7: Legendre coefficient a_3 versus photon energy

the tagging efficiency was constant throughout the experiment, with the exception of counter 25 ($\chi^2_{\rm red} = 5.7$) and counter 30 ($\chi^2_{\rm red} = 3.4$), whose data indicate a one-sigma fluctuation of 5% and 4% respectively. It should be noted that, if the beam current is reasonably steady, only the average tagging efficiency enters the calculation of the total tagged flux. Let $s(t)$ represent the instantaneous rate in a focal plane scaler, and $\epsilon(t)$ represent the tagging efficiency for that counter. Then the integrated flux of tagged photons is given by

$$\begin{aligned} f &= \int s(t)\epsilon(t)\,dt \\ &= \int (\bar{s}+\delta s)(\bar{\epsilon}+\delta\epsilon)\,dt \quad : \quad \bar{s} = \frac{1}{T}\int s(t)\,dt \;, \quad \bar{\epsilon} = \frac{1}{T}\int \epsilon(t)\,dt \\ &= \bar{s}\,\bar{\epsilon}\,T + \int \delta s(t)\,\delta\epsilon(t)\,dt \end{aligned} \tag{7.4}$$

where T is the total duration of the experiment. The second equality results from the fact that the fluctuations average to zero over all the experiment. Therefore, since the beam current was kept steady throughout the experiment at the level of $\pm 10\%$, a 5% fluctuation in the tagging efficiency translates to a 0.5% uncertainty in the total flux. Hence the systematic uncertainty in the tagging efficiency is determined by how well the average can be ascertained. Taking the average of the last five Brems runs, a typical uncertainty of 1% in the tagging efficiency is obtained for each counter, while the figure for counters 25 and 30 is 2%.

There are other systematic uncertainties inherent in the technique used to measure tagging efficiencies. These are related to the absorption of photons in the air between the LASA target and the NaI crystal, and the number of charged particles in the beam which have enough energy to exceed the gamma threshold on the NaI discriminator. Also included is the small portion of gammas which do not interact in the NaI crystal electromagnetically (i.e. photoneutron absorption), or which create showers that escape without depositing enough energy to pass the discriminator threshold (about 10 MeV). Estimates for all of these effects are in the regime $<1\%$. While averaging adjacent counters can reduce the systematic

error in the tagging efficiency, it does not affect the uncertainty from experimental systematics. Therefore an estimated systematic uncertainty of 1% is assigned to the total photon flux, applicable to the spectra summed over sets of eight counters, as well as the overall summed spectrum.

The next source of systematic error to be considered is the geometric acceptance function $\lambda_2(\theta)$. The uncertainty on this quantity is related to how precisely the positions of all of the LASA detector components are known. The wire chamber is all one piece and the dimensions are known to the precision of the machining, better than 10^{-2} cm. The dimensions of the scintillator paddles themselves are also well known. However, the radial distance from the detector axis to the centerline of the front face of the thin scintillator has some freedom, and varies from the mean by about ± 1 mm. The longitudinal placement of the scintillators varies with respect to the center-point of the wire chamber by about ± 2 mm. Shifting these dimensions and repeating the Monte Carlo calculation of λ_2 gives a net change in λ_2 of about 1% in the angular range between 36° and 141° . The percent uncertainty becomes quite large outside of these angular limits, where the absolute value of λ_2 is very small, so data from these bins were excluded from the spectra. The error on λ_2 is estimated to be 1%.

The remaining source of systematic error is the efficiency function $\varepsilon(\theta)$. This function is a product of several efficiency functions which were discussed in Sec. 6.3. The systematic uncertainty on the track efficiency function ε_0, discussed in Sec. 6.5 is 2%. The efficiencies associated with the explicit cuts were carefully quantified. An uncertainty of no more than 10% in the magnitude of the correction should be applied to any one of these, with the exception of the wire dE/dx cut.

The wire dE/dx cut was the first cut made, and so the data gave the least guidance as to where this cut should be placed. The decision was based entirely upon proton wire dE/dx spectra obtained from elastic p-p scattering at IUCF. The p-p events were different from the photodisintegration events in the respect that all

of the energetic protons had tracks with $\theta_{\rm lab}$ less than 60° . This means that they did not sample the region of the wires very close to the end-plates. A measurement of the wire gain versus z showed that it varied by less than 5% between $z = -40$ cm and $z = +40$ cm. It is expected that the gain should be significantly depressed in the region of the wire within 1 cm of the end-plate. Since this effect has not been measured, an allowance must be made for it in the systematic uncertainty. If all of the tracks which passed through the region of the wire within 1 cm of the end-plate were lost, there would be a 2% depression in the differential cross section in the vicinity of $\theta = 90°$. Therefore a 2% systematic uncertainty is assigned.

During the data reduction, a periodic check was made that all of the wires were firing regularly and giving reasonable pulse-heights. This check uncovered the fact that one of the wires on level B was firing at 1% the rate of the others. There being 128 wires on level B, a 1% systematic uncertainty is included for this wire. The complete list of systematic uncertainties which have been compiled is given in Table 7.4. Adding the errors in quadrature, the net systematic uncertainty is found to be 3.3%. This is drawn as a one-sigma error band of $\pm 3.3\%$ about the fitted curve in Fig. 7.8 between the angles 40° and 140° . Note that the implied uncertainties in the Legendre coefficients are somewhat larger than 3.3%, due to the large systematic uncertainty in the extrapolation of the differential cross section toward 0° and 180° .

The fact that the fit function went negative for $N = 4, 5$ indicates that the systematic error on the a_4 and a_5 coefficients was larger than the statistical error. This is the reason that the final results were reported with a series truncated after $n = 3$. Any set of coefficients which results in a curve that is contained within the one-sigma band of systematic error shown in Fig. 7.8 is consistent with the results of this experiment. An approximation to the systematic error on the Legendre coefficients can be obtained by varying each one independently until the fitted curve crosses the one-sigma boundary of the systematic uncertainty. The results

Table 7.4: Summary of systematic uncertainties

Description of source	Uncertainty (%)
tagging efficiency	1.0
geometric acceptance	1.0
track efficiency	2.0
χ^2 cut on track fit	0.0
vertex radius cut	0.2
wire dE/dx cut	2.0
plastic dE/dx cut	0.1
two-body $\phi_1 - \phi_2$ cut	0.2
two-body $\theta_1 + \theta_2$ cut	0.1
tagging coincidence cut	0.1
bad wire on level B	1.0
total systematic uncertainty	3.3

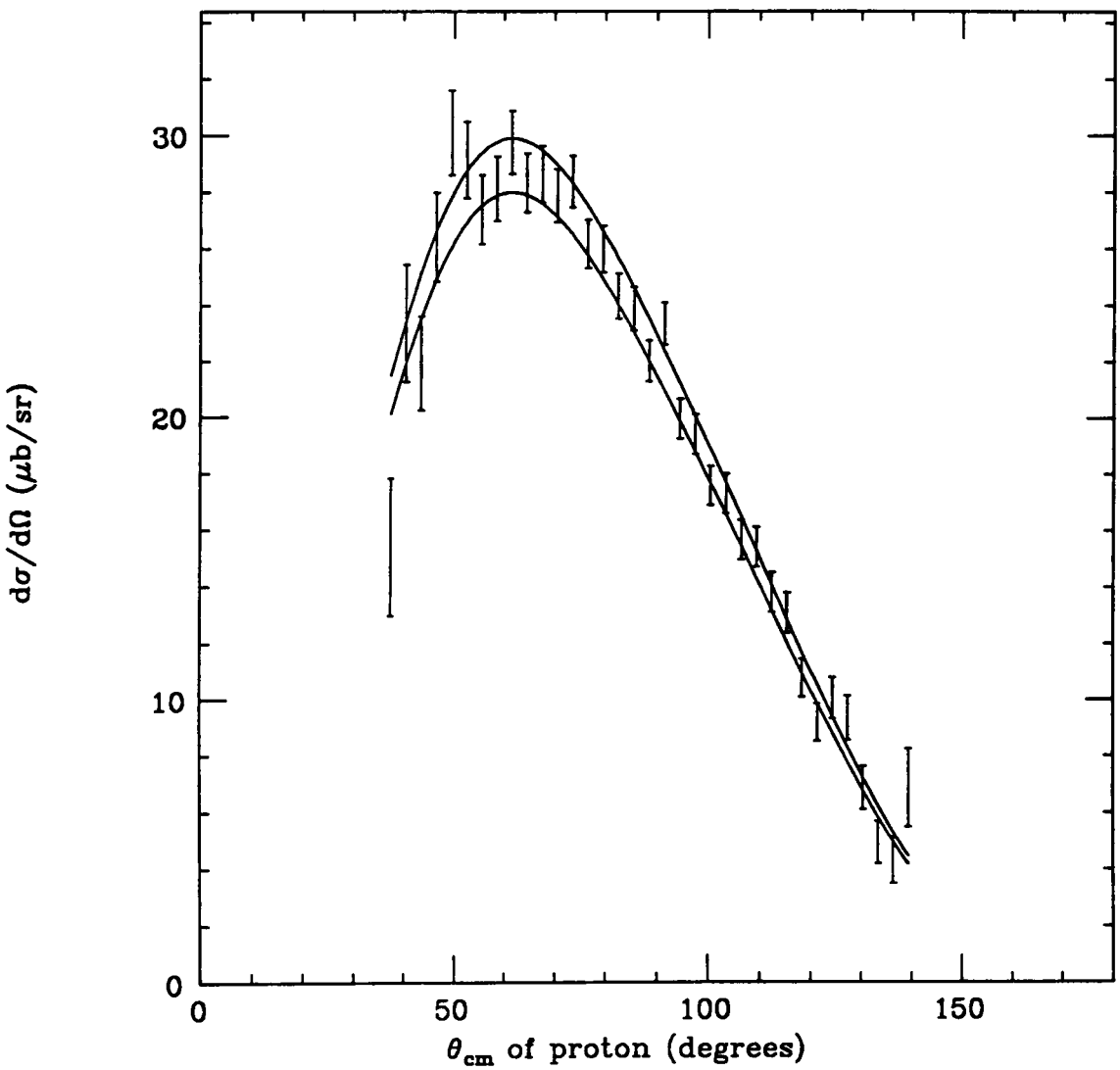

Figure 7.8: Differential cross section showing systematic error

are given in Table 7.5. Note that the systematic error is approximately equal to the statistical error, as listed in Table 7.3. These errors apply to all of the angular distribution spectra, regardless of their statistical error.

The total uncertainty can be estimated by summing the statistical and systematic errors in quadrature. This yields a value of 5% for the A_0 coefficient, and hence for the total cross section. As was reported in Sec. 6.3, a 2.8% contribution from the three-body and four-body photodisintegration channels exists in the final spectra. This may be corrected by subtracting 2.8% from the A_0 coefficient. Making this correction, and collecting all of the errors together, the final results are given in Table 7.6.

7.3 Comparison with Previous Results

The best set of existing data for the ^{4}He$(\gamma,\mathrm{p})^3$H in the energy range of this experiment is that of Gorbunov [13]. That experiment was performed with a bremsstrahlung photon beam and a cloud chamber. Due to the poor statistics obtained, the angular distribution spectra were summed over the photon energy range from 36 to 65 MeV, and from 65 to 170 MeV. The total cross section, however, is reported in 5 MeV energy bins, up to 80 MeV. Those points which lie between 55 and 80 MeV are shown in Fig. 7.9, along with the results from the present experiment. The error bars on the data points from the present experiment are the total errors, taken from Table 7.6.

In Ref. [13] the angular distributions were fitted to the alternate expansion of Eq. 1.36:

$$\frac{d\sigma}{d\Omega} = A(\sin^2\theta + \beta\sin^2\theta\cos\theta + \gamma\sin^2\theta\cos^2\theta + \delta + \varepsilon\cos\theta) \quad .$$

The transformation from the Legendre coefficients to the Greek set is given in Chap. 1. Gorbunov does not include the ε coefficient in his fit. In the present analysis, no value for γ can be reported since the Legendre series was truncated

Table 7.5: Systematic errors on the Legendre coefficients

Coefficient	Systematic error (%)
A_0	4
a_1	10
a_2	15
a_3	25

Table 7.6: Values of Legendre coefficients up to $n = 3$

Legendre coefficient	Photon energy	Measured value	Statistical error	Systematic error	Total error
A_0	64	19.24	0.49	0.77	0.91
	66	18.33	0.47	0.73	0.87
	68	17.20	0.43	0.69	0.81
	70	15.40	0.39	0.62	0.73
a_1	64	0.572	0.078	0.07	0.10
	66	0.538	0.080	0.07	0.11
	68	0.794	0.074	0.07	0.10
	70	0.772	0.075	0.07	0.10
a_2	64	−0.641	0.081	0.09	0.12
	66	−0.574	0.080	0.09	0.12
	68	−0.464	0.077	0.09	0.12
	70	−0.460	0.078	0.09	0.12
a_3	64	−0.403	0.102	0.10	0.14
	66	−0.477	0.100	0.10	0.14
	68	−0.182	0.104	0.10	0.14
	70	−0.390	0.103	0.10	0.14

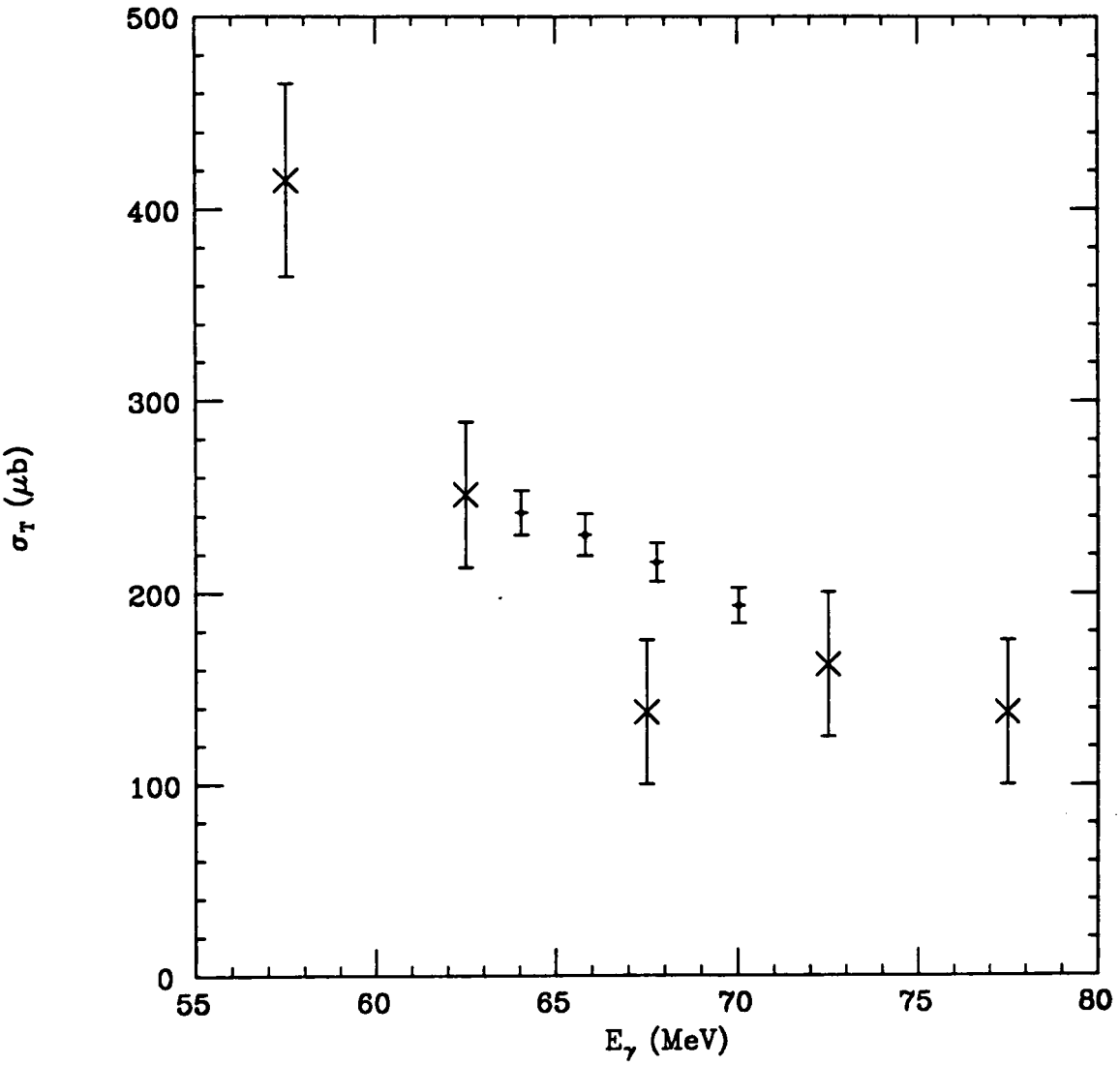

Figure 7.9: Comparison of the present data (•) with the total cross section measured by Gorbunov (×) [13].

after $n = 3$. Nevertheless some comparison can be made between the two data sets. The results from Table 7.6 were averaged together and transformed to the Greek coefficients ones, treating statistical and systematic uncertainties separately in propagating the errors. The results are given in Table 7.7, along with the Gorbunov values. The A coefficient of the above expansion, the same as A_0 of the Legendre series, simply measures the total cross section, and is not listed in Table 7.7.

The angular distribution data between the two measurements are in agreement, in spite of the fact that the Russian data was averaged over the energy range from 65 to 170 MeV. The apparent disagreement in the δ coefficient is explained by noting that

$$\delta = 1 + a_2 + a_4 \quad .$$

Since a_4 was not included in the final fit to the present data, the δ reported for this measurement in Table 7.7 was calculated as $\delta = 1 + a_2$. This is the same as setting $a_4 = 0 \pm 0$. However, as was shown in Sec. 7.1, the present data are consistent with a value of a_4 different from zero. In fact, since ε was not included in the fit of Gorbunov, his small value of δ can be interpreted as the statement that the differential cross section is small at 0° and 180° . This is consistent with the best fit to the present data using $N = 5$, shown in Fig. 7.2. Hence the conclusion can be drawn that, where comparisons are possible, the two measurements are in agreement.

There are three major theoretical calculations which can be compared with these data. These are the quasi-deuteron model calculation of Noguchi and Prats [35], the augmented shell-model calculation of Gari and Hebach [10], and that of Casel and Sandhas [33], done within the framework of "exact" few-body theory. Both Gari and Hebach, and Casel and Sandhas report a total cross section within the energy range of this experiment. The results of Gari and Hebach are shown in Fig. 7.10. Their independent-particle shell-model result, represented by the dotted curve,

Table 7.7: Comparison between the fitted coefficients of Gorbunov [13] on the gamma energy range 65-170 MeV with the present results, averaged over the four energy bins between 63 and 71 MeV.

Coefficient	Data of Ref. [13]	Present results
β	1.29 ± 0.27	0.91 ± 0.28
γ	-0.29 ± 0.42	$\cdots$
δ	0.10 ± 0.07	0.47 ± 0.10^a
ε	$\cdots$	0.31 ± 0.14

[a]This coefficient was calculated by setting the undetermined coefficient a_4 to 0 ± 0.

falls far below the data. The addition of nucleon correlations to the shell-model ground state of the ^{4}He nucleus results in the dot-dashed curve. The dashed curve represents the basic shell-model result with meson-exchange currents included. The solid curve is obtained when all three effects are included: shell-model one-body currents, modifications from nucleon correlations, and meson-exchange two-body currents. It is clear that exchange current effects are the dominant part of the cross section at these energies.

In their "exact" few-body calculations, Casel and Sandhas decompose the transition matrix element into what they call a Born term (in analogy to elastic two-body scattering) and a correction term which contains the final-state interactions. At energies above the GDR, they report the Born result for the total cross section, saying that they expect effects from final-state interactions to be small. Their result is shown in Fig. 7.11. The fact that it is somewhat too small is not surprising, since they only included E1 transitions in the calculations.

Noguchi and Prats do not report a cross section in the energy range of this experiment, but they do plot the quantity β from Eq. 1.36, which is also called the asymmetry coefficient. Their value at 70 MeV for the ^{4}He$(\gamma, \mathrm{p})^3$H reaction is 0.86, consistent with the experimental value of 0.91 ± 0.28. Gari and Hebach calculate the position of the maximum in the angular distribution, and report a value of 68° at 70 MeV. The experimental value is $62 \pm 3°$.

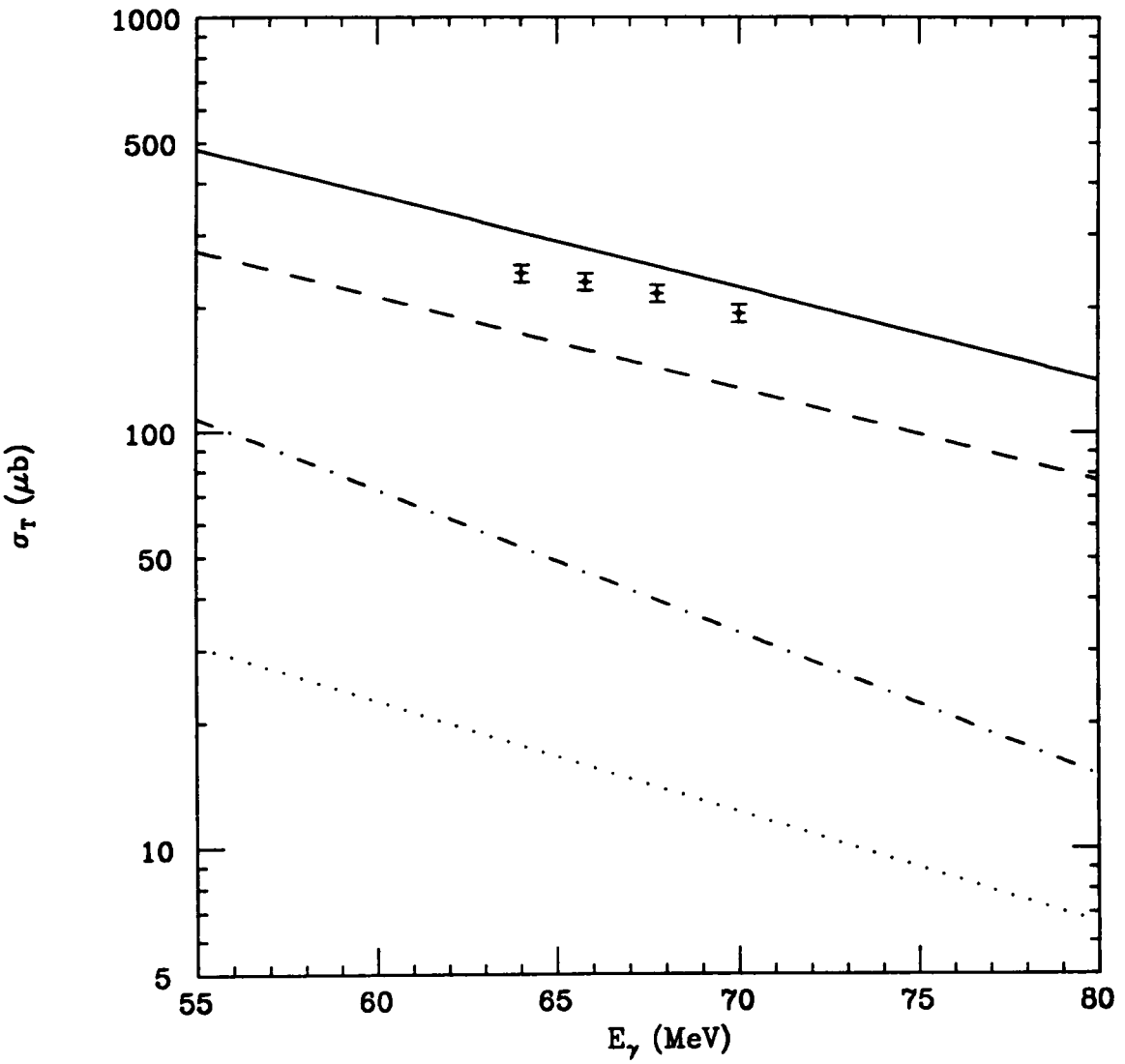

Figure 7.10: Comparison of the present data with the total cross section calculated by Gari and Hebach. The dotted curve is their basic shell-model result, the dot-dashed curve includes shell-model plus nucleon correlation effects, the dashed curve is the shell-model plus exchange-current result, and the solid curve includes all three effects.

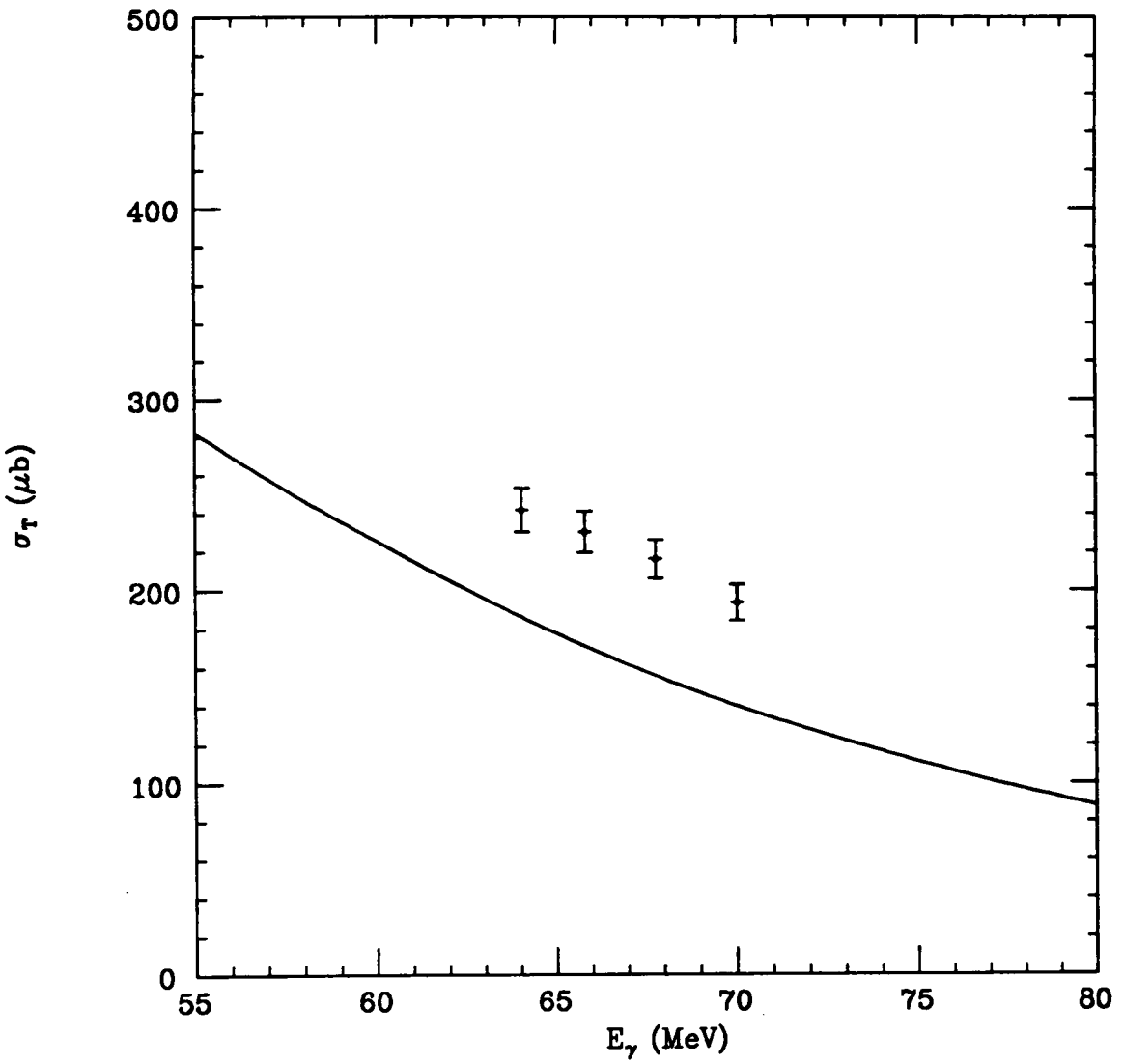

Figure 7.11: Comparison of the present data with the total cross section calculated by Casel and Sandhas. The calculation contains their Born contribution only.

Chapter 8

Summary and Conclusions

The photodisintegration of light nuclei is a unique proving ground for microscopic theories of the strong nuclear interaction. In the energy range between the GDR and the pion threshold, the cross section predominately arises from the two-body electromagnetic currents associated with the exchange of mesons between pairs of nucleons. Deuteron photodisintegration results have shown that these meson-exchange currents can be largely accounted for by the Siegert theorem, which derives the mesonic currents by imposing the requirement of current conservation upon the wave function for the nucleons. Since this result is only exact in the long-wavelength limit (low photon energy), deviations may be expected to occur a few tens of MeV above threshold, which hold important information about the dynamics of mesons within nuclei.

Since the meson-exchange current is a two-body operator, it reflects any correlations which exist between pairs of nucleons. In order to study nucleon correlations, it is necessary to go to nuclei with more than two nucleons, the simplest of which are the $A = 3, 4$ nuclides. Being the lightest nucleus with a binding energy per nucleon roughly equal to the average throughout the periodic table, ^{4}He is a unique nucleus for these studies.

A large solid-angle charged-particle detector (LASA) has been constructed at the University of Illinois Nuclear Physics Laboratory for the measurement of precise differential cross sections for photodisintegration of light nuclei. This device con-

sists of a gas target, operated at room temperature and pressure, surrounded by a three-level cylindrical wire chamber, and an annulus of plastic scintillator split into a thin and a thick part for particle identification. The photon beam is generated by bremsstrahlung of an electron beam on a thin radiator. The post-bremsstrahlung recoil electrons are analyzed in a spectrometer, and used to identify, by means of timing coincidence with the LASA trigger, the energy of the interacting photon.

The first production experiment performed with this device was a dual measurement of ^{2}H [71] and ^{4}He , using the tagged photon beam at the MUSL-II continuous-beam accelerator. These measurements were hampered by the large electromagnetic background which was associated with the photon beam. A rough calculation of the expected background arising from Compton scattering and pair production in the target showed that most of the electrons were coming from the region upstream of the target. With the maximum shielding permitted by the geometry, this was brought low enough for the initial experiment to proceed.

A loose trigger was formed online, in order to guarantee a good efficiency for photodisintegration events, which were at that point buried in the noise. Cuts were imposed during analysis to extract the photodisintegration signal from the dominant background. These cuts included the particle track goodness-of-fit cut, the event vertex cut, the wire dE/dx cut, the plastic dE/dx and total E cut, and the monochromator coincidence cut. In order to select $^4\mathrm{He}(\gamma,\mathrm{p})^3\mathrm{H}$ events over those from the reactions $^4\mathrm{He}(\gamma,\mathrm{pn})^2\mathrm{H}$ and $^4\mathrm{He}(\gamma,\mathrm{ppnn})$, a set of cuts was imposed on the relative angle of the pair of tracks associated with photodisintegration events, requiring them to be consistent with two-body kinematics. After the final cuts were imposed, the contamination from electrons was statistically consistent with zero, and that from the three-body and four-body breakup channels was at the level of 2.8%.

After the final sample of events was obtained, the contribution from random coincidences with the monochromator had to be subtracted from the angular distri-

bution spectra. A careful analysis of the efficiency for p,^{3}H events was performed, including the detector acceptance, track efficiency, and the inefficiency arising from each of the cuts mentioned above. The final differential cross section was reported in 35 data points between the c.m. angles of 36° and 141° , the average statistical error on each point being under 5%. An analysis of the systematic uncertainties inherent in the experiment and analysis procedure yielded an overall normalization error of 3%.

These data were then divided up into four photon-energy bins of 2 MeV each, centered at 64, 66, 68, and 70 MeV. The total cross section reported at each energy was assigned a total error of 5%. The angular distributions were fitted to a Legendre expansion including terms up to $P_3(\cos\theta)$. The precision on the coefficients a_1, a_2, and a_3 from this expansion are at the level of 15%, 20%, and 30% respectively.

These data are in good agreement with the previous data of Gorbunov [13]. The asymmetry coefficient β predicted by the quasi-deuteron calculation of Noguchi and Prats [35] is in agreement with the present results. The augmented shell-model calculation by Gari and Hebach [10] gives a total cross section result which lies above the data by 25%. Nevertheless, the calculation shows that it is necessary to augment the shell-model picture with both nucleon correlations and meson-exchange currents in order to obtain the observed cross section. The "exact" few-body calculation of Casel and Sandhas, including only E1 transitions and neglecting final-state interactions, falls below the data by 15%. The data available when these calculations were published were consistent with their results, within the experimental error. It is hoped that the new data will prompt further refinements to these promising theoretical approaches.

The results presented in this thesis are the first of a sequence of measurements with the LASA detector, which are planned to cover the energy region from photodisintegration threshold up to 100 MeV. The major experimental obstacle is the elimination of the large electromagnetic background. Work is underway both to

reduce the flux of background in the detector, and to develop a more sophisticated event trigger, which can reject most of the background online.

The other major goal is to extend the measurement to angles smaller than 36° and larger than 141° . This limit was imposed by the requirement that both the proton and the triton track had to be within the geometric limits of the detector. Now that the detector response is well understood, these data can be re-analyzed, only requiring the proton track to be complete, and estimating by comparison with the present results, the amount of three-body and four-body cross section to be subtracted. The three-body and four-body breakup cross sections are also interesting in themselves, and very little data for these channels presently exist. The cross section for these reactions contains new information about the correlations between nucleons in the nucleus. Further analysis, along these lines, of the present data is currently underway, and plans are being made to extend the measurements down to threshold and up to 100 MeV.

References

[1] T. DeForest and J. D. Walecka, Advances in Physics **15**, 1 (1966).

[2] M. A. Preston and R. K. Bhaduri, *Structure of the Nucleus* (Addison-Wesley, Reading, Massachusettes, 1975).

[3] H. Arenhovel, Nuovo Cimento **76A**, 256 (1983).

[4] E. Hadjimichael and D. P. Saylor, Physical Review Letters **45**, 1776 (1980).

[5] I. M. Barbour and A. C. Phillips, Physical Review **C1**, 165 (1970).

[6] B. F. Gibson, Nuclear Physics **A353**, 85c (1981).

[7] D. D. Faul, B. L. Berman, P. Meyer, and D. L. Olson, Physical Review **C24**, 849 (1981).

[8] J. Carlson, V. R. Pandharipande, and R. B. Wiringa, Nuclear Physics **A401**, 59 (1983).

[9] F. D. Santos, S. A. Tonsfelt, T. B. Clegg, E. J. Ludwig, Y. Tagishi, and J. F. Wilkerson, Physical Review **C25**, 3243 (1982).

[10] M. Gari and H. Hebach, Physics Reports, **72**, 1 (1981).

[11] H. Hebach, Nuovo Cimento **76A**, 231 (1983).

[12] D. M. Skopik and W. R. Dodge, Physical Review **C6**, 43 (1972).

[13] A. N. Gorbunov, P. N. Lebedev Institutes of Nuclear Physics **71**, 57 (1974).

[14] Yu. M. Arkatov, P. I. Vatset, V. I. Voloshchuk, I. M. Prokhorets, A. F. Khodyachikh, and V. I. Chmil, Soviet Journal of Nuclear Physics **16**, 6 (1973).

[15] M. M. Giannini and G. Ricco, Nuovo Cimento **8**, 1 (1985).

[16] A. J. F. Siegert, Physical Review **52**, 787 (1937).

[17] J. T. Londergan and C. M. Shakin, Physical Review Letters **28**, 1729 (1972).

[18] A. H. Chung, R. G. Johnson, and T. W. Donnelly, Nuclear Physics **A235**, 1 (1974).

[19] D. Halderson and R. J. Philpott, Physical Review Letters **42**, 36 (1979).

[20] D. Halderson and R. J. Philpott, Nuclear Physics **A359**, 365 (1981).

[21] J. A. Tjon, Physical Review Letters **40**, 1239 (1978).

[22] J. G. Zabolitzky and M. H. Kalos, Nuclear Physics **A356**, 114 (1981).

[23] J. A. Tjon, Nuclear Physics **A353**, 47c (1981).

[24] F. C. Barker, Australian Journal of Physics **37**, 583 (1984).

[25] H. M. Hofmann, W. Zahn, and H. Stöwe, Nuclear Physics **A357**, 139 (1981).

[26] B. Wachter, T. Mertelmeier, and H. M. Hofmann, Physical Review **C38**, 1139 (1988).

[27] N. de Botton, Lecture Notes in Physics **108**, 339 (1979).

[28] W. Böttger, A. Casel, and W. Sandhas, Physical Letters **92B**, 11 (1980).

[29] I. Elminyawi and J. S. Levinger, Physical Review **C28**, 82 (1983).

[30] P. Christillin, Preprint **IFUP TH-84/20**, Istituto Nationale di Fisica Nucleare, Pisa, Italy (1984).

[31] S. Boffi, Nuovo Cimento **76A**, 186 (1983).

[32] B. F. Gibson, Nuclear Physics **A416**, 503c (1984).

[33] A. Casel and W. Sandhas, Czech. Journal of Physics **36**, 300 (1986).

[34] S. A. Sofianos (private communication).

[35] J. S. Levinger, Physical Review **84**, 43 (1951).

[36] C. T. Noguchi and F. Prats, Physical Review **C14**, 1133 (1976).

[37] W. Glöckle, *The Quantum Mechanical Few-Body Problem* (Springer-Verlag, New York, 1983).

[38] J. S. McCarthy, I. Sick, and R. R. Whitney, Physical Review **C15**, 1396 (1977).

[39] V. A. Goldstein, E. L. Kuplennikov, R. I. Jibuti, and R. Y. Kezerashvili, Nuclear Physics **A355**, 333 (1981).

[40] J. F. J. van den Brand, H. P. Blok, R. Ent, E. Jans, G. J. Kramer, J. B. J. M. Lanen, L. Lapikas, E. N. M. Quint, G. van der Steenhoven, P. K. A. de Witt Huberts, Physical Review Letters **60**, 2006 (1988).

[41] W. R. Dodge and J. J. Murphy, Physical Review Letters **28**, 839 (1972).

[42] B. F. Gibson and H. T. Williams, Nuclear Physics **A163**, 193 (1971).

[43] D. S. Gemmel and G. A. Jones, Nuclear Physics **33**, 102 (1962).

[44] W. E. Meyerhof, M. Suffert, and W. Feldman, Nuclear Physics **A148**, 211 (1970).

[45] R. C. McBroom, H. R. Weller, N. R. Roberson, and D. R. Skopik, Physical Review **C25**, 1644 (1982).

[46] J. R. Calarco, S. S. Hanna, C. C. Chang, E. M. Diener, E. Kuhlmann, and G. A. Fisher, Physical Review **C28**, 483 (1983).

[47] B. L. Berman, S. C. Fultz, and M. A. Kelly, Physical Review **C4**, 723 (1971).

[48] C. K. Malcom, D. V. Webb, Y. M Shin, and D. M. Skopik, Physics Letters **47B**, 433 (1973).

[49] J. D. Irish, R. G. Johnson, B. L. Berman, B. J. Thomas, and K. G. McNeill, Canadian Journal of Physics **53**, 802 (1975).

[50] F. Balestra, E. Bollini, L. Busso, R. Garfagnini, C. Guaraldo, G. Piragino, R. Scrimaglio, and A. Zanini, Nuovo Cimento **38A**, 145 (1977).

[51] B. L. Berman, D. D. Faul, P. Meyer, and D. L. Olson, Physical Review **C22**, 2273 (1980).

[52] L. Ward, D. R. Tilley, D. M. Skopik, N. R. Roberson, and H. R. Weller, Physical Review **C24**, 317 (1981).

[53] H. R. Weller, N. R. Roberson, G. Mitev, L. Ward, and D. R. Tilley *et al.*, Physical Review **C25**, 2111 (1982).

[54] ***Physics with MAMI A***, Report by Institut für Kernphysik, Mainz, Germany, 1988, p. 212.

[55] J. R. Calarco, B. L. Berman, and T. W. Donnelly, Physical Review **C27**, 1866 (1983).

[56] G. D. Wait, S. K. Kundu, Y. M. Shin, and W. F. Stubbins, Physics Letters **33B**, 163 (1970).

[57] S. E. Kiergan, A. O. Hanson, and L. J. Koester, Physical Review **C8**, 431 (1973).

[58] P. E. Argan, Nuclear Physics **237**, 447 (1975).

[59] J. Arends, J. Eyink, A. Hegerath, H. Hartmann, B. Mecking, G. Nöldeke, and H. Rost, Nuclear Physics **A322**, 253 (1979).

[60] R. A. Shumacher, J. L. Matthews, W. W. Sapp, R. S. Turley, G. S. Adams, and R. O. Owens, Physical Review **C33**, 50 (1986).

[61] A. N. Gorbunov, JETP Letters **8**, 88 (1968).

[62] Y. M. Arkatov, P. I. Vatset, V. I. Volshchuk, V. V. Kirichenko, I. M. Prokhorets, A. F. Khodyachikh, Soviet Journal of Nuclear Physics **12**, 123 (1971).

[63] Y. M. Arkatov, P. I. Vatset, V. I. Voloshchuk, V. N. Gur'ev, V. A. Zolenko, and I. M. Prokhorets, JETP Letters **28**, 660 (1978).

[64] J. Uegaki, L. O. Dallin, and Y. M. Shin, Nuclear Instruments and Methods **179**, 55 (1981).

[65] B. L. Berman and S. C. Fultz, Reviews of Modern Physics **47**, 713 (1975).

[66] W. E. Meyerhof, W. Feldman, S. Gilbert, and W. O'Connell, Nuclear Physics **A131**, 489 (1969).

[67] J. M. Poutissou and W. Del Bianco, Nuclear Physics **A199**, 517 (1973).

[68] W. E. Meyerhof and S. Fiarman, *Proceedings of the International Conference on Photonuclear Reactions, Asilomar, Ca.*, 385 (1973).

[69] Dennis Wright, Ph.D. Thesis, University of Illinois, 1984.

[70] D. F. Measday, M. R. Menard and J. E. Spuller, *Kinematics Handbook*, TRIUMF internal report.

[71] Jonathan E. Knott, Ph.D. Thesis, University of Illinois, 1988.

[72] H. B. Jensen, *et al.*, IEEE Transactions in Nuclear Science **NS-33**, 40 (1986).

[73] F. Sauli, *Principles of Operation of Multiwire Proportional and Drift Chambers*, CERN Report **77-09**, 1977.

[74] R. T. Jones, Nuclear Instruments and Methods **A269**, 550 (1987).

[75] J. Fischer, A. Hrisoho, V. Radeka, and P. Rehak, Nuclear Instruments and Methods **A238**, 249 (1985).

[76] R. Madey, F. M. Waterman, A. R. Baldwin, and J. N. Knudson, Nuclear Instruments and Methods **151**, 445 (1978).

[77] R. T. Jones, *Fifth Conference on Real-Time Computer Applications in Nuclear, Particle, and Plasma Physics*, IEEE Transactions on Nuclear Science **NS34-4**, 917 (1987).

[78] V. White, P. Heinicke, E. Berman, P. Constanta-Fanourakis, B. MacKinnon, C. Moore, T. Nicinski, D. Petravic, R. Pordes, and L. Quigg, *Fifth Conference on Real-Time Computer Applications in Nuclear, Particle, and Plasma Physics*, IEEE Transactions on Nuclear Science **NS34-4**, 763 (1987).

[79] J. H. Hubbell, *Photon Cross Sections, Attenuation Coefficients, and Energy Absorption Coefficients from 10 keV to 100 GeV*, National Bureau of Standards **NSRDS-NBS 29**, 1969.

[80] B. Maréchal and M. Silva da Costa, Nuclear Instruments and Methods **A243**, 148 (1986).

[81] R. Brun, F. Bruyant, M. Maire, A. C. McPherson, and P. Zanarini, *GEANT3 User's Guide*, CERN report **CERN-DD/EE/84-1**, 1986.

[82] J. Motz, H. Olsen, and H. Koch, Reviews of Modern Physics **41**, 581 (1969).

[83] Y. Tsai, Reviews of Modern Physics **46**, 815 (1974).

[84] L. Wright, K. Sud, and D. Kosik, Physical Review **C36**, 562 (1987).

[85] P. Hough, Physical Review **74**, 80 (1948).

[86] V. Votruba, Bull. Intern. Acad. Tcheque des Sciences **49**, 19 (1948).

[87] M. Berger and S. Seltzer, *Tables of Energy-Losses and Ranges of Electrons and Positrons* in *Studies in Penetration of Charged Particles in Matter*, National Academy of Science – National Research Council Publication **1133**, Nuclear Science Series Report **39**, 205 (1964).

[88] C. Williamson, J. Boujot, and J. Picard, *Tables of Range and Stopping Power of Chemical Elements for Charged Particles of Energy .5 to 500 MeV*, Center of Nuclear Studies of Saclay Report **CEA-R302**, 1966.

[89] R. A. Fisher, *Statistical Methods for Research Workers* (Hafner Publishing Company, New York, 1948).

The vita has been removed from the scanned document